BAYESIAN INFERENCE OF PLASTIC PROPERTIES FROM INDENTATION

A Dissertation

by

YUPENG ZHANG

Submitted to the Graduate and Professional School of
Texas A&M University
in partial fulfillment of the requirements for the degree of

DOCTOR OF PHILOSOPHY

Chair of Committee,	Alan Needleman
Committee Members,	George M. Pharr
	Jeffrey D. Hart
	Michael J. Demkowicz
Head of Department,	Ibrahim Karaman

December 2021

Major Subject: Materials Science and Engineering

ABSTRACT

This dissertation concerns the relation between the response of materials in an indentation test and their inelastic mechanical properties. The connection between indentation responses and inelastic properties is not straightforward and may not be unique. A Bayesian-type statistical approach is developed to overcome this difficulty. In this approach, a finite subset of the possible parameter space is considered since the range of physically possible parameter values is known. Finite element indentation calculations are carried out for a relatively coarse grid of discrete property values. Interpolation of indentation responses is used to obtain predictions for material property values between grid points. A uniform initial probability is assigned to each prediction. This overcomes the disadvantage typically associated with using Bayesian statistics of a large number of calculated responses being needed for what is in principle an infinite parameter space. Various elastic-plastic constitutive descriptions have been considered including rate-independent isotropically hardening plastic materials, plastically compressible materials and power-law creep materials. In all cases computed, synthetic "experimental" indentation responses are used for the parameter identification. In order to overcome the non-uniqueness associated with identification based on using only the indentation force versus indentation depth response, the surface profile after unloading is taken to be an additional "measured" quantity. Both noise-free and noise-contaminated data is considered.

We start by considering conical indentation of a rate-independent isotropically hardening solid with power-law strain hardening. It is known that materials with very different uniaxial responses can give indistinguishable indentation force versus indentation depth responses. Three sets of values of flow strength and strain hardening exponent are considered that give indistinguishable indentation force versus indentation depth responses. The proposed Bayesian-type statistical approach, by additionally taking account of residual surface profiles, provides a good estimate of the uniaxial stress-strain response for all three materials, both in the absence of fluctuations and

in the presence of sufficiently small fluctuations. It is found that the sensitivity of the representation of the predicted uniaxial stress-strain response to fluctuations increases with increasing strain hardening.

Subsequently, motivated by the fact that the form of strain hardening relation that gives the best fit for a material is usually not known a priori, we study the influence of assumed strain hardening relations on plastic stress-strain response identification. We consider four power-law expressions as characterizations of the plastic uniaxial stress-strain response. Each expression is characterized by two material parameters, an initial flow strength and a strain hardening exponent. We found that each expression can provide a good representation of the same uniaxial stress-strain response but with different parameter values. The results obtained show that the identification of the hardening relation parameters and the associated uniaxial stress-strain response is not very sensitive to the form of the power-law strain hardening relation chosen even with data that has significant noise.

We then consider plastically compressible materials that are characterized by three material parameters. The "experimental" spherical indentation responses are obtained using two sets of parameter values that characterize the uniaxial responses of two real materials. We assume the materials can be characterized by a Deshpende-Fleck constitutive relation. The uniaxial stress-strain responses obtained by the Bayesian-type statistical approach provide good approximations of those of the "experimental" input materials, but the quality of the approximation decreases with increasing noise amplitude. The indentation force versus indentation depth responses with very different uniaxial stress-strain curves is found to be indistinguishable if the indentation depth is sufficiently small but are distinguishable if the indentation depth is sufficiently large. Plastic compressibility is found to have a relatively small effect on the correction factor in the Oliver-Pharr relation between the unloading slope and the effective (or reduced) elastic modulus. It is also found that the indentation response of these plastically compressible materials can be well-represented by a nearly incompressible plastic constitutive relation but that the inferred uniaxial stress-strain response is a poor representation of the "experimental" material uniaxial stress-strain response.

For materials that exhibit strong time and rate dependence, i.e. creep, the indentation depth versus time response is measured rather than the indentation force versus indentation depth. We consider power-law creep materials where the inelastic response is apparently characterized by two parameters, a creep exponent and a pre-exponential factor. However, the dimensions of the pre-exponential factor depend on the value of the creep exponent and comparing responses of different power-law creep materials requires consideration of three parameters, the creep exponent, a representative stress and a representative strain rate. Constant load and hold indentation creep tests are simulated for parameter values representative of three real materials. Uniaxial creep and uniaxial stress relaxation responses using the identified creep parameters from the Bayesian-type statistical approach were found to provide a very good approximation to the "experimental" responses for a sufficiently small values of creep exponent but a less good agreement for the largest value of creep exponent considered. The sensitivity to noise also increases with increasing stress exponent. The uniaxial creep response is found to be more sensitive to the accuracy of the predictions than the uniaxial stress relaxation response. As for time independent materials, the sensitivity to noise also increases with increasing stress exponent. The uniaxial creep response is found to be more sensitive to the accuracy of the predictions than the uniaxial stress relaxation response. A good agreement with the indentation response does not guarantee good agreement with the uniaxial responses. Comparison of the Bayesian-type statistical predictions for parameter values with the analytical models is carried out.

The Bayesian statistics formulation here used to relate indentation measurements to material properties has heuristic aspects. In order to provide a framework for relating that approach to a more rigorous Bayesian formulation for material property identification from experimental measurements, a Bayesian formulation with a normal likelihood quantifying noise and an inverse gamma prior expressing uncertainty about noise variance is derived. Using both analyses and numerical simulations, we show that the Bayesian-type statistical approach used in the studies of this thesis is a limiting form of the more rigorous formulation, with recommended prior parameter values of the rigorous Bayesian formulation. The results also show that the posterior probabilities

are insensitive to the choice of prior mode when the prior's shape parameter is taken to be small. With consideration of bias in measured signals especially when multiple signal types are analyzed simultaneously, a method using a weighted average of posterior distributions from different signal types is proposed. This method is compared with a classical Bayesian approach that uses a joint likelihood.

DEDICATION

In memory of my great-grandfather who gave me my name and united our large family.

ACKNOWLEDGMENTS

First and foremost I would like to express my greatest gratitude to my advisor Professor Alan Needleman for his guidance, inspiration and mentorship throughout my graduate research at Texas A&M University. My Ph.D. research significantly benefits from his profound insights in the broad fields of mechanics, statistics, material science and scientific computing. He has helped me grow immensely as a researcher, writer and speaker.

I would like to express my greatest gratitude to the members of my committee: Prof. Jeffrey D. Hart, Prof. George M. Pharr and Prof. Michael J. Demkowicz. Thank Prof. Hart very much for his guidance and inspiration on Bayesian statistics since the beginning of my Ph.D. work and his continuing mentorship even after his retirement from Texas A&M University. Thank Prof. Pharr very much for his guidance and mentorship on theory and practical experimental techniques of indentation and also discussion on specific topics for example indentation creep. Thank Prof. Pharr again for having me work in his lab and learn from colleagues in the lab. Thank Prof. Demkowicz very much for his guidance and mentorship on my faculty application package and his always insightful questions after talks.

I would like to express sincere gratitude to my colleagues at Texas A&M University: Prof. Amine Benzerga, Prof. Ankit Srivastava, Prof. Xiaofeng Qian, Prof. Ian McCue, Dr. Hepeng Ding, Dr. Babak Kondori, Prof. Jian-feng Wen, Prof. Mengying Liu, Dr. Yu Liu, Dr. Manish Vasoya, Dr. Guanglu Zhang, Prof. Hua Wang, Dr. Yuwei Zhang, Dr. Xinzhu Zheng, Wesley Higgins, Edwin Chiu, Alex Strasser, Lily Li and Dr. Tianyi Zhou. I would also like to thank my fellow graduate students for good times inside and ouside of lab: Dr. Ali Sangghaleh, Dr. Sanket Navale, Dr. Lei Xu, Dr. Baiyu Zhang, Prof. Peng Chen, Daniel Willhelm, Nathan Wilson, Ben Hackett, Daniel Lewis, Prof. Yang Yang, Haiying Yang and Xiuyu Tang.

I would also take this opportunity to express my greatest gratitude to Prof. Gengdong Cheng who recommended me to Prof. Needleman in 2014. I sincerely appreciate Prof. Biaosong Chen for providing a research assistant position for years in my undergraduate. I sincerely appreciate

Prof. Chunqiu Yang, Prof. Jun Yan, Prof. Haijun Peng, Prof. Sheng Zhang, Prof. Qinglin Duan, Prof. Rui Li and Kaijun Dong for their help in my undergraduate and continuing encouragements nowadays.

I would like to give a special gratitude to my friends: Prof. Yanfei Gao (University of Tennessee), Dr. Jin Yang (University of Wisconsin-Madison), Prof. Ruobing Bai (Northeastern University) for their insightful questions after talks and valuable advice. Thank Dr. Yabin Xiao for Dr. Yuntao Zeng for their insightful advice when I was in high school.

I thank Michael Elverud in the Machine shop of Materials Science and Engineering Department for his help with materials preparation. I thank the former and current staff of the Materials Science and Engineering Department: Erin Bandza, Jules Henry, Murat Kaynak, Sheri Stebenne, Sheila Dotson, Aida Carrillo and Christopher Crouch. There are so many people who helped me but I do not even know their names, thank you to all who helped me, your help made my life easier.

Finally, I am very grateful for the understanding and support from my family. I sincerely appreciate the love from my mother who always encourages me to follow my heart. Thank all who have helped me without you I would never come so far.

CONTRIBUTORS AND FUNDING SOURCES

Contributors

This work was supported by a dissertation committee consisting of Professors Alan Needleman (chair of the committee), George M. Pharr and Michael J. Demkowicz of the Department of Materials Science and Engineering and Professor Jeffrey D. Hart of the Department of Statistics.

All the work conducted for the dissertation was completed by the author.

Funding Sources

Only internal Texas A&M funding has been received for this dissertation.

TABLE OF CONTENTS

Page

LIST OF FIGURES

FIGURE Page

LIST OF TABLES

TABLE Page

1. INTRODUCTION

"In science, progress is possible. In fact, if one believes in Bayes' theorem, scientific progress is inevitable as predictions are made and as beliefs are tested and refined."

– Nate Silver

1.1 The meandering story of Bayes' theorem

The story began with Thomas Bayes, a Presbyterian minister lived outside of London in the early 1700s. Bayes tried to mathematically deal with the issue of cause and effect. He proposed a simple theorem that we could modify our initial guess (belief) with objective new information and get an updated belief. The theorem was filed away in a manuscript but did not get published by Bayes. After Bayes died, his friend Richard Price edited Bayes' notes containing Bayes' theorem. The resulting paper was published in the Philosophical Transactions of the Royal Society in 1763 [5].

In 1774, Pierre-Simon Laplace discovered the Bayes' theorem independently [6] (an English translation was published in 1986 [7]). Laplace used Bayesian in some of his later publications and it was his influential work that led to progress on the use of Bayes' theorem in probability and statistics [8, 9]. On the other hand, Lapalce also advocated for frequency based classical probability analyses and did significant contributions [8], for example, Lapalce helped establish the central limit theorem [10]. More discussion of the objective and subjective probability theory in mid-nineteenth century Britain was given by [11].

While Bayes' theorem dealt with belief, frequency based probability seemed to provide a more objective assessment. In the decades after Laplace's death the frequency approach to probability became dominant, the Bayesian approach was regarded as non-objective and fell out of fashion well into the 20th century. An eminent statistician and geneticist who was an opponent of the

Bayesian approach, Ronald Fisher, stated "The theory of inverse probability is founded upon an error, and must be wholly rejected" [12]. Indeed, "many statisticians were hostile to the Bayesian approach in statistical inference and 'Bayes' was a word to avoid for decades into the 20th century" according to S. B. McGrayne [13]. Luckily, there were a few defenders, one of them was Harold Jeffreys, who was a colleague and (surprisingly) a friend of Fisher at Cambridge University. Jeffreys kept Bayes' theorem alive and his book *Theory of Probability*, published right before the World War II, was the only book on systematic application of Bayes' theorem to scientific problems at that time [14].

Then World War II began and shed light on the modern revival of Bayesian statistics. One application was the use by Alan Turing and his coworkers on "deciphering the Enigma word scrambling machines used by German army, air force, navy, paramilitary and high command" [13]. One example was the team of U-boats, which could cut the food and strategical supplies of Allies of World War II. The story of Bayes' theorem at Bletchley Park on coding and decryption, especially on the main Japanese naval cipher JN 25, was described by Edward Simpson [15]. After Germany surrendered, astonishing but expectable, "Winston Churchill ordered to destroy all the materials on decryption, the relevant studies, e.g., sequential statistics, empirical Bayes, Markov chains, decision theory and electronic computers, were all ultraclassified" according to S. B. McGrayne [13]. Thus the contribution of Bayes' theorem to ending the World War II was unknown to the public.

In the middle of 1900s, one application of Bayes' theorem was by Arthur Bailey on calculation of the premium rate in insurance industry [16]. In academia, statisticians Leonard Jimmie Savage and Dennis Lindley advocated Bayes' theorem in United State and Britain, respectively [17, 18, 19, 20, 21]. Meanwhile, Bayes' theorem was used to provide statistical relation between possible causing factors and lung cancer and provide proof in medicine [22, 23, 24, 25].

In recent years the use of Bayesian methodology has grown explosively, mainly because computing challenges in its application have been overcome with the advent of Markov Chain Monte Carlo (MCMC) [26]. One of the most common MCMC methods is the Metropolis-Hastings algorithm primarily developed by Metropolis et al. in 1953 [27] and Hastings in 1970 [28], which

made numerical approximation of the probability distribution with high dimensions possible. Subsequently, Bayesian statistics has been applied in a wide range of areas, for example, analysis of image [29, 30, 31], exploration of gating mechanisms [32], Quantification of semiconductor composition [33], analysis of epidemics [34, 35], exploration of the reason that gene patterns differ in nuclear and mitochondrion for insects [36], assessment of radiation dose absorbed by an individual [37], control of material damage [38], applications in nuclear physics [39, 40], estimation of fatigue life [41], early warning and post analysis of earthquake [42, 43, 44], identification of elastic or plastic properties [45, 2, 46] and control of autonomous vehicles system [47].

1.2 Characterization of material properties

A material property is a parameter that quantifies how a material responds to a variety of initial/boundary conditions. The properties can be chemical, magnetic, electrical, thermal, mechanical or optical. Here we focus on mechanical properties, which are quantities associated with a constitutive theory that purports to represent its mechanical behavior in some range of circumstances. However, it is important to recognize that a property is not a characteristic of a material but is a parameter entering a constitutive description.

Mechanical tests are carried out to measure material properties. One use of such measured properties is to use the constitutive theory, with the measured properties, to predict the mechanical response of the material under loading conditions that differ from those in the tests. Another use is to order materials regarding their suitability for a particular application.

Characterization of material properties has been performed on a variety of materials and in significantly wide fields, for example, on human red blood cell to investigate connection between single cell mechanics and malaria [48], on ovine mitral valve anterior for development of bioprosthetic values [49], on gray and white matter brain tissue to understand the mechanical environment in neurodevelopment and neurological disorders [50], on violently-collapsing cavitation bubbles to expand the applicability and robustness of Inertial Microcavitation Rheometry in properties characterization [51], on lead-free solders to prevent failure behavior during isotherrmal aging [52], on heat-damaged concrete to evaluate the safety of nuclear reactors [53], on cancer cells to study

the time evolution of cells' mechanical behavior [54, 55], and on healing bones to monitor and evaluate the fracture healing process [56].

Bayesian statistics has been used in characterization of material properties. For example, electromechanical properties in piezoelectric energy harvesters [57], physical properties of yeast chromatin [58], optical properties of nearshore estuarine water [59], spatial distribution of elastic properties [45], elastic parameters of micro-swimmers [60], plastic properties of plastically compressible solids [46] and creep parameters [4].

1.3 Instrumented indentation

Instrumented indentation has been used to quantify indentation hardness of materials since the middle of 1900s [61, 62, 63]. Theoretical analyses have been carried out on fundamental issues, for example, analytical solutions of elastic contact and recovery [64, 65], slip-line field of rigid perfect plastic solids [66], application of expanding cavity model to indented material [67], theoretical study of the Brinell hardness test [68], and analytical solution of deformation fields in creeping solids [69].

Significant progress has been made on indentation techniques, for example, estimation of Young's modulus from load and depth sensing indentation [70], early development of nanoindentation [71, 72, 73], development of Oliver-Pharr method for determination of hardness and elastic modulus [74, 75], influence of pile-up and sink-in [76, 77, 78], measurement of residual stress [79], and introduction of the concept of effective indenter shape [80]. Relevant reviews are available on specific topics, for example, on the techniques for nanoindentation testing [81], and on the indentation size effect [82].

The basic idea of instrumented indentation is simple, i.e. use an indenter of known material to punch a specimen of unknown material and leave an impression. Most indentation instruments are force controlled, indeed the strain rate of loading can be set for an indentation test, but the strain rate is actually calculated by feedback control of the indentation load. According to the magnitude of indentation load, indentation tests can be specified as macro-indentation, micro-indentation and nanoindentation.

A variety of indenter shapes have been developed for extraction of different mechanical properties from diverse materials. According to the variation of the ratio between contact distance and indentation depth, indenters can be divided into two types: indenters with a self-similar geometry such as pyramid, cone, Berkovich, Vickers, and indenters that do not have a geometrical similarity, such as sphere. However, a spherical indenter can generate self-similar results with a varying radius.

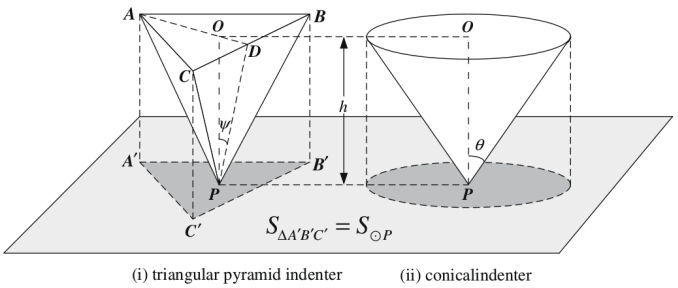

Figure 1.1: Illustration of a triangular pyramid indenter with an indenter angle ψ and the corresponding equivalent conical indenter with an indenter angle θ based on the equivalence of projected contact area. (after [1]).

Conical indenter is often used as an effective indenter for other complicated shapes due to its axisymmetry, especially in analytical analysis and numerical simulation. For example, a triangular indenter with an indenter angle ψ can be treated as a conical indenter with an equivalent indenter angle θ in Fig. 1.1. The projected contact area A_{py} at penetration depth h is $3\sqrt{3}h^2tan^2\psi$ for the triangular indenter. While for the conical indenter, the projected contact area A_{cone} is $\pi h^2 tan^2\theta$. We require them to have the same projected contact area at any penetration depth h, this gives

$$\theta = tan^{-1}\sqrt{\frac{3\sqrt{3}}{\pi}tan^2\psi}. \tag{1.1}$$

For a Berkovich indenter with $\psi = 65.3°$, it gives $\theta \approx 70.3°$.

Among all the experimental techniques, indentation, due to its nondestructive, small scale, con-

venience and simplicity, has attracted remarkable attention on the development of characterization methods. In recent decades, many studies have been carried out using various approaches in the attempt to extract plastic material properties from indentation force versus indentation depth data. Examples include using a representative strain, e.g. [83, 84]; using dimensional analysis together with finite element calculations, e.g. [85]; and using neural networks, e.g. [86, 87, 88, 89, 90].

For completeness, the classical plasticity theory, mainly for metals, is briefly summarized in the Appendix A. Besides the software ABAQUS, an in-house finite element code has been used in simulation. For completeness, the finite element formulations for finite plastic deformations in convected coordinates are briefly summarized in the Appendix B.

1.4 Outline of this dissertation

This dissertation proposes a Bayesian formulation for inference of material properties using various types of signals. In Chapter 2, a Bayesian-type statistical approach is proposed to identify plastic properties and distinguish different materials with essentially the same indentation force versus depth responses by additionally taking account of their corresponding residual surface profiles from conical indentation. In Chapter 3, influence of assumed strain hardening relation on plastic stress-strain response identification from indentation is studied and the uncertainty in identified stress-strain responses caused by various noise levels is quantified. In Chapter 4, characterization of plastically compressible materials from spherical indentation is studied by the Bayesian-type statistical approach. In Chapter 5, creep properties (both the exponent and pre-exponential factor in a power law strain rate hardening relation) are identified for three representative materials with various characteristic time scales and length scales from indentation using the Bayesian-type statistical approach. In Chapter 6, a rigorous Bayesian formulation is derived for inference of material properties using various signal types. The relation between the rigorous Bayesian formulation and the Bayesian-type statistical approach is discussed, and effective choices of prior parameters are recommended. Finally in Chapter 7, conclusions are drawn.

2. A BAYESIAN-TYPE STATISTICAL APPROACH FOR IDENTIFICATION OF PLASTIC PROPERTIES FROM CONICAL INDENTATION [†]

"As you will find in multivariable calculus, there is often a number of solutions for any given problem."

– John Forbes Nash Jr.

2.1 Introduction

A mechanical property of a material is a quantity associated with a constitutive theory that purports to represent its mechanical behavior, in some range of circumstances. Mechanical tests are carried out to measure material properties. One use of such measured properties is to use the constitutive theory, with the measured properties, to predict the mechanical response of the material under loading conditions that differ from those in the tests. Another use is to order materials regarding their suitability for a particular application.

Typically, such mechanical tests measure a structural response, not directly a material property, in the sense that the measured response depends on the geometry of the test specimen and the applied load. When the specimen deformation is heterogeneous as in a tension test after necking, in a micro-pillar test with extensive deformation localization and in indentation, relating measured response quantities to material properties is complex and may not even be unique.

In indentation, the indentation force can be measured as a function of indentation depth. For materials that can, at least approximately, be characterized by rate independent, isotropic hardening plasticity with power law strain hardening, one aim of carrying out an indentation test is to determine the flow strength and the strain hardening exponent. For a conical indenter that relation is non-unique, i.e. there is more than one combination of flow strength and strain hardening expo-

[†]Reprinted with permission from "Identification of plastic properties from conical indentation using a Bayesian-type statistical approach" by Yupeng Zhang, Jeffrey D. Hart and Alan Needleman, 2019, Journal of Applied Mechanics, 86, 011002. Copyright © 2019 by American Society of Mechanical Engineers.

nent that will give essentially the same indentation force versus indentation depth response, see for example [91, 92, 93].

Many studies have been carried out using various approaches in the attempt to extract plastic material properties from only indentation force versus indentation depth data. Examples include using a representative strain, e.g. [83, 84]; using dimensional analysis together with finite element calculations, e.g. [85]; and using neural networks, e.g. [86, 87, 88, 89, 90].

More recently, using displacement information from indentation tests in addition to or instead of indentation force versus indentation depth data has been explored. For example, Wang et al. [94] used both the indentation load-displacement curve and maximum pile-up point with finite element analyses to obtain plastic properties of an anisotropic solid. Wang et al. [95] used only the residual imprint of spherical indentation in conjunction with an optimization algorithm based on the difference between measured surface profiles and those obtained from finite element analyses to identify elastic-plastic properties. Mostafavi et al.[96, 97] suggested using vertical components of the displacement field under the indenter together with numerical simulations to quantify plastic properties.

Bayesian statistical approaches are now being used in a wide variety of areas of mechanics of materials, for example in metal fatigue, [98, 99], in constitutive identification [100, 101, 102, 103], in damage mechanics [104, 105], in identification of the spatial distribution of elastic material properties [45] and in identification of plastic properties from spherical indentation [106]. In particular, Fernandez-Zelaia et al. [106] used finite element modeling, construction of a surrogate model and together with a Bayesian framework and Markov Chain Monte Carlo sampling to extract properties associated with an elastic-plastic material model from spherical indentation data.

Here, we consider conical indentation and use both the indentation force versus indentation depth curve and the surface profile after unloading in a simplified Bayesian statistical approach to extract plastic material properties. We begin by solving the indentation problem for three sets of material properties that have essentially identical indentation force versus indentation depth curves and add fluctuations ("noise") to model experimental errors/uncertainties. We then consider this

data set as the "experimental" data from which we attempt to extract material properties. The main focus of our paper is the extent to which the simplified Bayesian statistical approach can identify the uniaxial stress-strain response of these three input materials.

2.2 Indentation problem formulation and numerical method

Indentation of a conical indenter into a half-space is modeled as sketched in Fig. 2.1. In the calculations, indentation into a finite region is analyzed but it is presumed that the size of the region is large enough to model a half-space. The deformations are presumed to be axisymmetric. The indentation depth h is the only length scale. As a consequence, the response is self-similar and independent of h when all length quantities are scaled with h. The nominal contact radius is $r_{\rm nom} = h/\tan\beta$ and the true contact radius $r_{\rm cont}$ is the radial coordinate of the point in contact with the rigid indenter that is furthest from $r = 0$. The indentation force F is the total $z-$direction force acting on the contact area.

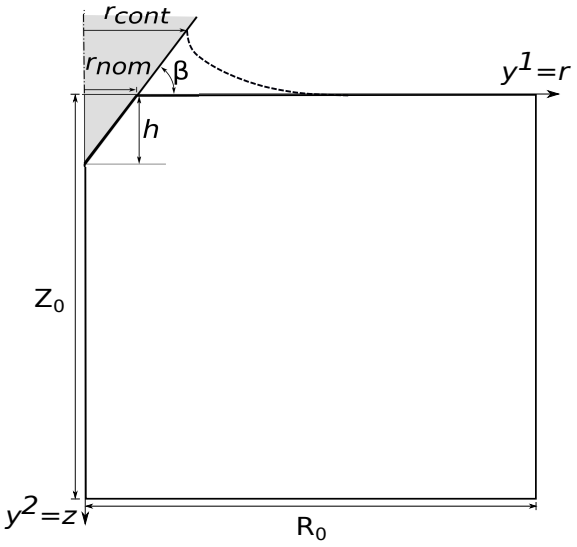

Figure 2.1: Sketch of the indentation configuration analyzed.

The formulation of the indentation problem, except for the constitutive relation, follows that in [107]. A Lagrangian formulation of the field equations is used with attention confined to quasi-

static deformations and body forces neglected. The rate form of the principle of virtual work is written as

$$\begin{aligned}\Delta t \int_V \dot{\mathbf{s}} \cdot\cdot \delta\mathbf{F}\, dV = \Delta t \int_S \dot{\mathbf{T}} \cdot \delta\mathbf{u}\, dS \\ -\Big[\int_V \mathbf{s} \cdot\cdot \delta\mathbf{F}\, dV - \int_S \mathbf{T} \cdot \delta\mathbf{u}\, dS\Big]\end{aligned} \tag{2.1}$$

Here,

$$\mathbf{u} = \mathbf{x} - \mathbf{X}\ ,\ \mathbf{F} = \frac{\partial \mathbf{x}}{\partial \mathbf{X}} \tag{2.2}$$

where $\mathbf{x}$ is the position of a point in the current configuration that was at $\mathbf{X}$ in the reference configuration. The traction vector $\mathbf{T}$ is given by

$$\mathbf{T} = \mathbf{n} \cdot \mathbf{s}\ ,\ \mathbf{s} = \mathbf{F}^{-1} \cdot \boldsymbol{\tau} \tag{2.3}$$

where $\mathbf{n}$ is the surface normal, $\boldsymbol{\tau} = J\boldsymbol{\sigma}$ is the Kirchhoff stress, $\boldsymbol{\sigma}$ is the Cauchy stress and $J = \det(\mathbf{F})$. The rate boundary conditions are

$$\dot{u}_r = 0 \qquad \dot{u}_z = \dot{h} \qquad \text{on} \quad S_{\text{contact}} \tag{2.4a}$$

$$\dot{u}_r = 0 \qquad \dot{T}_z = 0 \quad \text{on} \quad r = 0 \tag{2.4b}$$

$$\dot{u}_z = 0 \qquad \dot{T}_r = 0 \quad \text{on} \quad z = Z_0 \tag{2.4c}$$

and $\dot{\mathbf{T}} = \mathbf{0}$ on the remaining external surface. Eq. (2.4a) corresponds to perfect sticking of the material to the indenter, S_{contact} denotes the portion of the material surface in contact with the indenter and a superposed dot, $(\dot{})$ denotes the time derivative.

The material is characterized as an isotropically hardening elastic-viscoplastic solid. Elastic strains are assumed to be small and are given by

$$\mathbf{d}^{\text{e}} = \mathbf{L}^{-1} : \hat{\boldsymbol{\tau}} = \frac{1+\nu}{E}\hat{\boldsymbol{\tau}} - \frac{\nu}{E}\text{tr}(\hat{\boldsymbol{\tau}})\mathbf{I} \tag{2.5}$$

Table 2.1: Material parameters for three input materials used in the indentation calculations.

	m_1	m_2	m_3
E (GPa)	200	200	200
ν	0.3	0.3	0.3
m	0.005	0.005	0.005
Y (MPa)	650	490	330
N	0.10	0.20	0.31
Y/E	0.00325	0.00245	0.00165

where $\mathbf{L}$ is the fourth order tensor of elastic moduli, E is Young's modulus, ν is Poisson's ratio, $\mathrm{tr}(\cdot)$ denotes the trace, $\mathbf{I}$ is the identity tensor and $\hat{\boldsymbol{\tau}}$ is the Jaumann rate of Kirchhoff stress.

The plastic part of the rate of deformation tensor is taken as

$$\mathbf{d}^{\mathrm{p}} = \frac{3}{2}\frac{\dot{\epsilon}_{\mathrm{p}}}{\sigma_{\mathrm{e}}}\mathbf{p}\ ,\ \mathbf{p} = \boldsymbol{\tau} - \frac{1}{3}\,\mathrm{tr}(\boldsymbol{\tau})\mathbf{I} \tag{2.6}$$

with

$$\dot{\epsilon}_{\mathrm{p}} = \dot{\epsilon}_0 \left(\frac{\sigma_{\mathrm{e}}}{g}\right)^{1/m} . \tag{2.7}$$

Here, $\dot{\epsilon}_0$ is a reference strain rate, m is the rate sensitivity exponent, ϵ_{e} is the von Mises effective stress. The function $g(\epsilon_{\mathrm{p}})$ in Eq. (4.7) is taken to be a power law relation of the form

$$g\left(\epsilon_{\mathrm{p}}\right) = Y\left[1 + \frac{\epsilon_{\mathrm{p}}}{\epsilon_0}\right]^N \tag{2.8}$$

where Y is a reference flow strength and $\epsilon_0 = Y/E$.

For conical indentation into a half-space, the only characteristic length is the indentation depth h. In order to provide a dimensionless length measure, all lengths are normalized by a reference length h_{ref} which is taken to be the maximum indentation depth in the calculations. Also, the time scale is set by the parameter $\dot{\epsilon}_0$ in Eq. (4.7) and the indentation loading rate is taken to be $\dot{h}/(h_{\mathrm{ref}}\dot{\epsilon}_0) = 0.5$ for loading and $\dot{h}/(h_{\mathrm{ref}}\dot{\epsilon}_0) = -0.125$ for unloading. The indenter cone angle β is fixed at 19° (see Fig. 2.1).

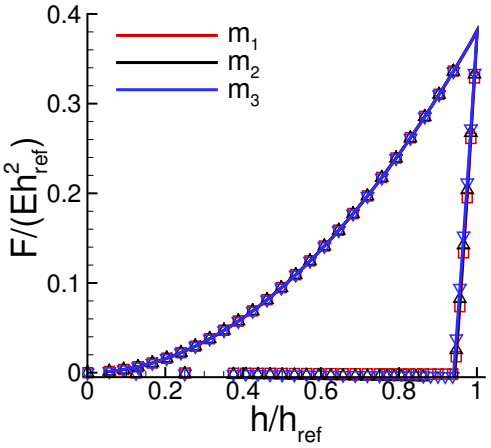

Figure 2.2: Normalized indentation force $F/(Eh_{\text{ref}}^2)$ versus normalized indentation depth h/h_{ref} during loading and unloading for three input materials. The symbols are the points used as the "experimental" values in the statistical calculations ($\boldsymbol{f}^{\text{input}}$). $\square$: m_1, Δ : m_2, ∇ : m_3. The parameters for the three input materials are given in Table 2.1.

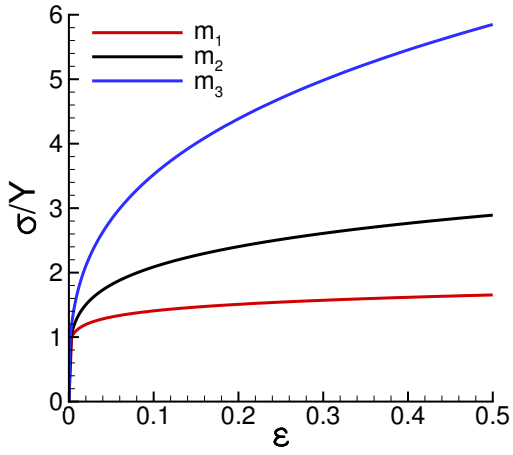

Figure 2.3: Uniaxial stress-strain curves for three input materials. The parameters for the three input materials are available in Table 2.1.

To illustrate the non-uniqueness of the force versus indentation depth response as shown by Cheng and Cheng [91], calculations are carried out for the three sets of material parameters shown

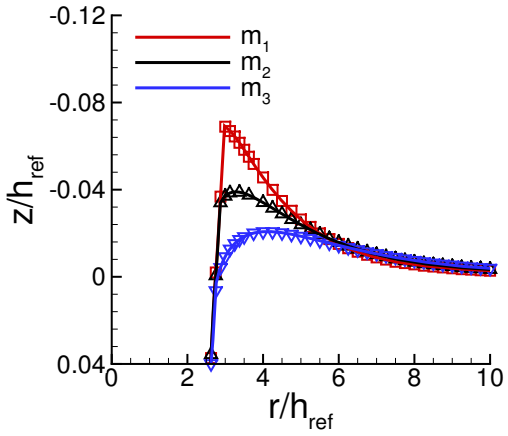

Figure 2.4: Normalized surface profiles near the indenter after unloading for the three input materials. The symbols are the points used as the "experimental" values in the statistical calculations ($\boldsymbol{s}^{\text{input}}$). $\square$: m_1, Δ : m_2, ∇ : m_3. The parameters for the three input materials are given in Table 2.1.

in Table 2.1. The elastic properties and strain rate sensitivity exponent m are fixed, with a small value of m used to give nearly rate independent response. As Fig. 2.2 shows the indentation force F versus indentation depth h responses are indistinguishable although the uniaxial stress-strain responses are very different as shown in Fig. 2.3. In Fig. 2.3 and subsequently, uniaxial stress-strain responses are shown for $\dot{\epsilon}_p/\dot{\epsilon}_0 = 1$ when $\sigma_e \geq Y$ and $\dot{\epsilon}_p = 0$ for $\sigma_e \leq Y$.

Fig. 2.4 shows the computed surface profiles near the indenter after unloading of these three materials. The points shown in Figs. 2.2 and 2.4 are interpolated from the calculated curves so that the independent variables, h/h_{ref} in Fig. 2.2, and r/h_{ref} in Fig. 2.4 are identical for all three materials. It is these points that are used as the "experimental" data points in the statistical analyses in Section 2.3.

The finite element calculations are carried out for a finite block with dimensions given by $R_0/h_{\text{ref}} = 37.5$ and $Z_0/h_{\text{ref}} = 37.5$. The finite element mesh consists of 65×58 rectangular elements, with each rectangle consisting of four "crossed" linear displacement triangular elements. A uniform 45×40 rectangular element mesh is used in a $3.75h_{\text{ref}} \times 3.125h_{\text{ref}}$ fine mesh region

near the indenter tip. The deformation history is calculated from Eq. (4.1) in a linear incremental manner.

In the calculations, the contact force F varies in discrete steps when a new nodal point comes in contact with or detaches from the indenter. In order to provide a clearer picture of the indentation response, the "raw" output curves from the computer code are smoothed by plotting the midpoint of the steps for force F versus indentation depth h relation. Such smoothed curves are shown in Fig. 2.2.

Some calculations were repeated with a finer 128×128 finite element mesh to check convergence. The surface profiles obtained using the two meshes essentially coincide except for the maximum extent of the pile-up for material m_1, where as seen in Fig. 2.4 there is a relatively sharp gradient near the indenter surface. The maximum value of $z/h_{\rm ref}$ obtained using the fine mesh is 0.068 while with coarse mesh the corresponding value is 0.069. For materials m_2 and m_3 the maximum values of $z/h_{\rm ref}$ in Fig. 2.4 differ by about 1%. The curves of normalized indentation force versus normalized indentation depth using the two meshes are within $\approx 1.5\%$ for all three materials. All results to be presented subsequently were obtained using the coarse mesh.

In the following, we use a Bayesian statistical approach with the aim of identifying the three uniaxial stress-strain responses of materials m_1, m_2 and m_3 from the indentation force versus indentation depth responses and the surface profiles in Figs. 2.2 and 2.4.

2.3 Bayesian statistical approach

Bayes' theorem can be stated as

$$p(\boldsymbol{\theta}|\boldsymbol{\mathcal{Y}}, \mathcal{M}) = \frac{p(\boldsymbol{\mathcal{Y}}|\boldsymbol{\theta}, \mathcal{M}) p(\boldsymbol{\theta}|\mathcal{M})}{Z} \tag{2.9}$$

where $\mathcal{M}$ is the assumed model, $\boldsymbol{\theta}$ is the vector of unknown parameters associated with $\mathcal{M}$ and $\mathcal{Y}$ are the observed data. The prior probability distribution, $p(\boldsymbol{\theta}|\mathcal{M})$, provides the investigator's probability that $\boldsymbol{\theta}$ is the true set of parameter values before data $\mathcal{Y}$ are observed. The likelihood $p(\boldsymbol{\mathcal{Y}}|\boldsymbol{\theta}, \mathcal{M})$ is the probability of obtaining the data $\boldsymbol{\mathcal{Y}}$ when $\mathcal{M}$ is the true model and the parameters

are $\boldsymbol{\theta}$. The posterior probability $p(\boldsymbol{\theta}|\boldsymbol{\mathcal{Y}}, \mathcal{M})$ is the updated probability (in light of the data) of the parameter values $\boldsymbol{\theta}$. The denominator in Eq. (3.3) is a normalizing constant given by the integral over the entire parameter space as

$$Z = \int_{\boldsymbol{\Theta}} p(\boldsymbol{\mathcal{Y}}|\boldsymbol{t}, \mathcal{M}) p(\boldsymbol{t}|\mathcal{M})\, d\boldsymbol{t} \tag{2.10}$$

The model $\mathcal{M}$ consists of the quasi-static indentation initial/boundary value problem described in Section 2.2 and the idealization of the material as a rate independent isotropic and isotropically hardening solid (even though the calculations are carried out using a viscoplastic constitutive relation). Hence, the plastic material response is characterized by the function $g(\epsilon_p)$ in Eq. (2.8). Assuming that the values of the elastic constants E and ν are known, the aim is, given data $\mathcal{Y}$ corresponding to the data in Figs. 2.2 and 2.4, to determine values of the initial flow strength normalized by the elastic modulus, Y/E, and strain hardening exponent N that provide a good representation of the stress-strain responses for materials m_1, m_2 and m_3 in Fig. 2.3. What is meant by "data corresponding to" is that we consider the responses shown in Figs. 2.2 and 2.4 as the "experimental" data and we also consider variations from those values due to fluctuations arising from experimental noise, including contributions from thermal drift, instrument compliance, imperfect indenter geometry, unknown friction between contact surfaces with certain roughness, measurement errors and calibration variations, etc.

We begin by creating a database of possible responses for various values of Y/E and N. The database consists of a normalized surface displacement, $z/h_{\rm ref}$ versus $r/h_{\rm ref}$ curve, and a normalized indentation force, $F/(Eh_{\rm ref}^2)$, versus normalized indentation depth, $h/h_{\rm ref}$, curve for each value of Y/E and N. For a pair of values $(Y/E)^i$ and N^i, the normalized displacement response, $z/h_{\rm ref}$, is denoted by $\boldsymbol{s}^i$ and the normalized force-normalized displacement response, $F/(Eh_{\rm ref}^2)$, is denoted by $\boldsymbol{f}^i$ with $i = 1, ..., K_{\rm total}$, where $K_{\rm total}$ is the total number of pairs of values $(Y/E)^i$ and N^i in the database. The "experimental" data $\boldsymbol{\mathcal{Y}}$ in Eq. (3.3) is denoted by two data vectors $(\boldsymbol{s}^{\rm m}, \boldsymbol{f}^{\rm m})$. The components of the vector $s_k^{\rm m}$, $k = 1, ..., K_{\rm s}$ are values, $z_k/h_{\rm ref}$ at radial coordinate

$r_k/h_{\rm ref}$, while the components of the vector $f_k^{\rm m}$, $k = 1, ..., K_{\rm f}$ are values of the indentation force $F_k/(Eh_{\rm ref}^2)$ at indentation depth $h_k/h_{\rm ref}$. Each database vector $\boldsymbol{s}^i$ consists of $K_{\rm s}$ points evaluated at $r_k/h_{\rm ref}$ and each database vector $\boldsymbol{f}^i$ consists of $K_{\rm f}$ points evaluated at $h_k/h_{\rm ref}$. Subsequently, $\mathcal{M}$ is no longer included in any expression since the model is fixed.

$$p(\boldsymbol{s}^i, \boldsymbol{f}^i|\boldsymbol{s}^{\rm m}, \boldsymbol{f}^{\rm m}) = \frac{p(\boldsymbol{s}^i|\boldsymbol{s}^{\rm m})p(\boldsymbol{f}^i|\boldsymbol{f}^{\rm m})}{Z_{\rm sf}} \tag{2.11}$$

where there is no sum on i in Eqs. (5.8) to (5.9) and

$$p(\boldsymbol{s}^i|\boldsymbol{s}^{\rm m}) = \frac{p(\boldsymbol{s}^{\rm m}|\boldsymbol{s}^i)p(\boldsymbol{s}^i)}{Z_{\rm s}} \tag{2.12}$$

$$p(\boldsymbol{f}^i|\boldsymbol{f}^{\rm m}) = \frac{p(\boldsymbol{f}^{\rm m}|\boldsymbol{f}^i)p(\boldsymbol{f}^i)}{Z_{\rm f}} \tag{2.13}$$

The normalizing constants $Z_{\rm s}$, $Z_{\rm f}$ and $Z_{\rm sf}$ are given by

$$Z_{\rm s} = \sum_{i=1}^{K_{\rm total}} p(\boldsymbol{s}^{\rm m}|\boldsymbol{s}^i)p(\boldsymbol{s}^i)\ ,\ Z_{\rm f} = \sum_{i=1}^{K_{\rm total}} p(\boldsymbol{f}^{\rm m}|\boldsymbol{f}^i)p(\boldsymbol{f}^i) \tag{2.14}$$

$$Z_{\rm sf} = \sum_{i=1}^{K_{\rm total}} p(\boldsymbol{s}^i|\boldsymbol{s}^{\rm m})p(\boldsymbol{f}^i|\boldsymbol{f}^{\rm m}) \tag{2.15}$$

We also assume that the differences between the "experimental" data and predicted responses in the database are independent and identically distributed as a mean zero normal distribution. The likelihood functions are given by

$$p(\boldsymbol{s}^{\rm m}|\boldsymbol{s}^i) = \prod_{k=1}^{K_{\rm s}} \frac{1}{\hat{\sigma}_{\rm s}^i\sqrt{2\pi}} \exp\left[-\frac{1}{2(\hat{\sigma}_{\rm s}^i)^2}\left(s_k^{\rm m} - s_k^i\right)^2\right] \tag{2.16}$$

$$p(\boldsymbol{f}^{\rm m}|\boldsymbol{f}^i) = \prod_{k=1}^{K_{\rm f}} \frac{1}{\hat{\sigma}_{\rm f}^i\sqrt{2\pi}} \exp\left[-\frac{1}{2(\hat{\sigma}_{\rm f}^i)^2}\left(f_k^{\rm m} - f_k^i\right)^2\right]. \tag{2.17}$$

In Eqs. (2.16) and (2.17), $K_{\rm s}$ and $K_{\rm f}$ are the number of data points on the surface profile curve and the number of data points on the indentation force versus indentation depth curve, respectively.

The variances $(\hat{\sigma}_{\rm s}^i)^2$ and $(\hat{\sigma}_{\rm f}^i)^2$ are given by maximum likelihood estimation as

$$(\hat{\sigma}_{\rm s}^i)^2 = \frac{1}{K_{\rm s}} \sum_{k=1}^{K_{\rm s}} (s_k^{\rm m} - s_k^i)^2 \ , \ (\hat{\sigma}_{\rm f}^i)^2 = \frac{1}{K_{\rm f}} \sum_{k=1}^{K_{\rm f}} (f_k^{\rm m} - f_k^i)^2, \tag{2.18}$$

where the subscript k denotes the kth data point in its corresponding vector.

Using Eq. (A-14) in Eqs. (2.16) and (2.17) gives the following expressions for the likelihood values

$$p(\boldsymbol{s}^{\rm m}|\boldsymbol{s}^i) = \Big(\frac{1}{\hat{\sigma}_{\rm s}^i\sqrt{2\pi}}\Big)^{K_s} \exp\Big(-\frac{K_s}{2}\Big) \tag{2.19}$$

$$p(\boldsymbol{f}^{\rm m}|\boldsymbol{f}^i) = \Big(\frac{1}{\hat{\sigma}_{\rm f}^i\sqrt{2\pi}}\Big)^{K_f} \exp\Big(-\frac{K_f}{2}\Big). \tag{2.20}$$

If the value of a standard deviation, $\hat{\sigma}_{\rm s}^i$ or $\hat{\sigma}_{\rm f}^i$, is very small the corresponding likelihood value in Eq. (3.9) and/or Eq. (3.10) becomes very large. However, due to the normalizations in Eqs. (3.5) and (5.9), the value of the posterior probability remains between 0 and 1. If a standard devaition is exactly zero, the corresponding likelihood is infinite and the posterior probability is set to one.

In the calculations a uniform prior is used:

$$p(\boldsymbol{s}^i) = p(\boldsymbol{f}^i) = \frac{1}{K_{\rm total}} \tag{2.21}$$

thus expressing our ignorance of the correct values of Y/E and N.

Expression (5.10) depends on a sum (rather than an integral as in Eq. (2.10) because of the discreteness of our parameter space for $(\boldsymbol{s}^i, \boldsymbol{f}^i)$. Also, in a formal Bayesian procedure the variances in Eqs. (2.16) and (2.17) would be treated as unknown parameters having a prior distribution. The variances would then be integrated out of the resulting posterior distribution, leading to a marginal posterior for $(\boldsymbol{s}^i, \boldsymbol{f}^i)$. However, it can be shown, see e.g. [108], that our use of the maximum likelihood estimates $(\hat{\sigma}_{\rm s}^i)^2$ and $(\hat{\sigma}_{\rm f}^i)^2$ leads to posterior probabilities that are very close to those of a proper Bayesian procedure when $K_{\rm s}$ and $K_{\rm f}$ become large.

We consider both noise-free and noise-contaminated data. With the computed responses in

Figs. 2.2 and 2.4 denoted by $\boldsymbol{f}^{\mathrm{input}}$ and $\boldsymbol{s}^{\mathrm{input}}$, the noise-contaminated data are given by

$$\boldsymbol{s}^{\mathrm{m}} = \boldsymbol{s}^{\mathrm{input}} + \boldsymbol{s}^{\mathrm{noise}} \ , \ \boldsymbol{f}^{\mathrm{m}} = \boldsymbol{f}^{\mathrm{input}} + \boldsymbol{f}^{\mathrm{noise}}. \tag{2.22}$$

Each component s_k^{noise} and f_k^{noise} is calculated using the MATLAB function normrnd [109]. This distribution has zero mean value and the values of the standard deviations σ_{s} and σ_{f} are taken to be related to the maximum residual depth $\max(s_k^{\mathrm{m}})$ and the maximum indentation force $\max(f_k^{\mathrm{m}})$, respectively, by

$$\sigma_{\mathrm{s}} = \eta_{\mathrm{s}} \max(s_k^{\mathrm{m}}) \ , \ \sigma_{\mathrm{f}} = \eta_{\mathrm{f}} \max(f_k^{\mathrm{m}}) \tag{2.23}$$

with $0 \leq \eta_{\mathrm{s}} < 1$ and $0 \leq \eta_{\mathrm{f}} < 1$.

Given the combinations of $(Y/E)^i, N^i$ chosen for the database, the deformation responses $(\boldsymbol{s}^i, \boldsymbol{f}^i)$ are calculated as outlined in Section 2.2. Then using Eq. (A-4) and the likelihood relations Eqs. (3.9) and (3.10), the posterior probability $p(\boldsymbol{s}^i, \boldsymbol{f}^i | \boldsymbol{s}^{\mathrm{m}}, \boldsymbol{f}^{\mathrm{m}})$ associated with $(Y/E)^i, N^i$ is obtained using Eq. (5.8).

2.4 Inference of the stress-strain response using a Bayesian statistical approach

The initial database is constructed for 20 uniformly spaced values of Y/E varying between 1.0×10^{-3} and 2.0×10^{-2} (so that the step size is 1.0×10^{-3}). The values of N vary between 0 and 1.0 with a step size of 0.02 (51 points), so that there are $K_{\mathrm{total}} = 1020$ combinations of $(Y/E)^i, N^i$ in this database, which is denoted by G_0. For database G_0, one finite element calculation was carried out for each set $(Y/E)^i, N^i$ in the database.

Another database denoted by G_1 is obtained by interpolations between data of nearby points on database grid G_0. G_1 has a step size 2.5×10^{-4} in Y/E and 0.01 in N giving $K_{\mathrm{total}} = 7777$. For these interpolated points, no finite element calculations were carried out. Rather, the components of the vectors $\boldsymbol{s}^i$ and $\boldsymbol{f}^i$ are obtained by linear interpolations of the corresponding vectors of nearby points.

We also explored using a modified database grid in the vicinity of the combination of Y/E and N with the largest posterior probability. The database denoted by G_2 has a locally refined step size

Table 2.2: Predicted values of Y/E, N and values of corresponding highest posterior probability p_1 using database grids G_0 and G_2.

	$(Y/E)_{G_0}$	N_{G_0}	p_{1G_0}	$(Y/E)_{G_2}$	N_{G_2}	p_{1G_2}
m_1	0.003	0.12	1.00	0.00325	0.10	1.00
m_2	0.003	0.14	1.00	0.00270	0.19	0.56
m_3	0.002	0.26	1.00	0.00175	0.31	0.85

in Y/E of 5.0×10^{-5} between nearest neighbors. An automatic refinement approach was used to create the database grid G_f. For database grid G_f the database grid was refined locally with a step size, in both Y/E and N, that is one half of the current step until the value of step size decreases to 6.25×10^{-6} in Y/E and 1.25×10^{-3} in N. Refinements of 3×3 or 5×5 database grids around the highest posterior probability point were used in each iteration. The interpolation procedures for database grids G_2 and G_f were conducted in the same way as for database grid G_1. We emphasize that finite element calculations were only carried out for the initial, coarsest database grid G_0.

The choice of the initial database grid can be important. If the initial database grid is too coarse, local refinement will not help, since the values of Y/E and N with highest posterior probability obtained from the coarse grid may differ significantly from the actual values. If a good initial choice of the database grid is made (and what is a good choice can be problem and parameter dependent) then local refinement can improve the prediction with relatively little increase in computational cost.

For all databases, the number of points for each surface profile vector $\boldsymbol{s}^i$ is $K_{\mathrm{s}} = 72$, distributed nonuniformly with an increased density of points near the indenter where pile-up or sink-in occurs, see Fig. 2.4. Each indentation force versus indentation depth vector, $\boldsymbol{f}^i$, has $K_{\mathrm{f}} = 67$ points also distributed nonunformly as marked in Fig. 2.2.

2.4.1 Inference based on noise-free data

The inferences for materials m_i $(i = 1, 2, 3)$ presuming noise-free data using database grids G_0 and G_2 are illustrated. Applying Bayes' theorem, the posterior probability distributions for $(Y/E, N)$ based on both force data and surface data can be obtained. The predicted combinations

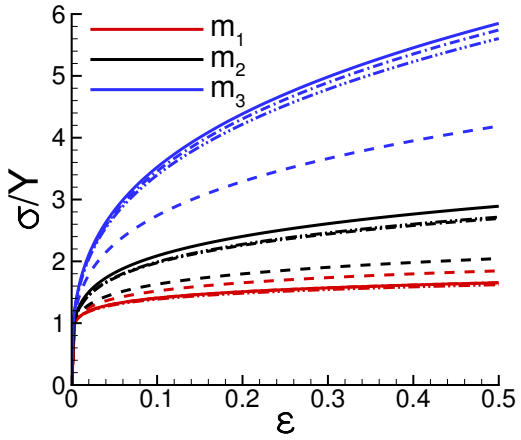

Figure 2.5: Uniaxial stress-strain curves showing the effect of the choice of database: G_0 (dashed lines); G_2 (dash dot lines); and G_{f} (dash dot dot lines). The stress-strain curves are for the predicted combinations of Y/E and N with the highest posterior probability for each database grid. The solid lines show the uniaxial stress-strain curves for the three input materials in Table 2.1. For material m_1 only the dash line does not overlap with the solid line. For material m_2 dash dot line and dash dot dot line overlap.

of Y/E and N with corresponding value of highest posterior probability, denoted by p_1, are shown in Table. 2.2.

The values of Y/E and N with the highest posterior probability are shown in Table. 2.2 for database grids G_0 and G_2, while the stress versus strain responses obtained from the highest posterior probability values of Y/E and N based on G_0, G_2 and G_{f} are shown in Fig. 2.5.

The predicted stress-strain responses for combinations of Y/E and N with highest posterior probability values using the database grid G_0 (dashed lines) differ significantly from the input materials stress-strain curves (solid lines). This discrepancy is largest for the material m_3. On the other hand, the difference between the stress-strain responses obtained from G_2 (dash dot lines) and G_{f} (dash dot dot lines) is not large and the results obtained from local refinement do not give a significant improvement compared with the ones using database grid G_2. For material m_3, the stress-strain curve predicted from database grid G_2 is even slightly better than the one from G_f. One possible reason is that when database grid becomes very fine, the inference becomes sensitive

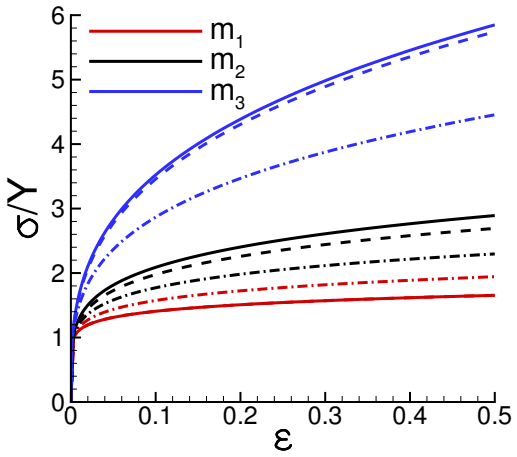

Figure 2.6: Uniaxial stress-strain curves comparing the predictions using only indentation force versus indentation depth data (dash dot lines) and both indentation force versus indentation depth and surface profile data (dashed lines). The stress-strain curves are for the predicted combinations of Y/E and N with the highest posterior probability using database grid G_2. The solid lines show the uniaxial stress-strain curves for the three input materials in Table 2.1. For material m_1 the solid line and the dashed line overlap.

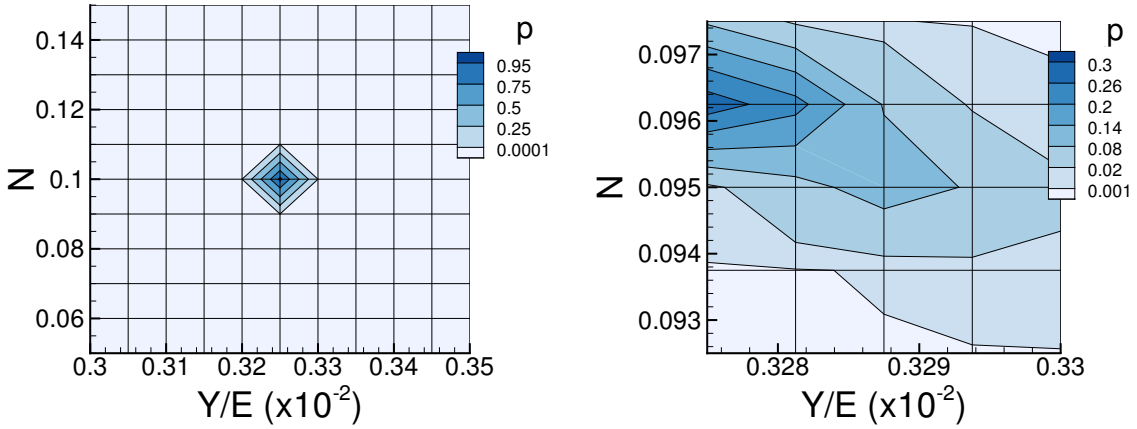

(a) (b)

Figure 2.7: Posterior probability distribution p for various combinations of Y/E and N for the material m_1 using database grids (a) G_2 and (b) G_{f}.

to numerical errors arising from the interpolations of the force data and surface data.

The predicted values (to the third significant figure) of Y/E and N for the stress-strain curves using database grid G_f in Fig. 2.5 are: $Y/E = 0.328 \times 10^{-2}$ and $N = 0.0963$ for material m_1; $Y/E = 0.267 \times 10^{-2}$ and $N = 0.191$ for material m_2; and $Y/E = 0.177 \times 10^{-2}$ and $N = 0.306$ for material m_3 with their corresponding highest posterior probability values 0.29, 0.14 and 0.20, respectively.

The predicted values of Y/E and N using only the indentation force versus indentation depth curves and the database grid G_2 are $Y/E = 0.300 \times 10^{-2}$ and $N = 0.13$ for material m_1; $Y/E = 0.275 \times 10^{-2}$ and $N = 0.16$ for material m_2; and $Y/E = 0.195 \times 10^{-2}$ and $N = 0.27$ for material m_3 with the corresponding highest posterior probability values 1.00, 0.55 and 1.00, respectively. With the supplementation of surface profiles, based on both force data and surface data, these values change to $Y/E = 0.325 \times 10^{-2}$ and $N = 0.10$ for material m_1; $Y/E = 0.270 \times 10^{-2}$ and $N = 0.19$ for material m_2; and $Y/E = 0.175 \times 10^{-2}$ and $N = 0.31$ for material m_3 with their corresponding highest posterior probability values 1.00, 0.56 and 0.85, respectively.

Fig. 2.6 shows stress-strain curves for the predicted values of Y/E and N with highest posterior probability values using both the indentation force versus indentation depth data and the surface profile data (dashed lines) compared with the corresponding curves using only indentation force versus indentation depth data (dash dot lines). Clearly, there is a significant increase in the accuracy of representing the input materials stress-strain curves (solid lines) by using the residual surface profiles in addition to the indentation force versus indentation depth data.

Stress-strain curves using only surface data are very close to those computed using both indentation force versus indentation depth data and surface profile data shown in Fig. 2.6. In a sense this is not surprising as the indentation force versus indentation depth response for the three materials is nearly identical, Fig. 2.2, but the surface profiles differ significantly, Fig. 2.4. We note that in some calculations, not shown here, materials with differing values of Y/E and N had nearly identical surface profiles but indentation force versus indentation depth responses that differ. Hence, it is expected that in general both the indentation force versus indentation depth response and the

surface profile would be needed to identify the plastic material parameters.

Fig. 2.7 shows the distributions of posterior probability in neighborhood of the predicted point with the corresponding highest posterior probability for material m_1 using database grids G_2, Fig. 2.7(a), and $G_{\rm f}$, Fig. 2.7(b). For the coarser database grid G_2 there is a rather sharp peak at the point with the highest posterior probability. On the other hand, for the refined database grid $G_{\rm f}$, where the step size is 6.25×10^{-6} for Y/E and 1.25×10^{-3} for N, the peak posterior probability is more diffuse and lower. This is because the small differences in Y/E and N in the vicinity of the peak give nearly indistinguishable responses.

2.4.2 Inference based on noise-contaminated data

For each noise measure defined by the set of values $\eta_{\rm s}, \eta_{\rm f}$ in Eq. (A-30), calculations of posterior probability are carried out for 100 realizations of $\boldsymbol{s}^{\rm noise}$ and $\boldsymbol{f}^{\rm noise}$ in Eq. (5.24). Of course, in a particular experiment one realization of these possible fluctuations will be obtained. The analyses in this section indicate that fitting one realization of the fluctuations (the "'noise") can lead to a misleading identification of the values of Y/E and N. What is needed is consideration of many possible fluctuation realizations with a given amplitude.

For each realization of $\boldsymbol{s}^{\rm noise}$ and $\boldsymbol{f}^{\rm noise}$ having the same values $\eta_{\rm s}, \eta_{\rm f}$, the values of Y/E and N with highest posterior probability were obtained. These values of Y/E and N could span a large range, the extent of which depends on the amplitude of the noise. Both the arithmetic average of the values of Y/E and N having the highest posterior probability and the weighted average of Y/E and N with corresponding posterior probability (Bayesian model averaging) were calculated. The two types of average for Y/E and N are very close with the same first two significant figures, and the standard deviations from Bayesian model averaging are slightly smaller than the ones from arithmetic average when data contains noise with $\eta_{\rm s} = \eta_{\rm f} = 0.01$. Here the arithmetic average of predictions with the highest posterior probability values were identified as the predicted material parameters for those values of $\eta_{\rm s}, \eta_{\rm f}$.

Uniaxial stress-strain curves for these average values of Y/E and N are compared with the input uniaxial stress-strain curves of materials m_1, m_2 and m_3 in Fig. 2.8. The curves shown are

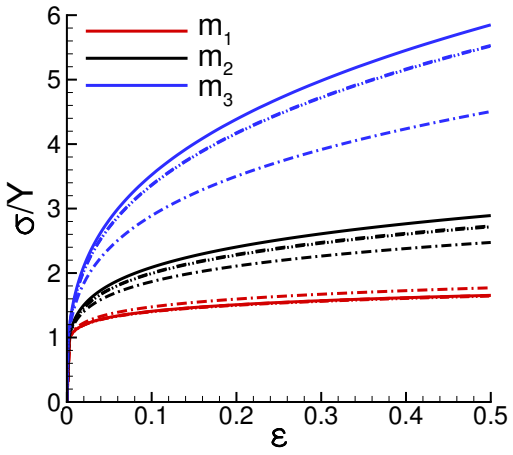

Figure 2.8: Uniaxial stress-strain curves showing the effect of the values of the noise measures η_s, η_f in Eq. (A-30): $\eta_s = \eta_f = 0.001$ (dashed lines); $\eta_s = 0.001$ and $\eta_f = 0.01$ (dash dot dot lines); $\eta_s = \eta_f = 0.01$ (dash dot lines). The stress-strain curves are for the predicted combinations of Y/E and N with the highest posterior probability using database grid G_2. The solid lines show uniaxial stress-strain curves for the three input materials in Table 2.1. For material m_1 only the dash dot line does not overlap with the solid line. For materials m_2 and m_3 the dashed line and the dash dot dot line overlap.

calculated using database grid G_2, while similar trends with the same relations between curves hold for calculations using database grid G_1. As for the noise free calculations in Fig. 2.6, the corresponding uniaxial stress-strain curves based on surface profile data alone differ little from those based on both indentation force versus indentation depth data and surface profile data.

The average values of Y/E and N used for the curves in Fig. 2.8 with $\eta_s = \eta_f = 0.001$ are $Y/E = 0.325 \times 10^{-2}$, $N = 0.10$ for m_1; $Y/E = 0.260 \times 10^{-2}$, $N = 0.19$ for m_2; and $Y/E = 0.175 \times 10^{-2}$, $N = 0.30$ for m_3. With $\eta_s = \eta_f = 0.01$ in Fig. 2.8 the corresponding average values of Y/E and N are $Y/E = 0.315 \times 10^{-2}$, $N = 0.11$ for m_1; $Y/E = 0.270 \times 10^{-2}$, $N = 0.17$ for m_2; and $Y/E = 0.195 \times 10^{-2}$, $N = 0.27$ for m_3. The average values of Y/E and N with $\eta_s = 0.001$, $\eta_f = 0.01$ were found to be the same as those with $\eta_s = \eta_f = 0.001$.

For material m_1, the stress-strain curve with $\eta_s = \eta_f = 0.001$ (red dashed line) coincides with the uniaxial stress-strain curve for the input material (red solid line). For all three materials, the

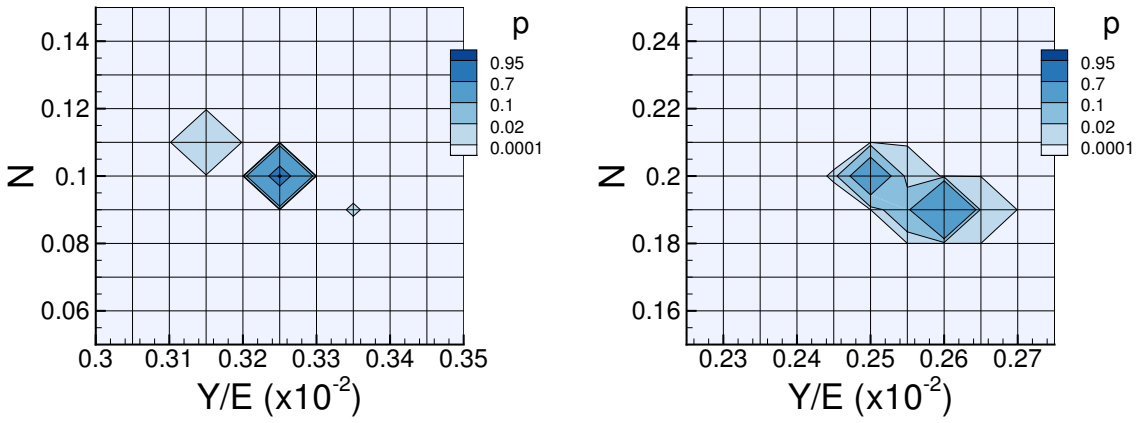

(a) (b)

Figure 2.9: One realization of posterior probability distribution p for various combinations of Y/E and N with values of the noise measures $\eta_{\mathrm{s}} = \eta_{\mathrm{f}} = 0.001$ using database grid G_2. (a) For material m_1. (b) For material m_2.

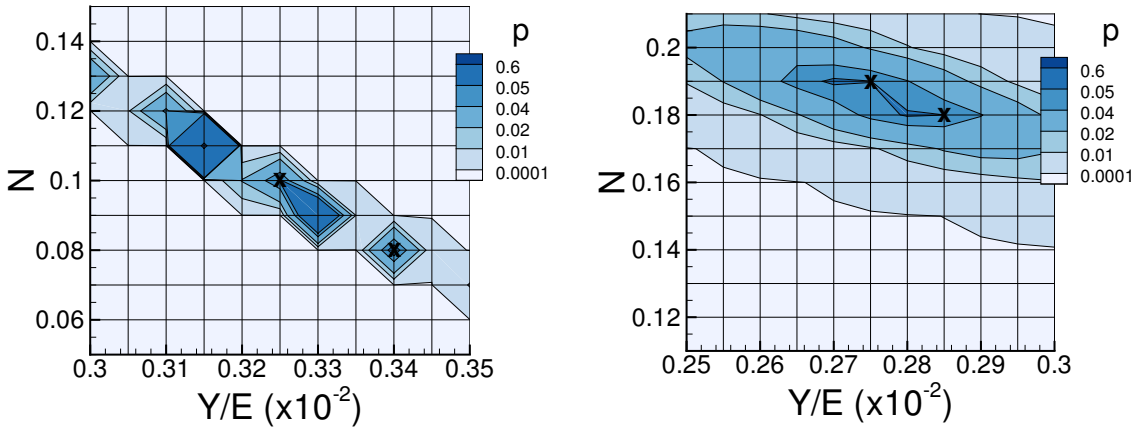

(a) (b)

Figure 2.10: One realization of posterior probability distribution p for various combinations of Y/E and N with values of the noise measures $\eta_{\mathrm{s}} = \eta_{\mathrm{f}} = 0.01$ using database grid G_2. (a) For material m_1. (b) For material m_2.

stress-strain curves with $\eta_{\rm s} = 0.001$, $\eta_{\rm f} = 0.01$ (dash dot dot lines) coincide with the curves with $\eta_{\rm s} = \eta_{\rm f} = 0.001$ and are closer to the curves for the input materials than those with $\eta_{\rm s} = 0.01$, $\eta_{\rm f} = 0.01$. In the circumstances analyzed here, the accuracy of the predicted uniaxial stress-strain response is more sensitive to noise in the surface profile data than to noise in the indentation force versus indentation depth curves.

The predicted stress-strain curve for m_1 is less sensitive to the values of the noise measures. The main reason for this is that it is a relatively low strain hardening material (small N). Fig. 2.8 shows that the stress-strain curves with noise for materials m_2 and m_3 increasingly deviate from those for the corresponding input materials with increasing strain. Hence, the agreement at larger strain values is sensitive to the predicted value of N.

One realization of the posterior probability distributions of Y/E and N with noise measure values $\eta_{\rm s} = \eta_{\rm f} = 0.001$ for materials m_1 and m_2 are shown in Fig. 2.9. The corresponding results obtained for $\eta_{\rm s} = \eta_{\rm f} = 0.01$ are shown in Fig. 2.10. Similar distributions were obtained for material m_3 but are not shown here. The posterior probability distributions with $\eta_{\rm s} = \eta_{\rm f} = 0.001$ are concentrated around a few points, while the posterior probability distributions with $\eta_{\rm s} = \eta_{\rm f} = 0.01$ are more spread out. As expected, Figs. 2.9 and 2.10 show that a higher value of the posterior probability is obtained for relatively noise-free data than when the data has significant noise.

In order to illustrate the variation of predicted stress-strain response with the value of the posterior probability, Fig. 2.11 shows the stress strain curves corresponding to the values of Y/E and N with the first, third and forth highest posterior probability values associated with one particular realization of noise with $\eta_{\rm s} = \eta_{\rm f} = 0.01$. The values of the third and forth highest posterior probability for materials m_1, m_2 and m_3 are $0.059, 0.053$; $0.050, 0.050$ and $0.0022, 0.00064$, respectively. These compare with the highest values of posterior probability of 0.65 for material m_1, 0.052 for material m_2 and 0.93 for material m_3. The quality of the fit to the input material uniaxial stress-strain curve decreases with increasing strain hardening. The results in Fig. 2.11 show that a high posterior probability associated with one realization of the noise does not necessarily provide a good fit to the input material stress-strain response.

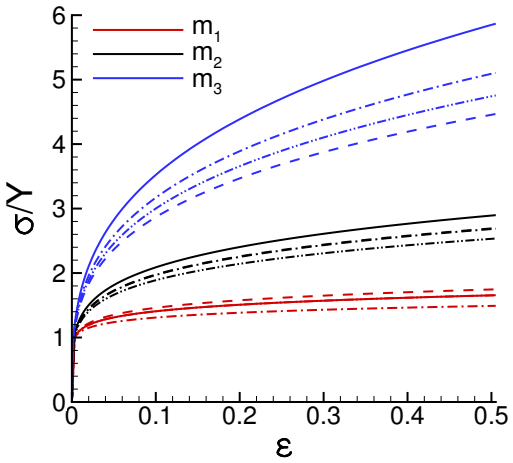

Figure 2.11: Uniaxial stress-strain curves obtained using the predicted values of Y/E, N that correspond to: the highest posterior probability value (dashed lines); the third highest posterior probability value (dash dot lines) and the fourth highest posterior probability value (dash dot dot lines). For materials m_1 and m_2 the third highest and fourth highest posterior probability values are marked by an x in Fig. 2.10 where $\eta_{\rm s} = \eta_{\rm f} = 0.01$. Database grid G_2 was used. The solid lines show the stress-strain curves for the three input materials in Table 2.1. For material m_1 the dash dot dot line overlaps with the solid line. For material m_2 the dash line and dash dot line overlap.

Fig.2.12 shows that the highest posterior probability value decreases as the noise measure increases (solid lines), while the second highest posterior probability value (dashed lines) varies in the opposite way. The values of η_s are those for which the average of the highest posterior probablility for the indentation force versus indentation depth data, Eq. (5.9), has the same value as the highest posterior probablility for the surface profile data, Eq. (3.5). The results for each database grid are terminated at the value of η_s at which the average of the highest posterior probability for the surface profile data in Eq. (3.5) reaches 0.3. When the noise amplitude is sufficiently small, a very strong posterior probability dominates the inference. With increasing noise amplitude, the posterior probability distribution becomes less concentrated with a decreasing maximum posterior probability value and with other posterior probability values increasing.

As noted by Vigliotti et al. [45], a finer database grid does not necessarily perform better than a coarser database grid in the presence of noise because the additional resolution goes into resolving

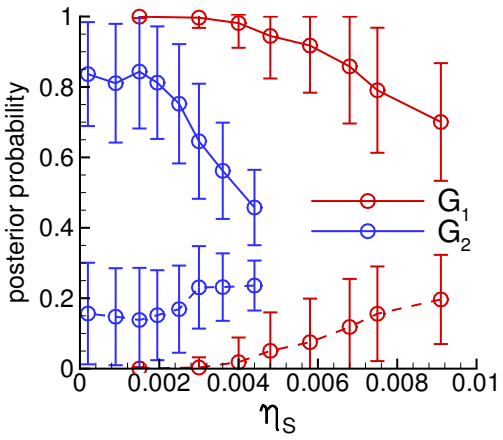

Figure 2.12: The variation of the average of predicted posterior probability with the value of surface data noise measure η_s for material m_3 using: database grid G_1 (red lines); database grid G_2 (blue lines). The solid lines show the average of the highest posterior probability and the dashed lines show the average of the second highest posterior probability. The bars show the corresponding standard deviations.

the noise rather than improving the fit to the underlying data. The posterior probability values based on the database grid G_2 (blue lines) are more sensitive to noise than the ones from database grid G_1 (red lines) as seen in Fig.2.12. Also, for a finer database grid there are more potential sites to compete for the highest probability value than for a coarser database grid, e.g. compare the posterior probability distributions in database grids G_2 and G_f in Fig. 2.7.

It is worth noting that the average value of the highest joint posterior probability obtained from using both indentation force-indentation depth data and surface profile data can be either greater than or less than the average of the highest posterior probability value using only surface data or the highest posterior probability value using only indentation force-indentation depth data. In many cases, the average of the highest posterior probability value associated with the individual data sources occur at values of Y/E and N that are at nearby grid points. However, particularly if a very fine grid is used, the highest posterior probability values associated with the indentation force-indentation depth data and the surface profile data can be at grid points that are not near each other. In such a case, the highest joint posterior probability obtained from using both indentation

force-indentation depth data and surface profile data can be less than each of these individually.

2.5 Summary and conclusions

We have presented a Bayesian-type statistical approach for extracting plastic uniaxial stress-strain response from conical indentation data for three input set of material parameters that give rise to essentially the same indentation force-indentation depth response. We have used both force versus indentation depth data and surface profile data. Our initial database grid was constructed based on 1020 finite element calculations. More refined database grids were obtained by interpolation. Once the initial database is constructed, the computations for the interpolation and for the statistical analysis are very light and can be quickly carried out on a personal computer.

1. The main result is that the Bayesian-type statistical approach using both force versus indentation depth data and surface profile data can distinguish the uniaxial stress-strain responses for materials that have essentially identical indentation force versus indentation depth curves.

2. For the three materials considered here, the uniaxial stress-strain responses obtained using only surface profile data differ little from those using both force versus indentation depth data and surface profile data for noise-free data and for data with superposed Gaussian noise.

3. For data with noise, the predicted values of the plastic material properties vary significantly for realizations having the same noise amplitude. Material properties obtained by averaging the highest posterior probability obtained for each of the 100 realizations gave plastic properties leading to a good fit to the uniaxial stress-strain response.

4. Refining the interpolated database grids gives improved predictions up to a point. Without noise an over refined database grid can lead to a somewhat less accurate prediction due to numerical errors associated with interpolation. With noise and with increasing database grid refinement there is a rather wide range of predicted values of the plastic properties with similar values of the posterior probability. Basically, as noted by Vigliotti et al. [45], over refinement can lead to an increasing range of predicted responses due to the refinement fitting

the noise and not only the underlying data.

5. The predicted uniaxial stress-strain response for a low strain hardening material is less sensitive to noise than for higher strain hardening materials.

3. INFLUENCE OF ASSUMED STRAIN HARDENING RELATION ON PLASTIC STRESS-STRAIN RESPONSE IDENTIFICATION FROM CONICAL INDENTATION [†]

"Since all models are wrong the scientist must be alert to what is importantly wrong. It is inappropriate to be concerned about mice when there are tigers abroad."

– George E. P. Box

3.1 Introduction

Indentation tests are relatively easy to carry out and can non-destructively assess the deformation resistance of materials using relatively small samples. However, obtaining a quantitative characterization of the material's deformation resistance is a challenge. The deformation and stress state in the vicinity of the indenter is complex and, in addition, materials with different uniaxial stress-strain curves can give indistinguishable indentation force versus indentation depth responses, as shown in Refs. [91, 110, 93].

Here, we focus on a relatively simple situation: conical indentation of a material that can be characterized as length scale independent, as elastically isotropic and as a rate independent isotropically hardening solid. A variety of approaches have been proposed to identify material parameters characterizing the plastic response of such materials based on indentation force versus indentation depth data using sharp and/or spherical indenters, including, for example, a representative strain approach [83, 111, 112, 84], dimensional analysis [85], optimization approaches [113, 114, 115], and neural networks [86].

Several approaches have been suggested for resolving the issue of the non-uniqueness of the relation between the indentation force versus indentation depth response and the uniaxial stress-strain curve. For example, Luo et al. [114] and Kang et al. [115] suggested using the indentation

[†]Reprinted with permission from "Influence of assumed strain hardening relation on plastic stress-strain response identification from conical indentation" by Yupeng Zhang and Alan Needleman, 2020, Journal of Engineering Materials and Technology, 142, 031002. Copyright © 2020 by American Society of Mechanical Engineers.

force versus indentation depth responses from more than one indenter shape while Also, in some studies, surface profiles have been used in addition to or instead of indentation force versus indentation depth data in the identification of material properties from sharp or spherical indentation, [96, 116, 97, 95, 2, 117].

Zhang et al. [2] were able to identify the uniaxial stress-strain response of materials having essentially the same indentation force versus indentation depth response using a Bayesian-type statistical analysis together with both indentation force versus indentation depth data and residual surface profile data even when the measurements were noisy. In Ref. [2], synthetic "experimental" data based on finite element analyses was used. The database needed for the Bayesian analysis was constructed using the same elastic-viscoplastic constitutive relation as was used to generate the "experimental" data. Also, all calculations were carried out with an in-house finite element code.

Even though structural metals exhibit some rate dependence, it is often convenient to idealize the response as being rate independent and, in practice, to use a generally available commercial or public domain general purpose finite element code. Also, of course, the form of the uniaxial stress-strain relation is not known a priori. Here, we explore the use of various characterization of the material's stress-strain response in the commercial finite element code ABAQUS [118] on the ability of the Bayesian-type approach of Zhang et al. [2] to identify the stress-strain response from conical indentation data.

3.2 Background

3.2.1 "Experimental" indentation response

In Zhang et al. [2], finite element, finite deformation, quasi-static analyses of conical indentation, as sketched in Fig. 3.1 were carried out. The calculations use a polar coordinate system (r, z, θ) and axisymmetric deformations are assumed so all field quantities are independent of θ. The indenter is taken to be rigid and the indenter angle β is taken to be 19° (this approximates a Berkovich indenter whose equivalent conical indenter angle is 19.7°). Also, perfect sticking

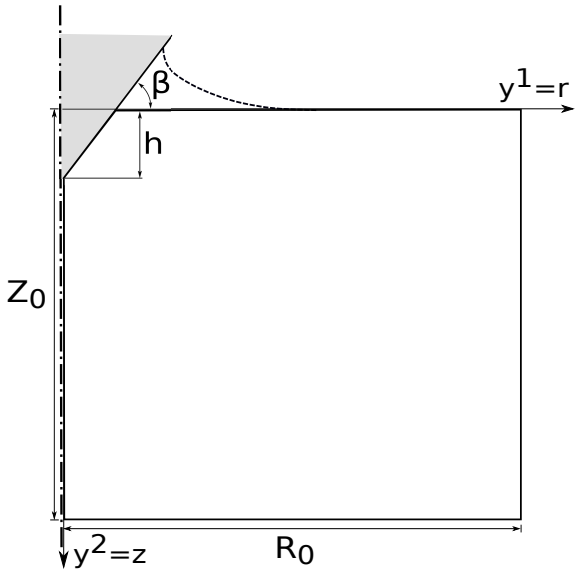

Figure 3.1: Sketch of the indentation configuration analyzed.

between the material and the indenter was assumed in Ref. [2].

Indentation results were obtained for rate dependent and isotropically hardening materials having the uniaxial stress-strain responses shown in Fig. 3.2 (the materials are also taken to be elastically isotropic) with strain hardening rule

$$\frac{g(\epsilon_{\rm p})}{Y} = \left(1 + \frac{\epsilon_{\rm p}}{\epsilon_0}\right)^N \tag{3.1}$$

and strain rate hardening rule

$$\dot{\epsilon}_{\rm p} = \dot{\epsilon}_0 \left(\frac{\sigma_{\rm e}}{g}\right)^{1/m} \tag{3.2}$$

where $g(\epsilon_{\rm p})$ is flow strength, $\epsilon_{\rm p}$ is effective plastic strain, $\sigma_{\rm e}$ is von Mises effective stress, N is strain hardening exponent and m is rate sensitivity exponent. Y is a reference stress gives $\epsilon_0 = Y/E$ with E being Young's modulus. $\dot{\epsilon}_{\rm p}$ and $\dot{\epsilon}_0$ are effective plastic strain rate and reference strain rate, respectively.

An advantage of conical indentation in this context is that because the indentation depth h is the only length scale in the problem, the solution is self-similar. The normalized indentation force,

$F/(Eh_{\rm ref})$ (E is Young's modulus and $h_{\rm ref}$ is a reference length), versus normalized indentation depth, $h/h_{\rm ref}$, responses of these three materials are indistinguishable, as shown in Fig. 3.3 even though the stress-strain responses are very different.

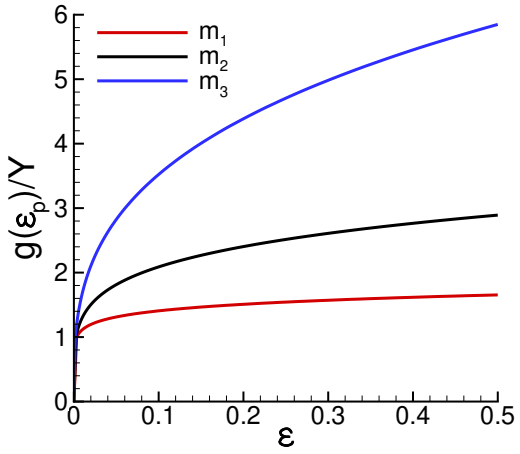

Figure 3.2: Uniaxial stress-strain curves for the three materials considered in Ref. [2] with plastic responses characterized by Eq. (3.1).

Zhang et al. [2] regarded the indentation force magnitude versus indentation depth magnitude responses in Fig. 3.3 and the residual surface profiles shown in Fig. 3.4 as "experimental" data and used a Bayesian-type statistical analysis to infer the stress-strain responses. The "experimental" data and the data sets used in the statistical analyses were all obtained using the same locally developed finite element code for rate dependent plasticity, with the material rate dependence set to a small value representative of metal plasticity at room temperature.

The Bayesian-type statistical analysis gave a very good representation of the input ("experimental") stress-strain responses even in the presence of noisy measurements, provided the noise was not extremely large, [2].

Various functional forms can be used to represent uniaxial stress-strain curves, and room temperature metal plasticity is often modeled as being rate independent. As in [2], we assume that the

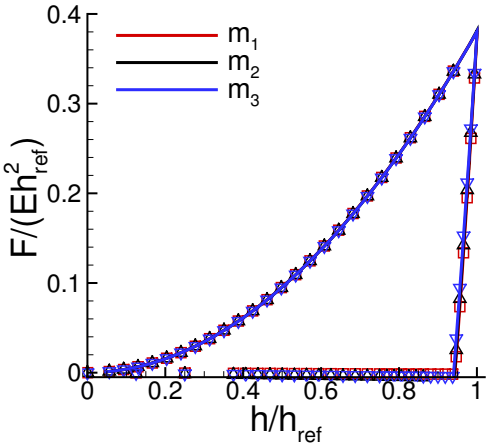

Figure 3.3: Normalized indentation force magnitude $F/(Eh_{\text{ref}}^2)$ versus normalized indentation depth magnitude h/h_{ref} during loading and unloading for the three "experimental" materials. From [2].

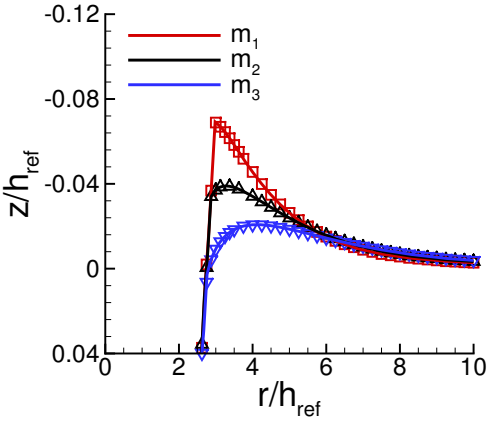

Figure 3.4: Normalized surface profiles in the vicinity of the indenter after unloading for three "experimental" materials. From [2].

material is known to be elastically and plastically isotropic, and that the elastic constants, Young's modulus E and Poisson's ratio ν are known. The plastic response is presumed to be characterized by two parameters: one characterizing initial yield and the other characterizing the strain harden-

ing. The issue addressed here is the sensitivity of predictions of the stress-strain response obtained from indentation to the assumed strain hardening rule.

3.2.2 Bayesian-type statistical approach

Bayes' theorem can be written as

$$p(\boldsymbol{\theta}|\boldsymbol{\mathcal{Y}}, \mathcal{M}) = \frac{p(\boldsymbol{\mathcal{Y}}|\boldsymbol{\theta}, \mathcal{M})p(\boldsymbol{\theta}|\mathcal{M})}{Z} \tag{3.3}$$

where $\mathcal{M}$ is an assumed model, $\boldsymbol{\theta}$ is the vector of unknown parameters associated with $\mathcal{M}$ and $\mathcal{Y}$ is observed data. The prior probability distribution, $p(\boldsymbol{\theta}|\mathcal{M})$, is the presumed initial probability that $\boldsymbol{\theta}$ is the set of parameter values that can represent the data $\mathcal{Y}$. The likelihood $p(\boldsymbol{\mathcal{Y}}|\boldsymbol{\theta}, \mathcal{M})$ is the probability that the model $\mathcal{M}$ with parameters $\boldsymbol{\theta}$ can represent the data $\boldsymbol{\mathcal{Y}}$. The posterior probability $p(\boldsymbol{\theta}|\boldsymbol{\mathcal{Y}}, \mathcal{M})$ gives the posterior probability that the parameter values $\boldsymbol{\theta}$ can represent the data $\boldsymbol{\mathcal{Y}}$. The denominator Z is a normalizing constant that results in the updated probability having a value between 0 and 1.

In the Bayesian-type statistical approach of Zhang et al [2] the data $\boldsymbol{\mathcal{Y}}$ is, for a given indentation, the curve of indentation force versus indentation depth, i.e. one of the curves in Fig. 3.3, and the residual (after the load has been removed) surface profile, i.e. one of the curves in Fig. 3.4. Hence, the data $\boldsymbol{\mathcal{Y}}$ consists of two vectors: ($\boldsymbol{s}^{\mathrm{m}}$ and $\boldsymbol{f}^{\mathrm{m}}$). The components of vector s_k^{m}, $k = 1, ..., K_{\mathrm{s}}$ are values of the surface coordinate, z_k/h_{ref} at radial coordinate r_k/h_{ref}, while the components of vector f_k^{m}, $k = 1, ..., K_{\mathrm{f}}$ are values of the indentation force $F_k/(Eh_{\mathrm{ref}}^2)$ at indentation depth h_k/h_{ref}.

For a specified strain hardening rule, a database of responses is constructed from finite element solutions. The database consists of a normalized surface displacement, z/h_{ref} versus r/h_{ref} curve, denoted by $\boldsymbol{s}^i$, and a normalized indentation force, $F/(Eh_{\mathrm{ref}}^2)$, versus normalized indentation depth, h/h_{ref}, curve, denoted by $\boldsymbol{f}^i$. The index i ranges from 1 to K_{total}, where K_{total} is the total number of cases in the database. Each database vector $\boldsymbol{s}^i$ consists of K_{s} points evaluated at r_k/h_{ref} and each database vector $\boldsymbol{f}^i$ consists of K_{f} points evaluated at h_k/h_{ref}.

Assuming the indentation force versus indentation depth data and the surface profile data can be treated as independent so that the posterior probability $p(\boldsymbol{s}^i, \boldsymbol{f}^i|\boldsymbol{s}^{\rm m}, \boldsymbol{f}^{\rm m})$ associated with $(\boldsymbol{s}^{\rm m}, \boldsymbol{f}^{\rm m})$ can be expressed as

$$p(\boldsymbol{s}^i, \boldsymbol{f}^i|\boldsymbol{s}^{\rm m}, \boldsymbol{f}^{\rm m}) = \frac{p(\boldsymbol{s}^i|\boldsymbol{s}^{\rm m})p(\boldsymbol{f}^i|\boldsymbol{f}^{\rm m})}{Z_{\rm sf}} \tag{3.4}$$

where

$$p(\boldsymbol{s}^i|\boldsymbol{s}^{\rm m}) = \frac{p(\boldsymbol{s}^{\rm m}|\boldsymbol{s}^i)p(\boldsymbol{s}^i)}{Z_{\rm s}} \tag{3.5}$$

$$p(\boldsymbol{f}^i|\boldsymbol{f}^{\rm m}) = \frac{p(\boldsymbol{f}^{\rm m}|\boldsymbol{f}^i)p(\boldsymbol{f}^i)}{Z_{\rm f}} \tag{3.6}$$

There is no sum on i in Eqs. (5.8) to (5.9).

The normalizing constants $Z_{\rm s}$, $Z_{\rm f}$ and $Z_{\rm sf}$ are given by

$$Z_{\rm s} = \sum_{i=1}^{K_{\rm total}} p(\boldsymbol{s}^{\rm m}|\boldsymbol{s}^i)p(\boldsymbol{s}^i)\ ,\ Z_{\rm f} = \sum_{i=1}^{K_{\rm total}} p(\boldsymbol{f}^{\rm m}|\boldsymbol{f}^i)p(\boldsymbol{f}^i) \tag{3.7}$$

$$Z_{\rm sf} = \sum_{i=1}^{K_{\rm total}} p(\boldsymbol{s}^i|\boldsymbol{s}^{\rm m})p(\boldsymbol{f}^i|\boldsymbol{f}^{\rm m}) \tag{3.8}$$

We also assume that the differences between the "experimental" data and calculated responses in the database are independent and identically distributed as a mean zero normal distribution. With the variances $(\hat{\xi}_{\rm s}^i)^2$ and $(\hat{\xi}_{\rm f}^i)^2$ given by maximum likelihood estimation, the likelihood values become (see Ref. [2])

$$p(\boldsymbol{s}^{\rm m}|\boldsymbol{s}^i) = \Big(\frac{1}{\hat{\xi}_{\rm s}^i\sqrt{2\pi}}\Big)^{K_{\rm s}} \exp\Big(-\frac{K_{\rm s}}{2}\Big) \tag{3.9}$$

$$p(\boldsymbol{f}^{\rm m}|\boldsymbol{f}^i) = \Big(\frac{1}{\hat{\xi}_{\rm f}^i\sqrt{2\pi}}\Big)^{K_{\rm f}} \exp\Big(-\frac{K_{\rm f}}{2}\Big). \tag{3.10}$$

where $K_{\rm s}$ and $K_{\rm f}$ are the number of data points on the surface profile curve and the number of data points on the indentation force versus indentation depth curve, respectively. If a standard deviation turns out to be exactly zero, the corresponding likelihood is infinite and the posterior probability is set to one.

A uniform prior is used for both $p(\boldsymbol{s}^i)$ and $p(\boldsymbol{f}^i)$ in the database and the values of $p(\boldsymbol{s}^i)$ and

$p(\boldsymbol{f}^i)$ are set to 0 outside that range.

Both noise-free and noise-contaminated data are considered. With the noise-free responses denoted by $\boldsymbol{f}^{\text{input}}$ and $\boldsymbol{s}^{\text{input}}$, the noise-contaminated data are given by

$$\boldsymbol{s}^{\text{m}} = \boldsymbol{s}^{\text{input}} + \boldsymbol{s}^{\text{noise}} \ , \ \boldsymbol{f}^{\text{m}} = \boldsymbol{f}^{\text{input}} + \boldsymbol{f}^{\text{noise}}. \tag{3.11}$$

Each component s_k^{noise} and f_k^{noise} is a random number from a normal distribution, calculated using the MATLAB function normrnd [109]. This distribution has zero mean value and the values of the standard deviations ξ_{s} and ξ_{f} are taken to be related to the pile-up height $s^{\text{m}}_{\text{pileup}}$ and the maximum indentation force $\max(f_k^{\text{m}})$, respectively, by

$$\xi_{\text{s}} = \eta_{\text{s}} s^{\text{m}}_{\text{pileup}} \ , \ \xi_{\text{f}} = \eta_{\text{f}} \max(f_k^{\text{m}}) \tag{3.12}$$

with $\eta_{\text{s}} \geq 0$ and $\eta_{\text{f}} \geq 0$, where η_{s} and η_{f} are referred to as the noise amplitudes. One difference from the analyses in [2] is that here ξ_{s} is defined in terms of the maximum residual pile-up height rather than the maximum residual indentation depth.

The Bayesian statistics calculation for one realization of a pair of "experimental" measurements (noise-free, $\boldsymbol{s}^{\text{input}}$ and $\boldsymbol{f}^{\text{input}}$, or noise-contaminated, $\boldsymbol{s}^{\text{m}}$ and $\boldsymbol{f}^{\text{m}}$) using a fixed database (without database refinement during Bayesian calculations) includes three steps:

Step 1: assign uniform (or other form of) prior probability distributions to $p(\boldsymbol{s}^i)$ and $p(\boldsymbol{f}^i)$;

Step 2: calculate posterior probability distributions based on only residual surface profiles data, Eq. (3.5), and based on only indentation force versus indentation depth data, Eq. (5.9). Where the likelihood functions are given in Eq. (3.9) and Eq. (3.10), and normalizing constants are given in Eq. (4.24a);

Step 3: calculate posterior probability distributions based on both residual surface profiles data and indentation force versus indentation depth data, Eq. (5.8). Where the normalizing constant is given in Eq. (5.10).

Note that a subjective prior probability distribution may affect the posterior probability distri-

bution. However, when the size of observed data (K_{s} or K_{f}) is large enough, the impact of prior probability distribution on posterior probability distribution can be ignored.

3.3 Numerical Implementation

3.3.1 Finite element calculations

The calculations to create the databases were carried out using ABAQUS [118]. The quasi-static boundary problem formulation is as described in Zhang et al. [2] except for the contact modeling and that here the response is independent of the imposed indentation rate $\dot{h}$. The ABAQUS "hard" contact option is specified along the direction normal to the indenter and the "penalty" option is used for the tangential direction. The friction coefficient is taken to be 0.4, which gives a response close to perfect sticking. This friction coefficient is selected to represent a full adhesion condition, which generates almost the same residual surface profile and indentation force versus indentation depth curve as the ones calculated from the setting of tangential contact with the "rough" option.

Geometric nonlinearity is taken into account by setting the Nlgeom option to be on; the error tolerance is set to 10^{-6}; the number of increments is 10^3 during loading and is 200 during unloading. The aim is to model indentation into a half-space but of course in the calculations a finite block is analyzed. Here, we use a block size of $R_0/h_{\mathrm{ref}} = 37.5 \times Z_0/h_{\mathrm{ref}} = 37.5$ to approximate the half-space. The magnitude of the maximum indentation depth is set to $h_{\mathrm{ref}}/Z_0 \approx 0.027$ where Z_0 is shown in Fig. 3.1.

As in [2], the indentation force directly obtained from the finite element calculations varies in discrete steps when a new nodal point comes in contact with or detaches from the indenter. In order to provide a clearer picture of the "experimental" indentation response obtained from the in-house finite element code, the raw output curves from the computer were smoothed by code by plotting the midpoint of the steps of the indentation force versus indentation depth relation. However, the indentation force versus indentation depth curves $\boldsymbol{f}^i$ used to construct all databases were taken to be the raw from ABAQUS output. The data directly obtained from ABAQUS were

more convenient to use directly and only the relative difference between the data in database and the experimental data matters.

The finite element mesh consists of 7921 $4-$node bilinear axisymmetric quadrilateral elements, corresponding to 8100 nodes. A uniform mesh with element size 0.05×0.05 is used in the $3.75h_{\text{ref}} \times 3.75h_{\text{ref}}$ fine mesh region near the indenter tip. Outside the uniform zone, the element size is gradually increased. Reduced integration with hourglass control is used.

The convergence of the calculations was investigated using a refined mesh with 19600 quadrilateral elements and 19881 nodes. The maximum difference in the surface profile values was $\approx 4.5\%$ and the maximum difference for the indentation force versus indentation depth values was $\approx 2.5\%$. These maximum values occurred for materials modeling ideal plasticity. More generally, the maximum difference in the surface profile values for the two meshes were within 1.5% and the maximum difference in the indentation force versus indentation depth values were within 0.6%.

3.3.2 Strain hardening rules

In the calculations here, the elastic strains remain small and the materials are plastically incompressible so that the plastic flow rule for an isotropically hardening Mises solid can be written as

$$\mathbf{d}^{\mathrm{p}} = \frac{3}{2}\frac{\dot{\epsilon}_{\mathrm{p}}}{\sigma_{\mathrm{e}}}\boldsymbol{\sigma}' \tag{3.13}$$

for plastic loading, where $\mathbf{d}^{\mathrm{p}}$ is the plastic part of the rate of deformation tensor, $\boldsymbol{\sigma}$ is the Cauchy stress, and

$$\sigma_{\mathrm{e}}^2 = \frac{3}{2}\boldsymbol{\sigma}' : \boldsymbol{\sigma}' \tag{3.14}$$

with

$$\boldsymbol{\sigma}' = \boldsymbol{\sigma} - \frac{1}{3}\mathrm{tr}(\boldsymbol{\sigma})\mathbf{I} \tag{3.15}$$

where $\mathrm{tr}(\boldsymbol{\sigma}) = \sigma_{11} + \sigma_{22} + \sigma_{33}$ and $\mathbf{I}$ is the identity tensor.

The effective plastic strain rate, $\dot{\epsilon}_{\rm p}$, in Eq. (3.13) is given by

$$\dot{\epsilon}_{\rm p} = \Big(\frac{1}{E_t} - \frac{1}{E}\Big)\dot{\sigma}_{\rm e} \tag{3.16}$$

while the effective strain rate, $\dot{\epsilon}_{\rm e}$, is

$$\dot{\epsilon}_{\rm e} = \frac{1}{E_t}\dot{\sigma}_{\rm e} \tag{3.17}$$

where E_t is the slope of the $\sigma_{\rm e}$ versus $\epsilon_{\rm e}$ relation (which also is the slope of the uniaxial stress-strain curve).

Four strain hardening rules are considered and are denoted by $\mathrm{F}_i (i = 0, 1, 2, 3)$. These are given by

$$\mathrm{F}_0: \quad \frac{\sigma_{\rm e}}{Y} = \left(1 + \frac{\epsilon_{\rm p}}{\epsilon_0}\right)^N \tag{3.18}$$

$$\mathrm{F}_1: \quad \frac{\sigma_{\rm e}}{Y} = \left(\frac{\epsilon_{\rm e}}{\epsilon_0}\right)^N \tag{3.19}$$

$$\mathrm{F}_2: \quad \frac{\sigma_{\rm e}}{Y} = \left[\left(\frac{\epsilon_{\rm e}}{\epsilon_0} - 1 + N\right)\frac{1}{N}\right]^N \tag{3.20}$$

$$\mathrm{F}_3: \quad \frac{\sigma_{\rm e}}{Y} = 1 + \left(\frac{\epsilon_{\rm p}}{\epsilon_0}\right)^N \tag{3.21}$$

where Y is the initial yield strength, N is the strain hardening exponent, $\epsilon_{\rm p} = \int \dot{\epsilon}_{\rm p} dt$, $\epsilon_{\rm e} = \int \dot{\epsilon}_{\rm e} dt$ and $\sigma_{\rm e}(\epsilon_{\rm p})$ in Eq. (A-6) is the same as $g(\epsilon_{\rm p})$ in Eq. (3.1) and is shown in Fig. 3.2.

Plastic loading takes place when $\sigma_{\rm e}$ is equal to the maximum of Y and the maximum of $\sigma_{\rm e}$ over the deformation history together with $\dot{\sigma}_{\rm e} > 0$.

Rules F_0 and F_3, are functions of the effective plastic strain $\epsilon_{\rm p}$, while rules F_1 and F_2 are functions of the effective strain $\epsilon_{\rm e}$. For strain hardening rule F_2 , E_t is continuous at the yield point [119]. We note that the rule F_3 is a specialization of the Johnson-Cook hardening model [120] to isothermal and rate independent material response.

The stress-strain curves for the three materials in Figs. 3.3 and 3.4 were generated in [2] using the following values of Y and N: material m_1, $Y = 650$MPa, $N = 0.10$; material m_2, $Y =$

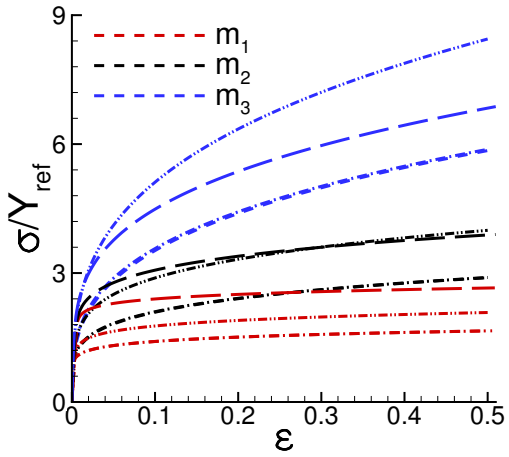

Figure 3.5: Normalized uniaxial stress-strain curves for the strain hardening rules: F_0 (dashed lines); F_1 (dash dot lines); F_2 (dash dot dot lines) and F_3 (long dash lines). For convenience, the reference stress Y_{ref} for each material is taken to be the value of Y specified for the "experimental" materials in Ref. [2]: 650MPa for m_1; 490MPa for m_2; and 330MPa for m_3. Also, the values of N for each material are those used in Ref. [2] and are specified in the text.

490MPa, $N = 0.20$; material m_3, $Y = 330$MPa, $N = 0.31$. In all cases, $E = 200$GPa and $\nu = 0.30$. So that Y/E for materials m_1, m_2 and m_3 are 0.00325, 0.00245 and 0.00165, respectively. Fig. 3.5 shows the stress-strain relations obtained from each of the rules F_i using these values of Y and N. As can be seen in Fig. 3.5, the plastic parameter values used in Ref. [2] can generate very different stress-strain responses when used in Eqs. (A-6) to (3.21).

3.4 Construction of the Databases

Four databases were constructed with four strain hardening rules F_0, F_1, F_2 and F_3. The range of parameters is the same for all databases as $1.0 \times 10^{-3} \leq Y/E \leq 2.0 \times 10^{-2}$ and $0 \leq N \leq 0.5$. Various database grids are available for the inference. The initial database grid, named as G_0, consists of 20 and 26 uniformly spaced values of Y/E and N, respectively, in the range. Thus there are $K_{\text{total}} = 520$ combinations of deformation responses $(\boldsymbol{s}^i, \boldsymbol{f}^i)$ corresponding to $(Y/E)^i, N^i$ in the database with grid G_0. It has step size 1.0×10^{-3} in Y/E and 0.02 in N. For database with grid G_0, one finite element calculation was carried out for each set $(Y/E)^i, N^i$ in the database.

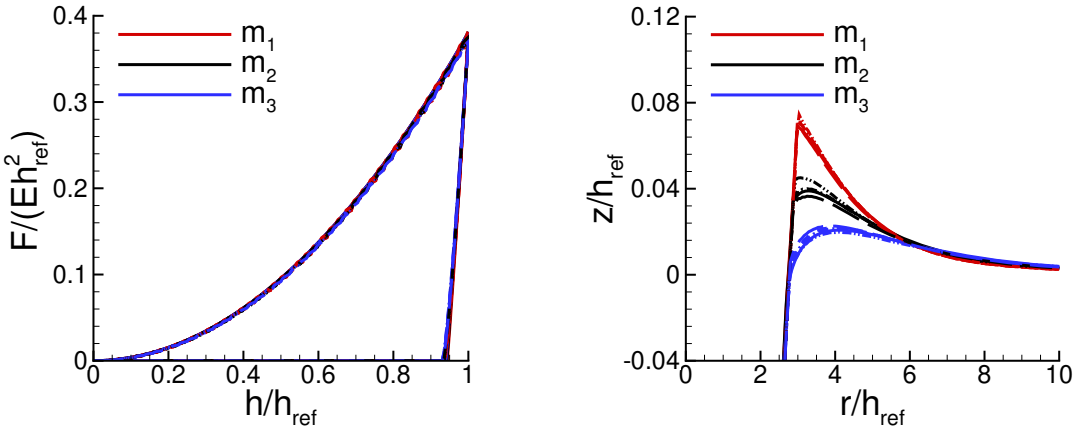

(a) (b)

Figure 3.6: (a) Normalized indentation force magnitude $F/(Eh_{\text{ref}}^2)$ versus normalized indentation depth magnitude h/h_{ref} during loading-unloading. (b) Normalized surface profiles near the indenter after unloading. The curves are the corresponding indentation responses to the predicted values of Y/E and N based on noise-free data from databases with strain hardening rules: F_0 (dashed lines); F_1 (dash dot lines); F_2 (dash dot dot lines) and F_3 (long dash lines) in Table. 3.1. The solid lines show the indentation force versus indentation depth curves for the three "experimental" materials in Figs. 3.3 and 3.4.

Another database denoted by G_1 is obtained by interpolations between data of nearby points on database grid G_0. G_1 has a step size 2.5×10^{-4} in Y/E and 0.01 in N giving $K_{\text{total}} = 3927$. For these interpolated points, no finite element calculations were carried out. Rather, the components of the vectors $\boldsymbol{s}^i$ and $\boldsymbol{f}^i$ were obtained by linear interpolations of the corresponding vectors of nearby points.

We also explored using a modified database grid in the vicinity of the combination of Y/E and N with the largest posterior probability. The database denoted by G_2 has a locally refined step size in Y/E of 5.0×10^{-5} between nearest neighbors and an unrefined step size 0.01 in N. The interpolation procedures for database grids G_2 was conducted in the same way as for database grid G_1. We emphasize that finite element calculations were only carried out for the initial, coarsest database grid G_0.

For all databases, the number of points for each surface profile vector $\boldsymbol{s}^i$ is $K_{\text{s}} = 72$, distributed

nonuniformly with an increased density of points near the indenter where pile-up or sink-in occurs. Each indentation force versus indentation depth vector, $\boldsymbol{f}^i$, has $K_{\mathrm{f}} = 67$ data points (25 for loading and 42 for unloading data) also distributed nonuniformly.

3.5 Results

3.5.1 Stress-strain curves obtained from noise-free data

The stress-strain curves based on noise-free measurements for materials m_1, m_2 and m_3 are calculated for each of the strain hardening rules F_0, F_1, F_2 and F_3. The predicted values of Y/E and N with the highest posterior probability values compared with the values of Y/E and N used to generate the "experimental" data are shown in Table. 3.1. Note that the predicted values of Y/E and N can depend on the hardening rule and that the values can differ from those used in Ref. [2] to generate the "experimental" stress-strain curves. For example, for material m_1, Y_{F_2}/E is 0.00275, Y_{F_3}/E is 0.00165 and Y_{inp}/E is 0.00325 while N_{F_2} is 0.0800, N_{F_3} is 0.140 and N_{inp} is 0.100. For material m_3, Y_{F_2}/E is 0.00100, Y_{F_3}/E is 0.000950 and Y_{inp}/E is 0.00165 while N_{F_2} is 0.300, N_{F_3} is 0.340 and N_{inp} is 0.310.

Table 3.1: Predicted values of Y/E and N with the highest posterior probability based on noise-free data from the four databases with the strain hardening rules F_0, F_1, F_2 and F_3 compared with the Y/E and N used to generate "experimental" data.

	m_1	m_2	m_3
Y_{inp}/E	0.00325	0.00245	0.00165
N_{inp}	0.100	0.200	0.310
Y_{F_0}/E	0.00315	0.00240	0.00170
N_{F_0}	0.100	0.200	0.300
Y_{F_1}/E	0.00315	0.00235	0.00155
N_{F_1}	0.100	0.200	0.310
Y_{F_2}/E	0.00275	0.00195	0.00100
N_{F_2}	0.0800	0.160	0.300
Y_{F_3}/E	0.00165	0.00125	0.000950
N_{F_3}	0.140	0.260	0.340

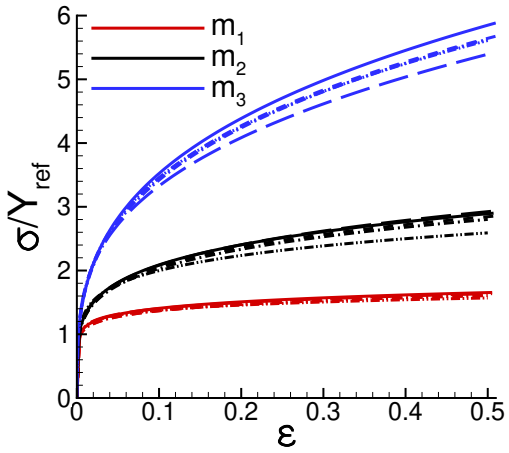

Figure 3.7: Normalized uniaxial stress-strain curves showing the effect of the choice of strain hardening rules: F_0 (dashed lines); F_1 (dash dot lines); F_2 (dash dot dot lines) and F_3 (long dash lines). The stress-strain curves are for the predicted combinations of Y/E and N with the highest posterior probability from noise-free data using database grid G_2. The solid lines show the uniaxial stress-strain curves for the three "experimental" materials in Figs. 3.3 and 3.4. For convenience, the reference stress Y_{ref} for each material is taken to be the value of Y specified for the "experimental" materials in Ref. [2]: 650MPa for m_1; 490MPa for m_2; and 330MPa for m_3.

Because $Y/E = 10^{-3}$ is the lower boundary of the parameter range and for material m_3 the optimal values of Y/E were near the database boundary for strain hardening rules for F_2 and F_3. Therefore, three values of Y/E were added to the database grid G_1, namely $Y/E = 2.5 \times 10^{-4}$, 5.0×10^{-4} and 7.5×10^{-4}. This augmented database grid is denoted by $G_{1\text{exp}}$ and it has $K_{total} = 4080$.

For the databases for F_0 and F_1, the database with database grid G_2 is interpolated from G_1, while for the databases for F_2 and F_3, the database with grid G_2 is interpolated from $G_{1\text{exp}}$. All the predicted values in Table 3.1 were calculated using the locally refined database grid G_2.

The corresponding normalized indentation force versus normalized indentation depth curves and the normalized residual surface profiles near the indenter of the predicted values of Y/E and N from the databases using various strain hardening rules in Table. 3.1 are shown in Fig. 3.6. All of the four strain hardening rules provide a good fit to the normalized indentation force versus

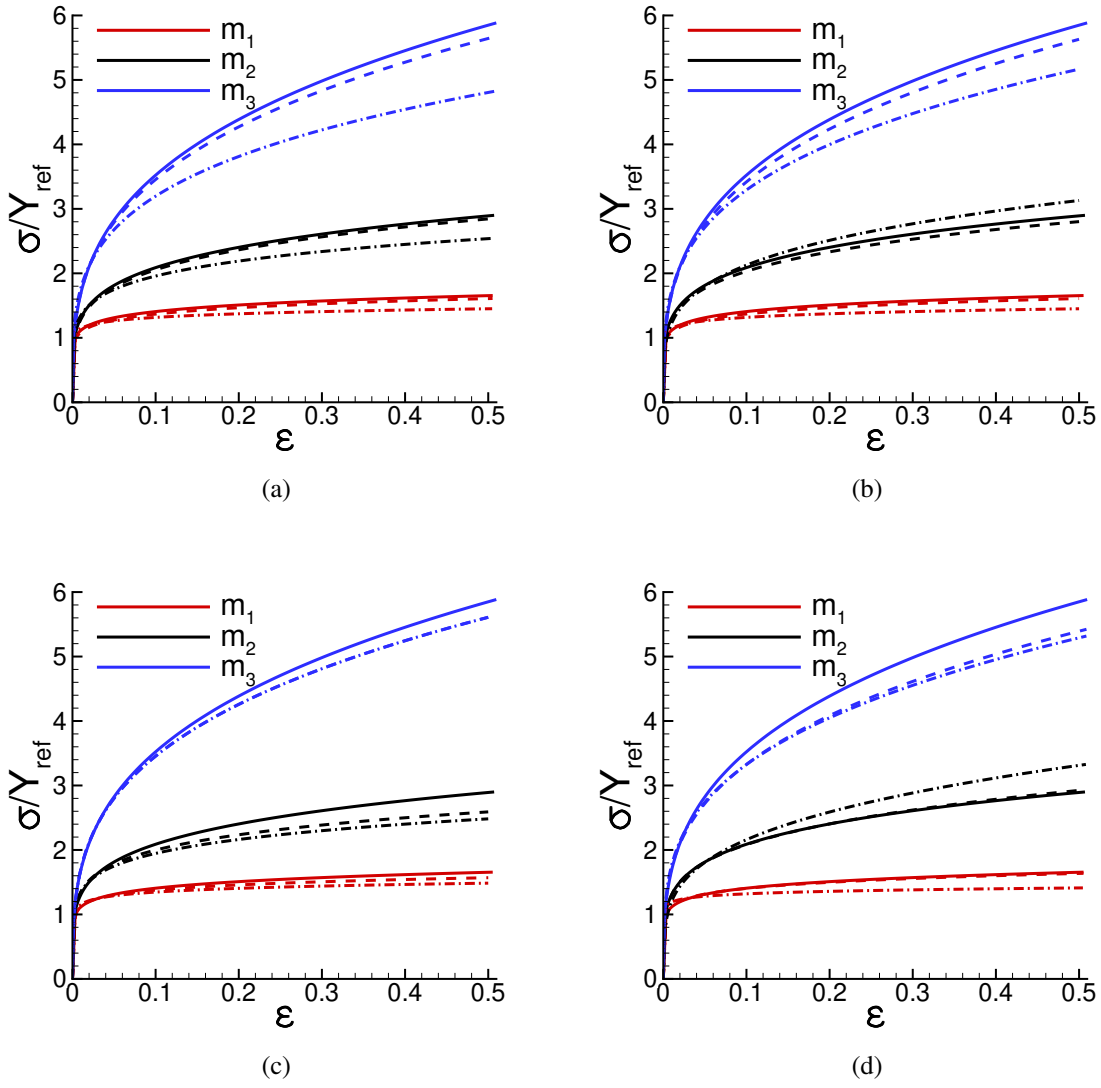

Figure 3.8: Uniaxial stress-strain curves comparing the predictions using only indentation force versus indentation depth data (dash dot lines) and both indentation force versus indentation depth and surface profile data (dashed lines) from the databases with strain hardening rules: (a)F_0, (b)F_1, (c)F_2 and (d)F_3. The stress-strain curves are for the predicted combinations of Y/E and N with the highest posterior probability based on noise-free data. For convenience, the reference stress Y_{ref} for each material is taken to be the value of Y specified for the three "experimental" materials in Ref. [2]: 650MPa for m_1; 490MPa for m_2; and 330MPa for m_3. The solid lines show the uniaxial stress-strain curves for the three "experimental" materials in Figs. 3.3 and 3.4. In (c), for material 3, the stress-strain curve based on both indentation force versus indentation depth and surface profile data (blue dashed line) coincides with that based on only indentation force versus indentation depth data (blue dash dot line).

indentation depth curves but the hardening rules F_2 (black dash dot dot line) and F_3 (blue long dash line) for materials m_2 and m_3 do not provide such a good fit to the the normalized residual surface profiles.

In Fig. 3.6(b), the surface profiles obtained based on strain hardening rules F_2 and F_3 do not provide a good agreement with the "experimental" profiles surface profiles, this indicates that in these cases the indentation force versus indentation depth data played a dominant role in determining the optimum values of Y/E and N.

The normalized uniaxial stress-strain curves for the predicted combinations of Y/E and N in Table. 3.1 and the three "experimental" materials are shown in Fig. 3.7. For material m_1, all uniaxial stress-strain curves for all four hardening rules are very close to that for the corresponding "experimental" material (the solid lines). For material m_2, strain hardening rule F_3 (the long dash line), F_0 (the dashed line) and F_1 (the dash dot line) overlap with the curve for the "experimental" material (the solid line). For material m_3, F_0 (the dashed line), F_1 (the dash dot line) and F_2 (the dash dot dot line) overlap. As in [2], the difference between the predicted stress-strain curves and the stress-strain curves of the "experimental" materials is found to be larger for higher strain hardening materials. Hence, at least for noise-free data, all four strain hardening rules are capable of providing a good fit to the uniaxial stress-strain response.

Fig. 3.8 shows the stress-strain curves for the predicted values of Y/E and N with highest posterior probability values from the databases with strain hardening rules F_0, F_1, F_2 and F_3 using both the indentation force versus indentation depth data and the residual surface profile data (dashed lines) compared with the corresponding curves using only indentation force versus indentation depth data (dash dot lines). The predictions using two types of data generally provide good fits to the "experimental" material's uniaxial stress-strain responses (solid lines) and provide better representations of the uniaxial stress-strain response than obtained using only indentation force versus indentation depth data. However, for material m_3, the predicted stress-strain responses from the databases with rules F_2 and F_3 using two types of data and using only indentation force versus indentation depth data nearly coincide. This shows that there are circumstances where there

is no significant improvement in the predicted uniaxial stress-strain response from using the surface profile data. Note that the indentation force versus indentation depth data played a dominant role in the Fig. 3.8.

3.5.2 Stress-strain curves obtained from noise-contaminated data

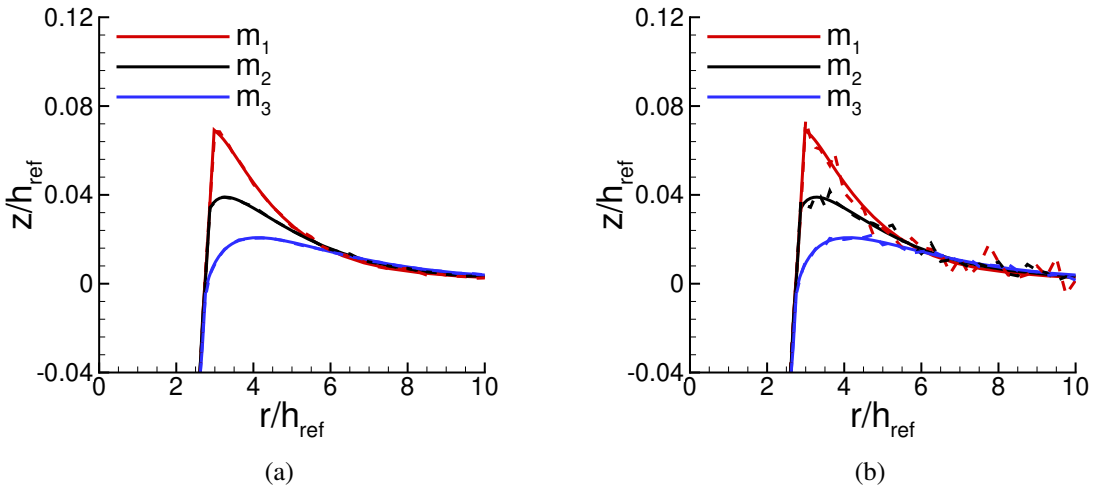

Figure 3.9: One realization of the normalized noise-contaminated surface profiles near the indenter with the noise amplitude (a) $\eta_s = 0.01$ and (b) $\eta_s = 0.05$ after unloading for the three "experimental" materials given in the text.

Fig. 3.9 shows "experimental" residual surface profiles near the indenter with a low value of the noise amplitude ($\eta_s = 0.01$), Fig. 3.9(a), and with a high value of the noise amplitude ($\eta_s = 0.05$), Fig. 3.9(b). Similarly, Fig. 3.10 shows "experimental" indentation force versus indentation depth curves with a low value of the noise amplitude ($\eta_f = 0.01$), Fig. 3.10(a), and with a high value of the noise amplitude ($\eta_f = 0.05$), Fig. 3.10(b).

As shown in Ref.[2], using one realization of noise-contaminated data with a given noise amplitude to identify the uniaxial plastic response can give a misleading prediction since the fitting procedure attempts to fit the given data and cannot distinguish between the underlying "actual"

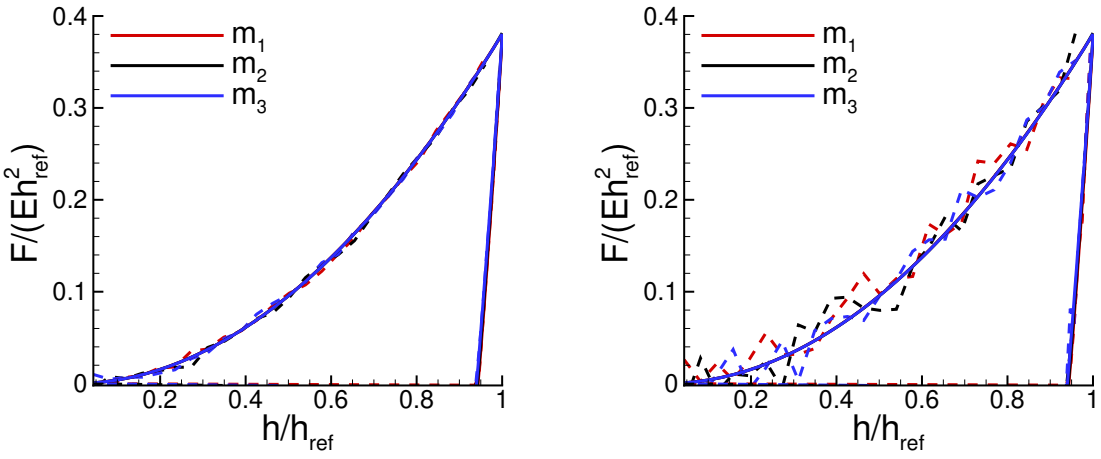

Figure 3.10: One realization of the normalized noise-contaminated indentation force versus indentation depth curves with the noise amplitude (a) $\eta_{\mathrm{f}} = 0.01$ and (b) $\eta_{\mathrm{f}} = 0.05$ for the three "experimental" materials given in the text.

data and the noise. Hence, obtaining an accurate identification requires considering a variety of realizations of a given amplitude of noise fluctuations. Here, for each pair of noise amplitude values $\eta_{\mathrm{f}} = \eta_{\mathrm{s}} = 0.01$ and $\eta_{\mathrm{f}} = \eta_{\mathrm{s}} = 0.05$, 100 realizations of $\boldsymbol{s}^{\mathrm{noise}}$ and $\boldsymbol{f}^{\mathrm{noise}}$ in Eq. (5.24) are used to identify the values of Y/E and N for each strain hardening rule. As in Ref. [2], for each of the 100 realizations, the values of Y/E and N associated with the highest posterior probability was obtained and the the arithmetic average of these 100 values of Y/E and N was then calculated. In addition, the values of the standard deviations for Y/E and N, denoted by $\xi_{Y/E}$ and ξ_N, over the 100 realizations were also calculated.

We note that the calculation of the posterior probability for each realization is a quick calculation carried out using a MATLAB [109] code on a personal computer. The calculation time includes 5 parts:

Part 1: load two types of data, indentation force versus indentation depth data ($\boldsymbol{f}^i$) and residual surface profile data ($\boldsymbol{s}^i$) for i runs from 1 to K_{total}, $K_{\mathrm{total}} = 520$ materials. And load one pair of "experimental" data, either noise-free, $\boldsymbol{f}^{\mathrm{inp}}$ and $\boldsymbol{s}^{\mathrm{inp}}$, or noise-contaminated, $\boldsymbol{f}^{\mathrm{m}}$ and $\boldsymbol{s}^{\mathrm{m}}$. The number

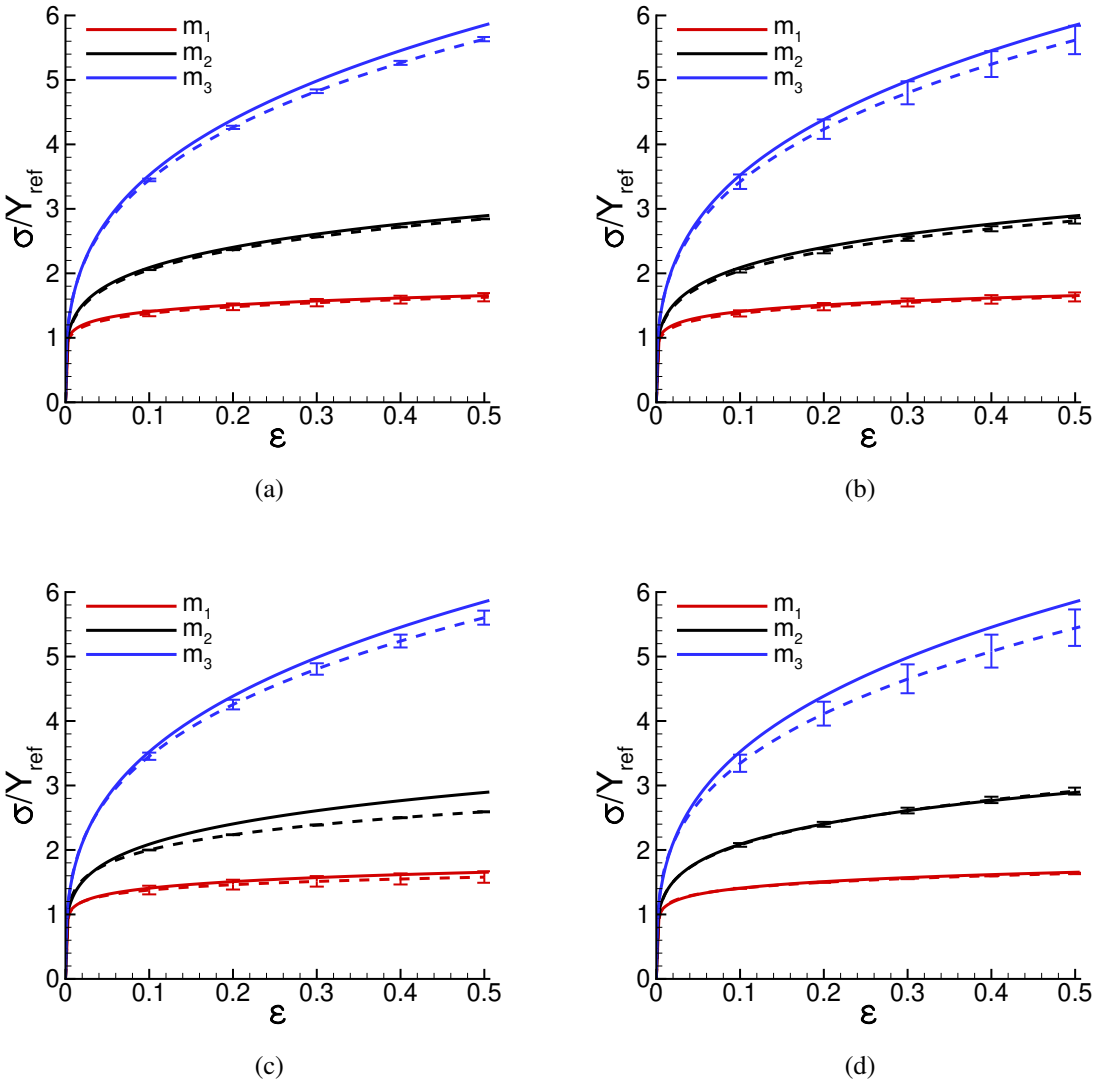

Figure 3.11: Uniaxial stress-strain curves of the averaged predicted Y/E and N, $(Y_{\text{ave}}/E, N_{\text{ave}})$ in dashed lines from the databases with strain hardening rules (a) F_0 (b) F_1 (c) F_2 and (d) F_3 with the noise amplitudes $\eta_{\text{s}} = \eta_{\text{f}} = 0.01$. The error bars denote the stress-strain curves for the combinations of average values with their corresponding standard deviations over the 100 realizations, $(Y_{\text{ave}}/E + \xi_{Y/E}, N_{\text{ave}} + \xi_N)$ and $(Y_{\text{ave}}/E - \xi_{Y/E}, N_{\text{ave}} - \xi_N)$. For convenience, the reference stress Y_{ref} for each material is taken to be the value of Y specified for the "experimental" materials in Ref. [2]: 650MPa for m_1; 490MPa for m_2; and 330MPa for m_3. The solid lines show the uniaxial stress-strain curves for the three "experimental" materials in Figs. 3.3 and 3.4.

of data points in these "raw" data is 10^3 during loading and 200 during unloading in indentation force versus indentation depth data, and is 90 in residual surface profile data;

Part 2: construct a database by interpolating data points in $\boldsymbol{f}^i$, $\boldsymbol{s}^i$, $\boldsymbol{f}^{\rm m}$ and $\boldsymbol{s}^{\rm m}$ (or $\boldsymbol{f}^{\rm inp}$ and $\boldsymbol{s}^{\rm inp}$) to $K_{\rm f}$ and $K_{\rm s}$ data points at specific positions for indentation force versus indentation depth data and residual surface profile data, respectively. Name the obtained vectors the same name, $\boldsymbol{f}^i$, $\boldsymbol{s}^i$, $\boldsymbol{f}^{\rm m}$ and $\boldsymbol{s}^{\rm m}$ (or $\boldsymbol{f}^{\rm inp}$ and $\boldsymbol{s}^{\rm inp}$) but with only $K_{\rm f}$ and $K_{\rm s}$ number of data points in the indentation force versus indentation depth data and residual surface profile data, respectively. The database is named as the database with database grid G_0;

Part 3: refine the database by interpolation between data of nearby points on database grid G_0 to get database with database grid G_1 (before Bayesian statistics calculation) and G_2 (during Bayesian statistics calculation);

Part 4: perform Bayesian statistics calculations using Eqs. (5.8)-(3.10) for one realization (noise-free case) or 100 realizations (noise-contaminated case);

Part 5: print summarized results on screen or generate output files.

The calculation time is 15 to 26 seconds for one realization of a pair of noise-free data, and is 80 to 105 seconds for 100 realizations of a pair of noise-contaminated data. The reported calculation time is corresponding to the parameter settings with, such as $K_{\rm s} = 72$, $K_{\rm f} = 67$, $K_{\rm total} = 520$ for database grid G_0, $K_{\rm total} = 3927$ for database grid G_1, and $K_{\rm total} = 121$ for database grid G_2. The number of data points is 1200 in "raw" indentation force versus indentation depth data, and is 90 in "raw" residual surface profile data. Variation of these parameters' values would affect the calculation time. Note that the Bayesian statistics calculation (part 4) is very quick once the database is constructed or refined.

Figs. 3.11 and 3.12 show the uniaxial stress-strain curves using the average values, $Y_{\rm ave}/E$ and $N_{\rm ave}$ over the 100 realizations from the databases for the four strain hardening rules F_0, F_1, F_2 and F_3 with various noise amplitudes. The error bars shown in Figs. 3.11 and 3.12 correspond to $(Y_{\rm ave}/E + \xi_{Y/E}, N_{\rm ave} + \xi_N)$ and $(Y_{\rm ave}/E - \xi_{Y/E}, N_{\rm ave} - \xi_N)$ since these give the largest variation and show the variation of predicted stress-strain responses that can occur for different realizations with the same noise amplitude.

For both a relatively small noise amplitude $\eta_{\rm s} = \eta_{\rm f} = 0.01$ and a relatively large noise $\eta_{\rm s} =$

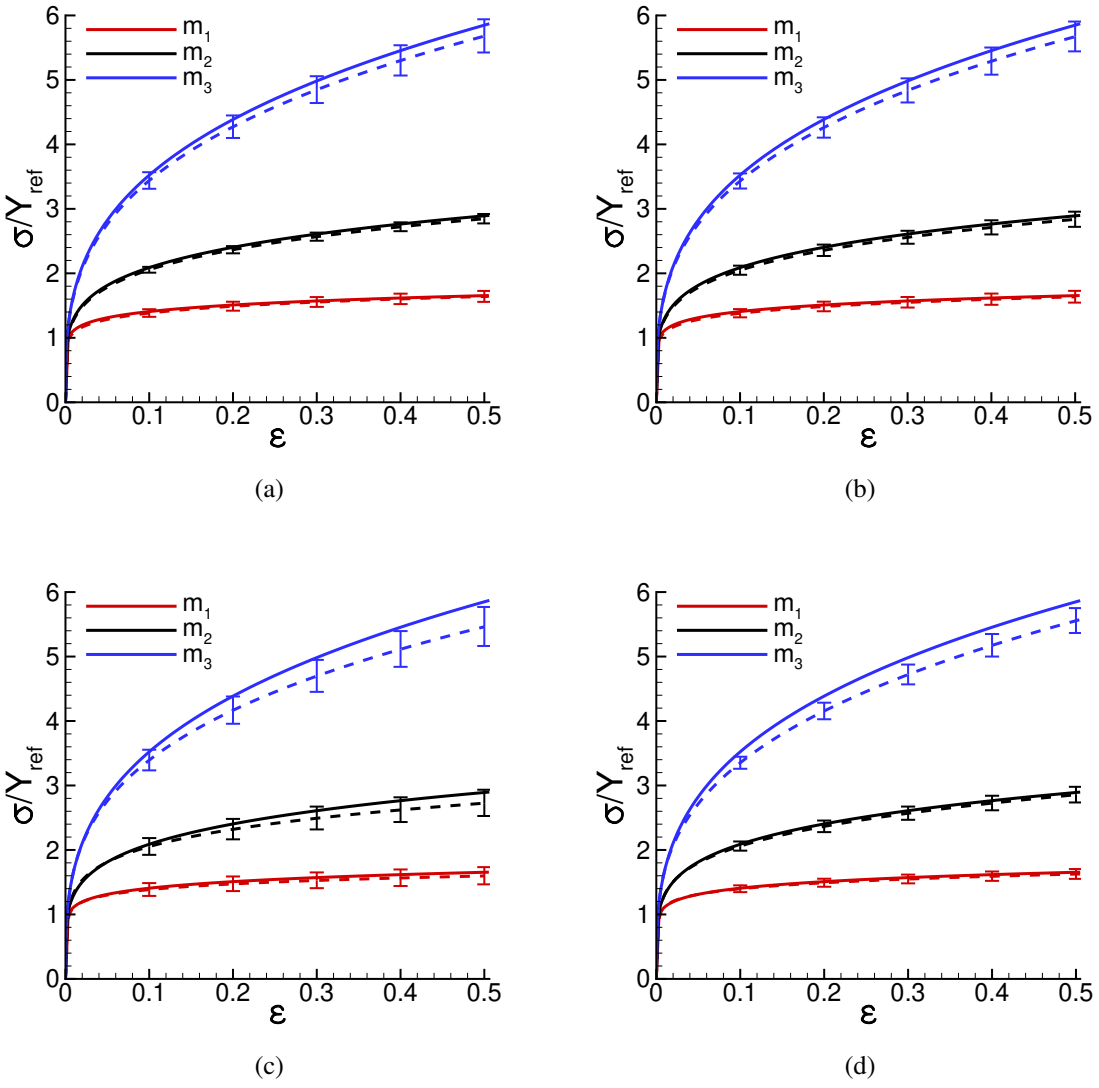

Figure 3.12: Uniaxial stress-strain curves of the averaged predicted Y/E and N, $(Y_{\text{ave}}/E, N_{\text{ave}})$ in dashed lines from the databases with strain hardening rules (a) F_0 (b) F_1 (c) F_2 and (d) F_3 with the noise amplitudes $\eta_{\text{s}} = \eta_{\text{f}} = 0.05$. The error bars denote the stress-strain curves for the combinations of average values with their corresponding standard deviations over the 100 realizations, $(Y_{\text{ave}}/E + \xi_{Y/E}, N_{\text{ave}} + \xi_N)$ and $(Y_{\text{ave}}/E - \xi_{Y/E}, N_{\text{ave}} - \xi_N)$. For convenience, the reference stress Y_{ref} for each material is taken to be the value of Y specified for the "experimental" materials in Ref. [2]: 650MPa for m_1; 490MPa for m_2; and 330MPa for m_3. The solid lines show the uniaxial stress-strain curves for the three "experimental" materials in Figs. 3.3 and 3.4.

$\eta_{\text{f}} = 0.05$, the stress-strain responses of the averaged predicted parameters from all four databases with hardening rules F_0, F_1, F_2 and F_3 provide reasonably good fits to the stress-strain curves of

Table 3.2: Average of the predicted values of Y/E and N over 100 realizations based on noise-contaminated data with noise amplitudes $\eta_{\rm s} = \eta_{\rm f} = 0.01$ from the four databases with strain hardening rules $\rm F_0$, $\rm F_1$, $\rm F_2$ and $\rm F_3$.

	m_1	m_2	m_3
$Y_{\rm F_0}/E$	0.00314	0.00240	0.00170
$N_{\rm F_0}$	0.103	0.200	0.300
$Y_{\rm F_1}/E$	0.00310	0.00236	0.00157
$N_{\rm F_1}$	0.106	0.200	0.308
$Y_{\rm F_2}/E$	0.00270	0.00195	0.00100
$N_{\rm F_2}$	0.0836	0.160	0.300
$Y_{\rm F_3}/E$	0.00165	0.00125	0.000946
$N_{\rm F_3}$	0.140	0.259	0.342

Table 3.3: Average of the predicted values of Y/E and N over 100 realizations based on noise-contaminated data with noise amplitudes $\eta_{\rm s} = \eta_{\rm f} = 0.05$ from the four databases with strain hardening rules $\rm F_0$, $\rm F_1$, $\rm F_2$ and $\rm F_3$.

	m_1	m_2	m_3
$Y_{\rm F_0}/E$	0.00313	0.00240	0.00162
$N_{\rm F_0}$	0.105	0.200	0.307
$Y_{\rm F_1}/E$	0.00311	0.00235	0.00154
$N_{\rm F_1}$	0.105	0.203	0.312
$Y_{\rm F_2}/E$	0.00265	0.00185	0.00101
$N_{\rm F_2}$	0.0874	0.175	0.295
$Y_{\rm F_3}/E$	0.00165	0.00127	0.000901
$N_{\rm F_3}$	0.139	0.253	0.352

the three "experimental" materials. When $\eta_{\rm s} = \eta_{\rm f} = 0.01$, The variation of the predicted stress-strain curves is small except for the prediction for material m_3 from database with rule F_3. When $\eta_{\rm s} = \eta_{\rm f} = 0.05$, the stress-strain curves of averaged predicted parameters generally provide as good fits as the ones based on data with a low noise level, but with larger variations (larger values of the standard deviations). This indicates that what is important to know regarding experimental measurements is the expected noise amplitude and that various statistical realizations with that amplitude should be considered in extracting the uniaxial stress-strain response.

It is worth noting that although the standard deviations in the values of Y/E and N for material

m_3 with noise amplitudes $\eta_{\rm s} = \eta_{\rm f} = 0.05$ and with strain hardening rules F_1, F_2 and F_3 are all smaller than the corresponding the standard deviations for m_2, the error bars in Figs. 3.11 and 3.12 associated with material m_3 are larger than those associated with material m_2 because the uniaxial stress-strain response of a higher strain hardening material is more sensitive to variations in the values of these parameters.

The prediction for material m_3 from the database with hardening rule F_3 is unusual in that the standard deviations for $\eta_{\rm s} = \eta_{\rm f} = 0.01$ ($\xi_{Y_{F_3\eta=0.01}/E} = 0.0019 \times 10^{-2}$ and $\xi_{N_{F_3\eta=0.01}} = 0.0069$) are larger than those for $\eta_{\rm s} = \eta_{\rm f} = 0.05$ ($\xi_{Y_{F_3\eta=0.05}/E} = 0.0017 \times 10^{-2}$ and $\xi_{N_{F_3\eta=0.05}} = 0.0038$). In this case, values of N in the range 0.33 to 0.36 provide good fit to the stress-strain response with $\eta_{\rm s} = \eta_{\rm f} = 0.01$ while with $\eta_{\rm s} = \eta_{\rm f} = 0.05$ the values of N for the 100 realizations only vary between 0.35 and 0.36. Consistent with this, the standard deviation $\xi_{N_{F_3\eta=0.01}}$ is about twice $\xi_{N_{F_3\eta=0.05}}$, while the standard deviations $\xi_{Y_{F_3\eta=0.01}/E}$ and $\xi_{Y_{F_3\eta=0.05}/E}$ have values that are very close. In most cases, as seen in Figs. 3.11 and 3.12, the extent of the error bars with $\eta_{\rm s} = \eta_{\rm f} = 0.05$ are larger than those with $\eta_{\rm s} = \eta_{\rm f} = 0.01$.

Table 3.2 shows the averaged predicted values of Y/E and N for the four strain hardening rules over 100 realizations with $\eta_{\rm f} = \eta_{\rm s} = 0.01$. Similarly, Table 3.3 shows the averaged predicted values of Y/E and N for the four strain hardening rules over 100 realizations with $\eta_{\rm f} = \eta_{\rm s} = 0.05$. The values of Y/E and N in Tables 3.2 and 3.3 are shown to three significant figures and are very close to the values in Table 3.1 showing that the Bayesian type approach used gives predicted plastic properties that are rather insensitive to noise in the data. For example, for strain hardening rule F_1, with no noise the predicted values of Y/E and N are 0.00315, 0.100 for material m_1; 0.00235, 0.200 for material m_2; and 0.00155, 0.310 for material m_3. With $\eta_{\rm f} = \eta_{\rm s} = 0.05$ in Table 3.3, the corresponding values are 0.00310, 0.106 for material m_1; 0.00236, 0.200 for material m_2; and 0.00157, 0.308 for material m_3.

The highest posterior probability values of the three materials with strain hardening rules $\rm F_0$, $\rm F_1$, $\rm F_2$ and $\rm F_3$ corresponding to Tables 3.1 (noise-free) and 3.2 (noise amplitudes $\eta_{\rm s} = \eta_{\rm f} = 0.01$) are similar. The highest posterior probability values correspond to Table 3.3 (noise amplitudes

$\eta_s = \eta_f = 0.05$) are noticeably smaller than the ones corresponding to Tables 3.1 and 3.2. For example, for material m_1 with strain hardening rule F_3, the highest posterior probability values are 0.89, 0.81 and 0.40 based on data with no noise, noise amplitudes $\eta_s = \eta_f = 0.01$ and noise amplitudes $\eta_s = \eta_f = 0.05$, respectively. For material m_3 with strain hardening rule F_2, the corresponding highest posterior probability values are 0.95, 0.87 and 0.59. Note that only the relative magnitude of the posterior probability value within its distribution is meaningful.

The calculations here show that even with a relatively large noise amplitude, the Bayesian-type statistical approach of Ref. [2], together with appropriate averaging over a number of realizations, can identify plastic parameters associated with a variety of power law strain hardening rules from conical indentation data that give a good representation of the uniaxial stress-strain behavior of the "experimental" material.

3.6 Conclusions

1. The ability of the predicted stress-strain response to represent the "experimental" stress-strain response is not sensitive to the choice of strain hardening rule, at least for the range of rules considered.

2. The specific form of strain hardening rule does not affect the sensitivity of the predicted stress-strain response to the noise amplitude in the data.

3. When the noise amplitude of the data is relatively small ($\eta_s = \eta_f = 0.01$), the influence of noise on the predicted uniaxial stress-strain response is small and the predicted uniaxial stress-strain curves are in good agreement with the predictions based on noise-free data. When noise in the measurements is relatively large ($\eta_s = \eta_f = 0.05$), the predicted uniaxial stress-strain curves can vary significantly with the particular realization. However, using plastic parameters obtained from an average of 100 realizations can provide a good representation of the uniaxial stress-strain response. The parameters obtained from this averaging are in good agreement with those obtained from noise-free data.

4. The uniaxial stress-strain curve for a high strain hardening material is more sensitive to dif-

ferences in the parameter values of the strain hardening rule than is a lower strain hardening material. Accordingly, the predicted uniaxial stress-strain response for a high strain hardening material can be more sensitive to noise than is the predicted uniaxial stress-strain response for a low strain hardening material.

Acknowledgments

The finite element calculations reported on were carried out using high performance research computing resources provided by Texas A&M University (https://hprc.tamu.edu). Y.Z. is grateful to Dr. Ankit Srivastava and Ms. Yu Liu's help with ABAQUS.

4. CHARACTERIZATION OF PLASTICALLY COMPRESSIBLE SOLIDS VIA SPHERICAL INDENTATION †

"One of the principal objects of theoretical research is to find the point of view from which the subject appears in the greatest simplicity."

– Josiah Willard Gibbs

4.1 Introduction

A variety of tests are carried out with the aim of characterizing the mechanical response of a material so that a quantitative assessment can be made of its performance in other circumstances of interest, for example in an engineering component or structure. The results of such tests are expressed in terms of "properties." However, it is important to recognize that a property is not a characteristic of a material but is a parameter entering a constitutive description. Indeed, a theory is needed to relate the response of a material in such a test to a property. For example, in a simple uniaxial tensile test, the more or less directly measured quantities are the change in length of the specimen and the force. Continuum mechanics theory states that the characterization of the mechanical response is in terms of the stress, the force divided by the cross section area, and the strain, the change in length divided by the length. The assumed constitutive relation provides a means of characterizing the stress versus strain response in terms of one or more properties that may be parameters, functions and/or functionals.

In other circumstances the connection between more or less directly measured quantities and a material property is not so straightforward. In particular, in instrumented indentation, the indentation depth and the indentation force are measured. Relating these measured quantities to the properties of some constitutive relation requires full field solutions of an initial/boundary value

†Reprinted with permission from "Characterization of plastically compressible solids via spherical indentation" by Yupeng Zhang and Alan Needleman, 2021, Journal of the Mechanics and Physics of Solids, 148, 104283.

problem with an assumed constitutive relation. A variety of approaches have been proposed to identify plastic constitutive relation properties from the indentation response including optimization, e.g., [113, 114, 115, 117], neural networks and machine learning, e.g., [86, 116, 121] and Bayesian statistics, e.g., [106, 2, 122, 123].

However, for a given constitutive framework, the relation between the indentation force versus indentation depth response and the uniaxial stress-strain response is not necessarily unique, [91, 2, 124], in the sense that two sets of plastic constitutive parameters with very different uniaxial stress-strain responses can give indistinguishable indentation force versus indentation depth responses. One approach considered to resolving the non-uniqueness is to use a surface profile associated with the indent instead of or in addition to the indentation force versus indentation depth response, [116, 125, 126, 95, 117, 2]. For conical indentation and presuming an isotropic hardening elastic-plastic constitutive relation with plastic incompressibility, [2] showed that including the residual surface profile in their Bayesian statistics formulation can render the relation unique.

Here, we consider a broader class of materials, namely materials that exhibit plastic compressibility, and explore the identification of plastic properties for such materials from spherical indentation. Plastically compressible materials, such as metallic foams, architected lattice materials and nano-porous solids, have a wide range of applications and potential applications, for example as impact-energy absorbers and as components in industrial machines where their light weight reduces inertia. A variety of studies of the indentation response of foams have been carried out to understand and characterize their mechanical behavior, including [127, 128, 129, 130, 131, 132, 133, 134, 135, 136, 137].

Here, we presume that the materials under consideration are appropriately characterized by a rate dependent Deshpande-Fleck type constitutive relation, [138, 107], but with very small rate sensitivity so that the response can be idealized as nearly rate independent. The plastic response is then characterized by three parameters, a strain hardening exponent, an initial flow strength and a scalar parameter characterizing the plastic compressibility.

Previous analyses of indentation of materials characterized by a Deshpande-Fleck type consti-

tutive relation include conical indentation into a bulk material, [107, 136], spherical and wedge indentation of low-density polymeric foams, [134], indentation of a thin film on a substrate by a cylindrical indenter, [139] and estimation of the plastic volume change parameter, assuming the other two plastic constitutive parameters are known, from the maximum indentation force versus maximum indentation depth relation in spherical indentation, [131, 132]. Here, a Bayesian-type statistical analysis is used to identify all three plastic material parameters from a single spherical indentation for two synthetic "experimental" plastically compressible materials with presumed known elastic properties. One material is representative of the uniaxial response (over a strain range of interest) of an open cell foam and the other of a closed cell foam. A database is constructed for each material for a range of values of the three constitutive parameters. A disadvantage of a Bayesian-type approach for parameter identification is that the number of full field solutions required can be large. To overcome this, as in [2, 140], a rather coarse database of full field solutions is constructed and then the more refined dataset of constitutive parameters that is used for material identification is obtained by interpolation. In identifying the plastic material parameters for the two materials, both noise-free and noise-contaminated data are considered.

In addition to identifying the material parameters for the two "experimental" materials, several questions are considered:

1. Are the identified plastic properties obtained using the spherical indentation force versus indentation depth response unique?

   (i) If not, can the property identification be rendered unique by considering the residual surface profile?

2. How does the plastic compressibility affect the correction factor β in the [81] method for determining the effective (or reduced) elastic modulus from the indentation force unloading response?

3. How does plastic compressibility affect the identification of plastic properties from indentation data?

4. What are the consequences of using an inappropriate plastic constitutive framework?

5. How sensitive is the identification of the plastic material properties to the specification of the elastic properties?

6. How do the responses in conical and spherical indentation compare?

We begin by specifying the spherical indentation initial/boundary value problem formulation, the numerical method and the porous plastic constitutive relation used
citesinica2015. We show the correspondence between the material parameters in that formulation and those of the [138] constitutive relation. For completeness, the formulas used for the Bayesian-type statistical calculations are presented. The finite element formulation is briefly described and some typical results for plastically compressible solids are shown. The construction of the needed database is described. Results for the identification of the material properties of the two "experimental" materials are presented. Parameter studies are then carried out to begin to address the questions listed above.

4.2 Problem formulation

4.2.1 Initial/boundary value problem

Although the initial/boundary value problem formulation is identical to that in [107] and [2], except for the indenter shape, for completeness, the problem formulation is briefly specified. Further details and additional references are given in [107].

A Lagrangian formulation of the field equations is used, with the position of a material point in the unstressed initial configuration, which serves as the reference configuration, denoted by $\mathbf{X}$. The displacement vector is $\mathbf{u} = \mathbf{x} - \mathbf{X}$ and the deformation gradient is $\mathbf{F} = \partial\mathbf{x}/\partial\mathbf{X}$, where $\mathbf{x}$ is the position in the current configuration of the material point at $\mathbf{X}$ in the initial configuration. The rate form of the principle of virtual work is written as

$$\int_V \dot{\mathbf{s}} \cdot\cdot \delta\mathbf{F}\, dV = \int_S \dot{\mathbf{T}} \cdot \delta\mathbf{u}\, dS - \frac{1}{\Delta t}\Big[\int_V \mathbf{s} \cdot\cdot \delta\mathbf{F}\, dV - \int_S \mathbf{T} \cdot \delta\mathbf{u}\, dS\Big] \tag{4.1}$$

The second term on the right hand side of Eq. (4.1) is used to reduce the drift from the equilibrium path due to the time step procedure. Also, V and S are the volume and surface, respectively, of the body in the reference configuration, t is time, $\dot{(\,)} = \partial()/\partial t$ at fixed $\mathbf{X}$, double inner dot product $\mathbf{A} \cdot\cdot \mathbf{B} = A^{ij}B_{ji}$ and $\mathbf{v} \cdot \mathbf{w} = v^i w_i$, and

$$\mathbf{T} = \mathbf{n} \cdot \mathbf{s} \ , \ \mathbf{s} = \mathbf{F}^{-1} \cdot \boldsymbol{\tau} \ , \ \boldsymbol{\tau} = J\boldsymbol{\sigma} \tag{4.2}$$

where $\mathbf{n}$ is the surface normal, $\boldsymbol{\tau}$ is the Kirchhoff stress and $\boldsymbol{\sigma}$ is the Cauchy stress ($J = \det(\mathbf{F})$).

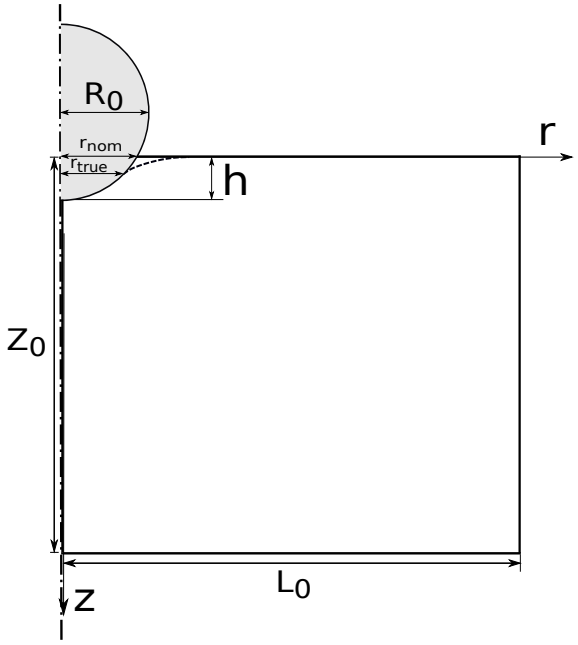

Figure 4.1: Sketch of the spherical indentation configuration analyzed.

We confine attention to axisymmetric deformations and a reference cylindrical coordinate system, (r, θ, z), is used with all field quantities independent of θ. The calculations are carried out for a rigid spherical indenter of radius R_0 pushed into a cylindrical block occupying $0 \leq r \leq L_0$, $0 \leq z \leq Z_0$ as sketched in Fig. 5.1.

Perfect sticking is assumed as soon as the block comes into contact with the indenter, so that

the rate boundary conditions are

$$\dot{u}_r = 0 \qquad \dot{u}_z = \dot{h} \qquad \text{on} \quad S_{\text{contact}} \tag{4.3}$$

where S_{contact} denotes the portion of the material surface in contact with the indenter.

With the origin of the coordinate system as shown in Fig. 5.1, the other boundary conditions are $\dot{u}_r = 0$, $\dot{T}_z = 0$ on $r = 0$, $\dot{u}_z = 0$, $\dot{T}_r = 0$ on $z = Z_0$ and $\dot{\mathbf{T}} = \mathbf{0}$ on the remaining external surface.

The deformations induced by spherical indenter are not self-similar and radius of the spherical indenter, R_0, serves as a characteristic length. Subsequently, length quantities are normalized by R_0.

For indentation into a foam, the indenter radius R_0 and the indentation depth h are presumed to be much larger than a length, such as a cell size, characterizing the foam microstructure so that the foam can be idealized as a homogeneous material.

4.2.2 Constitutive relation

The constitutive relation is the same as the one in [107] which, in turn, is a specialization to plastic normality of that introduced in [141]. The rate of deformation tensor, $\mathbf{d} = \mathrm{sym}(\dot{\mathbf{F}} \cdot \mathbf{F}^{-1})$, is taken to be the sum of elastic, $\mathbf{d}^{\mathrm{e}}$, and plastic, $\mathbf{d}^{\mathrm{p}}$, parts. The elastic strains, assumed small, are given by

$$\mathbf{d}^{\mathrm{e}} = \frac{1+\nu_{\mathrm{e}}}{E}\hat{\boldsymbol{\tau}} - \frac{\nu_{\mathrm{e}}}{E}\mathrm{tr}(\hat{\boldsymbol{\tau}})\mathbf{I} \tag{4.4}$$

where E is Young's modulus, ν_{e} is elastic Poisson's ratio, $\mathrm{tr}(\cdot)$ denotes the trace, $\mathbf{I}$ is the identity tensor and $\hat{\boldsymbol{\tau}}$ is the Jaumann rate of Kirchhoff stress. As noted in [107], although Eq. (4.4) is a hypoelastic relation, there is an elastic potential for the volumetric part.

The plastic part of the rate of deformation tensor can be written as

$$\mathbf{d}^{\mathrm{p}} = \dot{\Lambda}_{\mathrm{p}}\frac{\partial \Phi}{\partial \boldsymbol{\tau}} = \frac{3}{2}\left(\frac{\dot{\epsilon}_{\mathrm{p}}}{\tau_{\mathrm{e}}}\right)\mathbf{p} \tag{4.5}$$

with

$$\Phi = \tau_{\mathrm{e}} - \bar{\tau}(\epsilon_{\mathrm{p}}, \dot{\epsilon}_{\mathrm{p}}) = 0 \quad , \quad \mathbf{p} = \boldsymbol{\tau} - \alpha\, \mathrm{tr}(\boldsymbol{\tau})\mathbf{I} \tag{4.6a}$$

$$\tau_{\mathrm{e}}^2 = \frac{3}{2}\boldsymbol{\tau} : \mathbf{p} = \frac{3}{2}\left[\boldsymbol{\tau} : \boldsymbol{\tau} - \alpha\left(\mathrm{tr}(\boldsymbol{\tau})\right)^2\right] \tag{4.6b}$$

and

$$\dot{\epsilon}_{\mathrm{p}} = \dot{\epsilon}_0 \left(\frac{\bar{\tau}}{g}\right)^{1/m} \quad , \quad g\left(\epsilon_{\mathrm{p}}\right) = \bar{\tau}_0 \left[1 + \frac{\epsilon_{\mathrm{p}}}{\epsilon_0}\right]^N \tag{4.7}$$

Here, $\dot{\epsilon}_0$ is a reference strain rate, m is the rate sensitivity exponent, $\bar{\tau}_0$ is a reference stress and ϵ_0 is a reference strain.

The effective stress, τ_{e} in Eq. (4.6b), can also be written as

$$\tau_{\mathrm{e}}^2 = \tau_{\mathrm{M}}^2 + \frac{9}{2}\left(1 - 3\alpha\right)\tau_{\mathrm{h}}^2 \tag{4.8}$$

where

$$\tau_{\mathrm{M}}^2 = \frac{3}{2}\boldsymbol{\tau}' : \boldsymbol{\tau}' \quad , \quad \boldsymbol{\tau}' = \boldsymbol{\tau} - \frac{1}{3}\mathrm{tr}(\boldsymbol{\tau})\mathbf{I} \quad , \quad \tau_{\mathrm{h}} = \frac{1}{3}\mathrm{tr}(\boldsymbol{\tau}) \tag{4.9}$$

It is also worth noting that the plastic Poisson's ratio, ν_{p}, is given by, [107],

$$\nu_{\mathrm{p}} = \frac{\alpha}{1 - \alpha} \tag{4.10}$$

For $\alpha = 1/3$, the plastic flow rule reduces to that of a plastically incompressible Mises solid with $\nu_{\mathrm{p}} = 1/2$.

4.2.3 Relation to the Deshpande-Fleck formulation

The plastic flow rule in Section 4.2.2 differs from the relation of [138] in three significant respects: (i) it is a rate dependent flow rule whereas that in [138] is rate independent; (ii) it is based on Kirchhoff stress whereas that in [138] is based on Cauchy stress; and (iii) the form of the flow potential in [138] differs slightly from that in Section 4.2.2. Nevertheless, the two relations can be made to coincide once the Deshpande-Fleck relation is generalized to rate dependent material response.

The Deshpande-Fleck flow potential surface is written as

$$\Phi_{DF} = \hat{\sigma} - \bar{\sigma}(E_{\rm p}, \dot{E}_{\rm p}) = 0 \tag{4.11}$$

where $\hat{\sigma}$ is defined by

$$\hat{\sigma}^2 = \frac{1}{1 + (\alpha_{\rm DF}/3)^2} \left[\sigma_{\rm M}^2 + \alpha_{\rm DF}^2 \sigma_{\rm h}^2\right] \tag{4.12}$$

with $\sigma_{\rm M}$ and $\sigma_{\rm h}$ given by expressions of the form of Eq. (4.9) but with the Cauchy stress tensor replacing the Kirchhoff stress tensor.

The plastic flow rule takes the form

$$\mathbf{d}^{\rm p} = \frac{3}{2} \left(\frac{\dot{E}_{\rm p}}{\hat{\sigma}}\right) \hat{\mathbf{p}} \tag{4.13}$$

where

$$\hat{\mathbf{p}} = \frac{1}{1 + (\alpha_{\rm DF}/3)^2} \left[\boldsymbol{\sigma}' + \frac{2}{9} \alpha_{\rm DF}^2 \sigma_{\rm h} \mathbf{I}\right] \tag{4.14}$$

and

$$\dot{E}_{\rm p} = \dot{E}_0 \left(\frac{\bar{\sigma}}{\hat{g}}\right)^{1/m} \quad , \quad \hat{g}(E_{\rm p}) = \bar{\sigma}_0 \left[1 + \frac{E_{\rm p}}{E_0}\right]^N \tag{4.15}$$

With, as in [107], the identification

$$\alpha_{\rm DF}^2 = \frac{9}{2} (1 - 3\alpha) \tag{4.16}$$

from Eqs. (4.8) and (4.12)

$$\hat{\sigma} = \frac{1}{J\sqrt{1 + (\alpha_{\rm DF}/3)^2}} \tau_{\rm e} \tag{4.17}$$

The relations between $\bar{\sigma}$ and $\bar{\tau}$, and between $\hat{g}$ and g are also of the form of Eq. (4.17).

Since $\mathbf{p}$ in Eq. (4.6a), can be written as

$$\mathbf{p} = \boldsymbol{\tau}' + (1 - 3\alpha)\tau_{\rm h} \mathbf{I} = J \left[\boldsymbol{\sigma}' + \frac{2}{9} \alpha_{\rm DF}^2 \sigma_{\rm h} \mathbf{I}\right] \tag{4.18}$$

we have

$$\hat{\mathbf{p}} = \frac{1}{J[1+(\alpha_{\rm DF}/3)^2]}\mathbf{p} \quad , \quad \frac{\hat{\mathbf{p}}}{\hat{\sigma}} = \frac{1}{\sqrt{1+(\alpha_{\rm DF}/3)^2}}\frac{\mathbf{p}}{\tau_{\rm e}} \tag{4.19}$$

Therefore, with

$$\dot{E}_{\rm p} = \left[\sqrt{1+(\alpha_{\rm DF}/3)^2}\right]\dot{\epsilon}_{\rm p} = \left[\sqrt{1+(1-3\alpha)/2}\right]\dot{\epsilon}_{\rm p} \tag{4.20}$$

the plastic flow rules, Eqs. (4.5) and (4.13), coincide. Note also that the relation between $E_{\rm p}$ and $\epsilon_{\rm p}$ of the same form as Eq. (4.20) since the factor relating $\dot{E}_{\rm p}$ and $\dot{\epsilon}_{\rm p}$ is a constant independent of plastic strain and stress state.

Next, the values of the material parameters in Eqs. (4.7) and those in Eqs. (4.15) need to be related. The values of $\dot{\epsilon}_0$ and $\dot{E}_0$, and those of ϵ_0 and E_0 are related via Eq.(4.20). The values of $\bar{\tau}_0$ and $\bar{\sigma}_0$ are related by noting that at $\dot{\epsilon}_{\rm p}/\dot{\epsilon}_0 = \dot{E}_{\rm p}/\dot{E}_0 = 1$ and $\epsilon_{\rm p} = E_{\rm p} = 0$, $\tau_{\rm e} = \bar{\tau}_0$ and $\hat{\sigma} = \bar{\sigma}_0$. Then, for a uniaxial state of stress σ, $\hat{\sigma} = \bar{\sigma}_0 = |\sigma|$ while $\tau_{\rm e} = \bar{\tau}_0 = J_0\sqrt{1+(1-3\alpha)/2}|\sigma|$. Hence, we set

$$\bar{\tau}_0 = J_0\left[\sqrt{1+(1-3\alpha)/2}\right]\bar{\sigma}_0 \tag{4.21}$$

where J_0 is the value of the Jacobian when $E_{\rm p} = \epsilon_{\rm p} = 0$ and is presumed to be ≈ 1. With these identifications, the values of m and N are the same in both formulations.

To estimate the range of values of the term in brackets, consider values of $\nu_{\rm p}$ in Eq. (4.10) between 0 and $1/2$. For $\nu_{\rm p} = 1/2$, $\alpha = 1/3$ and the factor in brackets is 1. For $\nu_{\rm p} = 0$, $\alpha = 0$ and the value of the factor in brackets is 1.22. For an intermediate value, $\nu_{\rm p} = 0.176$, $\alpha = 0.15$ and the value of the factor in brackets is 1.13.

4.3 Bayesian-type statistical approach

The equations used to calculate the posterior probabilities in the Bayesian-type statistical approach are presented here. Background, a more complete description of the methodology and references are given in [2, 140].

The experimental data consists of two vectors: $\boldsymbol{s}^{\rm m}$ and $\boldsymbol{f}^{\rm m}$. The components of vector $s_k^{\rm m}$, $k = 1, ..., K_{\rm s}$ are values of height of the surface coordinate, z_k at specified values of radial coordinate

r_k, while the components of vector f_k^{m}, $k = 1, ..., K_{\mathrm{f}}$ are values of the indentation force F_k at some specified indentation depth h_k.

A database of indentation responses is constructed from finite element solutions consisting of a residual surface profile, denoted by $\boldsymbol{s}^i$, and an indentation force versus indentation depth response, denoted by $\boldsymbol{f}^i$. The index i ranges from 1 to K_{total}, where K_{total} is the total number of cases in the database.

The indentation force versus indentation depth data and the surface profile data are treated as independent so that the posterior probability $p(\boldsymbol{s}^i, \boldsymbol{f}^i | \boldsymbol{s}^{\mathrm{m}}, \boldsymbol{f}^{\mathrm{m}})$ associated with $(\boldsymbol{s}^{\mathrm{m}}, \boldsymbol{f}^{\mathrm{m}})$ can be expressed as

$$p(\boldsymbol{s}^i, \boldsymbol{f}^i | \boldsymbol{s}^{\mathrm{m}}, \boldsymbol{f}^{\mathrm{m}}) = \frac{p(\boldsymbol{s}^i | \boldsymbol{s}^{\mathrm{m}}) p(\boldsymbol{f}^i | \boldsymbol{f}^{\mathrm{m}})}{Z_{\mathrm{sf}}} \tag{4.22}$$

where

$$p(\boldsymbol{s}^i | \boldsymbol{s}^{\mathrm{m}}) = \frac{p(\boldsymbol{s}^{\mathrm{m}} | \boldsymbol{s}^i) p(\boldsymbol{s}^i)}{Z_{\mathrm{s}}} \quad , \quad p(\boldsymbol{f}^i | \boldsymbol{f}^{\mathrm{m}}) = \frac{p(\boldsymbol{f}^{\mathrm{m}} | \boldsymbol{f}^i) p(\boldsymbol{f}^i)}{Z_{\mathrm{f}}} \tag{4.23}$$

There is no sum on i in Eqs. (5.8) to (5.9). It is worth noting that, due to the multiplication of posterior probabilities, the parameter values obtained using the largest posterior probability value from Eq. (5.8) are not guaranteed to provide a better approximation to the input material uniaxial responses than those obtained from either of the posterior probabilities in Eq. (5.9).

The normalizing constants Z_{s}, Z_{f} and Z_{sf} are given by

$$Z_{\mathrm{s}} = \sum_{i=1}^{K_{\mathrm{total}}} p(\boldsymbol{s}^{\mathrm{m}} | \boldsymbol{s}^i) p(\boldsymbol{s}^i) \ , \ Z_{\mathrm{f}} = \sum_{i=1}^{K_{\mathrm{total}}} p(\boldsymbol{f}^{\mathrm{m}} | \boldsymbol{f}^i) p(\boldsymbol{f}^i) \tag{4.24a}$$

$$Z_{\mathrm{sf}} = \sum_{i=1}^{K_{\mathrm{total}}} p(\boldsymbol{s}^i | \boldsymbol{s}^{\mathrm{m}}) p(\boldsymbol{f}^i | \boldsymbol{f}^{\mathrm{m}}) \tag{4.24b}$$

It is also assumed that the differences between the input data and the calculated responses in the database are distributed as a mean zero normal distribution. With the variances $(\hat{\xi}_{\mathrm{s}}^i)^2$ and $(\hat{\xi}_{\mathrm{f}}^i)^2$,

the likelihood values are, [2],

$$p(\boldsymbol{s}^{\mathrm{m}}|\boldsymbol{s}^{i}) = \Big(\frac{1}{\hat{\xi}_{\mathrm{s}}^{i}\sqrt{2\pi}}\Big)^{K_{\mathrm{s}}} \exp\Big(-\frac{K_{\mathrm{s}}}{2}\Big) \quad , \quad p(\boldsymbol{f}^{\mathrm{m}}|\boldsymbol{f}^{i}) = \Big(\frac{1}{\hat{\xi}_{\mathrm{f}}^{i}\sqrt{2\pi}}\Big)^{K_{\mathrm{f}}} \exp\Big(-\frac{K_{\mathrm{f}}}{2}\Big) \tag{4.25}$$

where K_{s} and K_{f} are the number of data points on the residual surface profile and the number of data points on the indentation force versus indentation depth response, respectively. If a standard deviation turns out to be exactly zero, the corresponding likelihood is infinite and the posterior probability is set to one.

A uniform prior is used for both $p(\boldsymbol{s}^{i})$ and $p(\boldsymbol{f}^{i})$ in the database and the values of $p(\boldsymbol{s}^{i})$ and $p(\boldsymbol{f}^{i})$ are set to 0 outside that range.

Both noise-free and noise-contaminated data are considered. With the noise-free responses denoted by $\boldsymbol{s}^{\mathrm{input}}$ and $\boldsymbol{f}^{\mathrm{input}}$, the noise-contaminated data are given by

$$\boldsymbol{s}^{\mathrm{m}} = \boldsymbol{s}^{\mathrm{input}} + \boldsymbol{s}^{\mathrm{noise}} \ , \ \boldsymbol{f}^{\mathrm{m}} = \boldsymbol{f}^{\mathrm{input}} + \boldsymbol{f}^{\mathrm{noise}} \tag{4.26}$$

Each component s_{k}^{noise} and f_{k}^{noise} is a random number from a normal distribution, calculated using the [109] function normrnd which has zero mean value. The values of the standard deviations ξ_{s} and ξ_{f} are taken to be normalized by a reference length s_{ref} and by the maximum indentation force, respectively, so that

$$\xi_{\mathrm{s}} = \eta_{\mathrm{s}} s_{\mathrm{ref}} \ , \ \xi_{\mathrm{f}} = \eta_{\mathrm{f}} \mathrm{max}(f_{k}^{\mathrm{m}}) \tag{4.27}$$

with $\eta_{\mathrm{s}} \geq 0$ and $\eta_{\mathrm{f}} \geq 0$, and η_{s} and η_{f} are referred to subsequently as the noise amplitudes. The reference length s_{ref} is taken to be the indentation depth of the residual surface profile.

4.4 Plastic parameters identification from spherical indentation

The results of spherical indentation computations with specified material properties are taken as "experimental" input values. Two sets of input plastic material properties for plastically compressible materials characterized by a [138] type constitutive relation are specified. One set (termed

A-input) is taken to be representative of Alporas®*, a closed cell foam, and the other (termed D-input) is representative of Duocel®†, an open-cell foam. The Deshpande-Fleck material parameters are based on data in [142] and [138].

Both noise-free and noise-contaminated data are considered. Since the response in spherical indentation is not self-similar, the depth of indentation, h, relative to the spherical indenter radius, R_0, matters. Here, the indentation calculations are carried out to an indentation depth of $h/R_0 = 0.3$.

4.4.1 Finite element calculations

Solutions to the indentation problem specified in Section 4.2.1 were obtained using an in-house axisymmetric finite element code based on the one used in [107]. Indentation into a half-space is approximated by indenting a finite block with dimension $L_0/R_0 = 37.5$ and $Z_0/R_0 = 37.5$. The reference finite element mesh used consists of 200×100 quadrilateral elements, with each rectangle consisting of four "crossed" linear displacement triangular elements. Within a region $R_0 \times 0.75R_0$ under the indenter, a fine mesh was used with 160×50 quadrilateral elements that gradually increased in size. Outside this fine meshed region where the gradient of the deformation field is small, a much coarser mesh was used. The deformation history was calculated in a linear incremental manner. The contours of normalized hydrostatic Kirchhoff stress $\tau_{\rm h}/\bar{\tau}_0$ and effective plastic strain $\epsilon_{\rm p}$ of the A-input and D-input materials at an indentation depth $h/R_0 = 0.3$ are shown in Fig. 4.2. The normalized indentation force versus normalized indentation depth responses and the normalized surface profiles near the indenter after unloading for the A-input and D-input materials are shown in Fig. 4.3. The indentation responses in Fig. 4.3 clearly differ although the distributions of plastic strain and hydrostatic stress in Fig. 4.2 are similar. The A-input and D-input constitutive parameters are given subsequently in Table 4.1.

In the calculations, the indentation force F varies in discrete steps when a new nodal point comes in contact with or detaches from the indenter. In order to provide a clearer picture of the

*Shinko Wire Company, Amagasaki, Japan
†ERG Aerospace Corporation, Oakland, USA

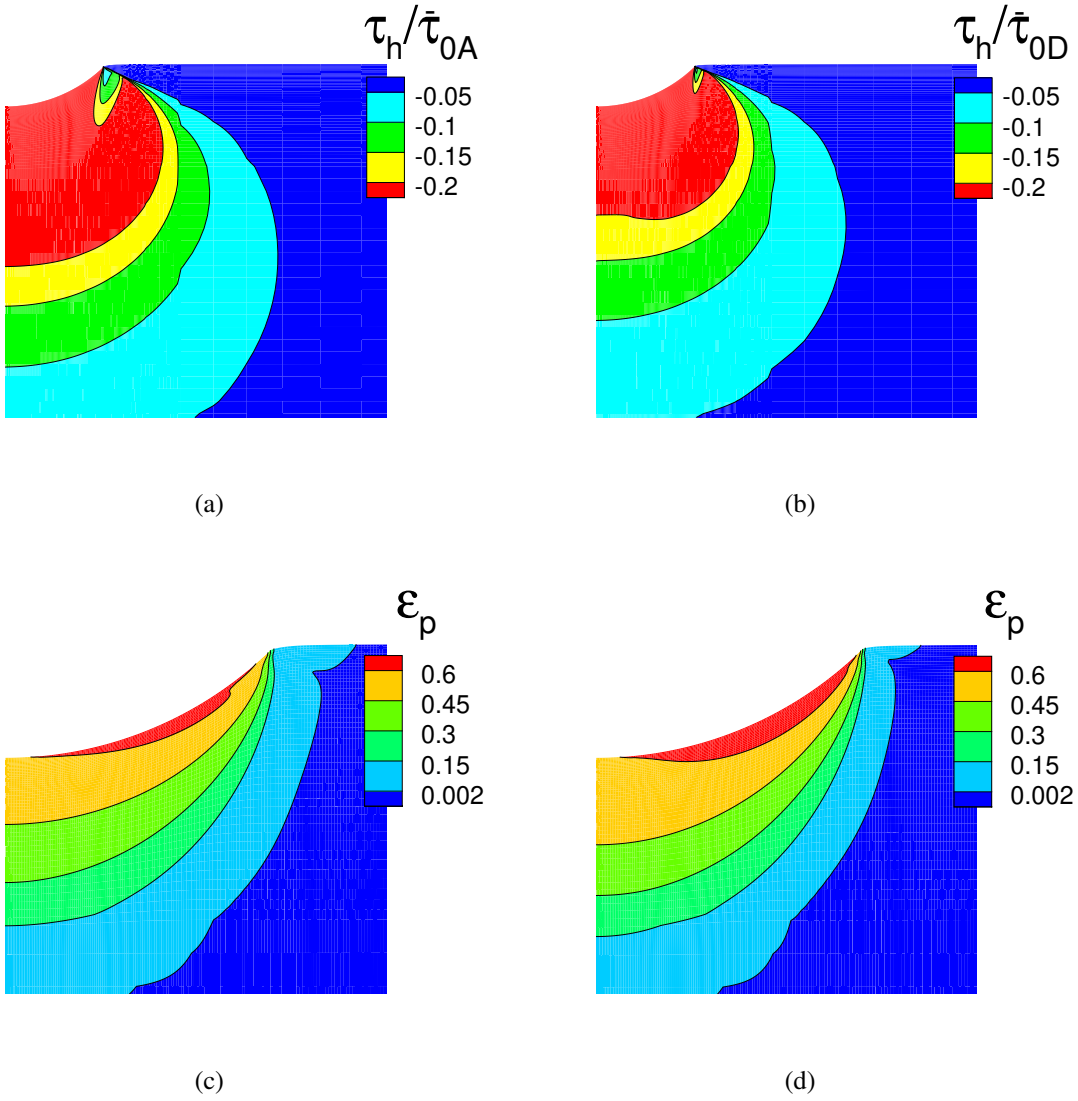

Figure 4.2: Field distributions in the vicinity of the indenter for the two "experimental" plastically compressible materials considered subsequently, termed the A-input material and the D-input material at an indentation depth $h/R_0 = 0.3$. The A-input and D-input constitutive parameters are given in Table 4.1. (a) Distribution of hydrostatic stress for A-input. (b) Distribution of hydrostatic stress for D-input. (c) Distribution of effective plastic strain ϵ_{p} for A-input. (d) Distribution of effective plastic strain ϵ_{p} for D-input.

indentation response, the loading part of the raw output results from the code are smoothed by plotting the midpoint of the steps of the indentation force F versus indentation depth h relation.

Convergence was investigated using a fine, mildly graduated 320×100 quadrilateral element

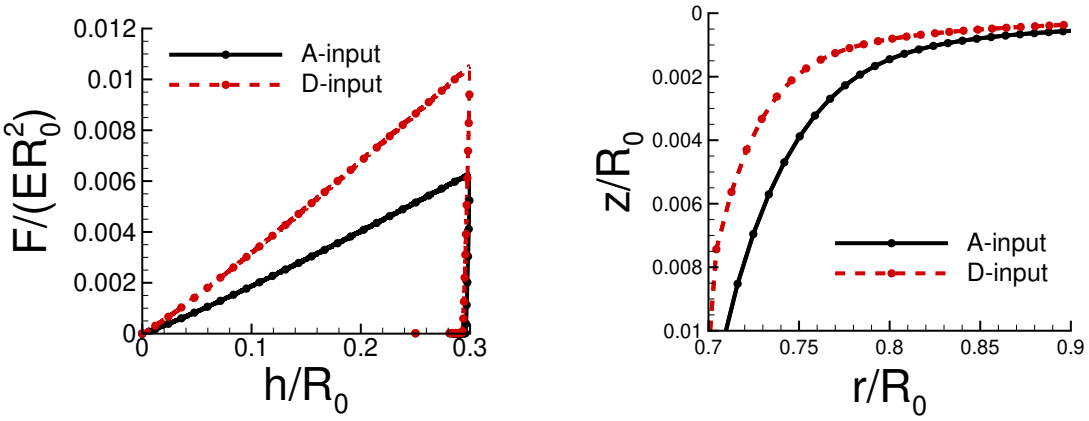

(a) (b)

Figure 4.3: Indentation responses for the A-input and D-input materials. The material parameter values are given in Table 4.1. (a) Normalized indentation force magnitude $F/(ER_0^2)$ versus normalized indentation depth h/R_0. (b) Normalized surface profiles near the indenter after unloading. The symbols denote the data points used in the Bayesian inference.

mesh in a $R_0 \times 0.75R_0$ region under the indenter. Outside the fine mesh region, where the gradient of the deformation field is small, a much coarser quadrilateral element mesh was used, giving a total of 380×180 quadrilateral elements. For both the A-input material and the D-input material, the indentation force versus indentation depth responses and residual surface profiles essentially coincided with the peak values of the normalized indentation force differing by less than 0.2% at the same value of indentation depth. The values of indentation depth at zero force for both materials also agreed to three significant figures. The normalized residual surface profiles obtained using the two meshes closely coincided, with the difference in values of z/R_0 generally being within 1.6% for $0.7 < r/R_0 < 0.9$. All results to be presented subsequently were obtained using the reference finite element mesh.

4.4.2 Construction of the databases

The focus here is on identifying the three plastic parameters, $\bar{\tau}_0/E, N$ and α, that characterize the plastic response of a material described by a [138] type constitutive relation.

The "experimentally" measured indentation response is presumed to consist of the indentation force versus indentation depth response $\boldsymbol{f}^{\mathrm{m}}$ and the residual surface profile $\boldsymbol{s}^{\mathrm{m}}$. In order to apply the Bayesian-type statistical approach described in Section 5.3, two databases are constructed, denoted by D^0_{A} for the material A-input, and D^0_{D} for the material D-input. The databases only differ in the values of Young's modulus E and elastic Poisson's ratio ν_{e}. In the database D^0_{A}, $E_{\mathrm{A}} = 1.000GPa$ and $\nu_{\mathrm{eA}} = 0.37$; In the database D^0_{D}, $E_{\mathrm{D}} = 0.634GPa$ and $\nu_{\mathrm{eD}} = 0.25$.

There are K^0_{total} combinations of indentation responses $\boldsymbol{s}^i$ and $\boldsymbol{f}^i$ corresponding to the parameter combinations $(\bar{\tau}_0/E)^i, N^i$ and α^i, with i ranging from 1 to K^0_{total}. Each vector, $\boldsymbol{s}^i$ and $\boldsymbol{f}^i$ consists of a set of discrete points. The number of points in each surface profile vector, $\boldsymbol{s}^i$, is $K_{\mathrm{s}} = 74$, distributed non-uniformly with an increased density of points near the indenter where sink-in or pile-up occurs. Each indentation force versus indentation depth vector, $\boldsymbol{f}^i$, consists of $K_{\mathrm{f}} = 55$ data points (25 for loading and 30 for unloading data) also distributed non-uniformly.

In both databases, $\bar{\tau}_0/E \in [0.001, 0.005]$ with step size 0.001 (5 points); $N \in [0.00, 0.15]$ with step size 0.05 (4 points); and $\alpha \in [0.00, 0.30]$ with step size 0.05 (7 points). Thus there are $K^0_{\text{total}} = 140$ combinations of parameters in each of these databases, which will be referred to as the coarse databases. For each of these 140 combinations of parameters, a finite element indentation calculation is carried out.

A disadvantage of a Bayesian approach is the computational effort needed to construct the required database of potential responses. Once the initial database is constructed, the computations for the Bayesian statistical analysis can be quickly carried out on a personal computer. In order to limit the number of needed computations, a more refined database is constructed for each input material by linear interpolation of the corresponding vectors of nearby points in the coarse databases with no additional finite element calculations being carried out. The interpolated database has step size 0.0002 in $\bar{\tau}_0/E$, 0.01 in N and 0.01 in α giving $K_{\text{total}} = 10416$. These databases for the A-input and D-input materials are denoted by D_{A} and D_{D}, respectively, and are referred to as interpolated databases. The predictions of material parameters are obtained using the interpolated databases. The accuracy of the predictions depends on the ability of the interpolated indentation responses

to represent the responses that would have been obtained using those constitutive parameters in a finite element calculation.

4.4.3 Material parameters representative of Alporas® and Duocel®

Considerable variation exists in the stress-strain response of metallic foams with the response being sensitive to the relative density of the foam, the density of the foam divided by the density of cell wall, [142, 138]. The mechanical properties selected for the A-input and D-input materials in Table 4.1 are taken to represent the uniaxial stress-strain response up to strains of ≈ 0.7, the high hardening that such foams can exhibit at larger strains is not represented, [142, 138]. We note that with a maximum indentation depth $h = 0.3R_0$, the maximum plastic strain is less than 0.7 as seen in Figs. 4.2 (c) and (d). The values of Young's modulus E and reference strength $\bar{\sigma}_0$ are taken from Table 4 of [142] (ERG was used to denote the foam with trade name Duocel®) and the elastic Poisson's ratio $\nu_{\rm e}$ is taken as the mean measured values under compression given by [142]. The reference strength values are taken to be the same in tension and compression as suggested by [143]. In addition to the values given in Table 4.1, for both materials the reference strain rate is taken to be $\dot{\epsilon}_0 = 0.01s^{-1}$ and the strain rate sensitivity exponent is set to $m = 0.005$ to approximate rate independent plastic deformations. The value of the strain hardening exponent N is chosen to qualitatively represent the observed hardening behavior under uniaxial compression.

The values taken for $\alpha_{\rm DF}$ are the values given by [138] based on a simplified version of the self-similar model and α is calculated from Eq. (4.16). The value of the plastic Poisson's ratio $\nu_{\rm p}$ is calculated from Eq. (4.10), so that $\nu_{\rm p} = 0.013$ for the A-input material and $\nu_{\rm p} = 0.174$ for the D-input material. The reference strength $\bar{\tau}_0$ in Eq. (4.7) is calculated from Eq. (4.21) with $J_0 \approx 1$ and $\sqrt{(1 + (1 - 3\alpha)/2)}$=1.2168 and 1.1302 for A-input and D-input, respectively. The reference strain, ϵ_0, is taken as $\bar{\tau}_0/E$.

Fig. 4.4 shows uniaxial responses for materials A-input and D-input calculated using the specified material parameters in a one quadrilateral element finite element calculation so the stress and deformation distributions are homogeneous. In Figs. 4.4 (a) and (b) the stress, σ, is the uniaxial force divided by the current cross-sectional area, and the strain, ϵ, is $\ln(\ell/\ell_{\rm ref})$, where $\ell_{\rm ref}$ is the

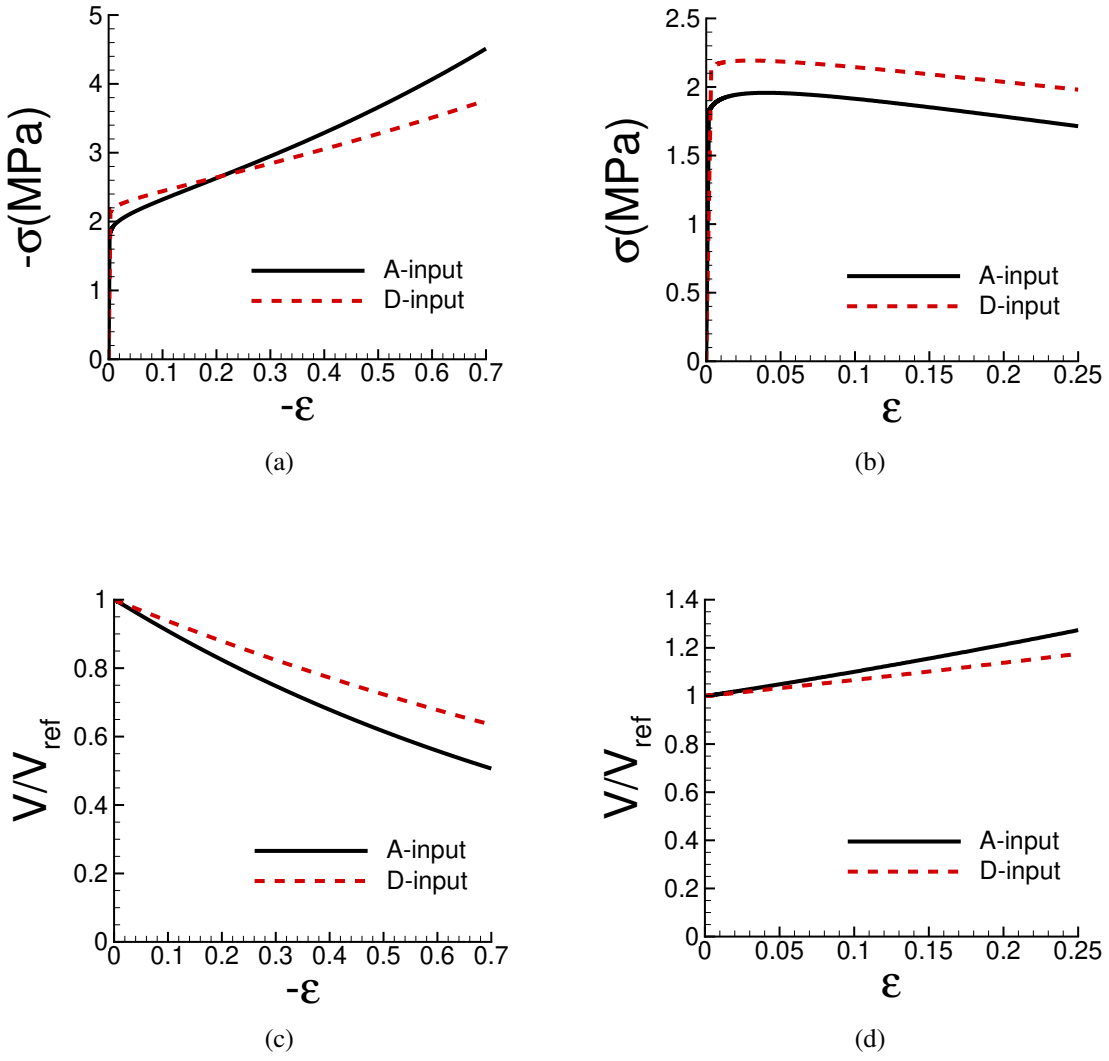

Figure 4.4: Uniaxial responses for the A-input and D-input materials. (a) Cauchy stress, σ, versus logarithmic strain ϵ in uniaxial compression. (b) Cauchy stress, σ, versus logarithmic strain ϵ in uniaxial tension. (c) Relative volume change, V/V_{ref}, versus ϵ in uniaxial compression. (d) Relative volume change, V/V_{ref}, versus ϵ in uniaxial tension.

Table 4.1: Constitutive parameters for the A-input and D-input materials.

	E(GPa)	ν_{e}	α	α_{DF}	N	$\bar{\tau}_0$(MPa)	$\bar{\tau}_0/E$	$\bar{\sigma}_0$(MPa)	$\bar{\sigma}_0/E$
A-input	1.000	0.37	0.0129	2.08	0.04	2.24	0.00224	1.84	0.00184
D-input	0.634	0.25	0.1484	1.58	0.02	2.45	0.00386	2.17	0.00342

length in the reference configuration and ℓ is its current value. The plastic flow potential is expressed in terms of Kirchhoff stress, $\boldsymbol{\tau} = J\boldsymbol{\sigma}$, so that the difference between using the Kirchhoff and Cauchy stress measures is greatest for small values of α, as for the A-input and D-input materials considered, and vanishes as $\alpha \to 1/3$. As a consequence of basing the flow potential on $\boldsymbol{\tau}$, the true stress versus logarithmic strain responses show hardening in compression, Fig. 4.4(a), and softening in tension, Fig. 4.4(b). Figs. 4.4 (c) and (d) show the ratio of current volume V to reference volume V_{ref} computed as

$$\frac{V}{V_{\text{ref}}} = \frac{\ell a^2}{\ell_{\text{ref}} a_{\text{ref}}^2} \tag{4.28}$$

where a and a_{ref} are the element radii in the current and reference configurations, respectively.

4.4.4 Identification of plastic properties for the A-input and D-input materials

The values of Young's modulus, E, and the elastic Poisson's ratio, ν_{e} are assumed known and the aim is to identify the values of $\bar{\tau}_0/E$, N and α from the indentation response.

4.4.4.1 Noise-free data

The "experimental" data consists of the vectors $\boldsymbol{s}^{\text{m}}$ and $\boldsymbol{f}^{\text{m}}$. Each entry in the databases, D_A and D_D, consists of vectors $\boldsymbol{s}^{\text{i}}$ and $\boldsymbol{f}^{\text{i}}$, where $i = 1, ..., K_{\text{total}}$ with $K_{\text{total}} = 10416$. The posterior probabilities are calculated using Eqs. (5.8) to (5.11) for each database entry. The set of values of $\bar{\tau}_0/E$, N and α that have the largest posterior probability value is identified as the set characterizing the plastic response of the material under consideration. For each database entry, three posterior probability values are computed: (i) the posterior probability, $p(\boldsymbol{f}^i|\boldsymbol{f}^{\text{m}})$, using only indentation force versus indentation depth values (denoted by F); (ii) the posterior probability, $p(\boldsymbol{s}^i|\boldsymbol{s}^{\text{m}})$, using only residual surface profile data (denoted by S); and (iii) the posterior probability, $p(\boldsymbol{s}^i, \boldsymbol{f}^i|\boldsymbol{s}^{\text{m}}, \boldsymbol{f}^{\text{m}})$, using both indentation force versus indentation depth values and residual surface profile data (denoted by FS).

The predicted parameters and the associated posterior probability values for the A-input material are given in Table 4.2. The predicted parameters using only residual surface profile (S) are rather close to the input values in Table 4.1, while the predicted values using only indentation force

versus indentation depth data (F) and the one using both indentation force versus indentation depth and residual surface profile (FS) are noticeably different from the input values. In particular, the value $\alpha = 0.13$ in Table 4.2, is much larger than the value for the A-input material in Table 4.1.

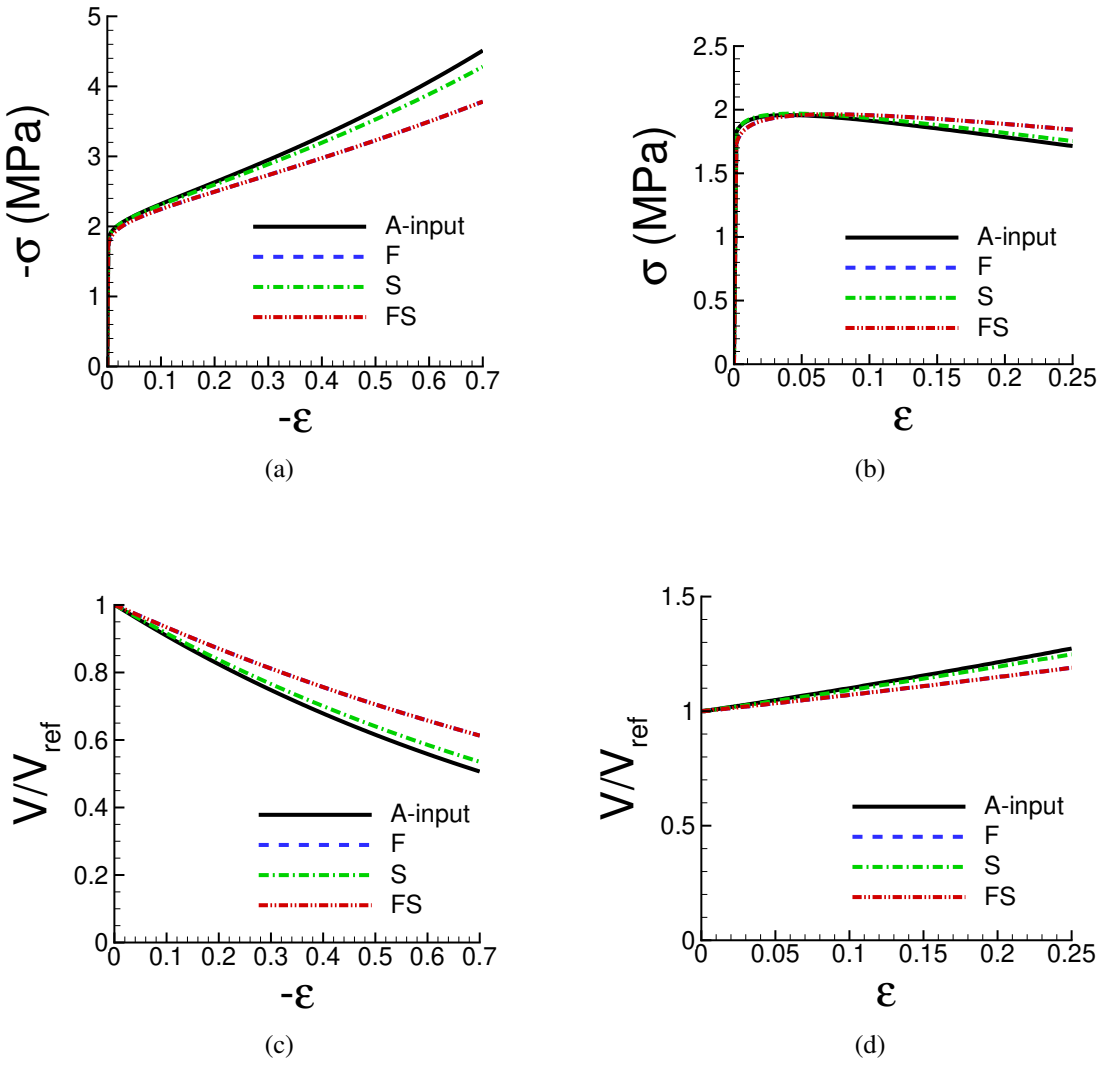

Figure 4.5: Uniaxial responses obtained from noise-free indentation data for the A-input material using the predicted plastic properties in Table 4.2. (a) σ versus ϵ in compression; (b) σ versus ϵ in tension; (c) V/V_{ref} versus ϵ in compression; (d) V/V_{ref} versus ϵ in tension. F: using only indentation force versus indentation depth data (dashed lines); S: using only residual surface profile data (dash dot lines); FS: using both indentation force versus indentation depth and residual surface profile data (dash dot dot lines). The solid lines show the responses for the A-input material values in Table 4.1. The dashed lines (F) coincide with the dash dot dot lines (FS).

Nevertheless, all the probability values in Table 4.2 are very close to 1. It is important to note that these probability values relate to the probability of representing the indentation response not the uniaxial stress-strain response.

Fig. 4.5 shows a comparison between the uniaxial compression and tension response obtained using the parameter values in Table 4.2 with the corresponding "experimental" responses for the A-input material. In Figs. 4.5(a) and (b), the prediction using only the residual surface profile data (S) gives the best representation of the uniaxial stress-strain behavior of the A-input material. The uniaxial responses predicted using only indentation force versus indentation depth data (F) and using both the indentation force versus indentation depth data and residual surface profile data (FS) show a significant difference from those of the A-input material in Figs. 4.5(a) and (b).

The evolution of the volume ratio, V/V_{ref}, versus axial strain, ϵ, both in uniaxial compression, Fig. 4.5(c), and in uniaxial tension, Fig. 4.5(d), also shows that the (S) prediction gives a much

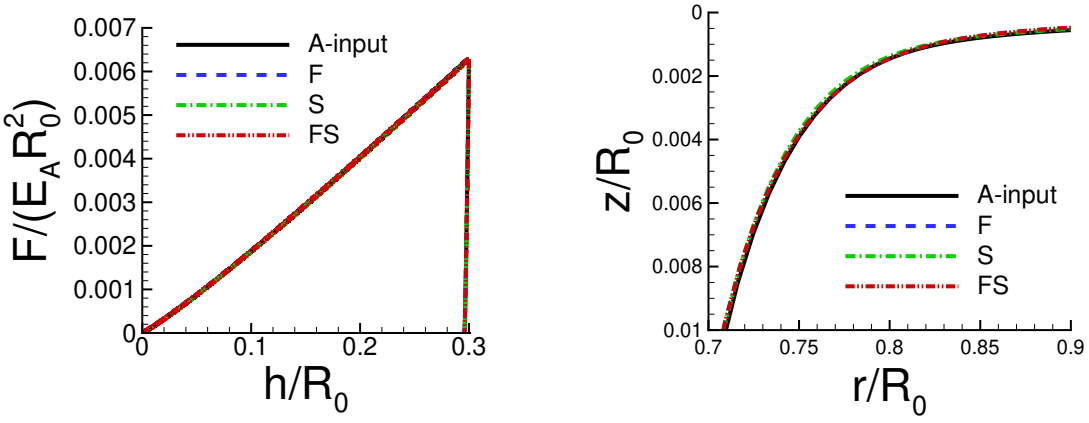

Figure 4.6: The indentation responses calculated using the predicted values of $\bar{\tau}_0/E_{\mathrm{A}}$, N and α for the A-input material in Table 4.2 based on noise-free data compared with the indentation responses obtained using the input values of A-input in Table 4.1 (solid lines). (a) Normalized indentation force magnitude $F/(E_{\mathrm{A}}R_0^2)$ versus normalized indentation depth h/R_0. (b) Normalized surface profiles near the indenter after unloading. The dashed lines (F) coincide with the dash dot dot lines (FS).

better fit to the "experimental" responses than the predictions using (F) data and (FS) data.

Fig. 4.6 shows a comparison between the normalized indentation force, $F/(E_A R_0^2)$, versus normalized indentation depth, h/R_0, and the near indenter residual surface profiles, the values of

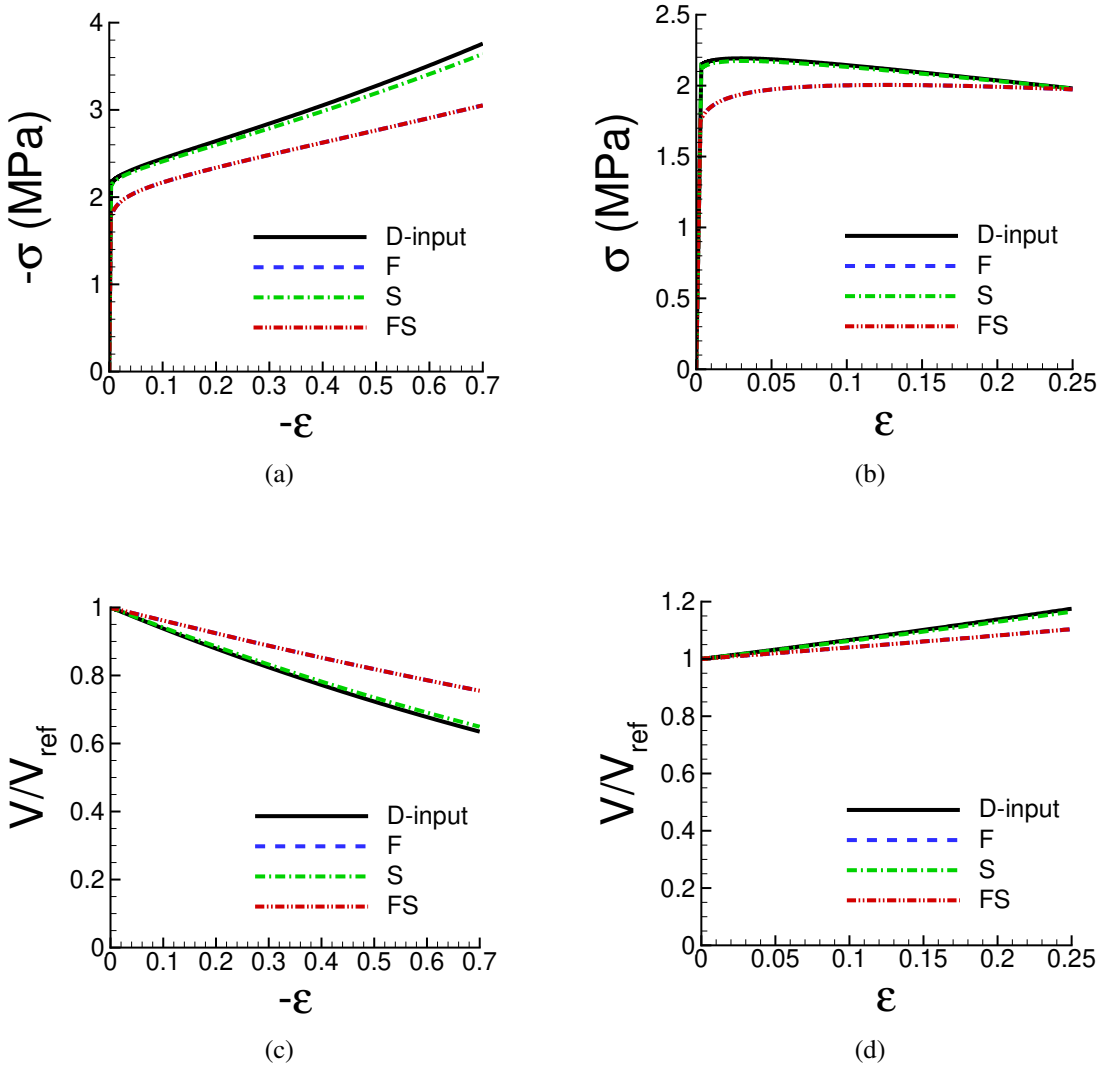

Figure 4.7: Uniaxial responses obtained from noise-free indentation data for the D-input material using the predicted plastic properties in Table 4.3. (a) σ versus ϵ in compression; (b) σ versus ϵ in tension; (c) V/V_{ref} versus ϵ in compression; (d) V/V_{ref} versus ϵ in tension. The solid lines show the uniaxial responses for the input values of D-input in Table 4.1. See the caption of Fig. 4.5 for the meanings of the notations F, S, and FS. The dashed lines (F) coincide with the dash dot dot lines (FS).

Table 4.2: Predicted values of $\bar{\tau}_0/E_{\rm A}$, N, α and the value of the associated largest posterior probability p_1 for the A-input material based on noise-free data. The notations F, S, and FS are defined in the text and in the caption of Fig. 4.5.

	α	N	$\bar{\tau}_0(GPa)$	$\bar{\tau}_0/E_{\rm A}$	p_1
F	0.13	0.05	0.002000	0.0020	1.00
S	0.05	0.04	0.002200	0.0022	0.99
FS	0.13	0.05	0.002000	0.0020	1.00

z/R_0, in the vicinity of the indenter obtained for the "experimental" material A-input with those based on the parameter values in Table 4.2. All the sets of parameter values in Table 4.2 give a very good representation of the indentation responses, although it is only the set of plastic material parameters based on the residual surface profile data (S) that gives a good representation of the uniaxial response of the A-input material, Fig. 4.5. These results illustrate that plastic material parameters that give essentially indistinguishable indentation responses (at least to $h/R_0 = 0.3$) can have different uniaxial responses.

It is worth noting that the likelihood function used in the Bayesian-type statistical calculations, Eq. (5.11), is a normal distribution with a very sharp peak at the center, which tends to give large posterior probability value for the best fit. Generally, when both indentation force versus indentation depth data and residual surface profile data (FS) are included, there are more parameter combinations that can approximate the "experimental" indentation response than the number of parameter combinations when only (F) or only (S) data is used. This can give a better fit to the indentation data but does not necessarily improve the representation of the uniaxial stress-strain response of the "experimental" material.

Table 4.3 shows the predicted parameters and associated posterior probability values for the D-input material based on noise-free data using database $D_{\rm D}$. For the D-input material, similarly, the predicted parameter values based on only the residual surface profile (S) are very close to the input values of D-input than the predicted parameter values using only the indentation force versus indentation depth data (F), and using both the indentation force versus indentation depth data and the residual surface profile data (FS). As for the A-input material, the prediction based

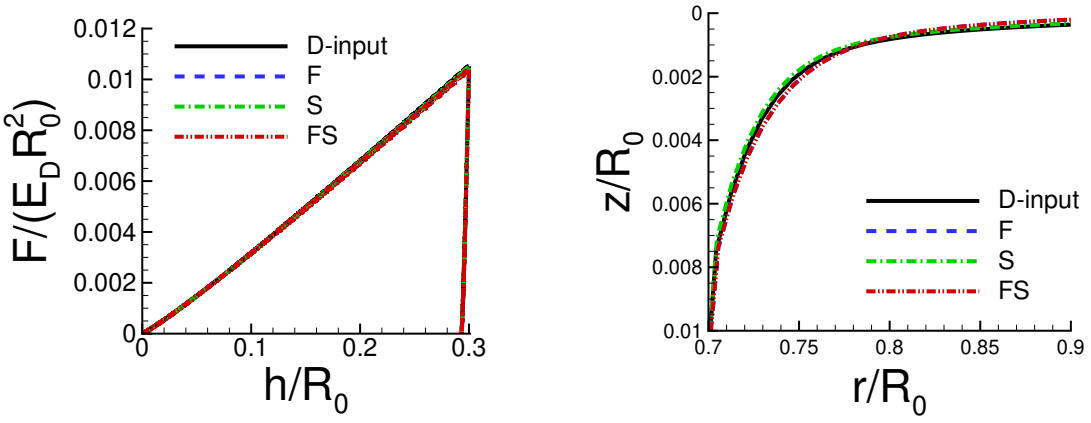

(a) (b)

Figure 4.8: The indentation responses calculated using the predicted values of $\bar{\tau}_0/E_{\rm D}$, N and α for the D-input material in Table 4.3 based on noise-free data compared with the indentation responses obtained using the input values of D-input in Table 4.1 (solid lines). (a) Normalized indentation force magnitude $F/(E_{\rm D}R_0^2)$ versus normalized indentation depth h/R_0. (b) Normalized surface profiles near the indenter after unloading. See the caption of Fig. 4.5 for the meanings of the notations F, S, and FS. The dashed lines (F) coincide with the dash dot dot lines (FS).

on the residual surface profile (S) provides a better representation of the uniaxial responses of the "experimental" D-input material in Fig. 4.7 than both the (F) and the (FS) based predictions.

Fig. 4.8 shows that the indentation responses of the "experimental" material D-input and the indentation responses for all three sets of predicted plastic material parameters in Table 4.3 give indistinguishable indentation responses. The plastic parameter values for the prediction based on the residual surface profile data (S) in Table 4.3 are very close to the values of the "experimental"

Table 4.3: Predicted values of $\bar{\tau}_0/E_{\rm D}$, N, α and the value of the associated largest posterior probability p_1 for the D-input material based on noise-free data. See the caption of Fig. 4.5 for the meanings of the notations F, S, and FS.

	α	N	$\bar{\tau}_0(GPa)$	$\bar{\tau}_0/E_{\rm D}$	p_1
F	0.23	0.05	0.001902	0.0030	1.00
S	0.16	0.02	0.002409	0.0038	1.00
FS	0.23	0.05	0.001902	0.0030	1.00

D-input material in Table 4.1. However, the values of $\bar{\tau}_0/E_D$, N and α for the (F) and the (FS) predictions in Table 4.3 differ significantly from the values for the D-input material in Table 4.1. Hence, also here, there are plastically compressible materials that have different plastic properties but have indistinguishable spherical indentation responses (at least to $h/R_0 = 0.3$).

For both the A-input material and the D-input material, the uniaxial responses predicted based on the residual surface profile data (S) provide a better representation of those of the "experimental" material than do those including indentation force versus indentation depth data, (F) and (FS). Indeed, [95] have shown the advantages of using the residual surface profile for extracting plastic material properties of plastically incompressible materials from spherical indentation tests.

4.4.4.2 Noise-contaminated data

The consideration of noise-contaminated data in material property identification from indentation responses was pioneered by [144]. Here, we use the approach of [2] to extract plastic material parameters from noisy indentation data. Fig. 4.9 shows realizations of noise-contaminated indentation force versus indentation depth data and residual surface profile data. Fig. 4.9(a) shows a realization of indentation force versus indentation depth data with a noise amplitude $\eta_{\mathrm{f}} = 0.01$ and Fig. 4.9(b) shows a realization of a residual surface profile with $\eta_{\mathrm{s}} = 0.01$, where the noise amplitudes η_{f} and η_{s} are defined in Eq. (A-30). The values of the noise amplitudes $\eta_{\mathrm{f}} = 0.01$ and $\eta_{\mathrm{s}} = 0.01$ are of the order that could occur in indentation measurements and are referred to as a low noise level. In order to explore the effect of a very large noise level, Figs. 4.9(c) and (d) show data with $\eta_{\mathrm{f}} = 0.10$ and $\eta_{\mathrm{s}} = 0.10$, respectively.

For a particular realization with noise amplitudes η_{f} and η_{s}, the "experimental" data consists of the noise-free response plus the superposed noise as shown in Fig. 4.9. This noisy "experimental" data is used in Eqs. (5.8) to (5.11) and the values of the plastic material properties, $\bar{\tau}_0/E$, N and α, with the largest posterior probability using both indentation force versus indentation depth data and residual surface profile data (FS) are identified. As found by [2], plastic parameter values obtained from single realization of noise with a specified amplitude can give rise to a predicted uniaxial stress-strain response that differs significantly from that of the input material. However,

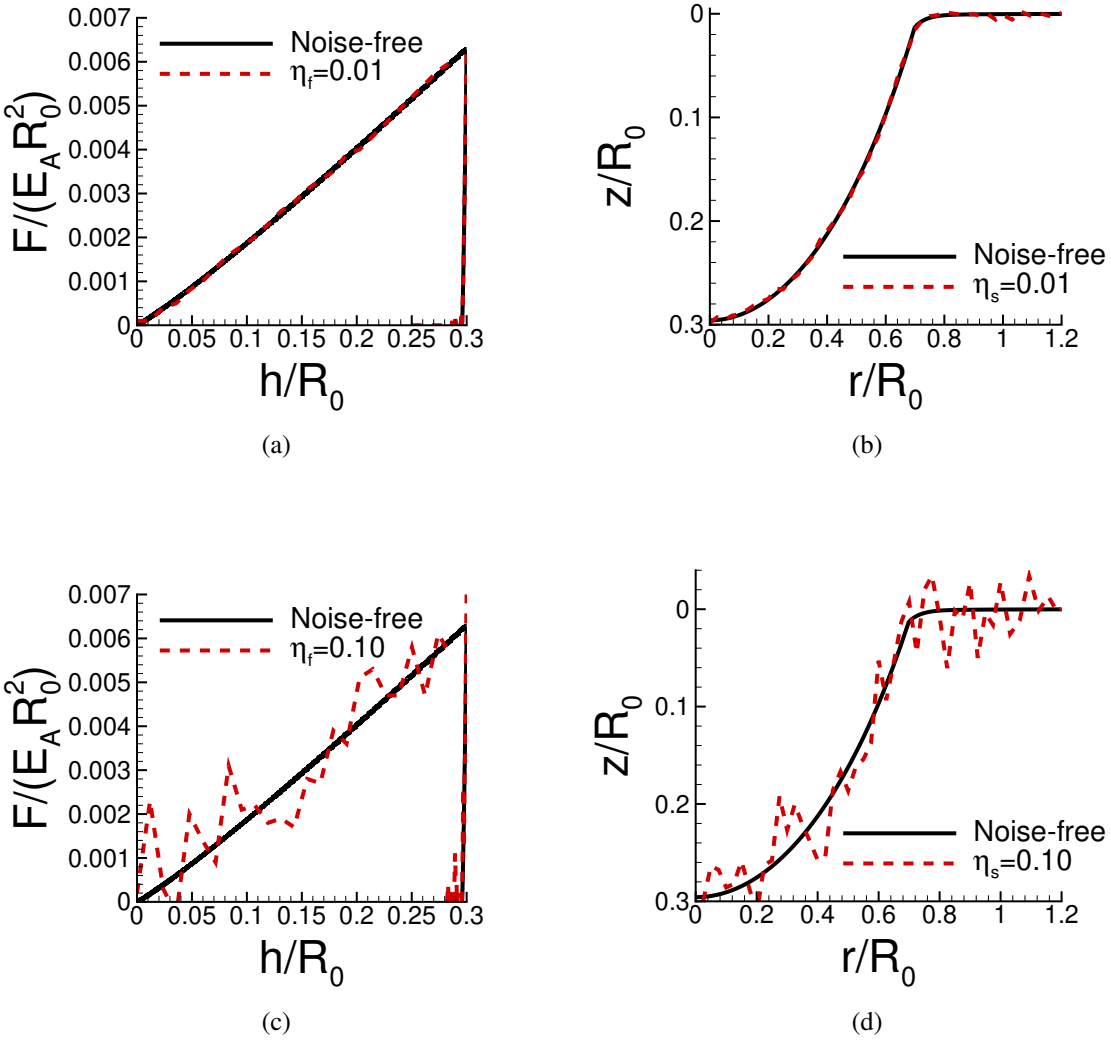

Figure 4.9: Illustration of noise-contaminated data for one realization of noisy data with a specified noise amplitude for the A-input material indentation response. (a) $F/(E_{\rm A}R_0^2)$ versus h/R_0 with $\eta_{\rm f} = 0.01$. (b) z/R_0 versus r/R_0 near the indenter with $\eta_{\rm s} = 0.01$. (c) $F/(E_{\rm A}R_0^2)$ versus h/R_0 with $\eta_{\rm f} = 0.10$. (d) z/R_0 versus r/R_0 near the indenter with $\eta_{\rm s} = 0.10$.

averaging over a sufficiently large number of realizations does give a good representation. Here, as in [2], calculations of the posterior probability distribution are carried out for 100 realizations with the same noise amplitude values. The arithmetic average of the 100 predicted plastic material property values having the largest posterior probability value for each realization is identified as the predicted material parameter values associated with the noise amplitudes $\eta_{\rm f}$ and $\eta_{\rm s}$. We emphasize

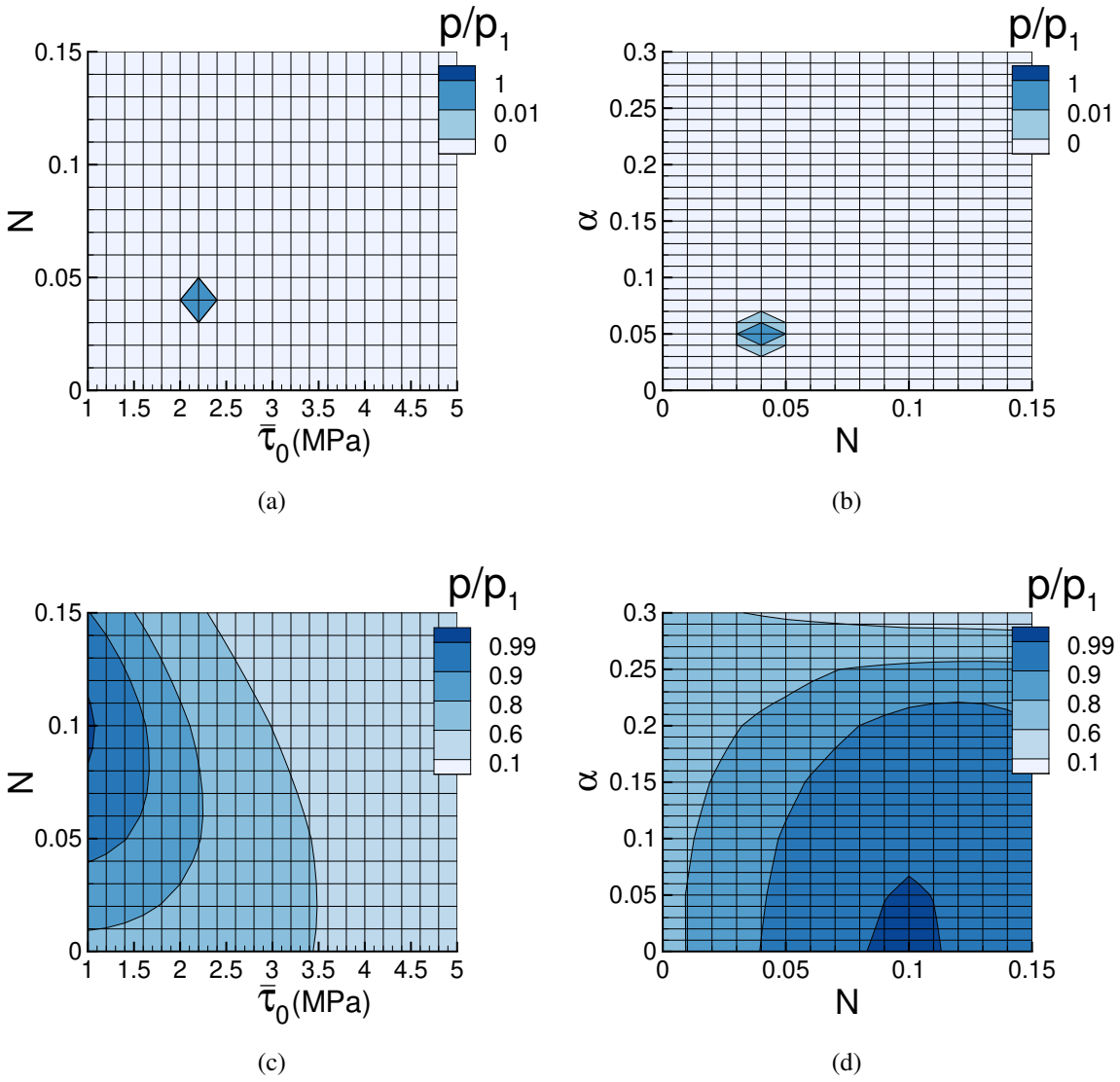

Figure 4.10: Normalized posterior probability distributions p/p_1 for the A-input material using only surface profile data of two plastic parameters when the third plastic parameter is fixed at the value corresponding to the largest posterior probability p_1. (a) N versus $\bar{\tau}_0$ at $\alpha = 0.05$ for noise-free surface. (b) α versus N at $\bar{\tau}_0 = 2.2$MPa for noise-free surface. (c) N versus $\bar{\tau}_0$ at $\alpha = 0.00$ for one realization with $\eta_s = 0.10$. (d) α versus N at $\bar{\tau}_0 = 1.0$MPa for one realization with $\eta_s = 0.10$.

that no additional finite element indentation calculations are carried out.

The predicted values, averaged over 100 realizations, of $\bar{\tau}_0/E_A$, N and α for the A-input material are shown in Table 4.4. Also, shown is the largest value of posterior probability, p_1, averaged over the 100 realizations. With $\eta_s = \eta_f = 0.01$, the predicted values are close to those of the

Table 4.4: Predicted values of $\bar{\tau}_0/E_{\rm A}$, N and α for the A-input material obtained from averaging the predicted values over 100 realizations with $\eta_{\rm s} = \eta_{\rm f} = 0.01$ and with $\eta_{\rm s} = \eta_{\rm f} = 0.10$ using both indentation force versus indentation depth data and residual surface profile data, and with $\eta_{\rm s} = 0.10$ using only surface profile data. Also, shown is the value of corresponding averaged largest posterior probability p_1.

	α	N	$\bar{\tau}_0(GPa)$	$\bar{\tau}_0/E_{\rm A}$	p_1
$\eta_{\rm s} = \eta_{\rm f} = 0.01$	0.11	0.05	0.0020	0.0020	0.57
$\eta_{\rm s} = \eta_{\rm f} = 0.10$	0.21	0.07	0.0016	0.0016	0.01
$\eta_{\rm s} = 0.10$	0.15	0.07	0.0020	0.0020	0.23×10^{-3}

noise-free FS data in Table 4.2. With the larger noise amplitudes $\eta_{\rm s} = \eta_{\rm f} = 0.10$, the plastic material property values differ significantly from those of the corresponding noise-free data. The average values of the posterior probability are $p_1 = 0.01$ with $\eta_{\rm s} = \eta_{\rm f} = 0.10$ and $p_1 = 0.57$ with $\eta_{\rm s} = \eta_{\rm f} = 0.01$. For comparison, $p_1 = 1.00$ with noise-free data. The value $p_1 = 0.23 \times 10^{-3}$ with only surface profile data and $\eta_{\rm s} = 0.10$ indicates that even with averaging over 100 realizations the posterior probability maximum is very shallow and spread out for this case.

Fig. 4.10 shows cross sections of distributions of normalized posterior probability, p/p_1, for the A-input material using only surface profile data. The cross sections are for two of the three plastic parameters, $\bar{\tau}_0, N, \alpha$ with the third parameter fixed at the value corresponding to the largest posterior probability value p_1 for the corresponding calculation. Figs. 4.10(a) and 4.10(b) are for noise-free data and show a sharply defined peak value with strong confidence. Figs. 4.10(c) and 4.10(d) are for one realization of noisy surface profile data with $\eta_{\rm s} = 0.10$. With $\eta_{\rm s} = 0.10$, distributions of p/p_1 are more spread out with similar values of p_1 for a range of parameter values. An increasingly spread out distribution of p/p_1 together with a shallow peak with increasing noise is typical of the cases considered although details of the distribution vary as can be seen by comparing Figs. 4.10(c) and 4.10(d) here with Fig. 10 of [2]. In some cases with large noise amplitudes, multiple local minima are found and the Bayesian statistical procedure can give parameter values associated with a local minimum rather than the global minimum.

Fig. 4.11 shows the uniaxial responses using the parameter values in Table 4.4. Here, and subsequently, only the compressive responses are shown. For the lower noise level, $\eta_{\rm s} = \eta_{\rm f} =$

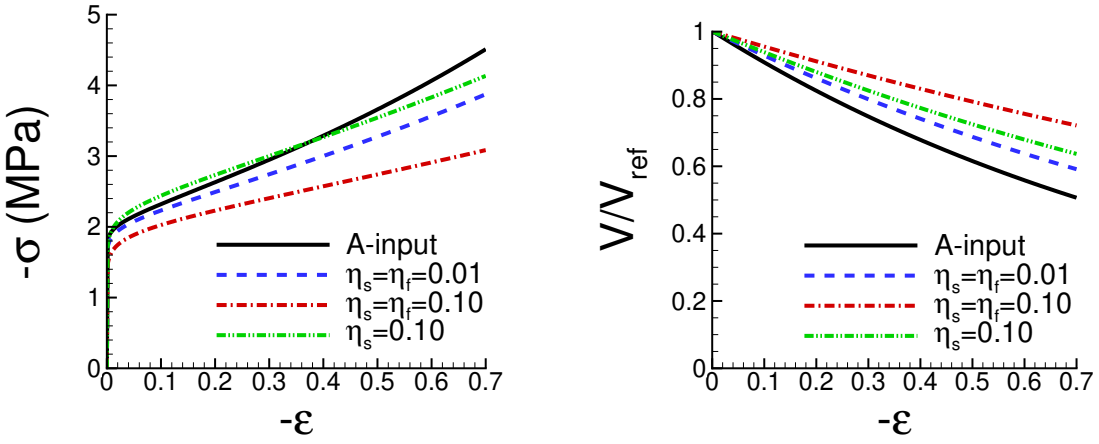

(a) (b)

Figure 4.11: Uniaxial responses in compression using the averaged predicted values of $\bar{\tau}_0/E_{\rm A}$, N and α for A-input over 100 realizations given in Table 4.4. The solid lines show the responses for the property values of the A-input material in Table 4.1; the dashed lines show the responses based on data with the noise amplitudes $\eta_{\rm s} = \eta_{\rm f} = 0.01$; the dash dot lines show the responses based on data with $\eta_{\rm s} = \eta_{\rm f} = 0.10$; the dash dot dot lines show the responses based on surface data with $\eta_{\rm s} = 0.10$. (a) σ versus ϵ. (b) $V/V_{\rm ref}$ versus ϵ.

0.01, the fit to the "experimental" stress-strain response is similar to the one based on noise-free data in Fig. 4.5. With $\eta_{\rm s} = \eta_{\rm f} = 0.10$, the predicted magnitude of the compressive stress at $\epsilon = -0.7$ is about 70% of that for the A-input material. The prediction of the values $V/V_{\rm ref}$ with $\eta_{\rm s} = \eta_{\rm f} = 0.01$, are closer to those of the A-input material than those with $\eta_{\rm s} = \eta_{\rm f} = 0.10$. The predictions based solely on surface data denoted by $\eta_{\rm s} = 0.10$ (averaged over 100 realizations) are very close to those with $\eta_{\rm s} = \eta_{\rm f} = 0.01$ indicating that the indentation force versus indentation depth response based predictions are more sensitive to noise than the surface profile predictions. This also illustrates that averaging noisy data over a large number of realizations can enable a reasonably good approximation of the uniaxial response to be obtained, even from very noisy indentation data when surface profile data is included.

On the other hand, the predicted indentation responses in Fig. 4.12 for both sets of noise amplitude values, $\eta_{\rm s} = \eta_{\rm f} = 0.01$ and $\eta_{\rm s} = \eta_{\rm f} = 0.10$, are very close to those of the A-input material.

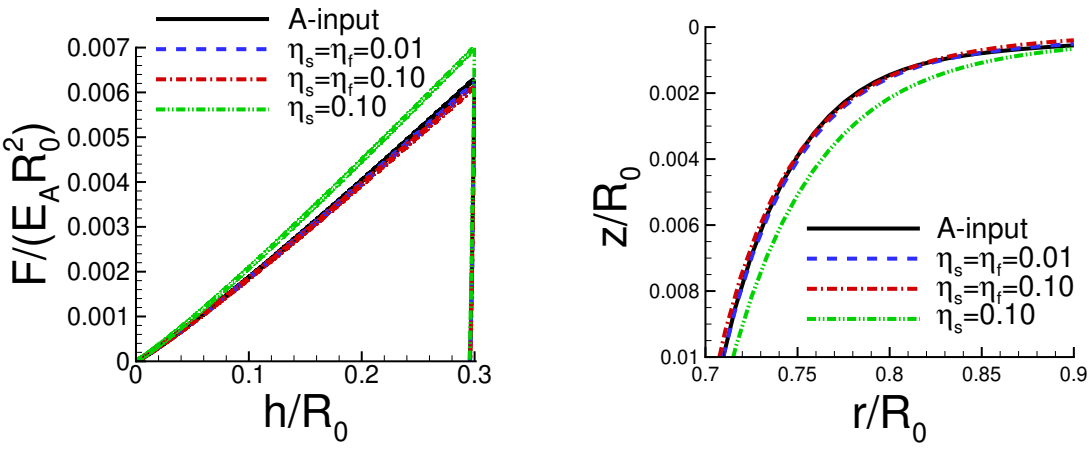

(a) (b)

Figure 4.12: Indentation responses calculated using the predicted values of $\bar{\tau}_0/E_{\rm A}$, N and α averaged over 100 realizations and given in Table 4.4 for the A-input material. The solid lines show the indentation responses computed using the input values for the A-input material in Table 4.1. (a) Normalized indentation force magnitude $F/(E_{\rm A}R_0^2)$ versus normalized indentation depth h/R_0 during loading and unloading. (b) Normalized surface profiles near the indenter after unloading. See the caption of Fig. 4.11 for the meanings of the notations $\eta_{\rm s}=\eta_{\rm f}=0.01$, $\eta_{\rm s}=\eta_{\rm f}=0.10$, and $\eta_{\rm s}=0.10$.

There is some dependence of the maximum indentation force on the noise amplitude in Fig. 4.12 (a), but the residual surface profiles predicted based on the two types of noise-contaminated data are indistinguishable from that of the A-input material, Fig. 4.12(b). Figs. 4.11 and 4.12 illustrate that a very good fit to the indentation response does not guarantee an equally good fit to the uniaxial response and that predictions based on only surface profile data are quite robust with respect to the noise level (when averaged over many realizations with a given amplitude).

Table 4.5 shows the predicted values of plastic material parameters $\bar{\tau}_0/E_{\rm D}$, N, α and the associated posterior probability averaged over 100 realizations for the D-input material with noise amplitudes $\eta_{\rm s}=\eta_{\rm f}=0.01$ and $\eta_{\rm s}=\eta_{\rm f}=0.10$. As for the A-input material, the values of plastic material parameters with $\eta_{\rm s}=\eta_{\rm f}=0.01$ are closer to those for noise-free data in Table 4.3 than are those with $\eta_{\rm s}=\eta_{\rm f}=0.10$. Also, the posterior probability with $\eta_{\rm s}=\eta_{\rm f}=0.10$ is 0.01.

The compressive stress-strain response in Fig. 4.13(a) for the predicted parameters in Table 4.5

Table 4.5: Predicted values of $\bar{\tau}_0/E_{\rm D}$, N and α for the D-input material obtained from averaging the predicted values over 100 realizations with $\eta_{\rm s} = \eta_{\rm f} = 0.01$ and with $\eta_{\rm s} = \eta_{\rm f} = 0.10$ using both indentation force versus indentation depth data and residual surface profile data, and with $\eta_{\rm s} = 0.10$ using only surface profile data. Also, shown is the value of corresponding averaged largest posterior probability p_1.

	α	N	$\bar{\tau}_0(GPa)$	$\bar{\tau}_0/E_{\rm D}$	p_1
$\eta_{\rm s} = \eta_{\rm f} = 0.01$	0.21	0.04	0.0021	0.0033	0.57
$\eta_{\rm s} = \eta_{\rm f} = 0.10$	0.19	0.07	0.0017	0.0027	0.01
$\eta_{\rm s} = 0.10$	0.18	0.08	0.0015	0.0024	0.23×10^{-3}

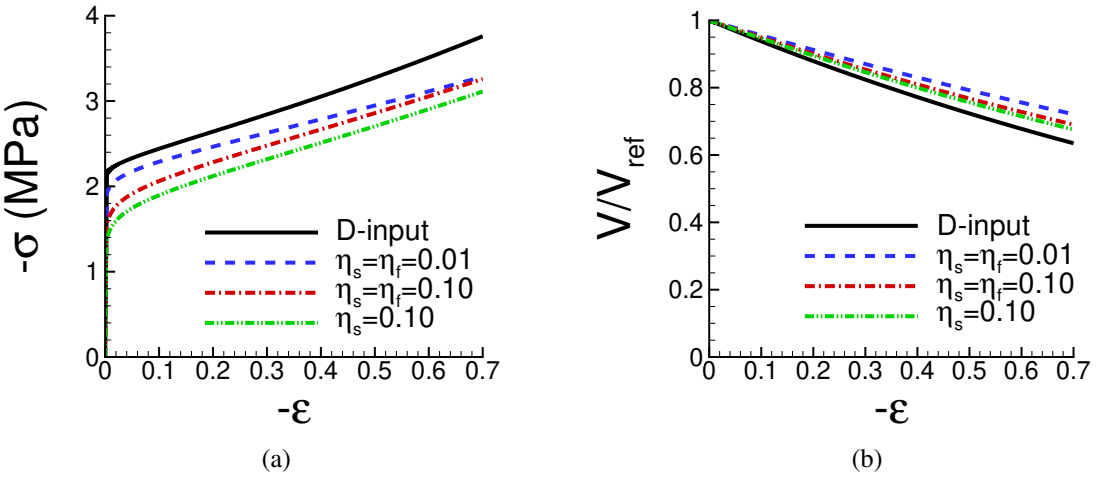

(a) (b)

Figure 4.13: Uniaxial responses in compression using the predicted values of $\bar{\tau}_0/E_{\rm D}$, N and α averaged over 100 realizations for the D-input material and given in Table 4.5. The solid lines show the responses for the property values of the D-input material in Table 4.1. (a) σ versus ϵ. (b) $V/V_{\rm ref}$ versus ϵ. See the caption of Fig. 4.11 for the meanings of the notations $\eta_{\rm s} = \eta_{\rm f} = 0.01$, $\eta_{\rm s} = \eta_{\rm f} = 0.10$, and $\eta_{\rm s} = 0.10$.

with a low noise level $\eta_{\rm s} = \eta_{\rm f} = 0.01$ is closer to that of the D-input material than the predicted response with a high noise level $\eta_{\rm s} = \eta_{\rm f} = 0.10$. The stress-strain curves with $\eta_{\rm s} = \eta_{\rm f} = 0.01$ and with $\eta_{\rm s} = \eta_{\rm f} = 0.10$ overlap at $\epsilon \approx -0.7$. As for the A-input material, with only surface profile data and $\eta_{\rm s} = 0.10$ the small value of the posterior probability maximum in Table 4.5 for the D-input material indicates a very shallow and spread out maximum. The evolution of $V/V_{\rm ref}$

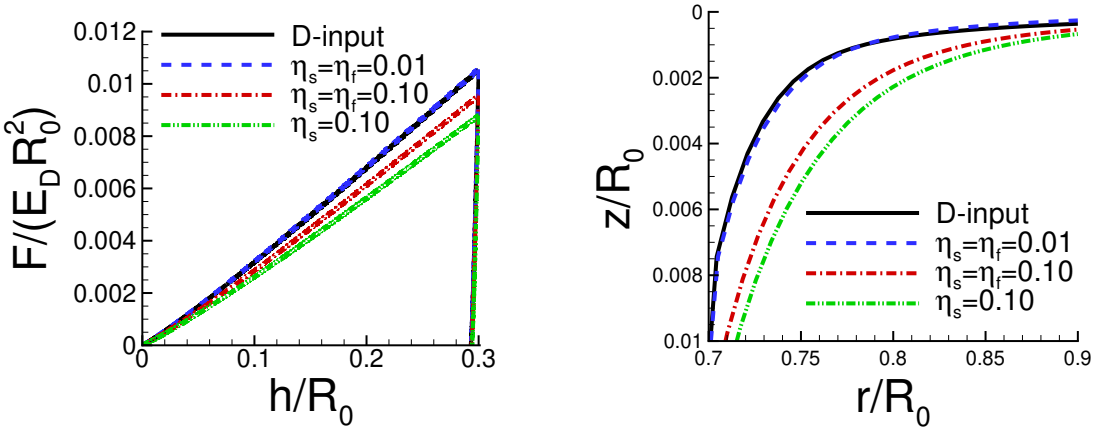

(a) (b)

Figure 4.14: Indentation responses calculated using the averaged predicted values of $\bar{\tau}_0/E_{\rm D}$, N and α over 100 realizations given in Table 4.5 for the D-input material. The solid lines show the indentation responses computed using the input values for the D-input material in Table 4.1. (a) Normalized indentation force magnitude $F/(E_{\rm D}R_0^2)$ versus normalized indentation depth h/R_0 during loading and unloading. (b) Normalized surface profiles near the indenter after unloading. See the caption of Fig. 4.11 for the meanings of the notations $\eta_{\rm s} = \eta_{\rm f} = 0.01$, $\eta_{\rm s} = \eta_{\rm f} = 0.10$, and $\eta_{\rm s} = 0.10$.

of the D-input material in Fig. 4.13(b) is reasonably well-predicted for all noise levels considered, and perhaps surprisingly the case with $\eta_{\rm s} = \eta_{\rm f} = 0.10$ provides a somewhat better fit than the response predicted with $\eta_{\rm s} = \eta_{\rm f} = 0.01$.

In Fig. 4.14(a), the normalized indentation force versus indentation depth responses show a clear dependence of the maximum indentation force on the noise amplitude. Both the normalized indentation force versus indentation depth responses and residual surface profiles of the average of predicted parameters using data with noise amplitudes $\eta_{\rm s} = \eta_{\rm f} = 0.01$ represent the D-input material indentation responses better than the ones with $\eta_{\rm s} = \eta_{\rm f} = 0.10$. Although the predicted indentation responses based solely on surface profile data with $\eta_{\rm s} = 0.10$ do not provide a good representation of the indentation responses in Fig. 4.14, a fairly good approximation of the uniaxial compression response is predicted in Fig. 4.13. However, the results do indicate that to obtain an accurate prediction of the uniaxial stress-strain response from noisy indentation data, the noise

level needs to be below a material dependent maximum noise amplitude.

4.4.4.3 Identification of the elastic stiffness via the Oliver-Pharr Method

In Sections 4.4.4.1 and 4.4.4.2, it was assumed that the elastic properties were known a priori. Here, we explore using the method of [74, 145, 81] to calculate the elastic stiffness from indentation measurements. Although mainly used for sharp indenters, the Oliver-Pharr relation has been used for spherical indentation, for example, [145, 146, 131, 132]. In particular, for the constitutive relation of [138], [131, 132] found that plasticity-related parameters do not affect the initial unloading slope and that the Young's modulus of metallic foams could be obtained from the spherical indentation unloading response. An effective modulus, E_{eff}, is calculated from the initial slope of the unloading indentation force versus indentation depth response, $S = dF/dh$ via

$$S = \beta \frac{2}{\sqrt{\pi}} E_{\text{eff}} \sqrt{A} \tag{4.29}$$

where A is the contact area and for a rigid indenter, the effective (or reduced) modulus E_{eff} is defined by

$$E_{\text{eff}} = \frac{E}{1 - \nu_{\text{e}}^2} \tag{4.30}$$

with β a dimensionless correction factor and ν_e the elastic Poisson's ratio, [81]. The value of β depends on the material properties and the indenter shape, [85, 147, 81], but with values typically around $\beta \approx 1.1$.

If the value of β and the elastic constants are known, Eq. (4.29), can be used to calculate the contact area. If the contact area is known, Eq. (4.29) can be used to determine E_{eff}. However, this does not provide a way to separately identify E and ν_{e}.

The values of S are calculated from the "experimental" unloading indentation force versus indentation depth response of the A-input and D-input materials. Two values of β were calculated. One based on the true contact area $A_{\text{true}} = \pi r_{\text{true}}^2$, where r_{true} is the maximum r value of points in contact with the indenter. The other is based on the nominal contact area, $A_{\text{nom}} = \pi r_{\text{nom}}^2$, where r_{nom} is what the contact radius would be if there were no pile-up or sink-in (see Fig. 5.1), and is

given by

$$r_{\rm nom} = \sqrt{h(2R_0 - h)} \tag{4.31}$$

For both the A-input and D-input materials, the values of $r_{\rm true}$ and $r_{\rm nom}$ differ little and the variation in β depending on this choice is within 1%.

A least squares fit to the first M data points, starting at the peak force is used, where M is chosen to be between 40 and 70. For the A-input material the fit value of β is $\beta = 1.08$ using $r_{\rm nom}$ and $\beta = 1.09$ using $r_{\rm true}$. The same value is obtained to three significant figures using either 40 points ($F/F_{\rm max} = 0.747$) or 70 points ($F/F_{\rm max} = 0.537$). The corresponding values of β for the D-input material are between 1.17 and 1.18 using either 40 points ($F/F_{\rm max} = 0.851$) or 70 ($F/F_{\rm max} = 0.725$) points, and using either $r_{\rm nom}$ or $r_{\rm true}$. Thus, the value of β varies somewhat with the elastic and plastic material properties. However, the range of values found here is similar to that found for plastically incompressible materials, [85, 147, 81].

4.5 Sensitivity to the constitutive characterization

4.5.1 Sensitivity to the value of the plastic compressibility parameter α

We consider the sensitivity of the identification of plastic material properties to the value of the plastic compressibility α. Fig. 4.15 shows the uniaxial compression stress-strain responses obtained using the D-input material properties and noise-free data with $\alpha = 0.20, 0.25, 0.28$ and 0.30. The values $\alpha = 0.20, 0.25, 0.30$ are values of α for which finite element calculations were carried out to populate the database. The indentation responses with $\alpha = 0.28$ are obtained by interpolation. For $\alpha = 0.25$ and 0.30, the Bayesian predictions essentially coincide with the D-input stress-strain response. For $\alpha = 0.20$, some deviation is seen, particularly for prediction based solely on the indentation force versus indentation depth data (F). The largest deviation between the D-input stress-strain response and the Bayesian based predictions occurs for $\alpha = 0.28$. This is most likely due to $\alpha = 0.28$ not being a value that is directly calculated but for which the Bayesian predictions are based on interpolation. Nevertheless, uniaxial compression stress-strain response based on surface profile data (S) and both indentation force versus indentation depth data and sur-

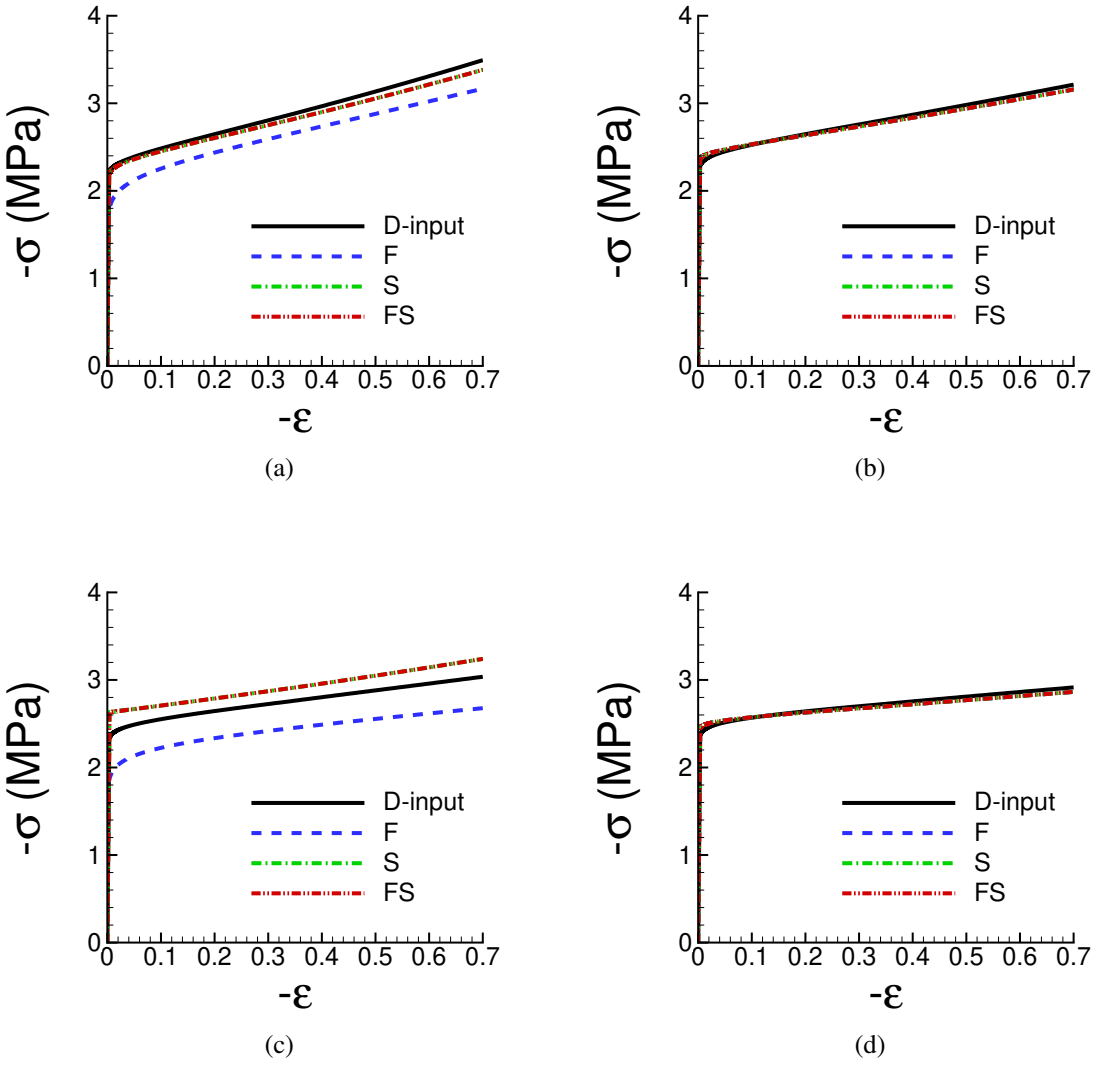

Figure 4.15: Uniaxial compression stress-strain responses of the predicted parameter values obtained using noise-free indentation data compared with the uniaxial compression stress-strain response of the D-input material when α is set to various values. (a) $\alpha = 0.20$; (b) $\alpha = 0.25$; (c) $\alpha = 0.28$; (d) $\alpha = 0.30$. See the caption of Fig. 4.5 for the meanings of the notations F, S, and FS. In (a) and (c), the S and FS lines coincide. In (b) and (d), the F, S and FS lines coincide.

face profile data (FS) well-approximate the D-input material response. The responses in Fig. 4.15 illustrate: (i) a deviation from the input material response with decreasing α particularly for predictions bases solely on indentation force versus indentation depth data; and (ii) a deviation from the input material response due to interpolation again particularly for predictions bases solely on

indentation force versus indentation depth data. Nevertheless, in all cases considered the uniaxial compression response is reasonably well-approximated, particularly if surface profile data is used.

4.5.2 Sensitivity to the characterization of plasticity

The identification of plastic material properties in Section 4.4 was made presuming that the mechanical behavior of the materials under consideration could be characterized appropriately by a Deshpande-Fleck constitutive relation. Of course, in a real indentation experiment, the appropriate constitutive framework is not known a priori. One possibility is to assume that the material response can be characterized as a plastically incompressible isotropic hardening Mises solid. This corresponds to $\alpha = 1/3$ giving $\nu_{\rm p} = 1/2$. However, our database is restricted to $\alpha \leq 0.30$ but the implications of adopting the assumption of an isotropic hardening Mises solid can be illustrated by confining the Bayesian fit to $\alpha = 0.30$ which corresponds to $\nu_{\rm p} = 0.429$. Attention is restricted to noise-free data.

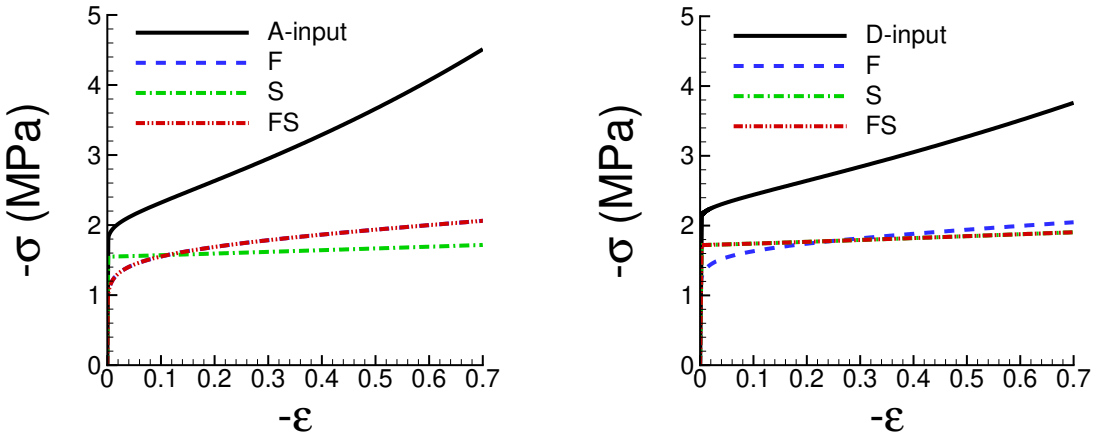

(a) (b)

Figure 4.16: Uniaxial compression stress-strain responses using the predicted values of $\bar{\tau}_0/E$, N obtained for $\alpha = 0.30$ compared with the uniaxial compression stress-strain response of the corresponding "experimental" material. (a) A-input material. (b) D-input material. See the caption of Fig. 4.5 for the meanings of the notations F, S, and FS. In (a), the F and FS lines coincide. In (b), the S and FS lines coincide.

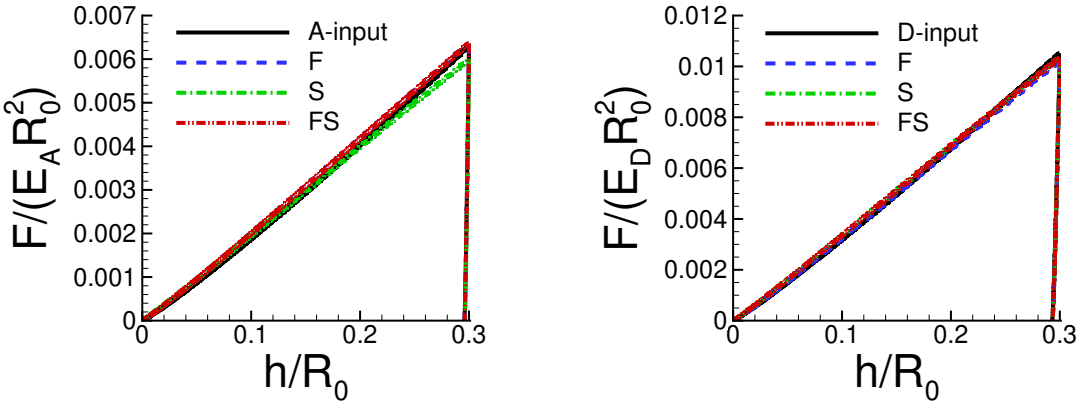

Figure 4.17: Normalized indentation force $F/(ER_0^2)$ versus normalized indentation depth h/R_0 responses using the predicted values of $\bar{\tau}_0/E$, N obtained for $\alpha = 0.30$ compared with the indentation responses of the corresponding "experimental" material. (a) A-input material. (b) D-input material. See the caption of Fig. 4.5 for the meanings of the notations F, S, and FS.

For the A-input material, the fit using only the indentation force versus indentation depth response (F) and the fit using both the indentation force versus indentation depth response and the residual surface profile data (FS) both give $N = 0.10$ and $\bar{\tau}_0/E_{\rm A} = 0.0010$ with a probability of one. For the D-input material, the fit (F) gives $N = 0.07$, $\bar{\tau}_0/E_{\rm D} = 0.0020$ with probability 0.97, while the fit (FS) gives $N = 0.00$, $\bar{\tau}_0/E_{\rm D} = 0.0028$ with probability $p = 0.86$.

Fig. 4.16 shows a comparison of the uniaxial compression response of the "experimental" input materials with the predicted uniaxial compression responses for the best fit values of N and $\bar{\tau}_0$ obtained with $\alpha = 0.30$. In Fig. 4.17(a) the indentation force versus indentation depth response using the values of $\bar{\tau}_0/E_{\rm A}$ and N obtained with $\alpha = 0.30$ is indistinguishable from that for the A-input material. Also for the D-input material the indentation force versus indentation depth responses computed with $\bar{\tau}_0/E_{\rm D}$ and N obtained with α restricted to 0.30 are indistinguishable for that of the corresponding "experimental" material, Fig. 4.17(b).

As seen in Fig. 4.17, a very good fit to the indentation force versus indentation depth response

can be obtained with an "inappropriate" constitutive description. This shows that obtaining a very good fit to an indentation force versus indentation depth response by whatever means, Bayesian statistics, machine learning, etc. does not necessarily mean that the associated constitutive description is an accurate representation of the material's mechanical response. Furthermore, including the representation of the surface profile does not resolve this issue. The constitutive framework must be broad enough to represent key features of the material's mechanical response. For the materials considered here, plastic compressibility is a key feature.

On the other hand, [140] showed that different power law representations of the uniaxial stress-strain relation lead to different predicted values of the strain hardening exponent and reference strength but the best fit plastic properties for all the representations considered gave a good fit to the uniaxial stress-strain response of the "experimental" material.

4.5.3 Sensitivity to the characterization of elasticity

If the elastic constants are not known a priori, the effective (or reduced) modulus can be obtained from the unloading indentation force versus indentation depth response using the relation Eq. (4.29), [74, 145, 81]. However, this requires knowing the factor β in Eq. (4.29) that can vary with plastic properties.

Here, we explore the sensitivity of the predicted plastic uniaxial stress-strain response to the value of the elastic constants by fitting the A-input material response using the database for the D-input material D_{D} and fitting the D-input material response using the database for the A-input material D_{A} (the two databases differ only in the elastic constants used to create them). The A-input material and D-input material values of the effective modulus differ by a factor of ≈ 0.6 which is much larger than the expected variation in β but gives an indication of the trend.

For the A-input material using the database D_{D}, the predicted plastic properties are:

(F): $N = 0.04$, $\bar{\tau}_0/E_{\mathrm{D}} = 0.0020$ (Note: normalized by E_{D}), $\alpha = 0.30$ with probability $p_1 = 0.20$.

(S) and (FS): $N = 0.04$, $\bar{\tau}_0/E_{\mathrm{D}} = 0.0022$ (Note: normalized by E_{D}), $\alpha = 0.03$ with probability $p_1 = 0.92$ (S) and $p_1 = 0.94$ (FS).

Because the database D_{D} is used to identify the plastic properties of the A-input material, the Young's modulus E_{D} is used to normalize $\bar{\tau}_0$ for the A-input material.

For the D-input material using the database D_{A}, the predicted plastic properties are:

(F): $N = 0.14$, $\bar{\tau}_0/E_{\mathrm{A}} = 0.0016$ (Note: normalized by E_{A}), $\alpha = 0.03$ with probability $p_1 = 0.07$.

(S) and (FS): $N = 0.02$, $\bar{\tau}_0/E_{\mathrm{A}} = 0.0038$ (Note: normalized by E_{A}), $\alpha = 0.17$ with probability $p_1 = 1.00$ for both (S) and (FS).

Fig. 4.18 shows comparisons between the predicted responses for the A-input material using the database D_{D} to obtain the plastic material parameters and the corresponding A-input material responses. Also, the predicted stress-strain responses in Fig. 4.18 (a) were calculated using the D-input material elastic properties. Neither the uniaxial compression stress-strain response nor the indentation force versus indentation depth response are well represented, Figs. 4.18(a) and 4.18(b). However, the residual surface profiles using the (S) and (FS) fits are indistinguishable from those of the A-input material. Calculating the uniaxial compression stress-strain response in Fig. 4.18(a) using the elastic constants of the A-input material and the (S) predicted plastic parameters (not shown) gives a good representation of the "experimental" A-input material response. This shows: (i) that the residual surface profile is not very sensitive to the choice of elastic constants; (ii) that plastic property identification based on the residual surface profile data (S) does not require accurate knowledge of the (isotropic) elastic constants; and (iii) that if the residual surface profile is used for a Bayesian-type statistical plastic parameter identification, the database does need to have accurate values of the (isotropic) elastic constants. Similar results (not shown) have been obtained for the D-input material using the A-input material database D_{A}.

At least for the materials considered here, as seen in Fig. 4.18, basing predictions on incorrect values of elastic constants does not permit both the residual surface profile and the indentation force versus indentation depth response to be well-represented. This may serve as an indication that the presumed values of elastic constants do not provide a good representation of the elastic response of the material.

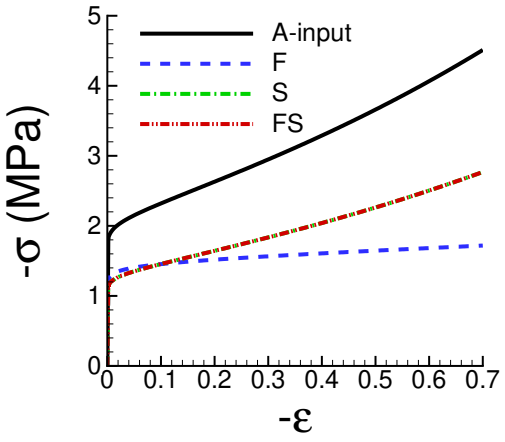

(a)

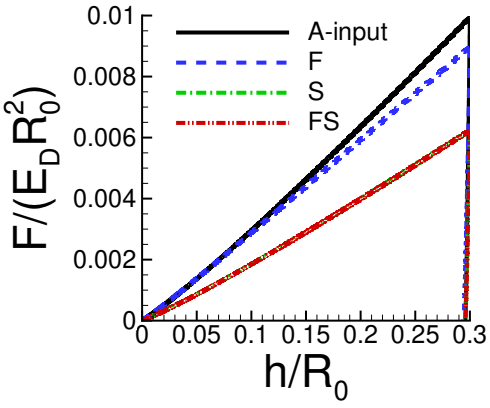

(b)

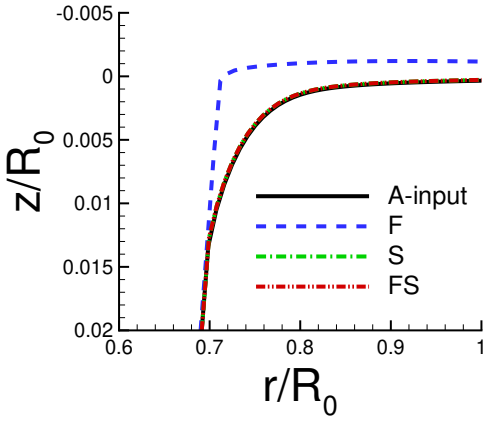

(c)

Figure 4.18: Predicted responses for the A-input material using the database D_{D} with the elastic constants for the D-input material compared with the corresponding "experimental" A-input material response. (a) Uniaxial compression stress-strain responses. (b) Normalized indentation force $F/(E_{\mathrm{D}}R_0^2)$ versus normalized indentation depth h/R_0. (c) Normalized surface profiles near the indenter after unloading.

4.6 Variation of indention response with indenter shape for plastically compressible and incompressible materials

As shown in the pioneering work of [91], in conical indentation, materials with very different uniaxial stress-strain curves can give indistinguishable indentation force versus indentation depth

responses. In [2], conical indentation calculations were carried out for three plastically incompressible materials that had very different uniaxial stress-strain responses but indistinguishable indentation force versus indentation depth responses. The materials were termed m_1, m_2 and m_3 and their constitutive behavior characterized by a constitutive relation of the form in Section 4.2.2, with $\alpha = 1/3$.

The elastic properties of the three materials were the same with $E = 200$ GPa and $\nu_e = 0.3$. The initial reference strength, $\bar{\sigma}_0$ and strain hardening exponent, N, for the three materials are $\bar{\sigma}_0 = 650$ MPa, $N = 0.10$ for material m_1, $\bar{\sigma}_0 = 490$ MPa, $N = 0.20$ for material m_2 and $\bar{\sigma}_0 = 330$ MPa, $N = 0.31$ for material m_3. The reference strain rate is set to $\dot{\epsilon}_0 = 0.01s^{-1}$ and strain rate sensitivity exponent is set to $m = 0.005$ to approximate rate independent plastic deformations. Two sets of materials are considered: the plastically incompressible materials m_1, m_2 and m_3 with $\alpha = 1/3$, and the plastically compressible materials m_1, m_2 and m_3 with $\alpha = 0$.

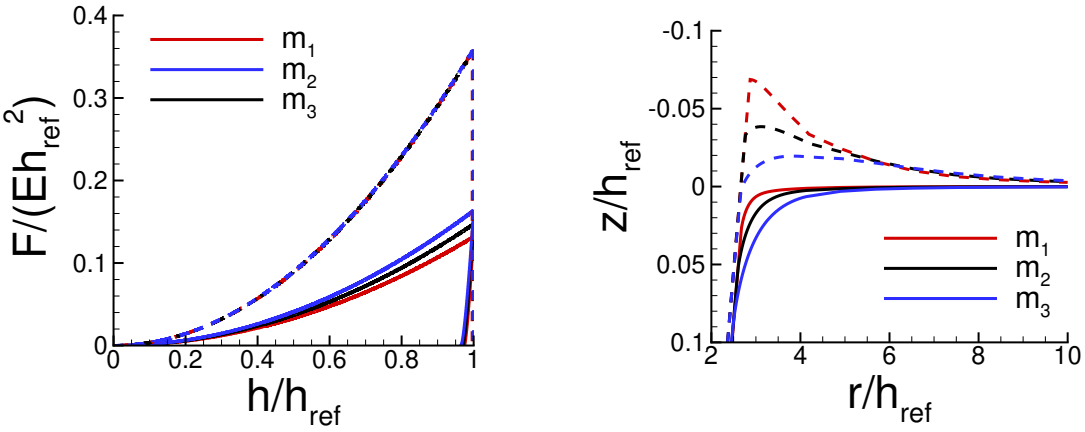

Figure 4.19: Comparison of the calculated indentation responses in conical indentation for plastically compressible materials ($\alpha = 0$; solid lines) with the responses calculated for a plastically incompressible materials ($\alpha = 1/3$; dashed lines). The flow strength and strain hardening values are those of materials m_1, m_2 and m_3 of [2], also given in the text. (a) Normalized indentation force $F/(Eh_{\text{ref}}^2)$ versus normalized indentation depth h/h_{ref}. (b) Normalized surface profiles near the indenter after unloading. Length quantities are normalized by a conveniently chosen indentation depth h_{ref}.

A comparison between the indentation responses for materials m_1, m_2 and m_3 with $\alpha = 1/3$ (dashed lines) with the materials m_1, m_2 and m_3 with $\alpha = 0$ (solid lines) in conical indentation is shown in Fig. 4.19. In the conical indentation analyses, quantities with the dimension of length are normalized by a conveniently chosen indentation depth h_{ref}. In Fig. 4.19(a), the indentation force versus indentation depth responses of the three plastically incompressible materials (dashed lines) are indistinguishable but the corresponding residual surface profiles (dashed lines) in Fig. 4.19(b) differ significantly. By considering both responses, it was possible to extract the "experimental" material properties in [2] using the Bayesian-type statistical approach described in Section 5.3. In contrast, both the indentation force versus indentation depth responses and residual surface profiles of the three plastically compressible materials (solid lines) in Fig. 4.19 can be distinguished. The indentation force magnitude and residual surface pile-up height for the plastically compressible materials are both smaller than those for the plastically incompressible materials for the same indentation conditions. The indentation response of plastically compressible materials is "softer" than for plastically incompressible materials because of the reduction in hydrostatic stress below the indenter as seen in [107].

For spherical indentation of the materials m_1, m_2 and m_3, the indentation force versus indentation depth responses of Fig. 4.20(a) are indistinguishable up to $h/R_0 \approx 0.07$ for the plastically incompressible materials (dashed lines), and up to $h/R_0 \approx 0.008$ for plastically compressible materials (solid lines). For larger values of h/R_0, the indentation force versus indentation depth responses are well separated. Also, as for conical indentation, the residual surface profiles in Fig. 4.20(b) for spherical indentation do not overlap. Thus, for spherical indentation, there is a value of indentation depth below which the indentation force versus indentation depth responses are indistinguishable, as also seen by [93]. In addition, the corresponding residual surface profiles can also be indistinguishable. For example, the indentation force versus indentation depth responses and residual surface profiles are indistinguishable in Figs. 4.6 and 4.8, while their corresponding uniaxial responses in Figs. 4.5 and 4.7 are different. However, the response in spherical indentation is not self-similar and for a sufficiently large indentation depth, the indentation force

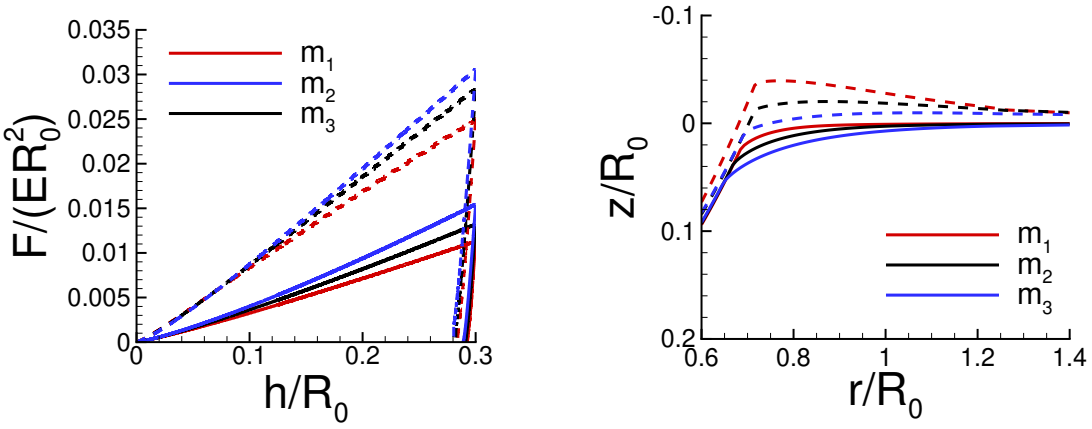

(a) (b)

Figure 4.20: Comparison of the indentation responses in spherical indentation calculated for plastically compressible materials ($\alpha = 0$; solid lines) with the indentation responses using plastically incompressible materials ($\alpha = 1/3$; dashed lines). The flow strength and strain hardening values are those of materials m_1, m_2 and m_3 of [2], also given in the text. (a) Normalized indentation force $F/(ER_0^2)$ versus normalized indentation depth h/R_0. (b) Normalized surface profiles near the indenter after unloading.

versus indentation depth responses separate. This indentation depth value is expected to depend on the specific sets of material parameters.

4.7 Conclusions

We have assumed that the elastic material properties are known and used the Bayesian-type statistical approach of [2] to identify the plastic properties, $\bar{\tau}_0/E$, N and α, of a [138] type constitutive description from the indentation force versus indentation depth response and the residual surface profile of two plastically compressible "experimental" materials, termed A-input and D-input. Databases obtained via $K_{\text{total}} = 140$ full field finite element solutions were constructed for each material. Linear interpolation between the finite element solution data was used to create the finer databases used for property identification. In this Bayesian identification process there is a trade-off between the number of finite element computations to be carried out to populate the database and the accuracy of the material identification. The correction factor β in the method of

[74, 145, 81] for determining the effective (or reduced) elastic modulus was evaluated from the unloading response of the "experimental" materials. Parameter studies were carried out exploring the effects of the choice of plastic constitutive relation and isotropic elastic constants on the predicted uniaxial responses. The indentation responses of plastically compressible and plastically incompressible materials in spherical and conical indentation were compared.

1. The uniaxial stress-strain responses calculated using the plastic properties identified from the spherical indentation indentation force versus indentation depth response and/or the residual surface profile on unloading can approximate those of the "experimental" input materials. The quality of the approximation decreases with increasing noise but can still provide at least a good qualitative representation for a moderate value of noise amplitude.

   (i) In the circumstances analyzed, the values of plastic material properties inferred solely from the residual surface profiles using noise-free data give the best representation of the uniaxial responses of the "experimental" materials.

   (ii) The indentation force versus indentation depth responses calculated using the identified plastic properties can be indistinguishable from that of the corresponding input "experimental" material even if the values of the identified plastic material properties differ from the input "experimental" values.

   (iii) A good fit to indentation data does not guarantee a good fit to the uniaxial stress-strain response of a material.

2. For the plastically compressible materials considered, the calculated correction factor β in the [81] method of identifying the effective (or reduced) elastic modulus from the indentation force unloading response depends on the plastic material parameters but is in a similar range to that found for plastically incompressible solids.

3. The accuracy of the identification of the material uniaxial stress-strain response improves with increasing values of the plastic compressibility parameter α ($\alpha = 1/3$ corresponds to plastic incompressibility), particularly for predictions including surface profile data.

4. Materials with a nearly plastically incompressible response can give indentation force versus indentation depth responses indistinguishable from that of the "experimental" plastically compressible input materials. The uniaxial stress-strain curves based on this fit do not quantitatively or qualitatively represent the uniaxial stress-strain responses of the "experimental" input materials. Thus, an "experimental" spherical indentation force versus indentation depth response does not uniquely identify an appropriate constitutive framework.

5. At least in the cases analyzed, the predicted indentation force versus indentation depth response is sensitive to the values of elastic properties but the residual surface profile is not. The plastic material properties obtained from this residual surface profile can provide a good representation of those of the "experimental" material indicating that a Bayesian statistics database used to identify plastic properties from the residual surface profile does not need to be based on accurate values of the elastic constants.

6. For plastically incompressible materials with indentation force versus indentation depth responses that are indistinguishable in conical indentation, the indentation force versus indentation depth responses can be distinguishable in spherical indentation if the indentation depth is sufficiently large. For both plastically incompressible and plastically compressible materials a material dependent indentation depth is found below which the spherical indentation force versus indentation depth responses are indistinguishable.

Acknowledgment

We are grateful for the high performance research computing resources provided by Texas A&M University.

5. ON THE IDENTIFICATION OF POWER-LAW CREEP PARAMETERS FROM CONICAL INDENTATION[†]

"One way to explain the complexity and unpredictability of historical systems, despite their ultimate determinacy, is to note that long chains of causation may separate final effects from ultimate causes lying outside the domain of that field of science."

– Jared Diamond

5.1 Introduction

The serviceability and reliability of a variety of engineering components, as for example in turbines used for electricity generation and in vehicle and airplane engines, are limited by continuing deformation at relatively low stress levels, i.e. creep. Instrumented indentation is attractive for identifying creep properties as it is non-destructive, requires a relatively small specimen, and has been used for the identification of mechanical properties of a broad range of materials. However, indentation involves a complex deformation field, and extracting material properties from experimentally measured indentation quantities can be complex and non-unique.

The creep deformation of polycrystalline structural metals often can be characterized appropriately by an isotropic power-law creep constitutive relation and there is a large literature on modeling the indentation response of power-law creeping materials using analytical methods, numerical methods or a combination of these, e.g., Refs. [148, 69, 149, 150, 151]. In particular, studies have been carried out using such analyses to extract power-law creep parameters from indentation responses, including, for example, Refs. [152, 153, 154, 3, 155, 156, 157, 158]. Specifically, in Refs. [3, 155, 151, 156] experimental creep indentation data was related to uniaxial power-law

[†]Reprinted with permission from "On the identification of power-law creep parameters from conical indentation" by Yupeng Zhang and Alan Needleman, 2021, Proceedings of the Royal Society A, 477, 20210233. Copyright © 2021 by the authors.

creep properties using analytical results from Bower et al. [69] and from the expanding cavity model of Ginder et al. [151].

Here, the Bayesian statistics based approach of Zhang et al. [2] is used to extract power-law creep parameters from the indentation depth versus time response and the residual surface profile. Finite element solutions for three materials with very different power-law creep properties are considered to be the "experimental" responses. The power-law creep parameters identified via indentation, using noise-free as well as noise-contaminated data, are compared with the corresponding uniaxial creep and stress relaxation responses of the input "experimental" materials.

The questions addressed include:

1. Can very different power-law creep parameters give nearly the same responses in load and hold indentation creep? There are sets of rate independent plastic material parameters that have indistinguishable force versus depth responses in conical indentation but very different uniaxial responses, [91, 93, 2].

2. Does using the residual surface profile in addition to or instead of the indentation depth versus time data improve the quality of the prediction?

3. How sensitive is the predicted creep response to noise in the "experimental" indentation data?

4. How do the power-law creep properties obtained using the analytical steady state creep results of Bower et al. [69] and Ginder et al. [151] compare with those predicted from the Bayesian-type statistical approach?

5.2 Problem formulation

Indentation into an isotropic elastic power-law creep solid by a conical indenter is modeled as sketched in Fig. 5.1. Quasi-static loading conditions are presumed. The dimensions of the region analyzed are taken to be large enough to approximate indentation into a half-space and the deformations are restricted to be axisymmetric.

Calculations are carried out for an indenter angle $\gamma = 70.3°$, which is the equivalent conical indenter angle to a Berkovich indenter assuming the same projected area on contact at a given indentation depth [159]. The indentation force in the z-direction is a prescribed function of time, the nominal indentation depth magnitude is denoted by h and the corresponding nominal contact radius is $r_{\text{nom}} = h \tan \gamma$ (see Fig. 5.1).

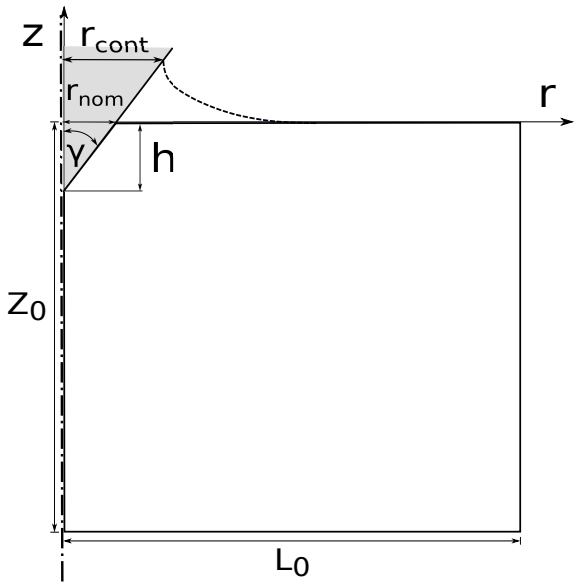

Figure 5.1: Sketch of the indentation configuration analyzed with h the indentation depth magnitude, r_{cont} the actual contact radius and r_{nom} the nominal contact radius.

The calculations are carried out using a quasi-static Lagrangian implementation in the commercial finite element program ABAQUS [118] standard. Elastic deformations are presumed small but finite creep strains are accounted for.

5.2.1 Initial/boundary value problem

The magnitude of the indentation force in the $z-$direction, P_z, is a prescribed function of time, $f(t)$, so that

$$P_z = \int_{S_{\text{contact}}} T_z ds = f(t) \tag{5.1}$$

where T_z is $z-$component of the traction vector, $\mathbf{T}$, on the contact surface S_{contact}.

As described in the ABAQUS [118] manual, the remaining conditions imposed on S_{contact} are

$$T_t = \mu T_n \text{ and } \min\Big[\int_{S_{\text{contact}}} (\Delta \dot{u}_n)^2 ds\Big] \tag{5.2}$$

Here, T_t and T_n are the components of $\mathbf{T}$ in the directions tangent and normal, respectively, to the indenter, and $\Delta \dot{u}_n$ is the difference in displacement rate components normal to the indenter, with $(\dot{})$ denoting the time derivative.

The coefficient of friction is taken to be $\mu = 0.4$, leading to very little slip along the contact surface and the contact boundary conditions in normal direction of Eq. (5.2) are termed "hard contact" in the ABAQUS [118] standard manual.

With r and z denoting the positions of material points in the initial configuration, the remaining boundary conditions are

$$T_r = T_z = 0 \quad \text{on} \quad r = L_0 \quad \text{and} \quad z = 0,\ S \neq S_{\text{contact}} \tag{5.3a}$$

$$\dot{u}_r = 0, \quad T_z = 0 \quad \text{on} \quad r = 0 \tag{5.3b}$$

$$\dot{u}_z = 0, \quad T_r = 0 \quad \text{on} \quad z = Z_0 \tag{5.3c}$$

5.2.2 Constitutive relation

The elastic-creep constitutive relation of ABAQUS [118] standard is used so that the (small) elastic strain-stress relation has the form

$$\boldsymbol{\epsilon}^{\text{e}} = \frac{(1+\nu)}{E}\boldsymbol{\tau} - \frac{\nu}{E}\text{tr}(\boldsymbol{\tau})\mathbf{I} \tag{5.4}$$

where $\boldsymbol{\tau} = J\boldsymbol{\sigma}$ is the Kirchhoff stress ($\boldsymbol{\sigma}$ is the Cauchy stress and J is current volume/reference volume), $\boldsymbol{\epsilon}^{\text{e}}$ is the elastic strain (based on the logarithmic strain), E is Young's modulus and ν is Poisson's ratio. Also, $\text{tr}(\ )$ denotes the trace and $\mathbf{I}$ denotes the identity tensor.

The creep part of the rate of deformation tensor, $\mathbf{D} = \mathrm{sym}(\dot{\mathbf{F}} \cdot \mathbf{F}^{-1})$, is

$$\mathbf{D}^{\mathrm{c}} = \frac{3}{2}\dot{\epsilon}_{\mathrm{c}}\frac{\boldsymbol{\tau}'}{\sigma_{\mathrm{e}}} = \frac{3}{2}\alpha\sigma_{\mathrm{e}}^{n-1}\boldsymbol{\tau}' \tag{5.5}$$

with

$$\dot{\epsilon}_{\mathrm{c}} = \dot{\epsilon}_0\left(\frac{\sigma_{\mathrm{e}}}{\sigma_0}\right)^n = \alpha{\sigma_{\mathrm{e}}}^n \tag{5.6}$$

and

$$\boldsymbol{\tau}' = \boldsymbol{\tau} - \frac{1}{3}\mathrm{tr}(\boldsymbol{\tau})\mathbf{I}\,, \quad \sigma_{\mathrm{e}} = \sqrt{\frac{3}{2}\boldsymbol{\tau}' : \boldsymbol{\tau}'} \tag{5.7}$$

where n is the creep exponent, $\dot{\epsilon}_0$ is a reference strain rate, σ_0 is a reference stress and $\alpha = \dot{\epsilon}_0/\sigma_0^n$ is the power law creep pre-exponential factor. Also, the effective creep strain ϵ_{c} is given by $\epsilon_{\mathrm{c}} = \int_0^t \dot{\epsilon}_{\mathrm{c}}dt$ and t is time.

5.3 Bayesian-type statistical approach

The equations of the Bayesian-type statistical approach used to infer the creep parameters n, σ_0 and $\dot{\epsilon}_0$ from an indentation depth versus time response, from a residual surface profile or from a combination of these are presented here. A more complete presentation, background on the methodology and references are given in Ref. [2].

The "experimental" indentation data consists of: (i) a vector characterizing the residual surface profile, $\boldsymbol{s}^{\mathrm{m}}$; and (ii) a vector characterizing the indentation depth versus time response, $\boldsymbol{h}^{\mathrm{m}}$. The components of the vector s_k^{m}, $k = 1, ..., K_{\mathrm{s}}$ are values of the normalized surface coordinate, z_k/h_{ref} (h_{ref} is a conveniently chosen reference length) at specified values of normalized radial coordinate r_k/h_{ref}. The components of the vector h_k^{m}, $k = 1, ..., K_{\mathrm{h}}$ are values of the normalized indentation depth h_k/h_{ref} at specified values of normalized time t_k/t_{ref}.

Finite element solutions for a normalized residual surface profile, denoted by $\boldsymbol{s}^i$, and for a normalized indentation depth versus time response, denoted by $\boldsymbol{h}^i$, are used to construct a coarse database of indentation responses, with $i = 1, 2, ..., K_{\mathrm{total}}$ and K_{total} is the total number of indentation response pairs ($\boldsymbol{s}^i$,$\boldsymbol{h}^i$) in the database. In practice, it is expected that there will be a delay

between unloading and measuring the surface profile. The measured surface profile will, at least to some extent, depend on this delay which, if specified, can be incorporated into the formulation. However, for simplicity and because a standard delay time remains to be established, the database here is constructed using the surface profile immediately after unloading.

Treating the indentation depth versus time data and the surface profile data as being independent, the posterior probability $p(\boldsymbol{s}^i, \boldsymbol{h}^i | \boldsymbol{s}^{\rm m}, \boldsymbol{h}^{\rm m})$ associated with the "experimental" data $(\boldsymbol{s}^{\rm m}, \boldsymbol{h}^{\rm m})$ is given by

$$p(\boldsymbol{s}^i, \boldsymbol{h}^i | \boldsymbol{s}^{\rm m}, \boldsymbol{h}^{\rm m}) = \frac{p(\boldsymbol{s}^i | \boldsymbol{s}^{\rm m}) p(\boldsymbol{h}^i | \boldsymbol{h}^{\rm m})}{Z_{\rm sh}} \tag{5.8}$$

where

$$p(\boldsymbol{s}^i | \boldsymbol{s}^{\rm m}) = \frac{p(\boldsymbol{s}^{\rm m} | \boldsymbol{s}^i) p(\boldsymbol{s}^i)}{Z_{\rm s}} \quad , \quad p(\boldsymbol{h}^i | \boldsymbol{h}^{\rm m}) = \frac{p(\boldsymbol{h}^{\rm m} | \boldsymbol{h}^i) p(\boldsymbol{h}^i)}{Z_{\rm h}} \tag{5.9}$$

In Eqs. (5.8) to (5.9) there is no sum on i.

The constants $Z_{\rm s}$, $Z_{\rm h}$ and $Z_{\rm sh}$, which assure that the posterior probability values lie in the range 0 to 1, are given by

$$Z_{\rm s} = \sum_{i=1}^{K_{\rm total}} p(\boldsymbol{s}^{\rm m} | \boldsymbol{s}^i) p(\boldsymbol{s}^i) \ , \ Z_{\rm h} = \sum_{i=1}^{K_{\rm total}} p(\boldsymbol{h}^{\rm m} | \boldsymbol{h}^i) p(\boldsymbol{h}^i) \ , \ Z_{\rm sh} = \sum_{i=1}^{K_{\rm total}} p(\boldsymbol{s}^i | \boldsymbol{s}^{\rm m}) p(\boldsymbol{h}^i | \boldsymbol{h}^{\rm m}) \tag{5.10}$$

The likelihood functions, which measure the difference between the "experimental" data and the predicted responses in the database, are (see Zhang et al. [2]),

$$p(\boldsymbol{s}^{\rm m} | \boldsymbol{s}^i) = \Big(\frac{1}{\hat{\xi}_{\rm s}^i \sqrt{2\pi}} \Big)^{K_{\rm s}} \exp\Big(-\frac{K_{\rm s}}{2} \Big) \quad , \quad p(\boldsymbol{h}^{\rm m} | \boldsymbol{h}^i) = \Big(\frac{1}{\hat{\xi}_{\rm h}^i \sqrt{2\pi}} \Big)^{K_{\rm h}} \exp\Big(-\frac{K_{\rm h}}{2} \Big) \tag{5.11}$$

where $K_{\rm s}$ is the number of data points on the residual surface profile curve, $K_{\rm h}$ is the number of data points on the indentation depth versus time curve and the variances $(\hat{\xi}_{\rm s}^i)^2$ and $(\hat{\xi}_{\rm h}^i)^2$ are given by the maximum likelihood estimates

$$(\hat{\xi}_{\rm s}^i)^2 = \frac{1}{K_{\rm s}} \sum_{k=1}^{K_{\rm s}} (s_k^{\rm m} - s_k^i)^2 \quad , \quad (\hat{\xi}_{\rm h}^i)^2 = \frac{1}{K_{\rm h}} \sum_{k=1}^{K_{\rm h}} (h_k^{\rm m} - h_k^i)^2 \tag{5.12}$$

where the subscript k denotes the kth component of each vector. If one of the variances in Eq. (A-14) is equal to 0, its corresponding likelihood in Eq. (5.11) is infinite and the corresponding posterior probability is set to 1.

For all sets of creep parameters in the database, a uniform prior is used for both $p(\boldsymbol{s}^i)$ and $p(\boldsymbol{h}^i)$ in Eq. (5.9). Outside the range of values in the database, $p(\boldsymbol{s}^i) = 0$ and $p(\boldsymbol{h}^i) = 0$. The posterior probabilities are evaluated by substituting the prior values and the likelihood values from Eq. (5.11) into Eq. (5.9).

5.4 Material parameters

The "experimental" materials considered are : (i) amorphous selenium (Se) at $35°$C; (ii) solid acid $CsHSO_4$ at $145°$C; and (iii) tin (Sn) at $129°$C. The values of the material parameters characterizing these materials are given in Table 5.1.

Table 5.1: Constitutive parameters characterizing the three input "experimental" materials.

	E(GPa)	ν	n	σ_0(MPa)	$\dot{\epsilon}_0(\mathrm{s}^{-1})$	$\alpha(\mathrm{Pa}^{-n}\mathrm{s}^{-1})$
Se ($35°$C)	9.2	0.33	1.15	8.740	1.0×10^{-4}	1.04×10^{-12}
$CsHSO_4$ ($145°$C)	1.2	0.33	3.59	0.01512	1.0	9.89×10^{-16}
Sn ($129°$C)	45	0.33	6.60	9.330	1.0	9.97×10^{-47}

For Se, the values of E, n and α are taken from [3], and the value of Poisson's ratio ν is from [160]. For $CsHSO_4$, the values of n and α are taken from Table 1 of [161]. The value of E is obtained by a linear fit to the uniaxial data at a strain rate of $10^{-2}\mathrm{s}^{-1}$ up to a stress of 6.0 MPa in Fig. 1(a) of [161]. For Sn, the value of n is taken from [162] and the value of α is obtained by a fit to data in Fig. 2(b) of [162]. The value of E is taken to be 45GPa [163] and the value of ν is taken from [164].

5.5 Indentation responses

5.5.1 Constant load and hold indentation creep

The imposed loading history models a constant load and hold indentation creep test, with the magnitude of the applied force on the indenter, $f(t)$ in Eq. (5.1), prescribed to be

$$f(t) = \begin{cases} \zeta h_{\text{ref}}^2 \sigma_0 t/t_1, & 0 \le t \le t_1 \\ \zeta h_{\text{ref}}^2 \sigma_0, & t_1 < t \le t_2 \\ \zeta h_{\text{ref}}^2 \sigma_0 (t_3 - t)/(t_3 - t_2), & t_2 < t \le t_3 \end{cases} \tag{5.13}$$

where the rise time is $t_1 \dot{\epsilon}_0 = 10^{-4}$, the hold time is $t_2 \dot{\epsilon}_0 = 1.0$, the load release time, $t_3 - t_2$, is given by $t_3 \dot{\epsilon}_0 = t_2 \dot{\epsilon}_0 + 10^{-4}$ and the normalizing length is taken to be $h_{\text{ref}} = 3.43 \times 10^{-4} L_0$ in all calculations. The value of σ_0 used in Eq. (5.13) for each material is given in Table 5.1. The value of non-dimensional factor ζ is selected, so that the indentation depth h is large compared with the finite element size near the indenter but with the large strain gradients confined to the region with the finest finite element resolution. The values of ζ used in the calculations are given in the Appendix C.

For power-law creep with elastic strains neglected, Eq. (5.6), Bower at al. [69] derived a relation for normalized indentation depth rate

$$\dot{\epsilon}_{\text{crp}} = \frac{1}{h_{\text{crp}}} \frac{dh_{\text{crp}}}{dt} = \beta p^n \tag{5.14}$$

with

$$p = \frac{f(t)}{\pi h_{\text{crp}}^2 \tan^2 \gamma} \tag{5.15}$$

where $\dot{\epsilon}_{\text{crp}}$ is indentation strain rate, p is the contact pressure (contact force/contact area) (see Fig. 5.1), and β is an indentation creep parameter.

For $f(t) \equiv f_{\text{const}}$, integration of Eq. (5.14) with respect to t gives

$$h_{\text{crp}} = (2n\beta)^{\frac{1}{2n}} \left(\frac{f_{\text{const}}}{\pi \tan^2 \gamma} \right)^{1/2} t^{\frac{1}{2n}} \tag{5.16}$$

Note that since the force magnitude is prescribed constant both the indentation pressure, p, and the indentation strain rate, $\dot{\epsilon}_{\text{crp}}$, vary with time.

For an elastic solid, the relation between indentation depth h and indentation force f_{const} in the axisymmetric Boussinesq problem is given by Sneddon [165]

$$h_{\text{ela}} = \left(\frac{\pi f_{\text{const}}}{2E^* \tan \gamma} \right)^{1/2} \tag{5.17}$$

with $E^* = E/(1-\nu^2)$.

As exploited by Su et al. [3], the indentation depths induced by a constant load for a power-law creeping solid, Eq. (5.16), and for an elastic solid, Eq. (5.17), are each proportional to $\sqrt{f_{\text{const}}}$ so that in the power-law creep regime

$$\frac{h_{\text{crp}}}{h_{\text{ela}}} = (2n\beta)^{\frac{1}{2n}} \left(\frac{2E^*}{\pi^2 \tan \gamma} \right)^{1/2} t^{\frac{1}{2n}} \tag{5.18}$$

hence, the ratio h/h_{ela} is independent of f_{const} both at the beginning of indentation when h_{ela} dominates and at steady state creep when h_{crp} dominates. Thus, h_{ela} provides a natural choice of reference length [3]. Attention here is confined to scaling relations associated with load and hold indentation, but we note that scaling relations for other loading histories have been given in Refs. [150, 3].

The values of h_{ela} are $h_{\text{ela,Se}} = 7.88 \times 10^{-4} L_0$ for Se, $h_{\text{ela,CsHSO}_4} = 3.43 \times 10^{-4} L_0$ for $CsHSO_4$ and $h_{\text{ela,Sn}} = 1.18 \times 10^{-3} L_0$ for Sn. If we take $f_{\text{const}} = 100$ mN, then h_{ela} is 2.33μm, 6.46μm and 1.06μm for Se, $CsHSO_4$ and Sn, respectively. For each of the three materials its value of h_{ela} is used as the reference length.

In their experiments Su et al. [3] found that the h/h_{ela} versus t response for amorphous sele-

nium at $35°$C under various applied indentation forces collapsed onto a single curve even in the transient regime. Here, calculations with indentation forces of 1/3 and 2 times of the $f(t)$ value in Eq. (5.13) were carried out for Se ($n = 1.15$), $CsHSO_4$ ($n = 3.59$) and Sn ($n = 6.60$), and the calculated curves of $h/h_{\rm ela}$ versus t collapsed onto a single curve.

5.5.2 Finite element implementation

The reference finite element mesh for the configuration in Fig. 5.1 consists of 8100 nodes, corresponding to 7921 $4-$node bilinear axisymmetric quadrilateral elements. In a $0.1L_0 \times 0.1L_0$ fine mesh region near the indenter tip, 60×60 elements are used with a uniform square element size $(1.7 \times 10^{-3})L_0 \times (1.7 \times 10^{-3})L_0$. Thus, the element size in the fine mesh region is $2.2h_{\rm ela,Se}$ for Se, $5.0h_{\rm ela,CsHSO_4}$ for $CsHSO_4$ and $1.4h_{\rm ela,Sn}$ for Sn. The element size is gradually increased outside the uniform meshed region. Reduced integration with hourglass control is used. Also, the error tolerance in ABAQUS [118] standard is set to 10^{-3}. More details on the ABAQUS [118] indentation implementation used are given in Ref. [140].

Convergence was investigated using a refined mesh with $1/4$ the element sizes of the reference mesh, giving 31684 quadrilateral elements and 32041 nodes. For all three materials, the indentation depth versus time responses calculated with the two meshes essentially coincided. The differences between indentation depths when $t\dot{\epsilon}_0 > 10^{-4}$ were less than $2.7\%, 0.2\%$ and 0.1% for Se, $CsHSO_4$ and Sn, respectively. The residual surface profile for Se involved sink-in with a maximum profile difference of 0.4%, while the surface profiles for $CsHSO_4$ and Sn involved pile-up with a maximum pile-up height difference of 1.8% between the two meshes. Also, the maximum indentation depths at non-dimensional time $t\dot{\epsilon}_0 = 1.0$ differed by less than 0.1%. All results to be presented subsequently were obtained using the reference finite element mesh.

5.5.3 "Experimental" indentation responses

Fig. 5.2(a) shows the computed normalized indentation depth, $h/h_{\rm ela,Se}$, versus time, t, response obtained using material parameters for Se in Table 5.1. The points are experimentally measured data from Fig. 6(b) of Su et al. [3] and show that the experimental and computed responses

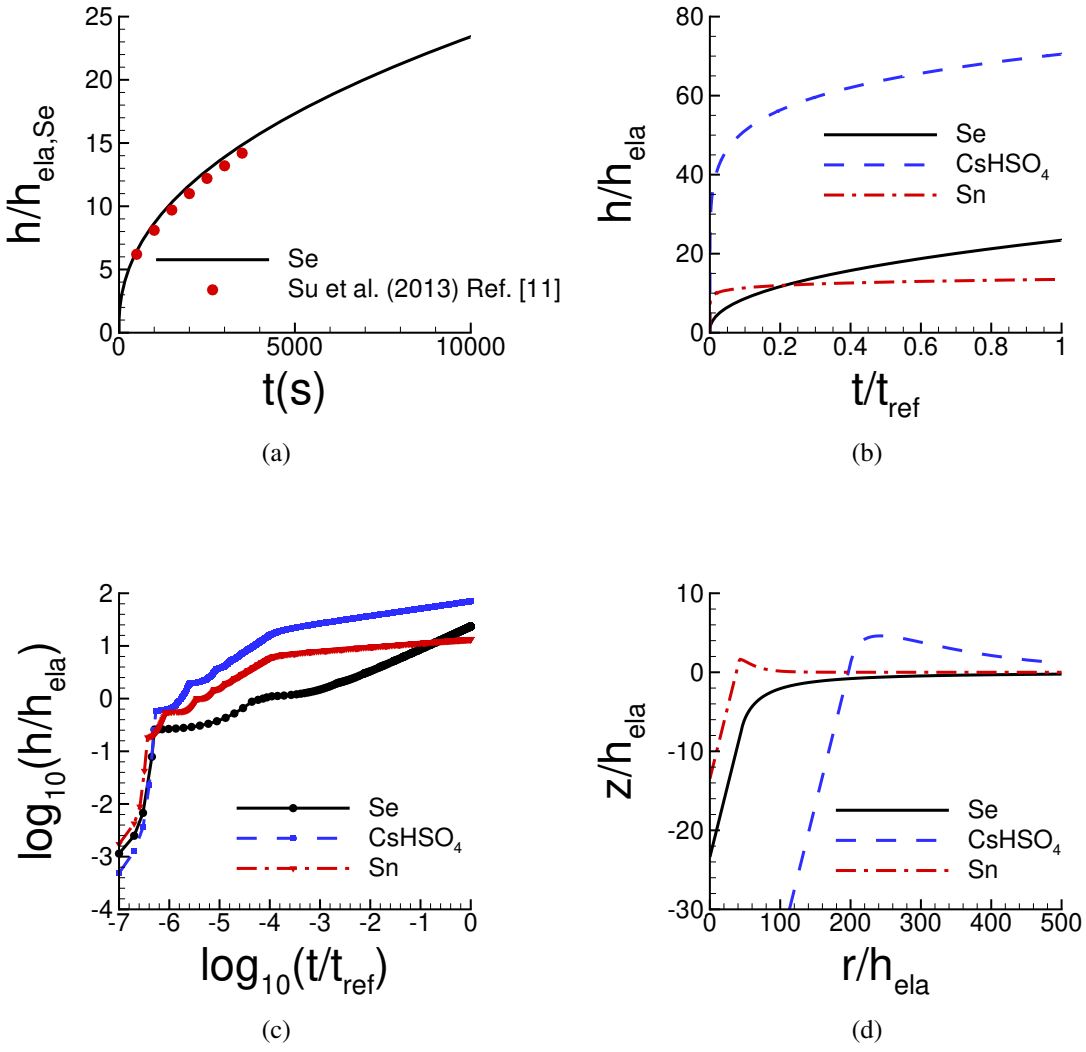

Figure 5.2: The indentation responses of the three "experimental" materials, Se, $CsHSO_4$ and Sn, in constant load and hold indentation, see Eq. (5.13). The material parameters are given in Table 5.1. (a) Normalized indentation depth $h/h_{\rm ela,Se}$ versus time t for Se. The points are data taken from Su et al. [3]. (b) $h/h_{\rm ela}$ versus $t/t_{\rm ref}$. (c) $\log_{10}(h/h_{\rm ela})$ versus $\log_{10}(t/t_{\rm ref})$. (d) Normalized surface profiles near the indenter after unloading. The values of $h_{\rm ela}$ and $t_{\rm ref} = 1/\dot{\epsilon}_0$ in (b), (c) and (d) are specific to each material.

are in very good agreement.

Fig. 5.2(b) shows $h/h_{\rm ela}$ versus $t/t_{\rm ref}$ responses for three sets of material parameters in Table 5.1, Se, $CsHSO_4$ and Sn, when $t_{\rm ref} = 1/\dot{\epsilon}_0$ and $h_{\rm ela}$ is taken to be the specified value for each

of the three materials. Fig. 5.2(c) shows a $\log_{10} - \log_{10}$ plot of the data in Fig. 5.2(b). Note that the value of $h/h_{\rm ela}$ at which each material enters steady state creep differs. The unloading parts of the responses are not shown in Figs. 5.2(a), (b) and (c), and are not used for identifying the power-law creep parameters.

In the early stages of indentation, the plot of indentation depth h versus time t is not smooth because when a new node comes into contact with the indenter, the contact length increases by the length of one-element. This discrete change in contact length occurs in the early stages of indentation when both t and h are small. In contrast to Ref. [2] the finite element output responses are not smoothed, since only the differences between the "experimental" input response and the responses of sets of material property values in the database matter, as described in Section 5.3.

Fig. 5.2(d) shows the normalized surface profiles near the indenter after unloading for the three materials. The residual surface profile of $CsHSO_4$ (dashed line) has a larger normalized indentation depth than those for Se (solid line) and Sn (dash dot line). The residual surface profile for Se exhibits sink-in while those for $CsHSO_4$ and Sn exhibit pile-up.

Fig. 5.3 shows distributions of effective creep strain, $\epsilon_{\rm c}$, and mean normal stress, $\sigma_{\rm m}$, for the "experimental" materials subject to constant load and hold loading Eq. (5.13), in the vicinity of the indenter at $t_2\dot{\epsilon}_0 = 1.0$ in Eq. (5.13). The size scale of the regions shown is material dependent, being $100h_{\rm ela,Se}$, $300h_{\rm ela,CsHSO_4}$ and $100h_{\rm ela,Sn}$ for Se, $CsHSO_4$ and Sn in Figs. 5.3 (a), (b) and (c), respectively. For each of the three materials, the state of deformation shown is at the maximum indentation depth $h_{\rm max}$ for each material just before unloading is initiated. For Se $h_{\rm max} = 0.0185L_0 = 23.4h_{\rm ela,Se}$, for $CsHSO_4$ $h_{\rm max} = 0.0241L_0 = 70.5h_{\rm ela,CsHSO_4}$ and for Sn $h_{\rm max} = 0.0159L_0 = 13.5h_{\rm ela,Sn}$.

The extent, in terms of $h_{\rm ela,CsHSO_4}$ of the region with relatively large values of $\epsilon_{\rm c}$ for $CsHSO_4$ is much larger , $\approx 300h_{\rm ela,CsHSO_4}$, than is the extent of the corresponding regions in terms of $h_{\rm ela}$ for Se and Sn. This is because the ratio σ_0/E for $CsHSO_4$ is more than one order of magnitude smaller than for the other two materials (see Table 5.1). The creep deformations for Sn are more localized under the indenter than for Se and $CsHSO_4$ because Sn has a larger value of n and a smaller value

of α.

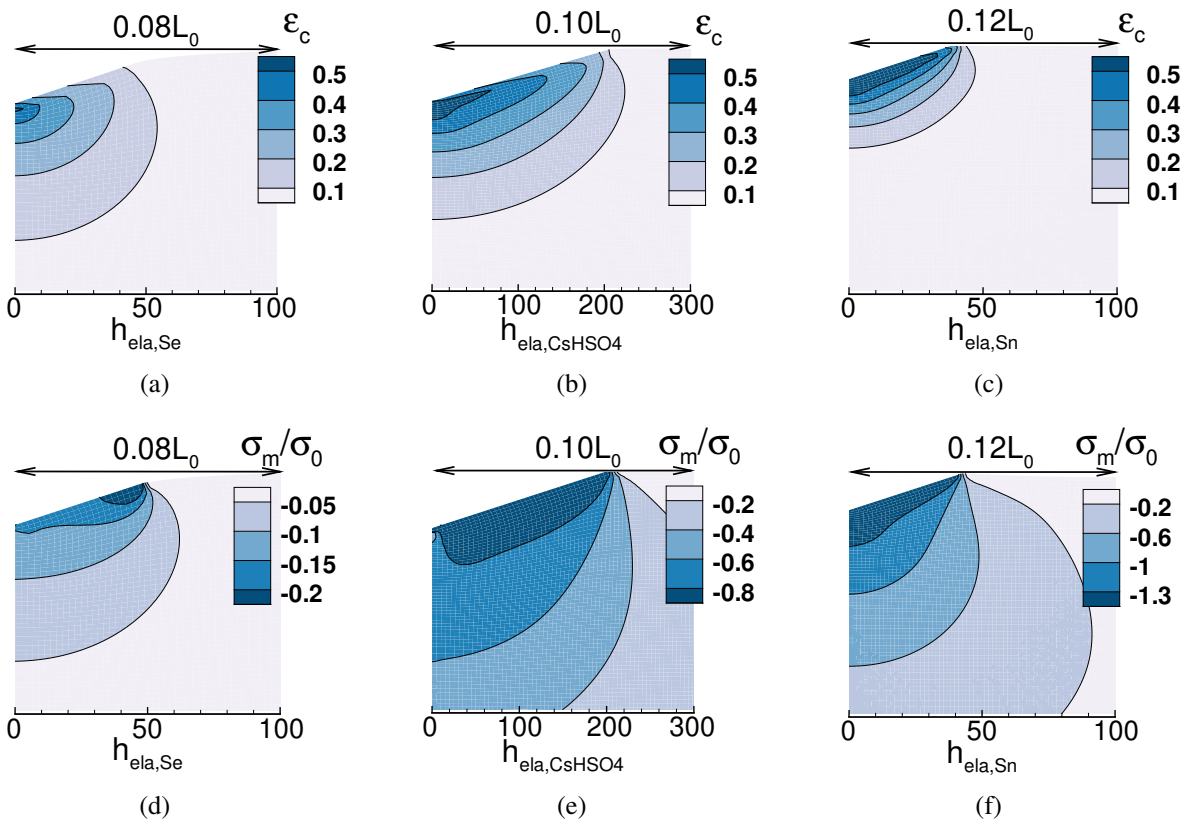

Figure 5.3: Distributions of effective creep strain, ϵ_{c}, and mean normal stress, σ_{m}, in the vicinity of the indenter at $t\dot{\epsilon}_0 = 1.0$ (where $\dot{\epsilon}_0$ is the value in Table 5.1 for each material). The indentation depths are $23.4h_{\mathrm{ela,Se}}$, $70.5h_{\mathrm{ela,CsHSO_4}}$ and $13.5h_{\mathrm{ela,Sn}}$ for Se, $CsHSO_4$ and Sn, respectively. (a) Distribution of ϵ_{c} for Se. (b) Distribution of ϵ_{c} for $CsHSO_4$. (c) Distribution of ϵ_{c} for Sn. (d) Distribution of $\sigma_{\mathrm{m}}/\sigma_0$ for Se. (e) Distribution of $\sigma_{\mathrm{m}}/\sigma_0$ for $CsHSO_4$. (f) Distribution of $\sigma_{\mathrm{m}}/\sigma_0$ for Sn.

Figs. 5.3 (d)-(f) show the contours of the corresponding mean normal stress $\sigma_{\mathrm{m}}/\sigma_0$ for Se, $CsHSO_4$ and Sn. The mean normal stress is given by

$$\sigma_{\mathrm{m}} = \frac{1}{3}\mathrm{tr}(\boldsymbol{\sigma}) \tag{5.19}$$

where $\boldsymbol{\sigma}$ is the Cauchy stress tensor (since the materials are nearly incompressible there is little

difference between the mean normal stress values based on Cauchy stress and based on Kirchhoff stress). The peak magnitude of $\sigma_{\rm m}/\sigma_0$ is much smaller for Se than for $CsHSO_4$ and Sn. For Se, the value of n is the smallest for the three materials and the value of α is the largest.

5.5.4 Construction of the databases

The creep exponent n and associated pre-exponential factor α in Eq. (5.6) define the power-law creep response. However, since the dimensions of α are stress^{-n}/time, it is not convenient to base the databases needed for the Bayesian analysis on α. Hence, for each material, the databases are constructed for the parameters n, σ_0 and $\dot{\epsilon}_0$.

For each of the three "experimental" materials in Table 5.1, one database was constructed consisting of indentation depth versus time responses and residual surface profiles directly calculated from finite element simulation. All the database indentation responses, $\boldsymbol{h}^i$ with $K_{\rm h} = 64$ data points and $\boldsymbol{s}^i$ with $K_{\rm s} = 56$ data points, where $i = 1, ..., K_{\rm total}$, are evaluated at specified values of $\dot{\epsilon}_0 t$ and $r/h_{\rm ela}$ that are obtained by interpolation of the computed responses. The specified values of $\dot{\epsilon}_0 t$ and $r/h_{\rm ela}$ are distributed in a material dependent nonuniform manner because of the large variation in time scales and length scales between the three materials. For the calculation of the likelihood functions, Eqs. (5.11), and of the variances, Eq. (A-14), the "experimental" indentation responses, $\boldsymbol{h}^m$ and $\boldsymbol{s}^m$, are evaluated at the same points.

In all three databases, the creep exponent $n \in [1.0, 7.0]$ with step size 0.1 (61 points) and $\dot{\epsilon}_0 t_2 \in [0.1, 1.0, 10.0, 100.0]$ (4 points). For Se and Sn, $\sigma_0/E \in [1 \times 10^{-4}, 1.1 \times 10^{-3}]$ with step size 1×10^{-4} (11 points) while for $CsHSO_4$, $\sigma_0/E \in [1 \times 10^{-5}, 1.1 \times 10^{-4}]$ with step size 1×10^{-5} (11 points). Thus there are $K_{\rm total} = 2684$ sets of parameter values in each of the three databases. For each set of parameter values, one finite element calculation was carried out.

As in Refs. [2, 140, 46], databases obtained directly from the finite element calculations are relatively coarse and interpolation is used to populate finer databases. Here, linear interpolation between nearby material parameters associated with database "points" (each database "point" consists of a vector of indentation depth versus time and a vector of surface profile points) in the coarse databases was used to define the responses associated with the "points" in the finer databases. The

interpolated finer databases have a step size of 0.02 in n and of 0.2 in $\log_{10}(\dot{\epsilon}_0 t_2)$ for all three materials, of 0.2×10^{-4} in σ_0/E for Se and Sn, and of 0.2×10^{-5} in σ_0/E for $CsHSO_4$. This results in $K_{\text{total}} = 245616$ points in the finer databases. The interpolated databases are used for the predictions of creep parameters.

The accuracy of the interpolation was checked by carrying out a few finite element calculations using interpolated values of material parameters. The agreement between calculated and interpolated responses was best for larger values of the creep stress exponent n and worse for values of n near 1. However, as the results to be presented subsequently will show, the lack of accuracy of the interpolated response for $n \approx 1$ does not adversely affect the ability to predict the indentation creep response and the associated power-law creep parameters.

5.6 Identification of power-law creep properties from indentation

Values of the creep material parameters n, σ_0 and $\dot{\epsilon}_0$ are obtained from the indentation responses. The predicted material parameters are then used to calculate the spatially uniform uniaxial creep and relaxation responses from a one-element finite element solution.

For uniaxial creep loading the prescribed stress σ is

$$\sigma = \begin{cases} \sigma_a t/t_{\text{C1}}, & 0 \le t \le t_{\text{C1}} \\ \sigma_a, & t_{\text{C1}} < t \le t_{\text{C2}} \end{cases} \tag{5.20}$$

where $\sigma_a = 0.5\sigma_0 = 4.37 \times 10^6$Pa, $t_{\text{C1}} = 10^{-4}$s, $t_{\text{C2}} = 3000$s for Se, $\sigma_a = 0.1\sigma_0 = 0.1512 \times 10^4$Pa, $t_{\text{C1}} = 10^{-7}$s, $t_{\text{C2}} = 500$s for $CsHSO_4$ and $\sigma_a = 0.2\sigma_0 = 1.866 \times 10^6$Pa, $t_{\text{C1}} = 10^{-5}$s, $t_{\text{C2}} = 4000$s for Sn, giving the strain rate values $\alpha\sigma_a^n$ to be $4.51 \times 10^{-5} s^{-1}$, $2.57 \times 10^{-4} s^{-1}$ and $2.44 \times 10^{-5} s^{-1}$ for Se, $CsHSO_4$ and Sn, respectively. The value of σ_0 is for each material given in Table 5.1.

For an imposed σ_a at $t = 0$ (i.e. with the rise time neglected),

$$\epsilon = \frac{\sigma_a}{E} + \alpha\sigma_a^n t \tag{5.21}$$

For uniaxial stress relaxation loading, the displacement rate is prescribed so that $\epsilon = \ln(\ell/\ell_0)$ is a constant, where ℓ is the current length and ℓ_0 the initial length, is given by

$$\epsilon = \begin{cases} \epsilon_a t/t_{\mathrm{R1}}, & 0 \le t \le t_{\mathrm{R1}} \\ \epsilon_a, & t_{\mathrm{R1}} < t \le t_{\mathrm{R2}} \end{cases} \tag{5.22}$$

where $\epsilon_a = 1 \times 10^{-7}$, $t_{\mathrm{R1}} = 10^{-3}$s, $t_{\mathrm{R2}} = 150$s for Se, $\epsilon_a = 5 \times 10^{-8}$, $t_{\mathrm{R1}} = 10^{-14}$s, $t_{\mathrm{R2}} = 500$s for $CsHSO_4$ and $\epsilon_a = 1 \times 10^{-5}$, $t_{\mathrm{R1}} = 10^{-11}$s, $t_{\mathrm{R2}} = 2 \times 10^4$s for Sn.

For an imposed ϵ_a at $t = 0$, and with $n > 1$,

$$\sigma = \frac{E\epsilon_a}{[1 + \alpha(E\epsilon_a)^n(n-1)\epsilon_a^{-1}t]^{1/(n-1)}} = \frac{\sigma_a}{[1 + \alpha\sigma_a^n(n-1)\epsilon_a^{-1}t]^{1/(n-1)}} \tag{5.23}$$

Note that with $n > 1$, $\sigma_a^n/\epsilon_a = (E\epsilon_a)^n/\epsilon_a = 0$ for $\epsilon_a = 0$. Also, in both Eqs. (5.21) and (5.23), the response is governed by $\alpha \times (\text{stress quantity})^n$.

A significant difference between the indentation depth versus time response in Eq. (5.18) and the uniaxial creep responses in Eqs. (5.21) and (5.23) is that $h_{\mathrm{crp}}/h_{\mathrm{ela}}$ is independent of the load magnitude (i.e. h_{crp} and h_{ela} have the same dependence on applied load) whereas the uniaxial creep responses strongly depend on the applied load magnitude.

5.6.1 Bayesian identification

For the three "experimental" materials in Table 5.1, the set of values n, σ_0 and $\dot{\epsilon}_0$ with the largest posterior probability is identified as the set of parameter values characterizing the creep response of the "experimental" material. The value of the pre-exponential factor α is then calculated using Eq. (5.6.

Once the initial database is constructed, the computations for the interpolation and for the statistical analysis are very light and are quickly carried out on a personal computer [140]:

5.6.1.1 Noise-free data

For each database, the posterior probability distribution is calculated from: (i) indentation depth versus time data (HT); (ii) residual surface profile data (S); (iii) both indentation depth versus time data and residual surface profile data (HTS). The values of n, σ_0 and $\dot{\epsilon}_0$ associated with the largest posterior probability value obtained from (i), (ii), (iii) and the responses based on these values are denoted by HT,S, HTS, respectively.

For Se, the predicted values of n, σ_0, $\dot{\epsilon}_0$ and therefore α using any of the three sets of data (HT, S and HTS) coincide. Fig. 5.4 shows the indentation responses (dashed lines and labeled "all cases") obtained using these predicted parameter values. For comparison, the indentation responses using the input properties of Se in Table 5.1 (solid lines) are also shown. The indentation responses of "all cases" are nearly indistinguishable from the "experimental" indentation responses.

The predicted parameter values n, σ_0, $\dot{\epsilon}_0$, α and associated largest posterior probability values p_1 using three types of data based on the noise-free "experimental" indentation responses of Se in Fig. 5.2 are given in Table 5.2. The predicted parameter values of n and α are the same for all three cases and are close to the input values but a direct comparison of the values of α is not meaningful unless the values of n coincide since the units of α vary with n.

Table 5.2: Predicted values of n, σ_0, $\dot{\epsilon}_0$, α and the associated largest value of posterior probability p_1 for Se obtained based on noise-free "experimental" indentation responses. The predicted values obtained using the indentation depth versus time data (HT), using the residual surface profile data (S) and using both the indentation depth versus time data and the residual surface profile data (HTS) all coincide and are denoted by "all cases."

	n	σ_0(MPa)	$\dot{\epsilon}_0(\mathrm{s}^{-1})$	$\alpha(\mathrm{Pa}^{-\mathrm{n}}\mathrm{s}^{-1})$	p_1
all cases	1.16	8.648	1.0×10^{-4}	0.898×10^{-12}	1.00

The uniaxial creep responses obtained from a one-element finite element uniaxial solution with the loading given by Eq. (5.20) for the "all cases" parameter values in Table 5.2 are shown in Fig. 5.5(a). The corresponding stress relaxation responses using Eq. (5.22) are shown in Fig. 5.5(b).

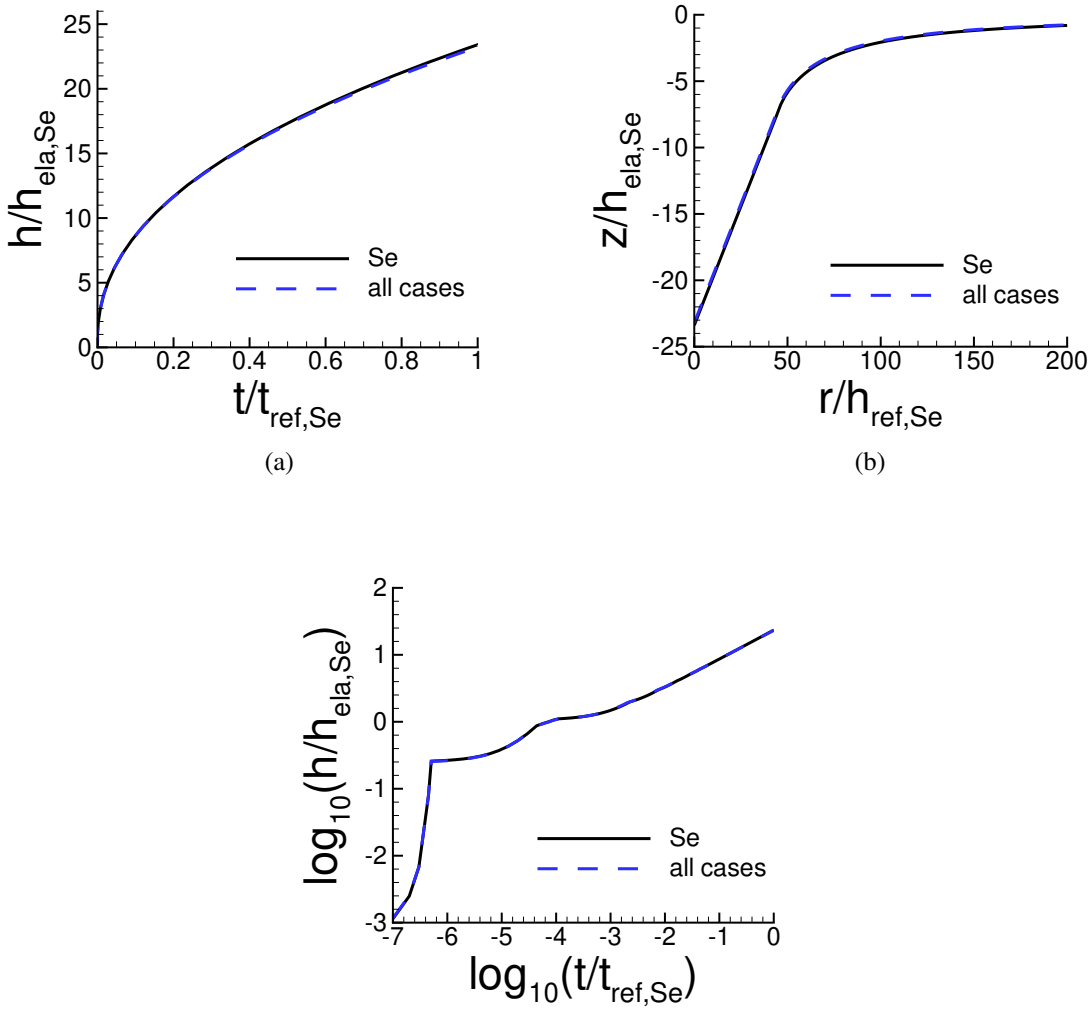

Figure 5.4: Comparison of predicted and "experimental" indentation responses for Se. The indentation responses with the largest value of posterior probability for the indentation depth versus time data (HT), for the residual surface profile data (S) and for both the indentation depth versus time data and the residual surface profile data (HTS) coincide and are denoted by "all cases." The associated values of n, σ_0, $\dot{\epsilon}_0$ and α are given in Table 5.2. (a) Normalized indentation depth $h/h_{\mathrm{ela,Se}}$ versus normalized time $t/t_{\mathrm{ref,Se}}$ where $t_{\mathrm{ref,Se}} = 1/\dot{\epsilon}_{0,\mathrm{Se}}$. (b) Normalized surface profiles, $z/h_{\mathrm{ela,Se}}$ versus $r/h_{\mathrm{ela,Se}}$, near the indenter after unloading. (c) $\log_{10}$-$\log_{10}$ plot of (a). On the scales in this figure, the "all cases" predictions are indistinguishable from the corresponding "experimental" responses.

In both figures, the predicted responses compare well with those obtained using the input material parameter values for Se in Table 5.1.

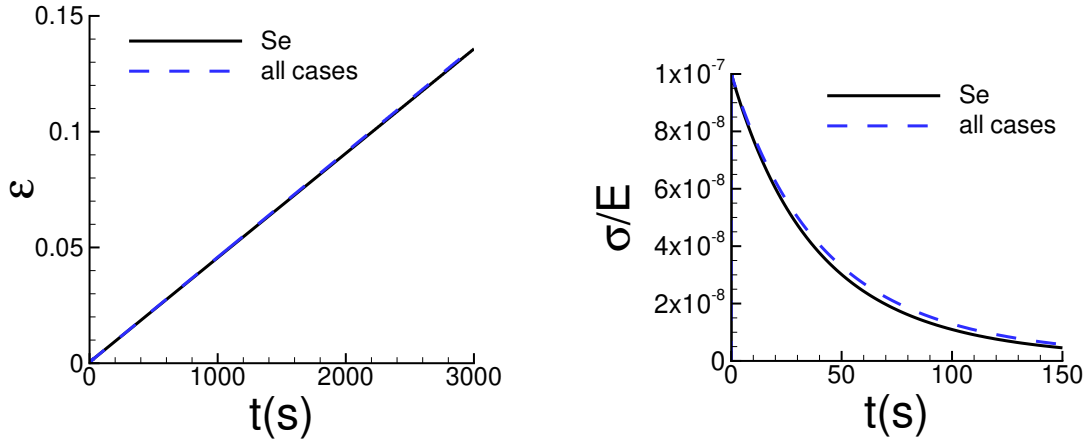

(a) (b)

Figure 5.5: Comparison of the predicted uniaxial creep and relaxation responses using the "all cases" parameter values in Table 5.2 with the corresponding "experimental" responses for Se. (a) Uniaxial logarithmic strain, ϵ, versus time, t. (b) Normalized uniaxial Cauchy stress, σ/E, versus time, t. On the scales in (a), the "all cases" prediction is indistinguishable from the corresponding "experimental" response.

Fig. 5.6 shows the indentation responses calculated using the creep properties for $CsHSO_4$ with the largest value of posterior probability p_1 compared with the "experimental" indentation responses. As seen in Fig. 5.6(a), for $CsHSO_4$, the representation of the indentation depth versus time response is improved by considering surface profile data. However, the improvement is small and is negligible for the $\log_{10} - \log_{10}$ plot in Fig. 5.6(c).

Table 5.3 shows the predicted parameter values for $CsHSO_4$ and the value of the associated largest posterior probability obtained from the Bayesian analysis and Fig. 5.7 shows the comparison between the uniaxial creep and uniaxial relaxation responses using the predicted creep parameter values in Table 5.3, for $CsHSO_4$ and the "experimental" responses. For $CsHSO_4$, neither the parameter values based on fitting the indentation depth versus time response (HT) nor the residual surface profile (S) gives a particularly good fit to the uniaxial creep and stress relaxation responses but when both sets of data are used (HTS) an excellent fit is obtained. We note that the the predicted values of reference strain rate for the HTS fit is a factor of 100 times the input value of

$\dot{\epsilon}_0 = 1\text{s}^{-1}$. Nevertheless, the predicted values of n and α are very close to the input "experimental" values.

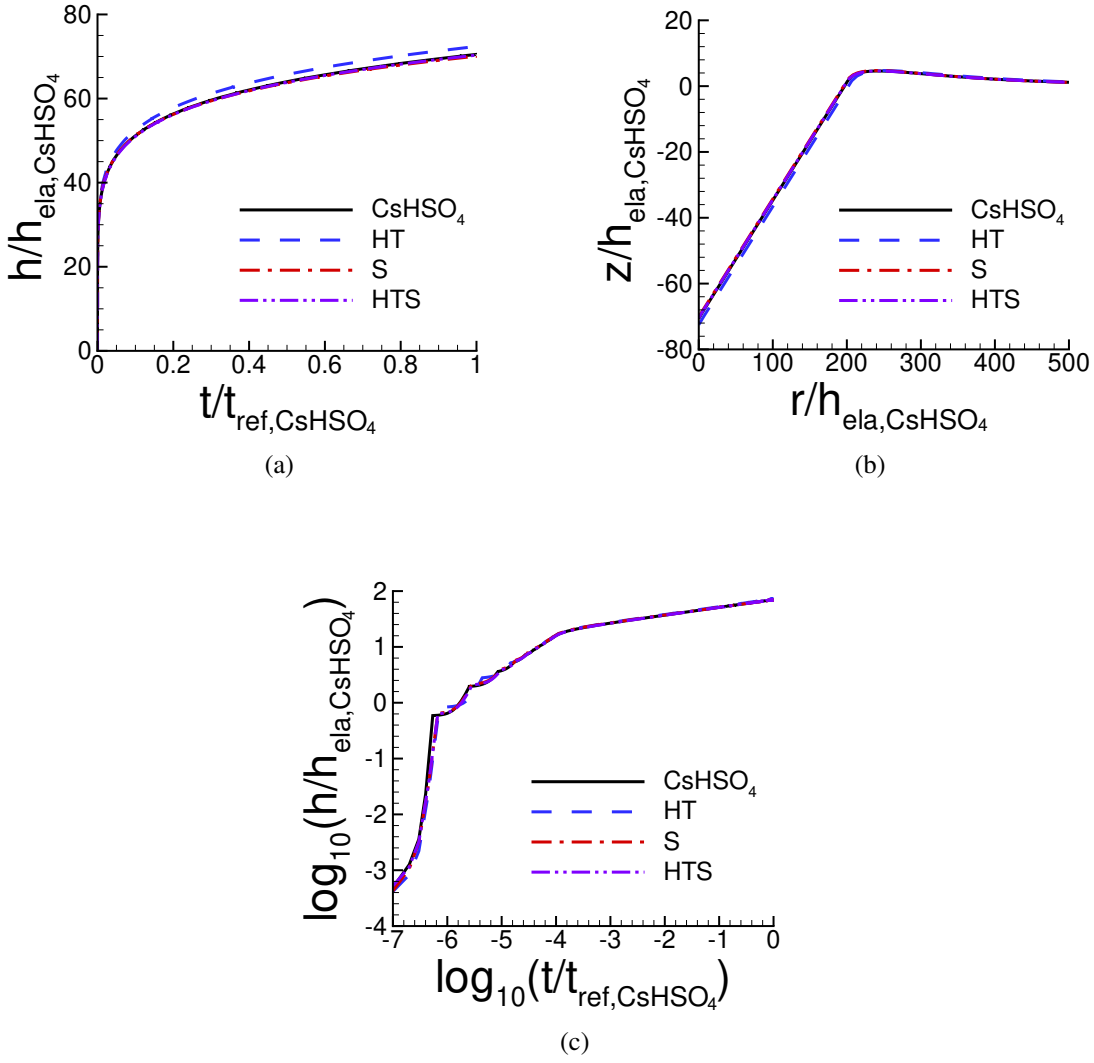

Figure 5.6: Comparison of predicted and "experimental" indentation responses for $CsHSO_4$. The indentation responses are those corresponding to the largest value of posterior probability for the indentation depth versus time data (HT), for the residual surface profile data (S) and for both the indentation depth versus time data and the residual surface profile data (HTS). The associated values of n, σ_0, $\dot{\epsilon}_0$ and α are given in Table 5.3. (a) Normalized indentation depth $h/h_{\text{ela,CsHSO}_4}$ versus normalized time $t/t_{\text{ref,CsHSO}_4}$ where $t_{\text{ref,CsHSO}_4} = 1/\dot{\epsilon}_{0,\text{CsHSO}_4}$. (b) Normalized surface profiles, $z/h_{\text{ela,CsHSO}_4}$ versus $r/h_{\text{ela,CsHSO}_4}$, near the indenter after unloading. (c) $\log_{10}$-$\log_{10}$ plot of (a). On the scales in this figure, the predictions with S and HTS data are indistinguishable from the corresponding "experimental" responses.

Table 5.3: Predicted values of n, σ_0, $\dot{\epsilon}_0$, α and the associated largest value of posterior probability p_1 for $CsHSO_4$ obtained based on noise-free "experimental" indentation responses. See the caption of Fig. 5.6 for the meanings of HT, S and HTS.

	n	σ_0(MPa)	$\dot{\epsilon}_0(\mathrm{s}^{-1})$	$\alpha(\mathrm{Pa}^{-\mathrm{n}}\mathrm{s}^{-1})$	p_1
HT	3.58	0.0312	15.8	12.9×10^{-16}	1.00
S	3.66	0.0528	100	5.19×10^{-16}	0.59
HTS	3.58	0.0552	100	10.6×10^{-16}	1.00

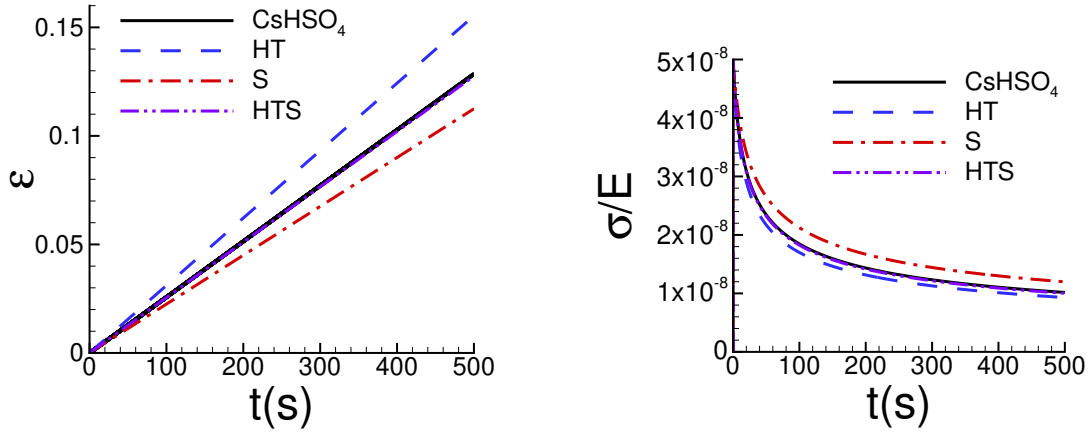

Figure 5.7: Comparison of the predicted uniaxial creep and relaxation responses using the parameter values in Table 5.3 with the corresponding "experimental" responses for $CsHSO_4$. See the caption of Fig. 5.6 for the meanings of HT, S and HTS. (a) Uniaxial logarithmic strain, ϵ, versus time, t. (b) Normalized uniaxial Cauchy stress, σ/E, versus time, t. On the scales in this figure, the predictions with HTS data are indistinguishable from the corresponding "experimental" responses.

Fig. 5.8 shows the indentation responses calculated using the creep parameter values for Sn that have the largest value of posterior probability p_1. As for $CsHSO_4$, the prediction of the indentation response of the "experimental" material is slightly improved by considering surface profile data, Fig. 5.8(a). For Sn, the creep parameter values in Table 5.4 obtained using only surface profile data (S) and those obtained using both indentation depth versus time data and surface profile data

(HTS) are identical. The HTS (or S) predicted value of $\dot{\epsilon}_0$ is a factor of 10 times the "experimental" input value of $\dot{\epsilon}_0$ for Sn in Table 5.1.

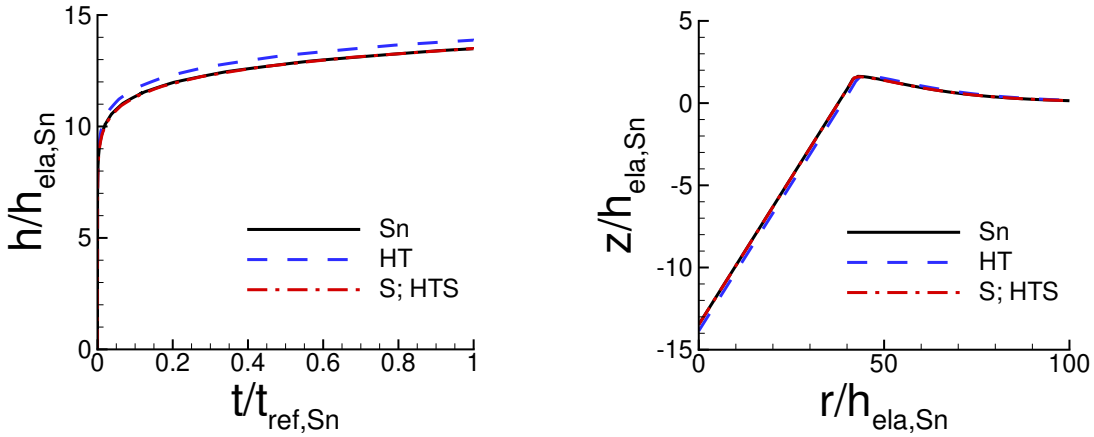

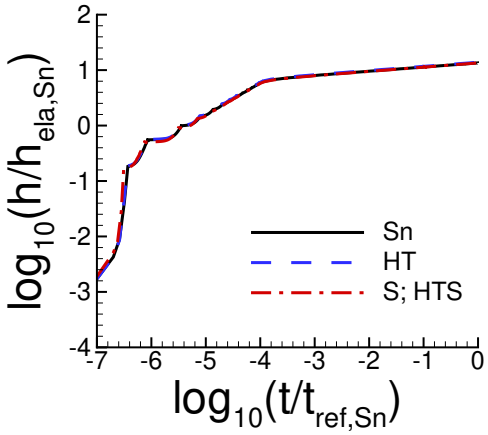

Figure 5.8: Comparison of predicted and "experimental" indentation responses for Sn. See the caption of Fig. 5.6 for the meanings of HT, S and HTS. The associated values of n, σ_0, $\dot{\epsilon}_0$ and α are given in Table 5.4. (a) Normalized indentation depth $h/h_{\mathrm{ela,Sn}}$ versus normalized time $t/t_{\mathrm{ref,Sn}}$ where $t_{\mathrm{ref,Sn}} = 1/\dot{\epsilon}_{0,\mathrm{Sn}}$. (b) Normalized surface profiles, $z/h_{\mathrm{ela,Sn}}$ versus $r/h_{\mathrm{ela,Sn}}$, near the indenter after unloading. (c) $\log_{10}$-$\log_{10}$ plot of (a). On the scales in (a) and (b), the predictions with S; HTS data are indistinguishable from the corresponding "experimental" responses. In (c) all three responses are indistinguishable.

Table 5.4: Predicted values of n, σ_0, $\dot{\epsilon}_0$, α and the associated largest value of posterior probability p_1 for Sn obtained based on noise-free "experimental" indentation responses. See the caption of Fig. 5.6 for the meanings of HT, S and HTS.

	n	σ_0(MPa)	$\dot{\epsilon}_0(\mathrm{s}^{-1})$	$\alpha(\mathrm{Pa}^{-\mathrm{n}}\mathrm{s}^{-1})$	p_1
HT	6.64	10.80	3.98	7.91×10^{-47}	0.85
S	6.46	13.50	10	86.7×10^{-47}	1.00
HTS	6.46	13.50	10	86.7×10^{-47}	1.00

Fig. 5.9 shows the uniaxial creep responses and uniaxial relaxation responses predicted for Sn using the creep parameter values in Table 5.4 compared with the corresponding "experimental" responses. Neither of the predicted responses for Sn in Fig. 5.9(a) provides a particularly good representation of the "experimental" uniaxial creep response, although the inclusion of surface profile data does improve the prediction. On the other hand, both the HT and S; HTS relaxation responses in Fig. 5.9(b) do provide a fairly good approximation of the "experimental" response. Interestingly, the HT response in Fig. 5.9(b) is actually slightly closer to the "experimental" response than is the S; HTS response. Indentation creep responses are often represented using $\log_{10} - \log_{10}$ plots so that it is worth noting that although the predicted and experimental indentation responses in Fig. 5.8(c) are indistinguishable on a $\log_{10} - \log_{10}$ scale, the uniaxial creep responses in Fig. 5.9(a) differ significantly.

For all three materials, predictions with a posterior probability $p_1 = 1.00$, have power-law creep parameters that differ from those of the corresponding "experimental" material. This is because the "experimental" input parameters are not in the coarse database. Even if the "experimental" input parameters are in the interpolated database, interpolation errors can preclude those material parameters giving the largest value of posterior probability. For $CsHSO_4$ and Sn, the predictions using both the indentation depth versus time data and the residual surface profile data (HTS) provide the best fit to the "experimental" responses, while for Se ($n \approx 1$), any of the three considered data sets, HT, S and HTS, gives an identical prediction and have a posterior probability $p_1 = 1.00$.

The indentation responses for $CsHSO_4$ and Sn obtained using the values of the HTS material parameters give a very good fit to the "experimental" indentation responses with a posterior prob-

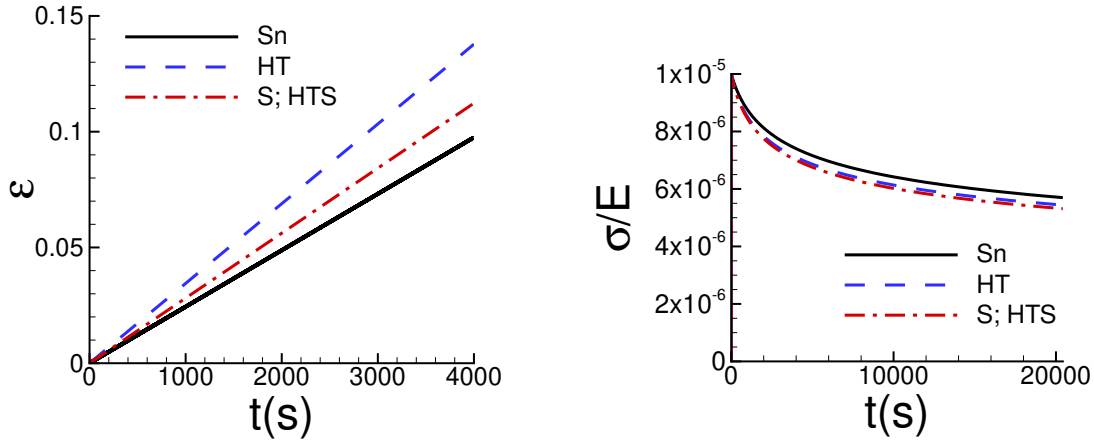

(a) (b)

Figure 5.9: Comparison of the predicted uniaxial creep and relaxation responses using the parameter values in Table 5.4 with the corresponding "experimental" responses for Sn. See the caption of Fig. 5.6 for the meanings of HT, S and HTS. (a) Uniaxial logarithmic strain, ϵ, versus time, t. (b) Normalized uniaxial Cauchy stress, σ/E, versus time, t.

ability $p_1 = 1.00$ even though the predicted values of $\dot{\epsilon}_0$ are very different from the input values. This shows that for constant load and hold indentation creep, different power-law creep parameters can have very similar indentation responses.

5.6.1.2 Noise-contaminated data

With the noise-free "experimental" responses denoted by $\boldsymbol{s}^{\text{input}}$ and $\boldsymbol{h}^{\text{input}}$, the noise-contaminated data is obtained by superposing Gaussian noise on the noise-free data by

$$\boldsymbol{s}^{\text{m}} = \boldsymbol{s}^{\text{input}} + \boldsymbol{s}^{\text{noise}} \ , \ \boldsymbol{h}^{\text{m}} = \boldsymbol{h}^{\text{input}} + \boldsymbol{h}^{\text{noise}} \tag{5.24}$$

The noise is added to each indentation response, $\boldsymbol{s}^{\text{noise}}$ and $\boldsymbol{h}^{\text{noise}}$, via a call to the MATLAB [109] function normrnd(0,ξ,[1,K]), where 0 is the mean value, $\xi = \xi_{\text{h}}$ or ξ_{s} is the standard deviation and $K = K_{\text{h}}$ or K_{s} is the length of a $1 \times K$ vector of random values with the specified mean and standard deviation. Each call to normrnd provides a different vector of random values.

The standard deviation ξ_{s} is related to a reference length s_{ref} with noise amplitude η_{s} and the

standard deviation $\xi_{\rm h}$ is related to the maximum indentation depth with noise amplitude $\eta_{\rm h}$ via

$$\xi_{\rm s} = \eta_{\rm s} s_{\rm ref} \ , \ \xi_{\rm h} = \eta_{\rm h} \max(h_k^{\rm m}) \tag{5.25}$$

with $k = 1, 2, ..., K_{\rm h}$, $\eta_{\rm s} \geq 0$ and $\eta_{\rm h} \geq 0$. The reference length $s_{\rm ref}$ is taken to be the indentation depth of the noise-free surface profile after unloading.

Fig. 6.4 shows examples of noise-contaminated indentation responses with values of the noise amplitudes $\eta_{\rm h} = 0.01$, $\eta_{\rm h} = 0.10$ and with $\eta_{\rm s} = 0.01$, $\eta_{\rm s} = 0.10$. The effect of noise on the prediction of the power-law creep parameters, we consider two noise levels: (i) a low noise level $\eta_{\rm h} = \eta_{\rm s} = 0.01$; and (ii) a high noise level $\eta_{\rm h} = \eta_{\rm s} = 0.10$.

As in Ref. [2], calculations of the posterior probability distribution are carried out for 100 realizations with the same values of the noise amplitudes $\eta_{\rm h}$ and $\eta_{\rm s}$. For each of the 100 realizations, the values of n, σ_0 and $\dot{\epsilon}_0$ having the largest posterior probability p_1 are determined. The arithmetic averages of these values are taken as the predicted power law creep parameter values associated with the specified noise amplitudes and the value of α is calculated from the resulting averaged values of n, σ_0 and $\dot{\epsilon}_0$. We note that no additional finite element calculations are required to determine these averaged values.

Fig. 5.11 shows the indentation responses predicted using noise-contaminated HTS data for Se compared with the corresponding noise-free "experimental" responses. The responses for a low noise level ($\eta_{\rm h} = \eta_{\rm s} = 0.01$) are indistinguishable from the experimental responses while those for a high noise level ($\eta_{\rm h} = \eta_{\rm s} = 0.10$) still provide a good representation.

The material parameters and associated posterior probability obtained based on indentation depth versus time data (HT), residual surface profile data (S) and on both indentation depth versus time data and residual surface profile data (HTS) are given in Table 5.5. In contrast to the noise-free case where the HT, S and HTS predictions coincided, the predictions based on different indentation data differ for noise-contaminated data. With a low noise level (subscript 0.01), the values of n and α obtained using HT data are closest to the "experimental" values in Table 5.1 even though the

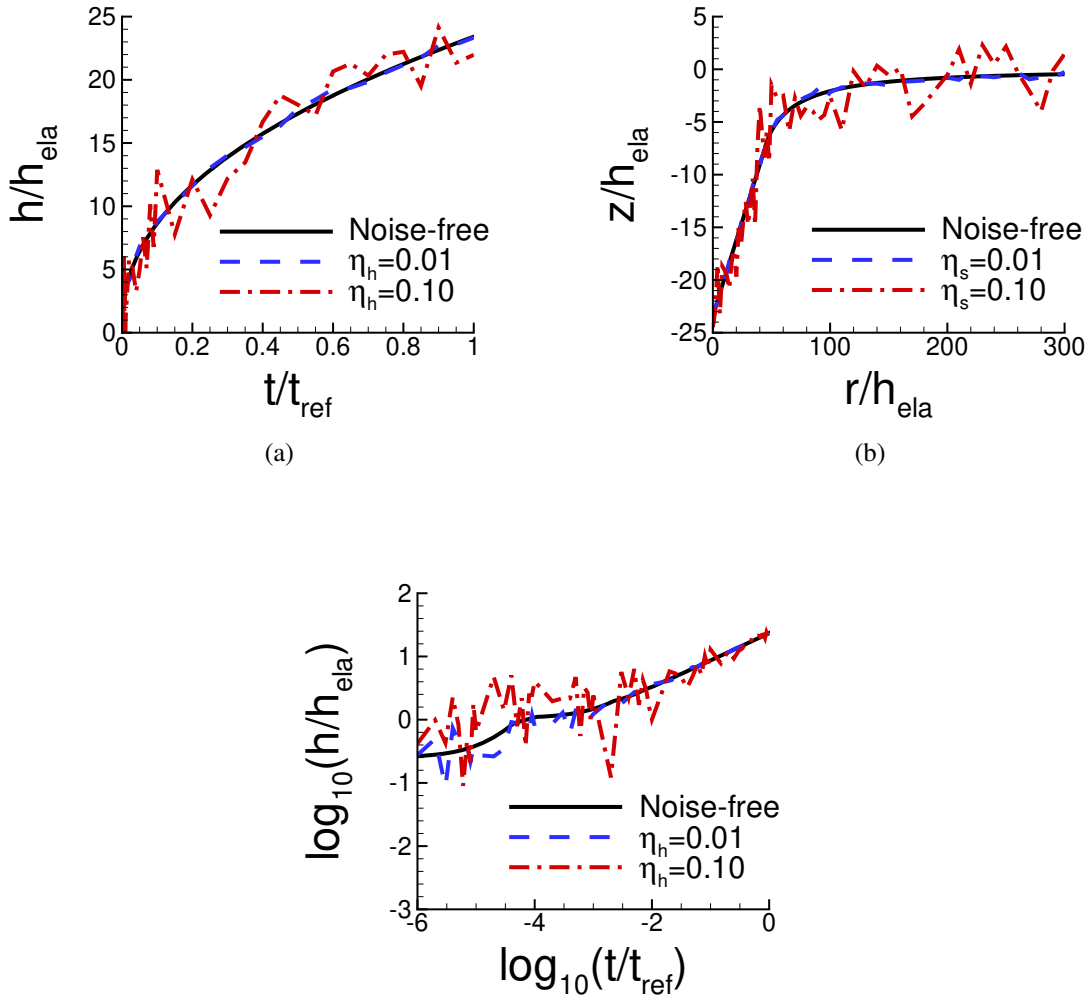

Figure 5.10: Illustration of realizations of noise-contaminated indentation data with noise amplitudes $\eta_{\rm h} = 0.01$, $\eta_{\rm s} = 0.01$, $\eta_{\rm h} = 0.10$ and $\eta_{\rm s} = 0.10$ superposed on the indentation data for Se. (a) Normalized indentation depth $h/h_{\rm ela}$ versus normalized time $t/t_{\rm ref}$. (b) Surface profiles near the indenter after unloading. (c) $\log_{10}$-$\log_{10}$ plot of (a).

posterior probability value is the smallest. On the other hand, the $\mathrm{HT}_{0.01}$ value of $\dot{\epsilon}_0$ is 60% of the input value. The posterior probability is significantly increased when surface profile data is used in the identification analysis, increasing to $p_1 = 0.93$ for the HTS based creep parameters. The values predicted for data with a high noise level (subscript 0.10) have much larger differences from the input values and have very low values of p_1, indicating a lack of confidence in them. Although

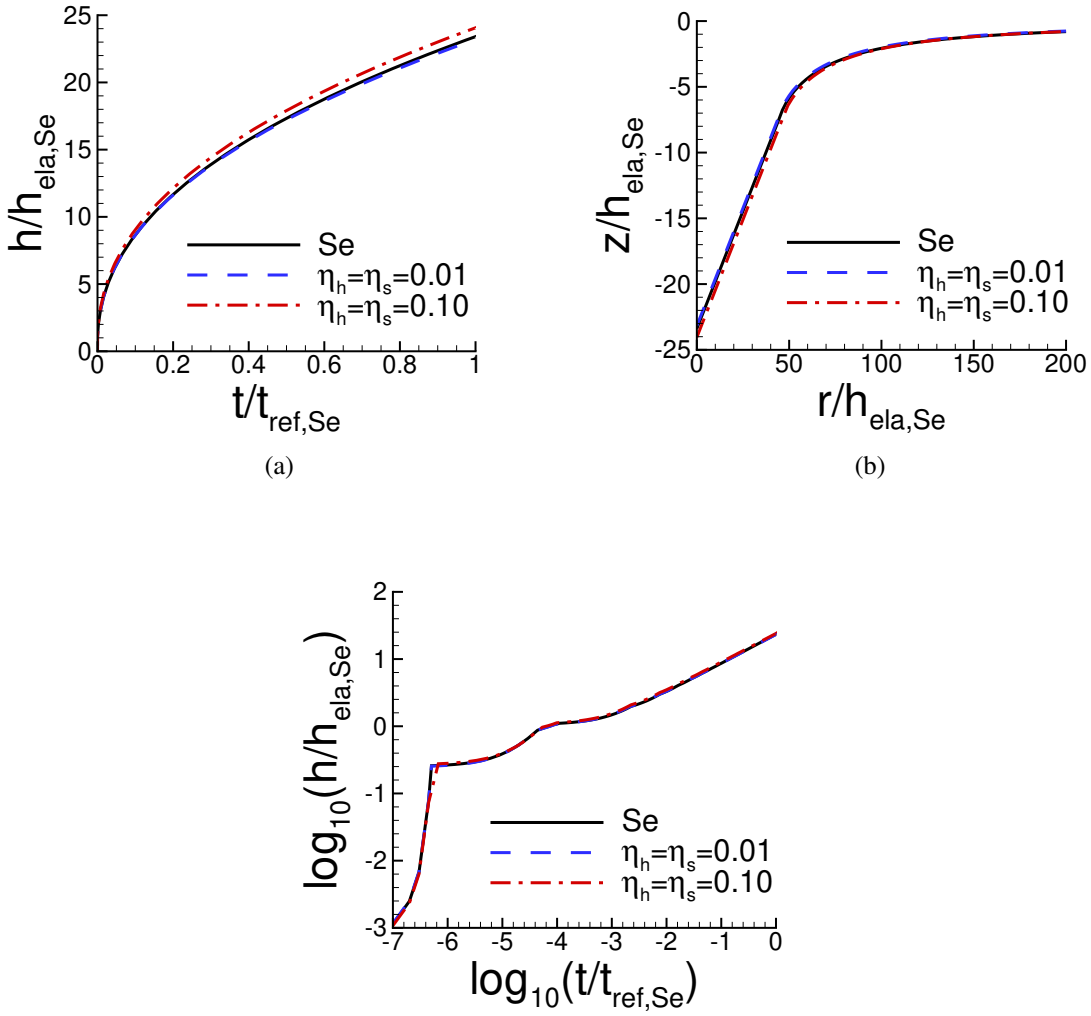

Figure 5.11: Comparison of predicted and "experimental" indentation responses for Se. The associated values of n, σ_0, $\dot{\epsilon}_0$ and α are obtained from noise-contaminated HTS data (averaged over 100 realizations) and given in Table 5.5. (a) Normalized indentation depth $h/h_{\rm ela,Se}$ versus normalized time $t/t_{\rm ref,Se}$. (b) Surface profiles near the indenter after unloading. (c) $\log_{10}$-$\log_{10}$ plot of (a). On the scales in this figure, the predictions with $\eta_{\rm h} = \eta_{\rm s} = 0.01$ are indistinguishable from the corresponding "experimental" responses.

the value of p_1 for the $\text{HTS}_{0.10}$ set of parameter values is low, it is much larger than those for the $\text{HT}_{0.10}$ and $\text{S}_{0.10}$ predictions.

The predicted uniaxial creep and relaxation responses for Se obtained from one-element finite

Table 5.5: Predicted values of n, σ_0, $\dot{\epsilon}_0$, α and the associated averaged largest posterior probability p_1 for Se obtained from averaging the predicted values over 100 realizations with $\eta_s = \eta_h = 0.01$ (subscript 0.01) and with $\eta_s = \eta_h = 0.10$ (subscript 0.10). See the caption of Fig. 5.6 for the meanings of HT, S and HTS.

	n	σ_0(MPa)	$\dot{\epsilon}_0(\mathrm{s}^{-1})$	$\alpha(\mathrm{Pa}^{-\mathrm{n}}\mathrm{s}^{-1})$	p_1
$\mathrm{HT}_{0.01}$	1.15	5.38	0.6×10^{-4}	1.09×10^{-12}	0.31
$\mathrm{S}_{0.01}$	1.16	8.57	1.0×10^{-4}	0.907×10^{-12}	0.78
$\mathrm{HTS}_{0.01}$	1.16	8.67	1.0×10^{-4}	0.895×10^{-12}	0.93
$\mathrm{HT}_{0.10}$	1.15	5.55	0.7×10^{-4}	1.23×10^{-12}	0.0066
$\mathrm{S}_{0.10}$	1.27	6.64	1.2×10^{-4}	0.260×10^{-12}	0.0085
$\mathrm{HTS}_{0.10}$	1.17	7.17	0.9×10^{-4}	0.858×10^{-12}	0.030

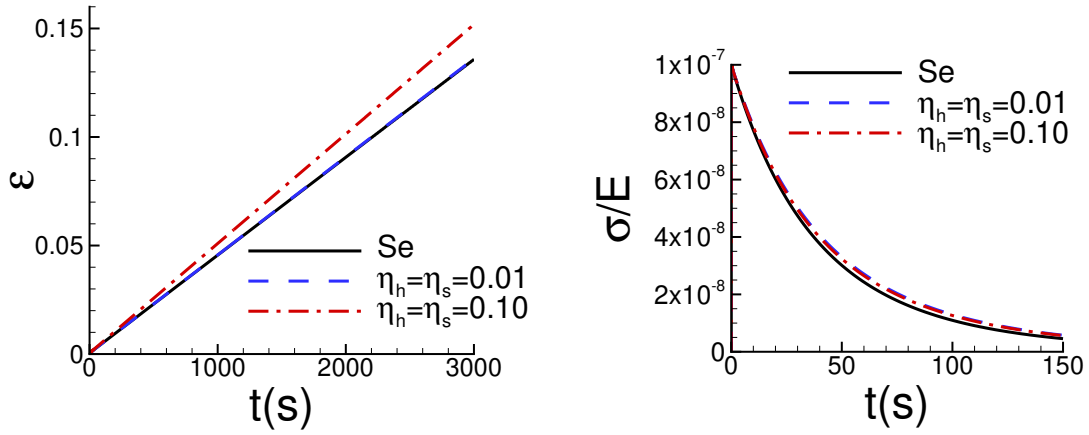

(a) (b)

Figure 5.12: Uniaxial creep and relaxation responses using the averaged predicted parameter values over 100 realizations for Se obtained with noise-contaminated HTS data in Table 5.5. The solid lines show the corresponding "experimental" responses. (a) Uniaxial logarithmic strain, ϵ, versus time t. (b) Normalized uniaxial Cauchy stress, σ/E, versus time, t. On the scales in (a), the prediction with $\eta_h = \eta_s = 0.01$ is indistinguishable from the corresponding "experimental" response. In (b) the prediction with $\eta_h = \eta_s = 0.01$ is indistinguishable from the prediction with $\eta_h = \eta_s = 0.10$.

element calculations (giving homogeneous stress and strain fields) using the creep properties in Table 5.5 are shown in Fig. 5.12. For comparison, the corresponding responses for the "experimental" material are shown. The creep parameters obtained using the low noise $\mathrm{HTS}_{0.01}$ indentation

data provide a good fit to the uniaxial creep and stress relaxation responses. The high noise level $HTS_{0.10}$ data also provides a rather good fit to the stress relaxation data but a much poorer fit to the uniaxial creep data. As will also be seen subsequently, the uniaxial creep response is more sensitive to the values of the creep parameters than is the stress relaxation response.

For $CsHSO_4$, Fig. 5.13 compares the indentation responses predicted using noise-contaminated HTS data and the "experimental" indentation responses. The responses predicted with low noise provide a very good representation of the "experimental" indentation responses while the indentation depth versus time response predicted with the high noise level differs somewhat from the corresponding "experimental" response.

The creep parameters and associated posterior probability values obtained for $CsHSO_4$ from noise-contaminated data are given in Table 5.6. The values of creep exponent n and associated pre-exponential factor α obtained based on $HTS_{0.01}$ are in good agreement with the "experimental" creep parameters in Table 5.1 and the posterior probability is $p_1 = 0.80$. However, the value of $\dot{\epsilon}_0$, as for the prediction based on noise-free data, is 100 times that for the "experimental" material. The values of α obtained using the $HT_{0.01}$ and the $S_{0.01}$ are significantly different from the input value for $CsHSO_4$ in Table 5.1 and the posterior probability values for these predictions are much smaller than p_1 for the $HTS_{0.01}$ prediction. The creep parameters obtained for $CsHSO_4$ from the high noise level data (subscript 0.10) differ substantially from the corresponding values for the "experimental" material and, consistent with this, the posterior probability values are small. Here, as in Fig. 10 of Ref. [46], with increasing noise, the posterior probability distribution is more spread out with similar values of posterior probability for a range of material constitutive parameter values.

Fig. 5.14 shows a comparison between the "experimental" uniaxial creep and stress relaxation responses for $CsHSO_4$ and those predicted based on noise-contaminated HTS data. For both the high noise level, $HTS_{0.10}$, based creep parameters and the low noise, $HTS_{0.01}$, based creep parameters in Table 5.6, there is very good agreement with the "experimental" stress relaxation response in Fig. 5.14(b). On the other hand, the creep response in Fig. 5.14(a) shows a large difference between the uniaxial creep response of the "experimental" material and the prediction based on

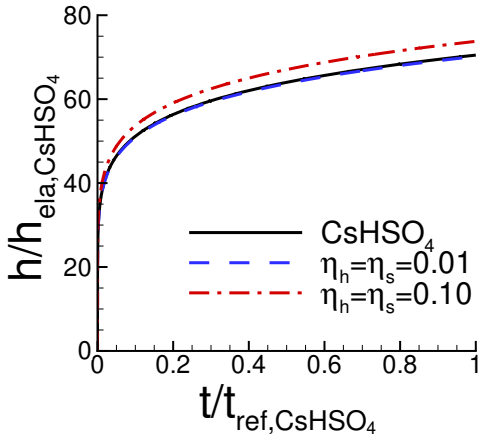

(a)

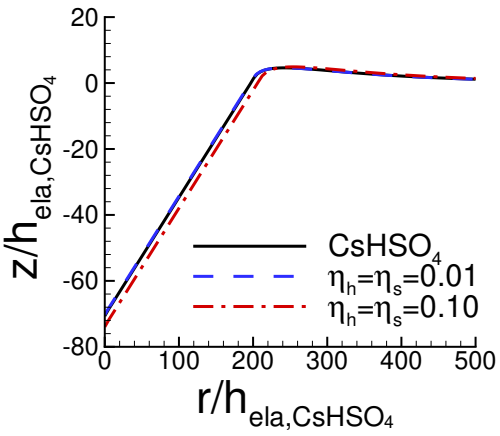

(b)

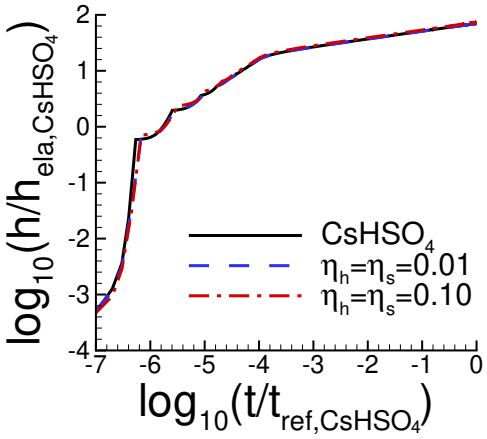

(c)

Figure 5.13: Comparison of predicted and "experimental" indentation responses for $CsHSO_4$. The associated values of n, σ_0, $\dot{\epsilon}_0$ and α are obtained from noise-contaminated HTS data (averaged over 100 realizations) and given in Table 5.6. (a) Normalized indentation depth $h/h_{\mathrm{ela,CsHSO_4}}$ versus normalized time $t/t_{\mathrm{ref,CsHSO_4}}$. (b) Surface profiles near the indenter after unloading. (c) $\log_{10}$-$\log_{10}$ plot of (a). On the scales in (a) and (b), the predictions with $\eta_{\mathrm{h}} = \eta_{\mathrm{s}} = 0.01$ are indistinguishable from the corresponding "experimental" responses. In (c) all three responses are indistinguishable.

the $\mathrm{HTS}_{0.10}$ data.

The comparison of "experimental" and noise-contaminated HTS data predicted indentation responses for Sn in Fig. 5.15 shows a noticeable difference even for a low noise ($\eta_{\mathrm{s}} = \eta_{\mathrm{h}} = 0.01$)

Table 5.6: Predicted values of n, σ_0, $\dot{\epsilon}_0$, α and the associated averaged largest posterior probability p_1 for $CsHSO_4$ obtained from averaging the predicted values over 100 realizations with $\eta_s = \eta_h = 0.01$ (subscript 0.01) and with $\eta_s = \eta_h = 0.10$ (subscript 0.10). See the caption of Fig. 5.6 for the meanings of HT, S and HTS.

	n	σ_0(MPa)	$\dot{\epsilon}_0(s^{-1})$	$\alpha(Pa^{-n}s^{-1})$	p_1
$HT_{0.01}$	3.59	0.0402	51.1	15.1×10^{-16}	0.20
$S_{0.01}$	3.68	0.0502	87.3	4.39×10^{-16}	0.25
$HTS_{0.01}$	3.59	0.0551	100	9.53×10^{-16}	0.80
$HT_{0.10}$	3.60	0.0362	44.6	17.3×10^{-16}	0.0025
$S_{0.10}$	4.56	0.0316	45.5	0.00138×10^{-16}	0.0013
$HTS_{0.10}$	3.62	0.0432	63.8	10.6×10^{-16}	0.0080

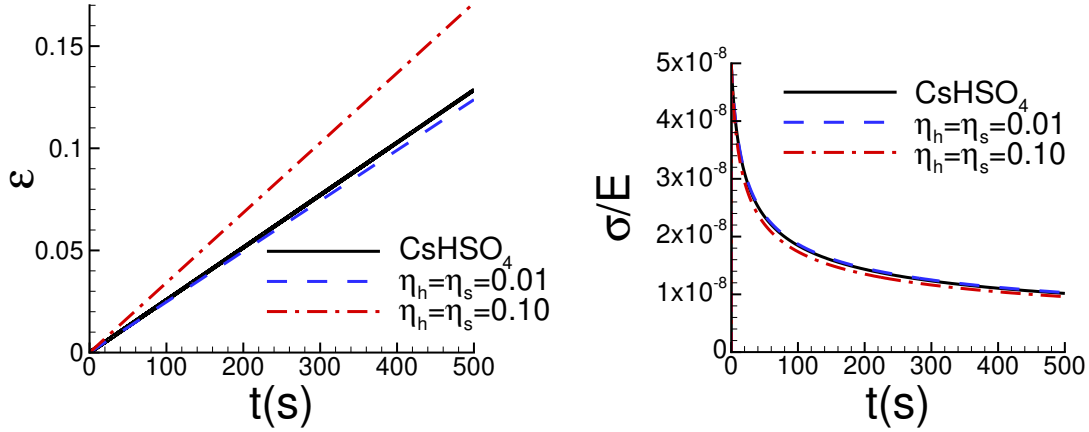

(a) (b)

Figure 5.14: Uniaxial creep and relaxation responses using the averaged predicted parameter values over 100 realizations for $CsHSO_4$ obtained with noise-contaminated HTS data in Table 5.6. The solid lines show the corresponding "experimental" responses. (a) Uniaxial logarithmic strain, ϵ, versus time t. (b) Normalized uniaxial Cauchy stress, σ/E, versus time, t. On the scales in (b), the prediction with $\eta_h = \eta_s = 0.01$ is indistinguishable from the corresponding "experimental" response.

level. The HTS based creep parameters are given in Table 5.7 along with the associated posterior probability value. The predicted values of the pre-exponential factor α all differ substantially from the input value for Sn in Table 5.1 except for the value based on $S_{0.01}$ and the largest value of

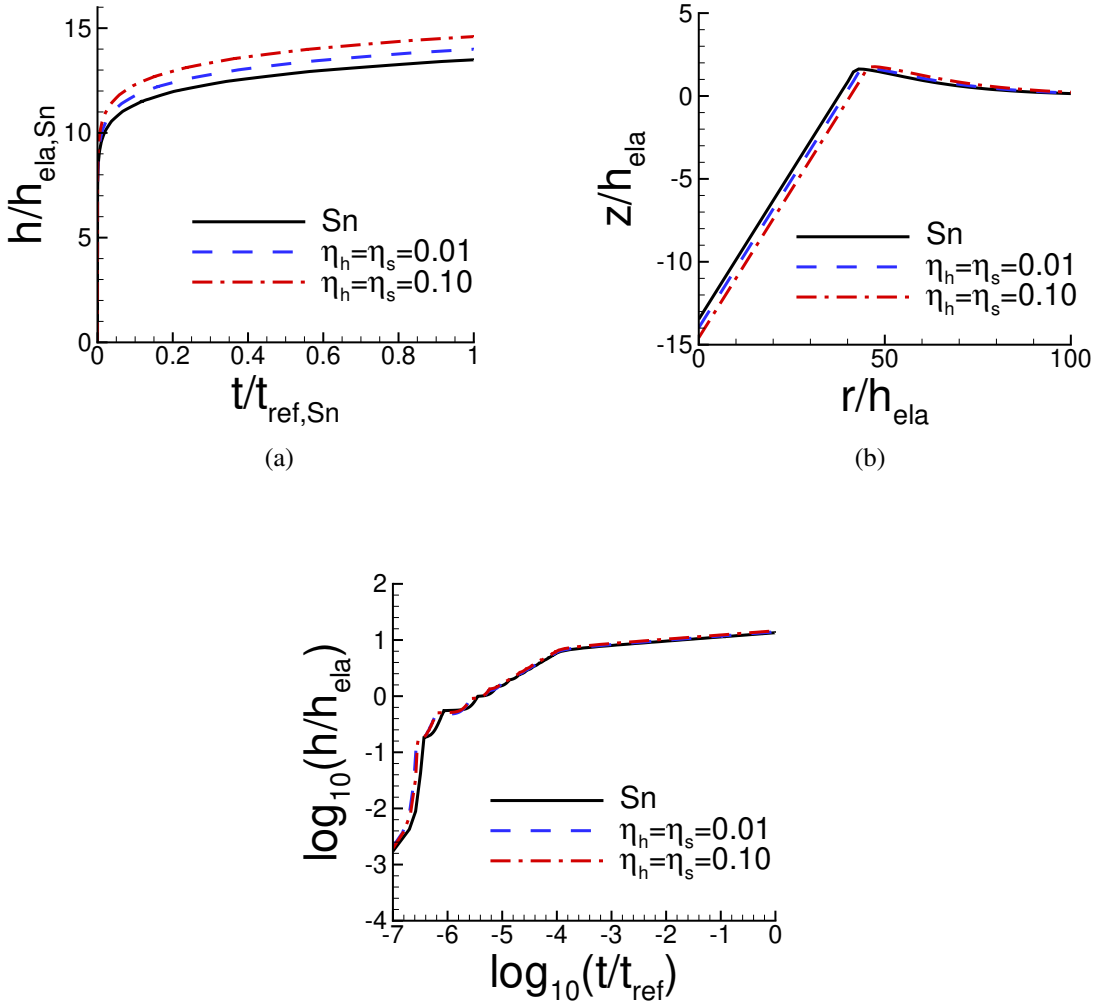

Figure 5.15: Comparison of predicted and "experimental" indentation responses for Sn. The associated values of n, σ_0, $\dot{\epsilon}_0$ and α are obtained from noise-contaminated HTS data (averaged over 100 realizations) and given in Table 5.7. (a) Normalized indentation depth $h/h_{\mathrm{ela,Sn}}$ versus normalized time $t/t_{\mathrm{ref,Sn}}$. (b) Surface profiles near the indenter after unloading. (c) $\log_{10}$-$\log_{10}$ plot of (a). On the scales in (c), all three responses are essentially indistinguishable.

posterior probability is only $p_1 = 0.38$ for $\mathrm{HTS}_{0.01}$. In contrast to the results for Se in Table 5.5 and for $CsHSO_4$ in Table 5.6, the predicted value of α based on $\mathrm{HTS}_{0.01}$ data differs from the input value of Sn in Table 5.1.

The noise-contaminated uniaxial creep and stress relaxation predictions for Sn in Fig. 5.16

Table 5.7: Predicted values of n, σ_0, $\dot{\epsilon}_0$, α and the associated averaged largest posterior probability p_1 for Sn obtained from averaging the predicted values over 100 realizations with $\eta_s = \eta_h = 0.01$ (subscript 0.01) and with $\eta_s = \eta_h = 0.10$ (subscript 0.10). See the caption of Fig. 5.6 for the meanings of HT, S and HTS.

	n	σ_0(MPa)	$\dot{\epsilon}_0(\mathrm{s}^{-1})$	$\alpha(\mathrm{Pa}^{-\mathrm{n}}\mathrm{s}^{-1})$	p_1
$\mathrm{HT}_{0.01}$	6.61	12.20	24.2	34.9×10^{-47}	0.11
$\mathrm{S}_{0.01}$	6.64	14.39	39.3	11.6×10^{-47}	0.19
$\mathrm{HTS}_{0.01}$	6.59	15.54	47.1	19.1×10^{-47}	0.38
$\mathrm{HT}_{0.10}$	6.54	11.92	25.5	134×10^{-47}	0.0016
$\mathrm{S}_{0.10}$	6.25	15.50	40.4	4643×10^{-47}	0.0013
$\mathrm{HTS}_{0.10}$	6.63	13.43	33.1	18.2×10^{-47}	0.0048

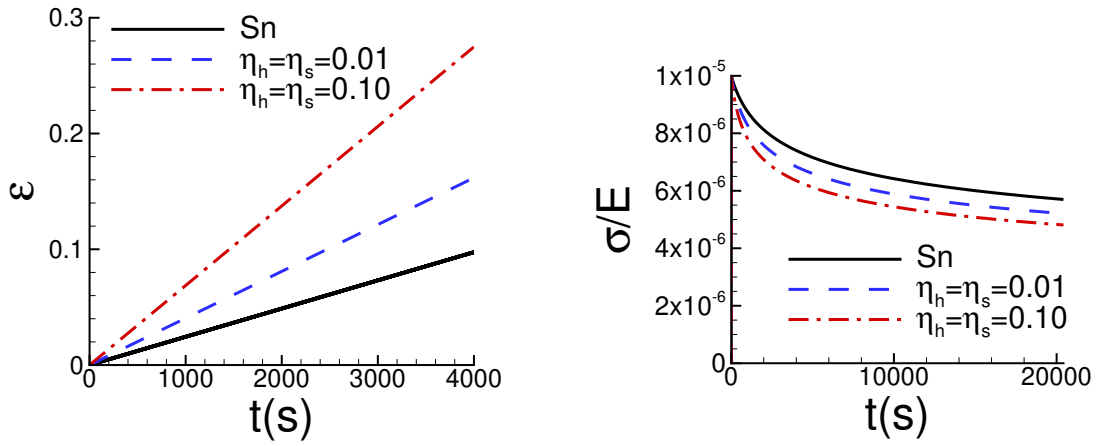

(a) (b)

Figure 5.16: Uniaxial creep and relaxation responses using the averaged predicted parameter values over 100 realizations for Sn obtained with noise-contaminated HTS data in Table 5.7. The solid lines show the corresponding "experimental" responses. (a) Uniaxial logarithmic strain, ϵ, versus time t. (b) Normalized uniaxial Cauchy stress, σ/E, versus time, t.

show a significant deviation from the corresponding responses of the "experimental" material. In particular, in Fig. 5.16(a), the creep responses predicted based on both the $\mathrm{HTS}_{0.01}$ data and the $\mathrm{HTS}_{0.10}$ data are very different from the responses of the "experimental" material.

For all three materials, values of n and α were calculated using a different 100 realizations. The $\mathrm{HTS}_{0.01}$ predicted values of n were the same to three significant figures and the values of α

differed by 1 in the third significant figure.

The results here show an increasing sensitivity to noise with increasing creep stress exponent n, with relatively little sensitivity for Se ($n = 1.15$), more sensitivity for $CsHSO_4$ ($n = 3.59$) and the most noise sensitivity for Sn ($n = 6.60$).

5.6.2 Comparison with analytical models

The aim of the analytical power-law creep models is to provide explicit expressions for relating measured indentation responses to the constitutive parameters n and α in Eq. (5.6). The first step is to identify the power-law creep regime of the $h/h_{\rm ela}$ versus time t responses. The steady-state portions of the indentation depth, $h/h_{\rm ela}$, versus time, t, responses in Fig. 5.2(c) are taken to be $-2 \leq \log_{10}(t/t_{\rm ref}) \leq 0$ for Se; $-3 \leq \log_{10}(t/t_{\rm ref}) \leq 0$ for $CsHSO_4$ and Sn. A least squares fit is used and, based on Eq. (5.18), the slope of the $\log_{10} - \log_{10}$ plot is identified with $1/(2n)$ and β is obtained from the least squares intercept. The least square fit used to determine the value of n involved $197, 455$ and 253 points for Se, $CsHSO_4$ and Sn, respectively. The values of n and β so obtained are then used in analytical expressions for power-law creep indentation derived by the Bower at al. [69] and Ginder et al. [151] to obtain the value of the pre-exponential factor α.

Using expressions derived by Bower et al. [69] and identifying p in Eq. (5.14) with the force per unit nominal area as in Su at al. [3]

$$\alpha_{\rm BFNO} = \beta(F^n c^{2n-1}) \cot\gamma \tag{5.26}$$

where both F and c are functions of n and the indenter angle γ (see Fig. 5.1). The values of F and c were estimated using the values for an indenter angle $\gamma = 70^\circ$ in Tables 1 and 2 of [3].

The closed-form algebraic expression for α obtained by Ginder et al. [151] based on an expanding cavity model is

$$\alpha_{\rm GNP} = \beta\Big(\frac{2n}{3}\Big)^n \cot\gamma \tag{5.27}$$

For the noise-contaminated predictions of the analytical models, noise is added to the power-law regime indentation depth versus time data using the MATLAB [109] function normrnd(0,ξ,[1,K])

Table 5.8: A comparison of the values of n, α and $\alpha\sigma_a^n$ obtained using the input "experimental" data in Table 5.1 (subscript inp), the Bayesian-type statistical approach with HTS data from Sections (5.6.1.1) and (5.6.1.2) (subscript Bayes), HT data with Eq. (5.26) (subscript BFNO), and HT data with Eq. (5.27) (subscript GNP). The subscript $(\,)_{\rm nf}$ denotes noise-free data and the subscript $(\,)_{0.01}$ denotes values averaged of predictions over 100 realizations with $\eta_{\rm h} = \eta_{\rm s} = 0.01$. Also, shown is the value of $\alpha\sigma_a^n$ where for each material, σ_a is the applied stress in Eq. (5.20). The values of n used in Eqs. (5.26) and (5.27) were obtained from a least squares fit to the steady-state portions of the "experimental" indentation depth versus time responses.

	Se	$CsHSO_4$	Sn
$n_{\rm inp}$	1.15	3.59	6.60
$\alpha_{\rm inp}(\mathrm{Pa^{-n}s^{-1}})$	1.04×10^{-12}	9.89×10^{-16}	9.97×10^{-47}
$\alpha_{\rm inp}\sigma_a^n\ (\mathrm{s^{-1}})$	4.50×10^{-5}	2.57×10^{-4}	2.44×10^{-5}
$n_{\rm Bayes,nf}$	1.16	3.58	6.46
$\alpha_{\rm Bayes,nf}(\mathrm{Pa^{-n}s^{-1}})$	0.898×10^{-12}	10.6×10^{-16}	86.7×10^{-47}
$\alpha_{\rm Bayes,nf}\sigma_a^n\ (\mathrm{s^{-1}})$	4.53×10^{-5}	2.56×10^{-4}	2.81×10^{-5}
$n_{\rm Bayes,0.01}$	1.16	3.59	6.59
$\alpha_{\rm Bayes,0.01}(\mathrm{Pa^{-n}s^{-1}})$	0.895×10^{-12}	9.53×10^{-16}	19.1×10^{-47}
$\alpha_{\rm Bayes,0.01}\sigma_a^n\ (\mathrm{s^{-1}})$	4.52×10^{-5}	2.48×10^{-4}	4.04×10^{-5}
$n_{\rm BFNO,nf}$	1.17	3.57	6.66
$\alpha_{\rm BFNO,nf}(\mathrm{Pa^{-n}s^{-1}})$	0.813×10^{-12}	11.6×10^{-16}	3.91×10^{-47}
$\alpha_{\rm BFNO,nf}\sigma_a^n\ (\mathrm{s^{-1}})$	4.78×10^{-5}	2.60×10^{-4}	2.27×10^{-5}
$n_{\rm BFNO,0.01}$	1.17	3.57	6.66
$\alpha_{\rm BFNO,0.01}(\mathrm{Pa^{-n}s^{-1}})$	0.832×10^{-12}	11.8×10^{-16}	4.59×10^{-47}
$\alpha_{\rm BFNO,0.01}\sigma_a^n\ (\mathrm{s^{-1}})$	4.89×10^{-5}	2.65×10^{-4}	2.67×10^{-5}
$n_{\rm GNP,nf}$	1.17	3.57	6.66
$\alpha_{\rm GNP,nf}(\mathrm{Pa^{-n}s^{-1}})$	0.769×10^{-12}	5.09×10^{-16}	12.3×10^{-47}
$\alpha_{\rm GNP,nf}\sigma_a^n\ (\mathrm{s^{-1}})$	4.52×10^{-5}	1.14×10^{-4}	7.15×10^{-5}
$n_{\rm GNP,0.01}$	1.17	3.57	6.66
$\alpha_{\rm GNP,0.01}(\mathrm{Pa^{-n}s^{-1}})$	0.790×10^{-12}	5.18×10^{-16}	14.2×10^{-47}
$\alpha_{\rm GNP,0.01}\sigma_a^n\ (\mathrm{s^{-1}})$	4.65×10^{-5}	1.16×10^{-4}	8.25×10^{-5}

where the K is the number of data points on the indentation depth versus time response that lie in the power-law regime (in the range 197 to 455). Note that although the mean and standard deviation are the same as for the Bayesian based calculations in Section (5.6.1.2), the number of data points and the specific realizations differ. The values of n and α for noise-contaminated data were again obtained by averaging over 100 realizations. As for the Bayesian statistics based predictions, carrying out the noise-contaminated calculations for a different 100 realizations with

$\eta_{\rm h} = \eta_{\rm s} = 0.01$ does not significantly change the results.

Table 5.8 shows a comparison between the values of the creep exponent n and the pre-exponential factor α associated with the input experimental materials, the Bayesian statistical analysis, the expression Eq. (5.26) and the expression Eq. (5.27). Note that the Bayesian statistics based predictions shown are based on HTS data whereas the analytical model predictions only use HT data. Also, because the values of n used in Eqs. (5.26) and (5.27) are obtained from the least squares fits to computed power-law regime responses, the same value of n appears for the BFNO and GNP entries in Table 5.8.

The values of α for the various entries in Table 5.8 are not directly comparable since the units of α vary with n. However, the quantity $\alpha\sigma_a^n$ has the dimension $1/\text{time}$ and can be directly compared. In the power-law creep regime, the uniaxial creep strain rate in Eq. (5.21) is given by $\alpha\sigma_a^n$, with σ_a the applied stress. Thus, the comparison between the various predictions for $\alpha\sigma_a^n$ with the "experimental" value provides a measure of the accuracy of the prediction.

For Se ($n = 1.15$), all the predictions of n and $\alpha\sigma_a^n$, both for noise-free data and for noise-contaminated data (with $\eta_{\rm h} = \eta_{\rm s} = 0.01$ in Table 5.8) provide a good representation of the "experimental" material. Perhaps surprisingly, the simple formula in Eq. (5.27) provides a slightly more accurate prediction than Eq. (5.26).

For $CsHSO_4$ ($n = 3.59$), the "experimental" values of n and $\alpha\sigma_a^n$ are well represented by the Bayesian statistical predictions and by Eq. (5.26) while the predictions of $\alpha\sigma_a^n$ from Eq. (5.27) differ from the "experimental" value by a factor of about 2.

For Sn ($n = 6.60$), the Bayesian statistical prediction and the prediction based on Eq. (5.26) are both rather accurate for noise-free data. The prediction based on Eq. (5.26) also provides a reasonably accurate value of $\alpha\sigma_a^n$ for the noise-contaminated data while the Bayesian statistics based prediction of $\alpha\sigma_a^n$ differs from the "experimental" value. This is may be due to the values of n and β used in Eq. (5.26) being obtained directly from the power-law regime indentation data, whereas the Bayesian statistics values of n and α are obtained based on database data which largely consists of interpolated approximations. Nevertheless, the Bayesian statistics values of n

and α based on noisy data are rather close to the "experimental" input values of Sn.

The accuracy of the predictions becomes more sensitive to noise for larger values of the stress exponent n. For example, for Se ($n = 1.15$) with $\eta_{\rm h} = \eta_{\rm s} = 0.10$, the predicted values of $\alpha\sigma_a^n = 5.04\times10^{-5}\text{s}^{-1}$, $6.23\times10^{-5}\text{s}^{-1}$, and $7.40\times10^{-5}\text{s}^{-1}$ for the Bayesian statistics approach, Eq. (5.26) and Eq. (5.27), respectively. For Sn ($n = 6.60$), the corresponding values are $6.86 \times 10^{-5}\text{s}^{-1}$, $1.61 \times 10^{-2}\text{s}^{-1}$ and $2.89 \times 10^{-2}\text{s}^{-1}$. Hence, for very noisy data, both analytical approximations for Sn ($n = 6.60$) are very inaccurate.

5.7 Conclusions

The Bayesian-type statistical approach of Zhang et al. [2] has been used to identify the power-law creep constitutive parameters, the creep exponent n and the pre-exponential factor α, from "experimental" load and hold indentation creep measurements, considering noise-free as well as noise-contaminated data. The indentation creep measurements are: (i) the indentation depth versus time response; and (ii) the residual surface profile. Material properties representative of three materials have been considered: amorphous selenium (Se), solid acid $CsHSO_4$ and tin (Sn). Finite element calculations were carried out to populate a coarse database of power-law creep parameters. The finer database used for the Bayesian statistical analyses was created by interpolation. Uniaxial creep and stress relaxation responses were computed using the power-law creep parameters obtained from the Bayesian-type statistical approach using noise-free as well as noise-contaminated data and compared with the corresponding responses of the "experimental" materials. The Bayesian statistics based predictions were also compared with predictions based on analytical power-law creep indentation expressions of Bower et al. [69] and Ginder et al. [151].

1. The Bayesian-type statistical approach provides the values of power-law creep parameters that provide a good fit to the indentation responses of all the materials considered when based on noise-free data and for sufficiently small noise amplitudes. The sensitivity to noise increases with increasing creep stress exponent n.

    - For Se ($n = 1.15$), the creep parameters obtained from both the noise-free and noise-

contaminated indentation responses provide a good fit to the uniaxial creep and stress relaxation responses.

- For Sn ($n = 6.60$), creep parameters that provide good fit to the load and hold indentation responses do not necessarily give a good fit to the uniaxial creep and stress relaxation responses.

2. Can very different power-law creep parameters give nearly the same responses in load and hold indentation creep? In the circumstances analyzed, different values of the power law creep parameters did give reasonably good fits to the "experimental" indentation data, particularly for noisy data, but no cases were found where very different values of both power-law creep parameters gave nearly the same indentation response.

3. Does using the residual surface profile in addition to or instead of the indentation depth versus time data improve the quality of the prediction? Using both indentation depth versus time data and residual surface profile data generally leads to an improved prediction of the uniaxial creep and stress relaxation responses. For Se ($n = 1.15$), the improvement over only using indentation depth versus time data is negligible.

4. How sensitive is the predicted creep response to noise in the "experimental" indentation data? The uniaxial creep response is more sensitive to the accuracy of the predicted values of the power-law creep parameters, and therefore to noise, than is the uniaxial stress relaxation response.

5. How do the power-law creep properties obtained using the analytical steady state creep results of Bower et al. [69] and Ginder et al. [151] compare with those predicted from the Bayesian-type statistical approach? For Se ($n = 1.15$), the predictions of both the analytical models of Bower et al. [69], and of Ginder et al. [151] are in very good agreement with those of the "experimental" material, while the model of Bower et al. [69] provides a good fit for all three values of creep stress exponent and the corresponding pre-exponential factor considered if the noise level is sufficiently small.

Acknowledgment

Y.Z. is grateful for helpful discussions of indentation creep with Professor George M. Pharr. The finite element calculations reported were carried out using high performance research computing resources provided by Texas A&M University (https://hprc.tamu.edu).

6. BAYESIAN INFERENCE FOR MATERIAL PROPERTIES

"Physicists believe that the Gaussian law has been proved in mathematics while mathematicians think that it was experimentally established in physics."

– Henri Poincaré

6.1 Introduction

Bayes' theorem was first published in the Philosophical Transactions of the Royal Society in 1763 [5]. The theorem itself is quite simple, but has enormous implications for statistical practice. In recent years the use of Bayesian methodology has grown explosively, mainly because computing challenges in its application have been overcome with the advent of Markov Chain Monte Carlo [26]. Bayesian statistics has been applied in a wide variety of research areas, for example, gating mechanisms [32], partially observed stochastic epidemics [34], semiconductor composition [33], radiation biodosimetry [37], material damage control [38], and fatigue life [41].

Characterization of material properties is the foremost step in, for example, fundamental research in biomechanics and bubble dynamics [48, 49, 50, 51], engineering applications ranging from characterizing materials for microsystem to materials for nuclear reactors [166, 52, 53], and clinical diagnosis of cancers [54, 55]. A material property is a scalar or tensor parameter that enters the constitutive description of a material. Such properties could be mechanical, electrical, thermal, magnetic, optical or chemical. Material properties characterization is the process of identifying the parameter values in a constitutive relationship by post processing of experimental measurements. For mechanical properties, Bayesian inference has been adopted to identify elastic properties, e.g. spatial distribution of elastic properties [45], Young's modulus parameter field [167] and elastic parameters of micro-swimmers [60], as well as plastic properties, e.g. rate-independent materials [2], impacts of strain hardening rules [140], plastically compressible materials [46] and creep

parameters [4].

In a uniaxial tension test with uniform deformations, Young's modulus of the sample can be quantified by applying Hooke's law on one pair of measurements, i.e. uniaxial Cauchy stress and uniaxial logarithmic strain. However in some cases, multiple types of measurements can be required for material properties characterization, for example in the identification of plastic properties from indentation. The strain (rate) hardening rule for an elastic and plastic material is nonlinear. The contact behavior during indentation process and the kinematics for finite strain are both nonlinear. Given these, the deformations of indented materials are nonuniform, where one pair of measurements may not be adequate to uniquely identify material properties. In particular, the relation between indentation force versus indentation depth response and the uniaxial stress versus strain response for an elastic and plastic material is not necessarily unique [91, 93, 124, 2]. One way to render the relation unique is by additionally considering the residual surface profiles of the indented materials [116, 2, 117].

Bayesian inference has been applied in the characterization of plastic properties from indentation, e.g. [106, 2, 46, 140, 4, 122, 123]. Specifically, a uniform prior was used in [106, 2, 46, 140, 4, 122, 123] and a normal prior was numerically considered in [106]. In this paper, we propose a rigorously derived Bayesian formulation for material properties identification using one signal type. An inverse gamma prior for the noise variance in a normal likelihood model is analyzed. Given the demand of multiple signal types, a rational way to account for multiple types of experimental measurements is provided. The following questions are to be addressed:

1. Given one pair of experimental measurements (single signal type), what would be a rigorous Bayesian formulation for the inference of material properties?

2. How do prior parameters in the Bayesian formulation affect the inference? What are effective choices for these parameters?

3. With multiple signal types, what are some rational approaches to inferring material properties using different signal types? In the presence of bias, is there an approach to diminish the

influence of bias from certain signal types?

We begin by specifying the material properties identification problem and derive the posterior probability for data of single signal type to answer question (i). The difference between this formulation and a Bayesian-type approach of Zhang et al. [2] is discussed. Asymptotic analysis of the derived posterior probability and numerical calculations of an analytical expression are carried out to answer question (ii). A classical Bayesian approach is used to account for multiple types of signals. Another method, using a weighted average of posterior probability distributions from different signal types, is also proposed to address possible bias of some signal types. We apply the formulations for both the single signal type and the multiple signal types to the creep properties identification from indentation problem of Zhang and Needleman [4]. The effect of prior parameters is studied to help answer questions (ii) and (iii).

6.2 Bayesian formulation

We consider material properties $\boldsymbol{\theta} = (\theta_1, \theta_2, \ldots, \theta_{K_\mathrm{p}})$ either from multiple scalar parameters or from multiple components of a tensor parameter. For a material with parameters $\boldsymbol{\theta}$, its response under a particular type of test and initial/boundary conditions is denoted $[x, f(x|\boldsymbol{\theta})]$, $x \in I$, where I is an interval that is the same for all components of $\boldsymbol{\theta}$.

In order to infer $\boldsymbol{\theta}$, we must measure experimental data from the same type of test that produces $[x, f(x|\boldsymbol{\theta})]$. These data are denoted $\boldsymbol{Y}$, which is a $K_\mathrm{d} \times 2$ matrix with Jth row (x_J, y_J), where

$$y_J = f(x_J|\boldsymbol{\theta}_0) + \delta_J, \quad J = 1, \ldots, K_\mathrm{d}. \tag{A-1}$$

The subscript on $\boldsymbol{\theta}_0$ reinforces the fact that $\boldsymbol{\theta}_0$ contains the true parameter values that produced the experimental data. The noise terms, $\delta_1, \ldots, \delta_{K_\mathrm{d}}$, are assumed to be independent of each other and to have a common normal distribution with mean 0 and (unknown) variance ξ^2.

Characterization of material properties can be understood as a process of identifying parameter values that best fit the experimental measurements. To do so, we build a database of possible response solutions obtained from an appropriate model for various values of $\boldsymbol{\theta}$. Specifically, the

parameter space for $\boldsymbol{\theta}$ is discretized using a database grid denoted by G. For example, G could be a quadrilateral mesh in a two-dimensional parameter space. A point in the grid G is denoted $\boldsymbol{\theta}_i = (\theta_1^i, \ldots, \theta_{K_\mathrm{p}}^i)$, $i = 1, \ldots, K_G$.

For each $\boldsymbol{\theta}_i \in G$, its corresponding response solution, denoted $\boldsymbol{Z}_i = [x, f^*(x|\boldsymbol{\theta}_i)]$, may be calculated under the same test type as that producing $[x, f(x|\boldsymbol{\theta}_0)]$ and $\boldsymbol{Y}$. This is done using appropriate models obtained from either analytic expressions or numerical simulations, such as finite element or finite difference. In practice, one calculates $\boldsymbol{Z}_i$ for each $\boldsymbol{\theta}_i$, where $\boldsymbol{Z}_i$ is the $K_\mathrm{d} \times 2$ matrix with Jth row $(x_J, f^*(x_J|\boldsymbol{\theta}_i))$, $J = 1, \ldots, K_\mathrm{d}$. The values of x_J in $\boldsymbol{Z}_i$ are the same as those in $\boldsymbol{Y}$.

We presume that $f^*(\cdot|\boldsymbol{\theta})$ well-approximates $f(\cdot|\boldsymbol{\theta})$. Therefore, if we can find $f^*(\cdot|\boldsymbol{\theta}_i)$ that provides a good fit to the data $\boldsymbol{Y}$, then $\boldsymbol{\theta}_i$ will be deemed a good approximation to $\boldsymbol{\theta}_0$, the true material properties. Our approach to identifying a function that fits the data well is Bayesian. We propose a probability model for $\boldsymbol{Y}$, an appropriate prior distribution for the parameters of this model, and then determine $f^*(\cdot|\boldsymbol{\theta}_i)$ to maximize the posterior distribution.

6.2.1 A single signal type

We first consider the case where there is only one type of experimental data (or signal). Since the noise terms $\delta_1, \ldots, \delta_{K_\mathrm{d}}$ in Eq. (A-1) are assumed to be independent and identically distributed (i.i.d.) normal variates having mean 0 and variance ξ^2, we have

$$p(\boldsymbol{Y}|\boldsymbol{Z}_i, \xi^2) = \prod_{J=1}^{K_\mathrm{d}} \frac{1}{\xi\sqrt{2\pi}} \exp\left[-\frac{1}{2\xi^2}\left[y_J - f^*(x_J|\boldsymbol{\theta}_i)\right]^2\right]. \tag{A-2}$$

Our notation emphasizes that both $\boldsymbol{Z}_i$ and ξ^2 are unknown parameters, in which case a prior distribution $p(\boldsymbol{Z}_i, \xi^2)$ is required. The posterior probability distribution of $\boldsymbol{Z}_i$ and ξ^2 given observation $\boldsymbol{Y}$ is expressed by

$$p(\boldsymbol{Z}_i, \xi^2|\boldsymbol{Y}) = \frac{p(\boldsymbol{Y}|\boldsymbol{Z}_i, \xi^2)p(\boldsymbol{Z}_i, \xi^2)}{m(\boldsymbol{Y})}, \tag{A-3}$$

and we assume that the prior has the form

$$p(\boldsymbol{Z}_i, \xi^2) = U(\boldsymbol{Z}_i)\pi(\xi^2|\alpha, \beta). \tag{A-4}$$

The prior U for $\boldsymbol{Z}_i$ is (discrete) uniform over all choices for $\boldsymbol{Z}_i$ in the range of the database, and zero outside that range, while the prior for ξ^2 is the following inverse gamma density:

$$\pi(x|\alpha, \beta) = \frac{\beta^\alpha}{\Gamma(\alpha)} x^{-(\alpha+1)} \exp\left(-\frac{\beta}{x}\right), \quad x > 0, \tag{A-5}$$

where Γ is the gamma function, $\alpha > 0$ is a shape parameter and $\beta > 0$ is a scale parameter.

Setting $U(\boldsymbol{Z}_i) = 1/K_G$, expressions (A-2), (A-4) and (A-5) imply that expression (A-3) is

$$p(\boldsymbol{Z}_i, \xi^2|\boldsymbol{Y})m(\boldsymbol{Y}) = \frac{1}{K_G}\frac{\beta^\alpha}{\Gamma(\alpha)}\left(\frac{1}{\sqrt{2\pi}}\right)^{K_\mathrm{d}} (\xi^2)^{-(\alpha+1+K_\mathrm{d}/2)} \exp\left[-\frac{\beta + \hat{S}_i/2}{\xi^2}\right], \tag{A-6}$$

where

$$\hat{S}_i = \sum_{J=1}^{K_\mathrm{d}} \left[y_J - f^*(x_J|\boldsymbol{\theta}_i)\right]^2. \tag{A-7}$$

Comparing Eq. (A-6) with Eq. (A-5) reveals that $p(\xi^2|\boldsymbol{Y}, \boldsymbol{Z}_i)$, the conditional posterior of ξ^2 given $\boldsymbol{Z}_i$, is proportional to $\pi(\xi^2|\alpha', \beta')$, with $\alpha' = \alpha + K_\mathrm{d}/2$ and $\beta' = \beta + \hat{S}_i/2$. This implies that the inverse gamma distribution is a conditional conjugate prior distribution, since $p(\xi^2|\boldsymbol{Y}, \boldsymbol{Z}_i)$ and the prior of ξ^2 are both inverse gamma densities. With a different parameterization, the gamma distribution would become a conditional conjugate prior.

Integrating Eq. (A-6) over ξ^2 leads to the marginal posterior probability distribution of $\boldsymbol{Z}_i$:

$$p(\boldsymbol{Z}_i|\boldsymbol{Y})m(\boldsymbol{Y}) = \int_0^\infty p(\boldsymbol{Z}_i, \xi^2|\boldsymbol{Y})m(\boldsymbol{Y})d\xi^2. \tag{A-8}$$

Making the change of variable $\kappa = (\beta + \hat{S}_i/2)/\xi^2$ in the integrand of Eq. (A-8),

$$p(\boldsymbol{Z}_i|\boldsymbol{Y})m(\boldsymbol{Y}) = C_Y(\beta + \hat{S}_i/2)^{-(\alpha+K_\mathrm{d}/2)}, \tag{A-9}$$

where

$$C_Y = \frac{1}{K_G}\frac{\beta^\alpha}{\Gamma(\alpha)}\left(\frac{1}{\sqrt{2\pi}}\right)^{K_\mathrm{d}}\Gamma(\alpha + K_\mathrm{d}/2). \tag{A-10}$$

Since the number of data points K_d does not depend on i, C_Y does not depend on $\boldsymbol{Z}_i$. The evidence $m(\boldsymbol{Y})$ is also a constant given by

$$m(\boldsymbol{Y}) = \sum_{i=1}^{K_G}\int_0^\infty p(\boldsymbol{Y}|\boldsymbol{Z}_i, \xi^2)p(\boldsymbol{Z}_i, \xi^2)d\xi^2. \tag{A-11}$$

With Eqs. (A-9)-(A-11), we have the posterior probability distribution for $\boldsymbol{Z}_i$, $i = 1, \ldots, K_G$, in the form

$$p(\boldsymbol{Z}_i|\boldsymbol{Y}) \propto (\beta + \hat{S}_i/2)^{-(\alpha+K_\mathrm{d}/2)}. \tag{A-12}$$

Again, the corresponding parameters $\boldsymbol{\theta}_i$ of $\boldsymbol{Z}_i$ would be the inferred parameter values. If we are only interested in finding the maximizer of the posterior, we do not need to calculate the constant in the posterior probability distribution. On the other hand, the discreteness of $\boldsymbol{Z}_i$ makes normalizing (A-12) straightforward. One simply divides $\psi_i = (\beta + \hat{S}_i/2)^{-(\alpha+K_\mathrm{d}/2)}$ by the sum of ψ_i over all $\boldsymbol{Z}_i$ considered.

The quantity $\hat{S}_i$ can be written

$$\frac{\hat{S}_i}{K_\mathrm{d}} = \hat{\xi}^2 + D_i^2 + \Delta_i, \tag{A-13}$$

where

$$\hat{\xi}^2 = \frac{1}{K_\mathrm{d}}\sum_{J=1}^{K_\mathrm{d}}\delta_J^2, \qquad D_i^2 = \frac{1}{K_\mathrm{d}}\sum_{J=1}^{K_\mathrm{d}}[f^*(x_J|\boldsymbol{\theta}_i) - f(x_J|\boldsymbol{\theta}_0)]^2$$

and

$$\Delta_i = \frac{2}{K_\mathrm{d}}\sum_{J=1}^{K_\mathrm{d}}\delta_J[f(x_J|\boldsymbol{\theta}_0) - f^*(x_J|\boldsymbol{\theta}_i)].$$

The quantity D_i is a distance that measures how close $f^*(\cdot|\boldsymbol{\theta}_i)$ is to the true signal $f(\cdot|\boldsymbol{\theta}_0)$. Since expression (A-12) is monotone decreasing in $\hat{S}_i$, it follows that *if* each Δ_i was 0, then the posterior probability would be maximized at the $\boldsymbol{Z}_i$ that is closest to the truth. Of course, for noisy data

the Δ_is are not 0, but fortunately Δ_i converges in probability to 0 as $K_{\rm d}$ becomes large. One can therefore expect (A-12) to provide a good assessment of the various signals in the database.

6.2.2 Relation to a previous Bayesian-type approach

The Bayesian formulation for a single type of signal in Section 26.2.1 differs from the Bayesian-type approach of Zhang et al. [2] in that the noise variance is dealt with differently. The formulation in Section 26.2.1 treats the variance as an unknown parameter having a prior distribution. The variance is then integrated out of the joint posterior, producing the marginal posterior of $\boldsymbol{Z}_i$. This approach recognizes that ξ^2 is merely a nuisance parameter. In the Bayesian-type approach of [2], the variance is estimated by a maximum likelihood estimate (MLE).

In [2], the prior for $\boldsymbol{Z}_i$ is uniform and the likelihood for $\boldsymbol{Y}$ is Gaussian. Instead of assigning a prior to ξ^2, it is replaced in the likelihood by the following MLE:

$$(\hat{\xi}_i)^2 = \frac{1}{K_{\rm d}} \sum_{J=1}^{K_{\rm d}} [y_J - f^*(x_J|\boldsymbol{\theta}_i)]^2, \quad i = 1, ..., K_G. \tag{A-14}$$

The index i on each variance estimate indicates that this statistic maximizes the likelihood at the particular response solution $\boldsymbol{\theta}_i$ in the database with grid G. Using a uniform prior for $\boldsymbol{Z}_i$, the posterior distribution then becomes

$$p(\boldsymbol{Z}_i|\boldsymbol{Y}) \propto \hat{\xi}_i^{-K_{\rm d}}. \tag{A-15}$$

Comparing Eqs. (A-7) and (A-14), we have $\hat{S}_i = K_{\rm d}\hat{\xi}_i^2$. Expressions (A-6) and (A-8) remain valid when $\alpha = \beta = 0$, in spite of the fact that the prior is improper in that case. Therefore, if $\alpha = \beta = 0$, then Eq. (A-12) becomes

$$p(\boldsymbol{Z}_i|\boldsymbol{Y})|_{\alpha=\beta=0} \propto (\hat{S}_i/2)^{-K_{\rm d}/2} = (2/K_{\rm d})^{K_{\rm d}/2} \hat{\xi}_i^{-K_{\rm d}} \propto \hat{\xi}_i^{-K_{\rm d}}. \tag{A-16}$$

We therefore see that the posterior probability in the approach of Zhang et al. [2] is a limiting case $(\alpha = \beta = 0)$ of the general formula Eq. (A-12).

6.2.3 Limiting version of posterior probabilities as K_{d} and/or α become large

Ideally the prior for ξ^2 would be centered at the true variance, ξ_0^2. However, ξ_0^2 is unknown and it is of interest to investigate how the parameters chosen for the prior affect $p(\boldsymbol{Z}_i|\boldsymbol{Y})$. The mode of the inverse gamma is $M = \beta/(\alpha+1)$, and we may reparameterize in terms of M and α. Per our discussion in section 26.2.1,

$$\begin{aligned} p(\boldsymbol{Z}_i|\boldsymbol{Y}) &\propto (M(\alpha+1) + \hat{S}_i/2)^{-(\alpha+K_{\mathrm{d}}/2)} \\ &\approx \left[M(\alpha+1) + K_{\mathrm{d}}(\xi_0^2 + D_i^2)/2\right]^{-(\alpha+K_{\mathrm{d}}/2)} \\ &= (K_{\mathrm{d}}\xi_0^2)^{-(\alpha+K_{\mathrm{d}}/2)} \left[\frac{M(\alpha+1)}{K_{\mathrm{d}}\xi_0^2} + (1 + D_i^2/\xi_0^2)/2\right]^{-(\alpha+K_{\mathrm{d}}/2)}, \end{aligned} \tag{A-17}$$

where the approximation holds for large K_{d} since Δ_i and $\hat{\xi}^2$ converge in probability to 0 and ξ_0^2, respectively, as K_{d} tends to ∞. Defining $A_i = (1 + D_i^2/\xi_0^2)/2$, we have

$$p(\boldsymbol{Z}_i|\boldsymbol{Y}) \propto A_i^{-(\alpha+K_{\mathrm{d}}/2)} \left[1 + \frac{M(\alpha+1)}{2\xi_0^2 A_i (K_{\mathrm{d}}/2)}\right]^{-(\alpha+K_{\mathrm{d}}/2)} \tag{A-18}$$

$$\approx A_i^{-(\alpha+K_{\mathrm{d}}/2)} \exp\left(-\frac{M(\alpha+1)}{2\xi_0^2 A_i}\right), \tag{A-19}$$

where the last approximation holds when K_{d} is large and $K_{\mathrm{d}}/2 \gg \alpha$ using the fact that $\lim_{k\to\infty}(1 + A/k)^k = \exp(A)$.

For two signals $\boldsymbol{Z}_i$ and $\boldsymbol{Z}_j$ with distances $D_i > D_j$, the ratio of their corresponding posterior probabilities is

$$\frac{p(\boldsymbol{Z}_i|\boldsymbol{Y})}{p(\boldsymbol{Z}_j|\boldsymbol{Y})} \approx \left(\frac{D_j^2 + \xi_0^2}{D_i^2 + \xi_0^2}\right)^{\alpha+K_{\mathrm{d}}/2} \exp\left[\frac{M(\alpha+1)}{2\xi_0^2}\left(\frac{1}{A_j} - \frac{1}{A_i}\right)\right]. \tag{A-20}$$

Since $D_i > D_j$, Eq. (A-20)$\to 0$ as $K_{\mathrm{d}} \to \infty$. This implies that for a fixed α, the signal with the smallest value of D_i will have a posterior probability tending to 1 as K_{d} tends to ∞. A commonly used noninformative but improper prior for ξ_0^2 uses $\alpha = 0$. It is thus important to point out that the analysis leading to Eq. (A-20) still holds if $\alpha = 0$.

For a given mode M, the inverse gamma density becomes ever more concentrated at M as α tends to ∞. Therefore, large α corresponds to a strong belief that ξ_0^2 is very close to M. What is the consequence of choosing α large when in fact ξ_0^2 is not close to M? The natural logarithm of the right hand side of (A-20) is

$$(\alpha + K_{\mathrm{d}}/2)(\ln x_j - \ln x_i) + (\alpha + 1)\left(\frac{1}{x_j} - \frac{1}{x_i}\right), \tag{A-21}$$

where

$$x_i = 2\xi_0^2 A_i/M, \quad x_j = 2\xi_0^2 A_j/M. \tag{A-22}$$

Note that $(\alpha + K_{\mathrm{d}}/2)\ln x + (\alpha+1)/x$ is a decreasing function of $x < (\alpha+1)/(\alpha + K_{\mathrm{d}}/2)$ and an increasing function of $x \geq (\alpha+1)/(\alpha+K_{\mathrm{d}}/2)$. This means that if $M < (\alpha+K_{\mathrm{d}}/2)(\xi_0^2+D_j^2)/(\alpha+1)$ as α and K_{d} become large, then Eq. (A-20) will tend to 0. In other words, a strong but incorrect belief that M is relatively small is not troublesome. If $M > (\alpha + K_{\mathrm{d}}/2)(\xi_0^2 + D_i^2)/(\alpha + 1)$ as α becomes large, the consequences are potentially dire, since then (A-20) could tend to ∞, even though $D_j < D_i$. However, one may guard against this eventuality by choosing α to be $o(K_{\mathrm{d}})$ as α and K_{d} become large. Doing so guarantees that ultimately M will be no larger than $(\alpha + K_{\mathrm{d}}/2)(\xi_0^2 + D_i^2)/(\alpha + 1)$ for any distance D_i considered, and hence the signal with smallest distance will have posterior probability tending to 1.

Eq. (A-20) suggests that using a prior with both M and α small will prevent any potentially deleterious effects of poor choice of prior parameters. In particular, the noninformative prior with $\alpha = \beta = 0$ seems like a reasonable default choice. In spite of being improper, this prior still produces a proper posterior for $\boldsymbol{Z}_i$ and ξ^2.

6.2.4 Numerical results

Section 26.2.3 provides asymptotic analyses of posterior probabilities when K_{d} and/or α are large. In this Section we calculate our approximations to the posterior probabilities and find that they are consistent with the analytical analyses.

Fig. 6.1 provides examples of the inverse gamma density Eq. (A-5). When the mode M is

fixed, the density becomes more concentrated at the mode with an increase in α. Similarly, when α is fixed, a smaller mode M makes the density more concentrated near M. Generally speaking, smaller values of α correspond to more noninformative priors and larger values to more informative priors.

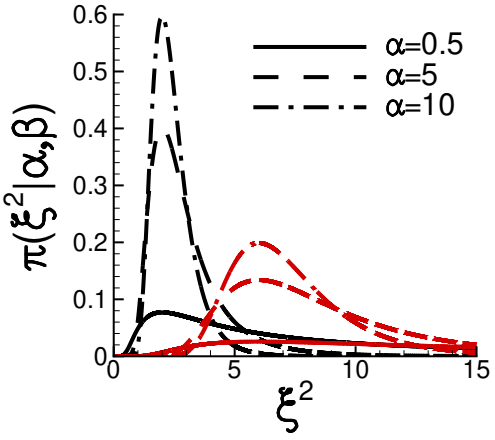

Figure 6.1: The inverse gamma density prior with various values of shape parameter α and mode M where $M = \beta/(\alpha+1)$. Black and red lines denote $M = 2$ and $M = 6$, respectively.

From Eq. (A-17) we have

$$p(\boldsymbol{Z}_i|\boldsymbol{Y}) \propto \left[\frac{(\alpha+1)}{K_{\mathrm{d}}}\frac{M}{\xi_0^2} + \frac{1}{2}\frac{D_i^2}{\xi_0^2} + \frac{1}{2}\right]^{-(\alpha+K_{\mathrm{d}}/2)} = C \cdot f(\alpha, K_{\mathrm{d}}, M/\xi_0^2, D_i/\xi_0), \qquad \text{(A-23)}$$

where the constant C is such that $f(\alpha, K_{\mathrm{d}}, M/\xi_0^2, D_i/\xi_0)$ sums to 1 over a relevant range of values for D_i/ξ_0. Define P_λ to be a summation of the posterior probabilities over a collection of D_i/ξ_0 in the interval $[0, \lambda]$:

$$P_\lambda(\alpha, K_{\mathrm{d}}, M/\xi_0^2) = \sum_{0 \le D_i/\xi_0 \le \lambda} f(\alpha, K_{\mathrm{d}}, M/\xi_0^2, D_i/\xi_0). \qquad \text{(A-24)}$$

Computing a sum such as P_λ seems like a more realistic way to investigate the posterior distribution

than simply calculating the posterior probability of the best model. Typically there will be a number of different signals that are all very close to the best model. In the sequel the value of λ is chosen to be half the largest value of D_i/ξ_0 considered.

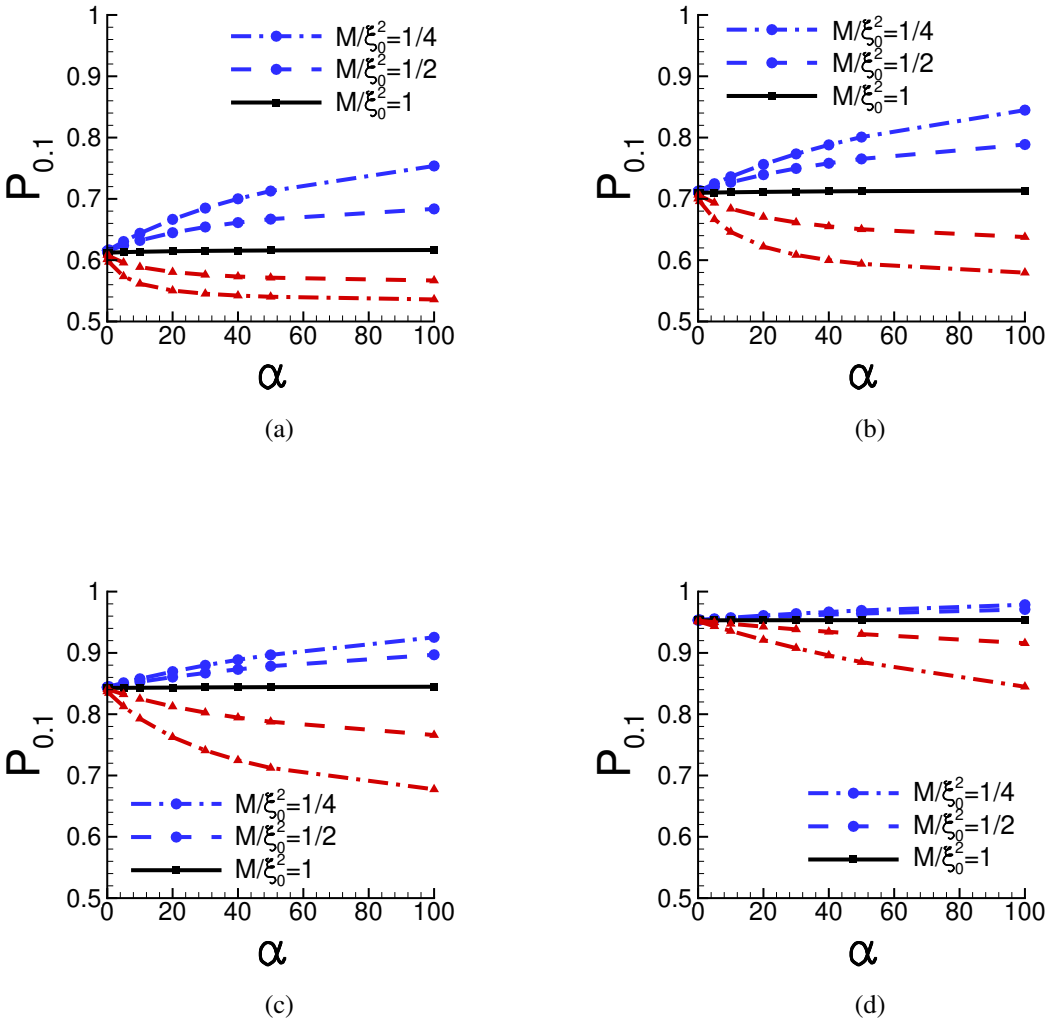

Figure 6.2: $P_{0.1}$, Eq. (A-24), for various parameter values M/ξ_0^2, α and $K_{\rm d}$. One thousand evenly spaced points are considered for $D_i/\xi_0 \in [0, 0.2]$. (a) $K_{\rm d} = 50$. (b) $K_{\rm d} = 100$. (c) $K_{\rm d} = 200$ and (d) $K_{\rm d} = 400$. In all four plots, the curves from top to bottom correspond to $M/\xi_0^2 = 1/4$, $M/\xi_0^2 = 1/2$, $M/\xi_0^2 = 1$, $M/\xi_0^2 = 2$ and $M/\xi_0^2 = 4$, respectively.

Fig. 6.2 provides $P_{0.1}$ for various choices of M/ξ_0^2, α and K_{d}. When the prior is centered at the correct ξ^2, i.e. $M/\xi_0^2 = 1$, the posterior probabilities hardly change with α. Arguably, the posterior probabilities are "correct" when M/ξ_0^2=1 since in this case the prior is centered at the true noise variance. Importantly, when α is small, all the posterior probabilities are close to what they are when $M/\xi_0^2 = 1$, which seems to be a strong argument for choosing α to be small.

When the prior mode M is not centered at ξ_0^2, the posterior probabilities deviate from the middle curve (corresponding to $M/\xi_0^2 = 1$) when α is large. Specifically, when $M/\xi_0^2 < 1$ and $M/\xi_0^2 > 1$, $P_{0.1}$ tends to be larger and smaller, respectively, than $P_{0.1}$ for $M/\xi_0^2 = 1$. This is consistent with the analytical analysis in Section 26.2.3. With M/ξ_0^2 and α fixed, the posterior probabilities $P_{0.1}$ increase toward 1 as K_{d} increases. Again, this is consistent with the conclusions of Section 26.2.3.

To summarize, if correct information about ξ^2 is used, i.e. $M/\xi_0^2 = 1$, the choice of α does not matter. If the prior distribution for ξ^2 is not centered at ξ_0^2, then posterior probabilities can be misleading if α is large. Therefore, it makes sense to choose α small whether one is confident or not in the prior information about ξ^2. Finally, we note that the largest possible value for K_{d} is always recommended, since the larger K_{d} is the less important it is to correctly quantify information about the noise variance.

6.2.5 Multiple signal types

In general, multiple types of test on the same material could be performed and we organize the experimental measurements in the form $\boldsymbol{Y} = (\boldsymbol{Y}_1, ..., \boldsymbol{Y}_{K_y})$, where each $\boldsymbol{Y}_q$, $q = 1, ..., K_y$, has the same data structure as $\boldsymbol{Y}$ in Section 26.2.1 and K_y is the number of test types. For each $\boldsymbol{\theta}_i \in G$, $\boldsymbol{Z}_i$ is, in the present context, a matrix consisting of response solutions of the K_y types. In other words, $\boldsymbol{Z}_i = (\boldsymbol{Z}_{i1}, ..., \boldsymbol{Z}_{iK_y})$, which are fitted to the experimentally measured responses $(\boldsymbol{Y}_1, ..., \boldsymbol{Y}_{K_y})$, respectively. Each $\boldsymbol{Z}_{iq}$, $q = 1, ..., K_y$, is of the same form as $\boldsymbol{Z}_i$ in Section 26.2.1.

Letting ξ_q^2 be the error variance for the qth data type, $q = 1, \ldots, K_y$, the prior is taken to be

$$p(\boldsymbol{Z}_i, \xi_1^2, ..., \xi_{K_y}^2) = \frac{1}{K_G} \prod_{q=1}^{K_y} \pi(\xi_q^2 | \alpha_q, \beta_q), \tag{A-25}$$

implying that each $\boldsymbol{\theta}_i$ has the same prior probability. Assuming that data of different types are independent given the parameters, the likelihood is

$$p(\boldsymbol{Y}|\boldsymbol{Z}_i, \xi_1^2, ..., \xi_{K_y}^2) = \prod_{q=1}^{K_y} p(\boldsymbol{Y}_q|\boldsymbol{Z}_{iq}, \xi_q^2), \tag{A-26}$$

which yields the posterior

$$p(\boldsymbol{Z}_i, \xi_1^2, \ldots, \xi_{K_y}^2|\boldsymbol{Y}) \propto \prod_{q=1}^{K_y} \pi(\xi_q^2|\alpha_q, \beta_q) p(\boldsymbol{Y}_q|\boldsymbol{Z}_{iq}, \xi_q^2).$$

It follows that the marginal posterior of $\boldsymbol{Z}_i$ can be obtained by integrating out each ξ_q^2 separately, leading to

$$p(\boldsymbol{Z}_i|\boldsymbol{Y}) \propto \prod_{q=1}^{K_y} p(\boldsymbol{Z}_{iq}|\boldsymbol{Y}_q), \tag{A-27}$$

where each $p(\boldsymbol{Z}_{iq}|\boldsymbol{Y}_q)$ has the same form as Eq. (A-12). An estimate of $\boldsymbol{\theta}_0$ is provided by the $\boldsymbol{\theta}_i$ corresponding to the $\boldsymbol{Z}_i$ that maximizes the joint posterior Eq. (A-27).

Another way of estimating $\boldsymbol{\theta}_0$ is to use a convex combination of $\boldsymbol{\theta}$ values that correspond to estimates of $\boldsymbol{Z}_{i1}, \ldots, \boldsymbol{Z}_{iK_y}$. In this approach the estimates of $\boldsymbol{Z}_{iq}$ are obtained by maximizing the K_y posteriors of the different data types *separately*. A classical, asymptotic argument, provided in the Appendix D, shows that the approach of choosing $\boldsymbol{\theta}_i$ to maximize (A-27) is usually more efficient than such a convex combination, in the sense of leading to an estimator with smaller variance.

6.2.6 Additive approach to deal with bias

Suppose that a bias exists in the measurements $\boldsymbol{Y}$, in the sense that

$$y_J = f(x_J|\boldsymbol{\theta}_0) + b(x_J, ...) + \delta_J, \quad J = 1, \ldots, K_{\mathrm{d}}, \tag{A-28}$$

where $b(x_J, ...)$ is a bias function which could consist of a constant term and terms that depend on x_J and other test parameters, such as environmental factors and test facilities. In practice,

identification of the bias function $b(x_J, ...)$ could be challenging. Often, one would be unaware of $b(x_J, ...)$ and it would simply become merged into the true function $f(x_J|\boldsymbol{\theta}_0)$. Unless the bias is negligible, poor estimates of $f(x_J|\boldsymbol{\theta}_0)$ are likely to result from failure to account for the bias. The efficiency of the approach in Section 26.2.5 is only guaranteed when the assumed model is correct, and hence does not necessarily lead to accurate inference in the presence of bias.

While the exact nature of bias may be unknown, the investigator may be aware that some data sources are more unreliable than others. To deal with such a scenario we propose that one choose $\boldsymbol{Z}_i$ to maximize the following:

$$p(\boldsymbol{Z}_i|\boldsymbol{Y}) = \sum_{q=1}^{K_y} p(\boldsymbol{Z}_{iq}|\boldsymbol{Y}_q) W_q, \tag{A-29}$$

where each $p(\boldsymbol{Z}_{iq}|\boldsymbol{Y}_q)$ is of the same form as Eq. (A-12), $q = 1, ..., K_y$, and $W_1, \ldots, W_{K_y}$ are positive weights that add to 1. The idea is that data types suspected to be more biased receive smaller weights.

6.3 Application to creep properties identification from indentation

The Bayesian-type approach of [4] (discussed in Section 26.2.2), which corresponds to setting $\alpha = 0$ and $\beta = 0$ in Eq. (A-12), has been used to characterize creep parameters, both the creep exponent and the associated pre-exponential factor, from indentation measurements [4]. Here, the general Bayesian formulations in Sections 26.2.1 and 26.2.5 are applied to the creep properties identification to study the influence of statistical parameters and method for multiple types of signals on the posterior probabilities.

The indentation problem is briefly summarized here. Background, initial/boundary conditions, constitutive relation, constant load and hold indentation creep, normalization of responses, finite element implementation, construction of databases and a more complete description are given in Zhang and Needleman [4].

The axisymmetric part of a conical indenter indenting a half space with bottom frictionless support and other free surfaces traction-free is considered, Fig. 6.3. The indenter is rigid with

an angle $\gamma = 70.3°$ and the contact between indenter and the specimen is non-slip. During the indentation process, the reaction force along z direction on the indenter is recorded as F, the corresponding penetration depth without considering pile-up or sink-in is recorded as h. Values of F and h are recorded for each time step t during the whole test process, where $t = 0$ at the beginning of the test.

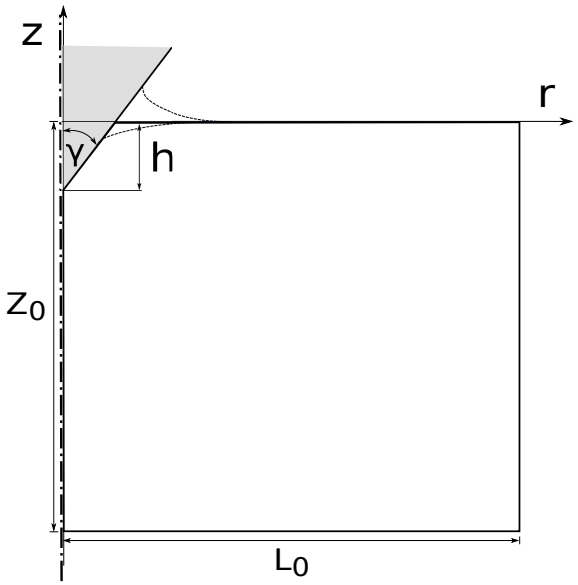

Figure 6.3: Sketch of the indentation configurations with a conical indenter.

The specimen being indented is an elastic-creep material provided in Abaqus standard [118], where the small elastic strain is governed by Hooke's law and the creep part of the rate of deformation is given by J2 flow theory with a power-law creep strain rate hardening rule.

The constant load and hold indentation process basically holds a maximum indentation force F for a period of time. The indentation depth h versus time t response is recorded (denoted HT signal) and the residual surface profile, z versus r, after unloading is recorded (denoted S signal). Other type of measurements, e.g. surface components of strain [168], can be used as well. Here, only S signal and HT signal are considered for inference.

We only consider amorphous selenium (Se) at $35°$C, its numerically generated normalized

noise-free "experimental" responses are shown by the solid lines in Fig. 6.4, where (a) shows normalized indentation depth $h/h_{\rm ela}$ versus normalized time $t/t_{\rm ref}$ responses and (b) shows the normalized surface profiles near the indenter after unloading, where $h_{\rm ela}$ is the elastic solution of indentation depth with an indentation force for an axisymmetric indenter by Sneddon [165], $t_{\rm ref}$ is the inverse of a reference strain rate [4]. Convergence of the mesh and other numerical concerns have been verified in [4]. The original database was constructed (denoted G_0) with number of sets of parameters $K_{G_0} = 2684$ and an interpolated database was obtained (denoted G) with sets of parameters $K_G = 245616$. The accuracy of interpolation in the database has been checked in [4] and the interpolated database G is used for inference.

Recall that the noise terms, $\delta_1, \ldots, \delta_{K_{\rm d}}$ in Eq. (A-1), are independent of each other and have a common normal distribution with mean 0 and variance ξ_0^2. The standard deviation ξ_0 is defined as a product of noise amplitude η and a reference value $s_{\rm ref}$ or $h_{\rm ref}$,

$$\xi_{0s} = \eta_{\rm s} s_{\rm ref} \,, \quad \xi_{0h} = \eta_{\rm h} h_{\rm ref} \tag{A-30}$$

where noise amplitudes $\eta_{\rm s} \geq 0$ and $\eta_{\rm h} \geq 0$ quantify the noise to signal ratio. The reference length $s_{\rm ref}$ is taken to be the indentation depth of the noise-free residual surface profile. The reference length $h_{\rm ref}$ is taken to be the maximum indentation depth. To generate noise, we call the MATLAB [109] function normrnd$(0, \xi_0)$ for each noise term in $\delta_{\rm s}$ or $\delta_{\rm h}$, where 0 is the mean value.

The dashed and dash-dot lines in Fig. 6.4 show examples of noisy normalized indentation depth versus normalized time signals in (a) and noisy normalized residual surface profile signals in (b). Here $\eta_{\rm h} = \eta_{\rm s} = 0.01$ is for a low noise condition and $\eta_{\rm h} = \eta_{\rm s} = 0.10$ is for a high noise condition. The reference values $s_{\rm ref}$ and $h_{\rm ref}$ turn out to be the same to the third significant figure for Se, $s_{{\rm ref}/h_{\rm ela}}$=23.4. When noise amplitudes are $\eta_{\rm h} = 0.01$, $\eta_{\rm s} = 0.01$, we have $\xi_{\rm h} = \xi_{\rm s} = 0.234$, and when $\eta_{\rm h} = 0.10$, $\eta_{\rm s} = 0.10$, $\xi_{\rm h}$ and $\xi_{\rm s}$ are 10 times as large as those in the low noise condition.

The effect of parameter choice on posterior probabilities was investigated using simulated data. For each data set and choice of parameters, we computed $P_{\rm sum}$ = the sum of the posterior prob-

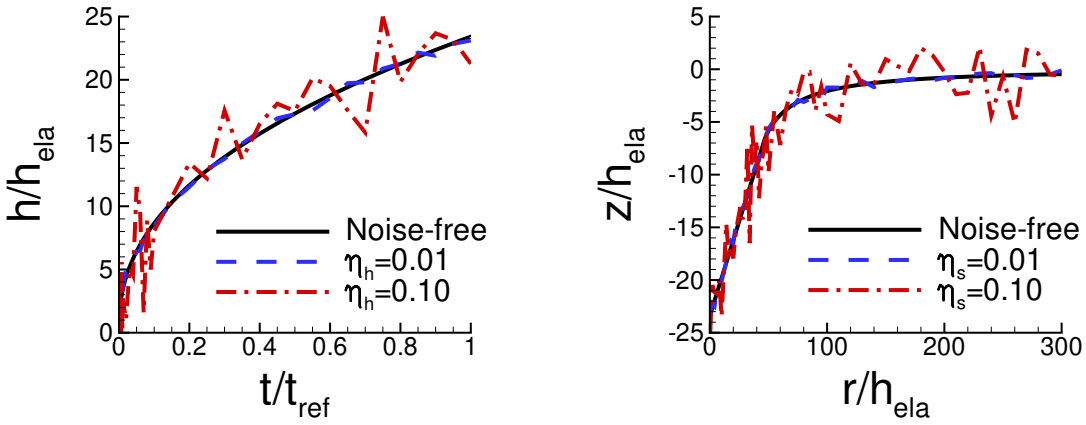

(a) (b)

Figure 6.4: Noise-free indentation responses and realizations of noisy indentation responses with noise amplitudes $\eta_{\rm h} = 0.01$, $\eta_{\rm s} = 0.01$, $\eta_{\rm h} = 0.10$ and $\eta_{\rm s} = 0.10$ for Se. (a) Normalized indentation depth $h/h_{\rm ela}$ versus normalized time $t/t_{\rm ref}$. (b) Normalized residual surface profiles near the indenter. Similar to Figs.10(a) and (b) in [4].

abilities corresponding to the three smallest D_i values. Fig. 6.5 shows, for various choices of M/ξ_0^2 and α, averages of $P_{\rm sum}$ over 100 replications. The number of data points on the signals are $K_{\rm d} = 56$ and 64 for S type and HT type signals, respectively. The results in Fig. 6.5 are consistent with the conclusions of the theoretical analysis in Section 26.2.4.

The $P_{\rm sum}$ values at α near 0 are different for HT and S signal types since their corresponding calculated D values are different. The values of $P_{\rm sum}$ are 0.43 and 0.89 when $M/\xi_0^2 = 1$ and $\alpha = 0$ for low noisy HT signals in Fig. 6.5(a) and low noisy S signals in Fig. 6.5(b), respectively. When noise amplitude increases from $\eta = 0.01$ to $\eta = 0.10$, the $P_{\rm sum}$ values at α near 0 drop by two orders of magnitude. Specifically, $P_{\rm sum} = 0.77 \times 10^{-2}$ and 0.87×10^{-2} when $M/\xi_0^2 = 1$ and $\alpha = 0$ for high noisy HT signals in Fig. 6.5(c) and high noisy S signals in Fig. 6.5(d), respectively.

Table 6.1 lists the standard deviations of $P_{\rm sum}$ for various M/ξ_0^2 and α values using S type signals and noise amplitude $\eta_{\rm s} = 0.01$. Each standard deviation is calculated from 100 replications. The standard deviations become one order of magnitude smaller when α is larger and $M/\xi_0^2 = 16$. The standard deviations are at similar values when α is close to 0.

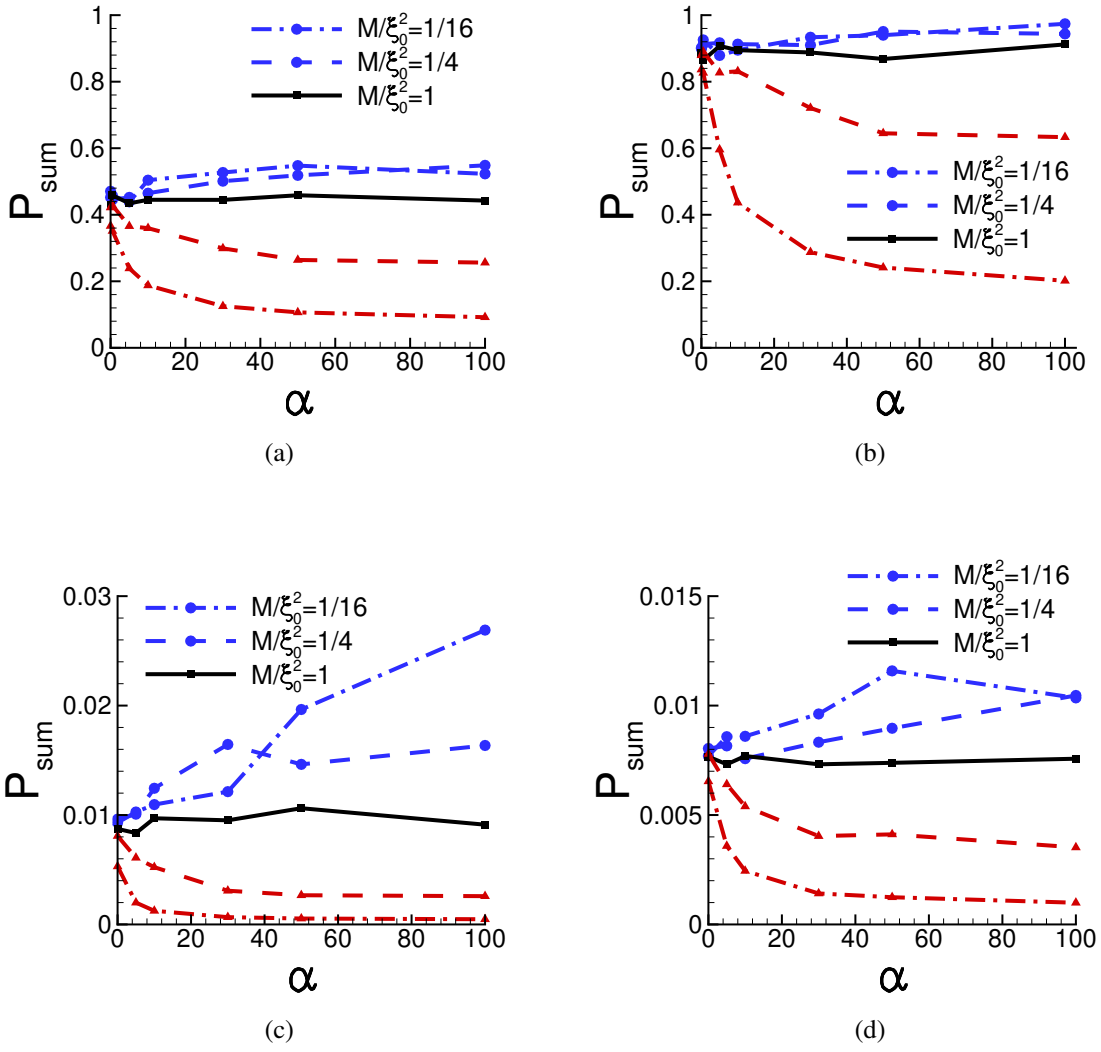

Figure 6.5: Averages of $P_{\rm sum}$, the sum of posterior probabilities corresponding to the three smallest D_i values, for various parameter values M/ξ_0^2 and α. The four plots correspond to (a) noisy HT signals with $\eta_{\rm h} = 0.01$, (b) noisy S signals with $\eta_{\rm s} = 0.01$, (c) noisy HT signals with $\eta_{\rm h} = 0.10$ and (d) noisy S signals with $\eta_{\rm s} = 0.10$. In all four plots, the curves from top to bottom correspond to $M/\xi_0^2 = 1/16$, $M/\xi_0^2 = 1/4$, $M/\xi_0^2 = 1$, $M/\xi_0^2 = 4$ and $M/\xi_0^2 = 16$, respectively.

Fig. 6.6 shows averages of the largest posterior probability p_1 over 100 realizations using both the S type and HT type of signals with multiplicative approach Eq. (A-27) or additive approach (A-29) with equal weights $W_q = 0.5$. The impacts of M/ξ_0^2 and α on p_1 are similar to those on $P_{0.1}$ and $P_{\rm sum}$. For signals with the same noise amplitude η, the p_1 values from the additive approach at

Table 6.1: Standard deviations of $P_{\rm sum}$ for various M/ξ_0^2 and α values using noisy S signals with $\eta_{\rm s} = 0.01$, corresponds to Fig. 6.5(b).

α	0	0.5	5	10	30	50	100
$M/\xi_0^2 = 1/16$	0.16	0.16	0.23	0.23	0.20	0.21	0.11
$M/\xi_0^2 = 1/4$	0.16	0.15	0.18	0.18	0.22	0.17	0.19
$M/\xi_0^2 = 1$	0.16	0.22	0.17	0.20	0.20	0.22	0.17
$M/\xi_0^2 = 4$	0.19	0.16	0.17	0.14	0.15	0.16	0.13
$M/\xi_0^2 = 16$	0.17	0.14	0.10	0.11	0.04	0.04	0.03

α near 0 (Fig. 6.5(b) and (d)) are smaller than the corresponding p_1 values from the multiplicative approach (Fig. 6.5 (a) and (c)). Similar to $P_{\rm sum}$ calculated from each individual type of signal in Fig. 6.5, p_1 values at $\alpha = 0$ using signals with high noise level $\eta_{\rm s} = \eta_{\rm h} = 0.10$ are more than one order of magnitude smaller than those using signals with low noise level $\eta_{\rm s} = \eta_{\rm h} = 0.01$.

6.4 Conclusions

The posterior probability distribution (A-12) based on an inverse gamma prior and a normal likelihood has been derived for data from a single signal type. The posterior probability can be written as a function of four dimensionless quantities. Asymptotic study shows that the largest posterior probability value tends to 1 when the number of data points tends to ∞. A critical ratio is the mode of the inverse gamma prior to the true variance of the normally distributed noise. This ratio determines how the posterior probability varies with the shape parameter of the inverse gamma prior. Numerical results based on the analytic expression (A-23) are consistent with the conclusions of our theoretical analysis: sums of a few of the largest posterior probabilities are very similar to each other when the shape parameter is close to 0, regardless of the chosen prior mode.

To apply the Bayesian formulation, Eq. (A-12), we consider an identification of creep parameters from indentation. This problem was studied by Zhang and Needleman [4] using a Bayesian-type approach that turns out to be a special case of the methodology in the current paper. Simulations were conducted in which noisy data were generated for two types of indentation signals using pre-calculated solutions in a database. Analyses of 100 different realizations are performed for each combination of noise level and data type. The results of the simulation are consistent with

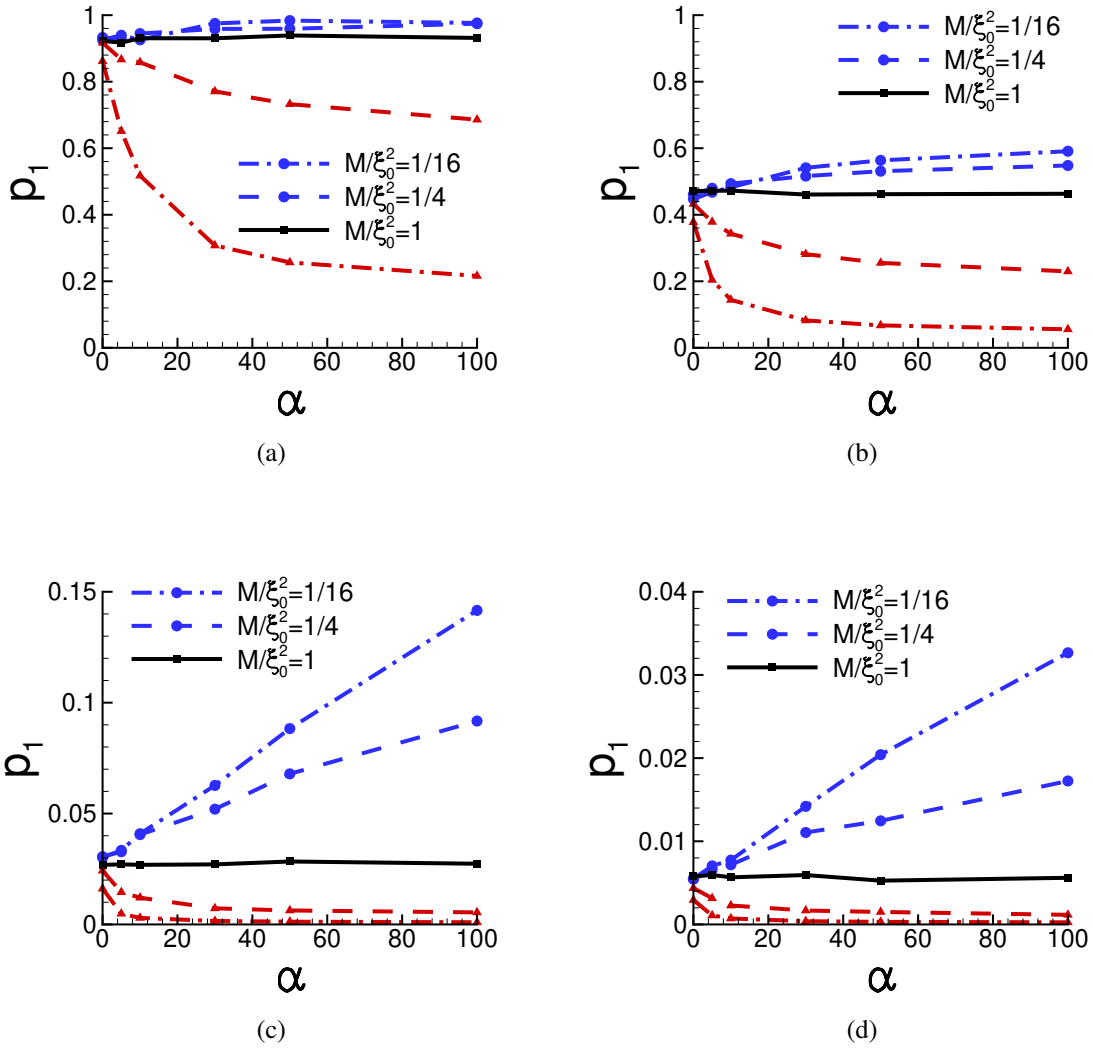

Figure 6.6: Variation of p_1, averages of largest posterior probability over 100 replications, with various parameter values M/ξ_0^2 and α. The four plots correspond to (a) Multiplicative approach Eq. (A-27) with $\eta_s = \eta_h = 0.01$. (b) Additive approach Eq. (A-29) with $\eta_s = \eta_h = 0.01$. (c) Multiplicative approach Eq. (A-27) with $\eta_s = \eta_h = 0.10$. (d) Additive approach Eq. (A-29) with $\eta_s = \eta_h = 0.10$. In all four plots, the curves from top to bottom correspond to $M/\xi_0^2 = 1/16$, $M/\xi_0^2 = 1/4$, $M/\xi_0^2 = 1$, $M/\xi_0^2 = 4$ and $M/\xi_0^2 = 16$, respectively.

the conclusions from both the analytical analysis in Section 26.2.3 and the numerical calculations from the analytical expression, Eq. (A-23). A comparison between the classical Bayesian approach and an additive approach is provided.

Importantly, our analysis confirms that the noninformative prior corresponding to $\alpha = \beta = 0$ is a good default choice for the prior of ξ^2.

7. CONCLUSIONS AND FUTURE WORK

"I may not have gone where I intended to go, but I think I have ended up where I needed to be."

– Douglas Adams

A Bayesian-type statistical approach was developed that incorporates heuristic aspects in order to limit the amount of computation needed for plastic material property identification. The proposed approach was used to identify plastic material properties for three types of elastic-plastic constitutive descriptions: rate-independent isotropically hardening plastic materials, plastically compressible materials and power-law creep materials. Synthetic "experimental" indentation responses were used for the parameter identification for both noise-free and noise-contaminated data.

We started by considering conical indentation for three sets of plastic material properties that give rise to essentially identical curves of indentation force versus indentation depth. We built the database for the Bayesian-type analysis using finite element calculations for a relatively coarse set of parameter values and use interpolation to refine the database. We showed that by taking account of residual surface profiles in addition to indentation force versus indentation depth data, the plastic properties could be identified using the proposed Bayesian-type statistical approach. The effect of fluctuations ("noise") superposed on the "experimental" data was also considered and a good estimate of the uniaxial stress-strain response was obtained for each material both in the absence of fluctuations and in the presence of sufficiently small fluctuations. The sensitivity of the representation of the predicted uniaxial stress-strain response to fluctuations increases with increasing strain hardening. Refining the interpolated database grids gives improved predictions up to a point. Without noise, an over refined database grid can lead to a somewhat less accurate prediction due to numerical errors associated with interpolation. With noise and with increasing database grid refinement, there is a rather wide range of predicted values of the plastic properties with similar values of the posterior probability. Over refinement can lead to an increasing range of

predicted responses due to the refinement fitting the noise and not only the underlying data.

We then considered four characterizations of plastic uniaxial stress-strain response in a rate-independent plastic framework and used the databases constructed with these four strain hardening relations to infer the uniaxial plastic stress-strain response of three weakly rate-dependent materials. We used the Bayesian-type statistical approach and showed that the identification of the hardening relation parameters and the associated uniaxial stress-strain response is not very sensitive to the form of the power-law strain hardening relation chosen even with data that has significant noise. We also found that the specific form of strain hardening relation does not affect the sensitivity of the predicted stress-strain response to the noise amplitude of the data.

Next we identified the plastic property values and the corresponding uniaxial stress-strain responses of two sets of plastically compressible properties represented for two real materials. The materials are characterized by a Deshpande-Fleck constitutive relation with three plastic properties. Both noise-free and noise-contaminated responses from spherical indentation were considered in the Bayesian-type statistical approach. The initial coarse database with only 140 full field finite element solutions was constructed for each material. Linear interpolation between the finite element solution data was used to create the finer databases with 10416 solutions used for property identification. We found that the identified uniaxial stress-strain responses are good approximations of those of the "experimental" input materials, particularly if surface profile data is used. The quality of the approximation decreases with increasing noise amplitude, but can still provide at least a good qualitative representation for a moderate value of noise amplitude. A good fit to indentation data does not guarantee a good fit to the uniaxial stress-strain response of a plastically compressible material. Plastic compressibility was found to have a relatively small effect on the correction factor in the Oliver-Pharr relation [81] between the unloading slope and the effective (or reduced) elastic modulus. The indentation response of the plastically compressible materials can be well-represented by a nearly incompressible plastic constitutive relation but the inferred uniaxial stress-strain response is a poor representation of the "experimental" material uniaxial stress-strain response. The predicted residual surface profile is less dependent on the assumed elastic constant

values than is the indentation force versus indentation depth response. The indentation force versus indentation depth responses in spherical indentation for three materials with very different uniaxial stress-strain curves were found to be indistinguishable if the indentation depth is sufficiently small but are distinguishable if the indentation depth is sufficiently large.

We also characterized power-law creep parameters as well as the corresponding uniaxial creep response and uniaxial stress relaxation response for materials representative of three real materials. The creep response is apparently characterized by two parameters, a creep exponent and a pre-exponential factor. However, the dimensions of the pre-exponential factor depend on the value of the creep exponent and comparing responses of different power-law creep materials requires consideration of three parameters, the creep exponent, a representative stress and a representative strain rate. We simulated the constant load and hold indentation creep tests, considered the residual surface profile and the indentation depth versus time response. We found that the Bayesian-type statistical approach provides the values of power-law creep parameters that provide a good fit to the indentation responses of all the materials considered when based on noise-free data and for sufficiently small noise amplitudes. The uniaxial creep and uniaxial stress relaxation responses using the identified creep parameters were found to provide a very good approximation to the "experimental" responses for a sufficiently small values of creep exponent (Se with $n = 1.15$) but a less good agreement for the largest value of creep exponent (Sn with $n = 6.60$) considered. A good agreement with the indentation response does not guarantee good agreement with the uniaxial responses. In the circumstances analyzed, different values of the power-law creep parameters did give reasonably good fits to the "experimental" indentation data, particularly for noisy data, but no cases were found where very different values of both power-law creep parameters gave nearly the same indentation response. The uniaxial creep response is found to be more sensitive to the accuracy of the predictions, and therefore to noise, than the uniaxial stress relaxation response. As for time independent materials, the sensitivity to noise also increases with increasing stress exponent. We found that if the noise level is sufficiently small, for Se (n = 1.15), the predictions of both the analytical models of Bower et al. [69] and of Ginder et al. [151] are in very good

agreement with those of the "experimental" material, while the model of Bower et al. [69] provides a good fit for all three values of creep stress exponent and the corresponding pre-exponential factor.

We further derived a rigorous Bayesian formulation for material properties identification considering single signal type as well as various signal types. Both analyses and numerical simulations were used to show that the Bayesian-type statistical approach used in the studies of this thesis is a limiting form of the more rigorous formulation with recommended prior parameter values. A method using a weighted average of posterior distributions from different signal types was proposed for circumstances where multiple signal types are analyzed simultaneously. This method was compared with a classical Bayesian approach that uses a joint likelihood.

All cases of material property identification in this dissertation have been based on numerically generated "experimental" responses thus the application of the approach to real experimental measurements would be an important further step. Also, the constitutive relations considered have been rather simple. Extension to more complex constitutive relations accounting for plastic anisotropy as for single crystals and textured polycrystals is possible in principle and would be worthwhile. As is well-known, at the scale of microns and below, there is a significant indentation size effect. A wide variety of size dependent constitutive relations have been proposed with parameters that are difficult to identify. Using the Bayesian-type formulation developed to identify such parameters would be useful.

The extent to which the more rigorous formulation can improve the prediction of material properties from indentation measurements, particularly, for more complex constitutive descriptions, merits exploration. Finally, as noted with regard to size dependent plasticity, but true more generally, the appropriate constitutive description to characterize the mechanical response of a material in some circumstances of interest is not known. Extending the framework here to assess the appropriateness of competing constitutive relations would be an important development.

REFERENCES

[1] Z. Shi, X. Feng, Y. Huang, J. Xiao, and K. C. Hwang, "The equivalent axisymmetric model for berkovich indenters in power-law hardening materials," *International Journal of Plasticity*, vol. 26, 2010.

[2] Y. Zhang, J. D. Hart, and A. Needleman, "Identification of plastic properties from conical indentation using a bayesian-type statistical approach," *Journal of Applied Mechanics*, vol. 86, no. 1, p. 011002, 2019.

[3] C. Su, E. G. Herbert, S. Sohn, J. A. LaManna, W. C. Oliver, and G. M. Pharr, "Measurement of power-law creep parameters by instrumented indentation methods," *Journal of the Mechanics and Physics of Solids*, vol. 61, 2013.

[4] Y. Zhang and A. Needleman, "On the identification of power-law creep parameters from conical indentation," *Proceedings of the Royal Society A*, vol. 477, no. 2252, p. 20210233, 2021.

[5] T. Bayes, "Lii. an essay towards solving a problem in the doctrine of chances. by the late rev. mr. bayes, frs communicated by mr. price, in a letter to john canton, amfr s," *Philosophical transactions of the Royal Society of London*, no. 53, pp. 370–418, 1763.

[6] P. S. Laplace, "Mémoire sur la probabilité de causes par les évenements," *Mémoire de l'académie royale des sciences*, 1774.

[7] P. S. Laplace, "Memoir on the probability of the causes of events," *Statistical science*, vol. 1, no. 3, pp. 364–378, 1986.

[8] O. B. Sheynin, "Ps laplace's work on probability," *Archive for History of Exact Sciences*, vol. 16, no. 2, pp. 137–187, 1976.

[9] L. Daston, "How probabilities came to be objective and subjective," *Historia Mathematica*, vol. 21, no. 3, pp. 330–344, 1994.

[10] P.-S. Laplace, "Mémoire sur les approximations des formules qui sont fonctions de très grands nombres et sur leur applications aux probabilités," *Memoires de l'Academie des Sciences de Paris*, 1810.

[11] L. M. Verburgt, "The objective and the subjective in mid-nineteenth-century british probability theory," *Historia Mathematica*, vol. 42, no. 4, pp. 468–487, 2015.

[12] J. Aldrich, "R. a. fisher on bayes and bayes' theorem," *Bayesian Analysis*, vol. 3, no. 1, pp. 161–170, 2008.

[13] S. B. McGrayne, *The theory that would not die*. Yale University Press, 2011.

[14] H. Jeffreys, *Theory of Probability*. Clarendon Press, Oxford, 1939.

[15] E. Simpson, "Edward simpson: Bayes at bletchley park," *Significance*, vol. 7, no. 2, pp. 76–80, 2010.

[16] A. Bailey, "Credibility procedures: Laplace's generalization of bayes' rule and the combination of collateral knowledge with observed data," *New York State Insurance Department.*, 1950.

[17] L. J. Savage, *The Foundations of Statistics*. Wiley, New York, 1954.

[18] L. H. Edwards, W. and L. Savage, "Bayesian statistical inference for psychological research," *sychological review*, no. 70, p. 193, 1950.

[19] D. Lindley, "A statistical paradox," *Biometrika*, no. 44(1/2), pp. 187–192, 1957.

[20] D. Lindley, "The future of statistics: a bayesian 21st century," *Advances in Applied Probability*, no. 7), pp. 106–115, 1975.

[21] D. Lindley, "Some comments on bayes factors," *Journal of Statistical Planning and Inference*, no. 61), pp. 181–189, 1997.

[22] J. Cornfield, "Method of estimating comparative rates from clinical data. applications to cancer of the lung, breast and cervix," *Journal of the National Cancer Institute*, no. 11), pp. 1269–75, 1951.

[23] A. B. Hill, "Observation and experiment," *New England Journal of Medicine*, 1953.

[24] J. Cornfield, "Statistical relationships and proof in medicine," *The American Statistician*, 1954.

[25] J. Cornfield *et al.*, "Smoking and lung cancer: Recent evidence and a discussion of some questions," *Journal of the National Cancer Institute*, 1959.

[26] P. Diaconis, "The markov chain monte carlo revolution," *Bulletin of the American Mathematical Society*, vol. 46, no. 2, pp. 179–205, 2009.

[27] N. Metropolis, A. W. Rosenbluth, M. N. Rosenbluth, A. H. Teller, and E. Teller, "Equation of state calculations by fast computing machines," *The journal of chemical physics*, vol. 21, no. 6, pp. 1087–1092, 1953.

[28] W. K. Hastings, "Monte carlo sampling methods using markov chains and their applications," 1970.

[29] J. Besag, "Digital image processing: Towards bayesian image analysis," *Journal of Applied statistics*, vol. 16, no. 3, pp. 395–407, 1989.

[30] J. Besag, J. York, and A. Mollié, "Bayesian image restoration, with two applications in spatial statistics," *Annals of the institute of statistical mathematics*, vol. 43, no. 1, pp. 1–20, 1991.

[31] K. M. Hanson, "Introduction to bayesian image analysis," in *Medical Imaging 1993: Image Processing*, vol. 1898, pp. 716–731, International Society for Optics and Photonics, 1993.

[32] F. Ball, Y. Cai, J. Kadane, and A. O'hagan, "Bayesian inference for ion–channel gating mechanisms directly from single–channel recordings, using markov chain monte carlo," *Proceedings of the Royal Society of London. Series A: Mathematical, Physical and Engineering Sciences*, vol. 455, no. 1988, pp. 2879–2932, 1999.

[33] A. D. Marrs, "Sequential bayesian estimation for tracking the composition of growing silicon-germanium alloys," *Proceedings of the Royal Society of London. Series A: Mathematical, Physical and Engineering Sciences*, vol. 457, no. 2009, pp. 1137–1151, 2001.

[34] P. D. O'Neill and G. O. Roberts, "Bayesian inference for partially observed stochastic epidemics," *Journal of the Royal Statistical Society: Series A (Statistics in Society)*, vol. 162, no. 1, pp. 121–129, 1999.

[35] F. Altarelli, A. Braunstein, L. Dall'Asta, A. Lage-Castellanos, and R. Zecchina, "Bayesian inference of epidemics on networks via belief propagation," *Physical review letters*, vol. 112, no. 11, p. 118701, 2014.

[36] C.-P. Lin and B. N. Danforth, "How do insect nuclear and mitochondrial gene substitution patterns differ? insights from bayesian analyses of combined datasets," *Molecular phylogenetics and evolution*, vol. 30, no. 3, pp. 686–702, 2004.

[37] M. Higueras, P. Puig, E. A. Ainsbury, and K. Rothkamm, "A new inverse regression model applied to radiation biodosimetry," *Proceedings of the Royal Society A: Mathematical, Physical and Engineering Sciences*, vol. 471, no. 2174, p. 20140588, 2015.

[38] E. Prudencio, P. Bauman, D. Faghihi, K. Ravi-Chandar, and J. Oden, "A computational framework for dynamic data-driven material damage control, based on bayesian inference and model selection," *International Journal for Numerical Methods in Engineering*, vol. 102, no. 3-4, pp. 379–403, 2015.

[39] G. King, A. Lovell, L. Neufcourt, and F. Nunes, "Direct comparison between bayesian and frequentist uncertainty quantification for nuclear reactions," *Physical review letters*, vol. 122, no. 23, p. 232502, 2019.

[40] L. Yang, C. Lin, Y. Zhang, P. Wen, H. Jia, D. Wang, N. Ma, F. Yang, F. Zhong, S. Zhong, *et al.*, "Bayesian analysis on interactions of exotic nuclear systems," *Physics Letters B*, vol. 807, p. 135540, 2020.

[41] R. Bandyopadhyay, V. Prithivirajan, A. D. Peralta, and M. D. Sangid, "Microstructure-sensitive critical plastic strain energy density criterion for fatigue life prediction across various loading regimes," *Proceedings of the Royal Society A*, vol. 476, no. 2236, p. 20190766, 2020.

[42] G. Cua and T. Heaton, "The virtual seismologist (vs) method: A bayesian approach to earthquake early warning," in *Earthquake early warning systems*, pp. 97–132, Springer, 2007.

[43] D. Walsh, R. Arnold, and J. Townend, "A bayesian approach to determining and parametrizing earthquake focal mechanisms," *Geophysical Journal International*, vol. 176, no. 1, pp. 235–255, 2009.

[44] H. Vasyura-Bathke, J. Dettmer, A. Steinberg, S. Heimann, M. P. Isken, O. Zielke, P. M. Mai, H. Sudhaus, and S. Jónsson, "The bayesian earthquake analysis tool," *Seismological Research Letters*, vol. 91, no. 2A, pp. 1003–1018, 2020.

[45] A. Vigliotti, G. Csányi, and V. Deshpande, "Bayesian inference of the spatial distributions of material properties," *Journal of the Mechanics and Physics of Solids*, vol. 118, pp. 74–97, 2018.

[46] Y. Zhang and A. Needleman, "Characterization of plastically compressible solids via spherical indentation," *Journal of the Mechanics and Physics of Solids*, vol. 148, p. 104283, 2021.

[47] J. Ma, H. Xie, K. Song, and H. Liu, "A bayesian driver agent model for autonomous vehicles system based on knowledge-aware and real-time data," *Sensors*, vol. 21, no. 2, p. 331, 2021.

[48] S. Suresh, J. Spatz, J. P. Mills, A. Micoulet, M. Dao, C. Lim, M. Beil, and T. Seufferlein, "Connections between single-cell biomechanics and human disease states: gastrointestinal cancer and malaria," *Acta biomaterialia*, vol. 1, no. 1, pp. 15–30, 2005.

[49] G. Krishnamurthy, D. B. Ennis, A. Itoh, W. Bothe, J. C. Swanson, M. Karlsson, E. Kuhl, D. C. Miller, and N. B. Ingels Jr, "Material properties of the ovine mitral valve anterior

leaflet in vivo from inverse finite element analysis," *American Journal of Physiology-Heart and Circulatory Physiology*, vol. 295, no. 3, pp. H1141–H1149, 2008.

[50] S. Budday, R. Nay, R. de Rooij, P. Steinmann, T. Wyrobek, T. C. Ovaert, and E. Kuhl, "Mechanical properties of gray and white matter brain tissue by indentation," *Journal of the mechanical behavior of biomedical materials*, vol. 46, pp. 318–330, 2015.

[51] J. Yang, H. C. Cramer III, and C. Franck, "Extracting non-linear viscoelastic material properties from violently-collapsing cavitation bubbles," *Extreme Mechanics Letters*, vol. 39, p. 100839, 2020.

[52] H. Ma and J. C. Suhling, "A review of mechanical properties of lead-free solders for electronic packaging," *Journal of materials science*, vol. 44, no. 5, pp. 1141–1158, 2009.

[53] S.-H. Kee, J. W. Kang, B.-J. Choi, J. Kwon, M. Candelaria, *et al.*, "Evaluation of static and dynamic residual mechanical properties of heat-damaged concrete for nuclear reactor auxiliary buildings in korea using elastic wave velocity measurements," *Materials*, vol. 12, no. 17, p. 2695, 2019.

[54] S. Suresh, "Biomechanics and biophysics of cancer cells," *Acta Materialia*, vol. 55, no. 12, pp. 3989–4014, 2007.

[55] M. S. Molla, D. R. Katti, and K. S. Katti, "Mechanobiological evaluation of prostate cancer metastasis to bone using an in vitro prostate cancer testbed," *Journal of Biomechanics*, vol. 114, p. 110142, 2021.

[56] L. Claes and J. Cunningham, "Monitoring the mechanical properties of healing bone," *Clinical Orthopaedics and Related Research®*, vol. 467, no. 8, pp. 1964–1971, 2009.

[57] P. Peralta, R. O. Ruiz, and A. A. Taflanidis, "Bayesian identification of electromechanical properties in piezoelectric energy harvesters," *Mechanical Systems and Signal Processing*, vol. 141, p. 106506, 2020.

[58] J.-M. Arbona, S. Herbert, E. Fabre, and C. Zimmer, "Inferring the physical properties of yeast chromatin through bayesian analysis of whole nucleus simulations," *Genome biology*, vol. 18, no. 1, pp. 1–15, 2017.

[59] B. S. Michalopoulou, Z.H. and L. Axe, "Bayesian estimation of optical properties of nearshore estuarine waters: A gibbs sampling approach," *IEEE transactions on geoscience and remote sensing*, 2009.

[60] F. Plouraboué, E. I. Thiam, B. Delmotte, and E. Climent, "Identification of internal properties of fibres and micro-swimmers," *Proceedings of the Royal Society A: Mathematical, Physical and Engineering Sciences*, vol. 473, no. 2197, p. 20160517, 2017.

[61] D. Tabor, *The hardness of metals*. Oxford university press, 1951.

[62] G. E. Dieter and D. J. Bacon, *Mechanical metallurgy*, vol. 3. McGraw-hill New York, 1976.

[63] H. Chandler *et al.*, *Hardness testing*. ASM international, 1999.

[64] H. Hertz, "On the contact of elastic solids," *Z. Reine Angew. Mathematik*, vol. 92, pp. 156–171, 1881.

[65] N. Stilwell and D. Tabor, "Elastic recovery of conical indentations," *Proceedings of the Physical Society (1958-1967)*, vol. 78, no. 2, p. 169, 1961.

[66] R. Hill, *The mathematical theory of plasticity*, vol. 11. Oxford university press, 1950.

[67] K. Johnson, "The correlation of indentation experiments," *Journal of the Mechanics and Physics of Solids*, vol. 18, no. 2, pp. 115–126, 1970.

[68] R. Hill, B. Storåkers, and A. Zdunek, "A theoretical study of the brinell hardness test," *Proceedings of the Royal Society of London. A. Mathematical and Physical Sciences*, vol. 423, no. 1865, pp. 301–330, 1989.

[69] A. Bower, N. A. Fleck, A. Needleman, and N. Ogbonna, "Indentation of a power law creeping solid," *Proceedings of the Royal Society of London. Series A: Mathematical and Physical Sciences*, vol. 441, no. 1911, pp. 97–124, 1993.

[70] S. Bulychev, V. Alekhin, M. Shorshorov, A. Ternovskii, and G. Shnyrev, "Determining young's modulus from the indentor penetration diagram," *Ind. Lab.*, vol. 41, no. 9, pp. 1409–1412, 1975.

[71] J. B. Pethicai, R. Hutchings, and W. C. Oliver, "Hardness measurement at penetration depths as small as 20 nm," *Philosophical Magazine A*, vol. 48, pp. 593–606, apr 1983.

[72] J. Loubet, J. Georges, O. Marchesini, and G. Meille, "Vickers indentation curves of magnesium oxide (mgo)," 1984.

[73] M. F. Doerner and W. D. Nix, "A method for interpreting the data from depth-sensing indentation instruments," *Journal of Materials Research*, vol. 1, 1986.

[74] W. Oliver and G. Pharr, "An improved technique for determining hardness and elastic modulus using load and displacement sensing indentation experiments," *Journal of Materials Research*, vol. 7, 1992.

[75] G. M. Pharr and W. C. Oliver, "Measurement of thin film mechanical properties using nanoindentation," *MRS Bulletin*, vol. 17, 1992.

[76] A. Bolshakov, W. C. Oliver, and G. M. Pharr, "Finite element studies of the influence of pile-up on the analysis of nanoindentation data," 1996.

[77] T. Y. Tsui, W. C. Oliver, and G. M. Pharr, "Indenter geometry effects on the measurement of mechanical properties by nanoindentation with sharp indenters," 1996.

[78] A. Bolshakov and G. M. Pharr, "Influences of pileup on the measurement of mechanical properties by load and depth sensing indentation techniques," *Journal of Materials Research*, vol. 13, 1998.

[79] J. G. Swadener, B. Taljat, and G. M. Pharr, "Measurement of residual stress by load and depth sensing indentation with spherical indenters," *Journal of Materials Research*, vol. 16, 2001.

[80] G. M. Pharr and A. Bolshakov, "Understanding nanoindentation unloading curves," *Journal of Materials Research*, vol. 17, 2002.

[81] W. C. Oliver and G. M. Pharr, "Measurement of hardness and elastic modulus by instrumented indentation: Advances in understanding and refinements to methodology," *Journal of Materials Research*, vol. 19, 2004.

[82] G. M. Pharr, E. G. Herbert, and Y. Gao, "The indentation size effect: A critical examination of experimental observations and mechanistic interpretations," *Annual Review of Materials Research*, vol. 40, 2010.

[83] M. Dao, N. Chollacoop, K. J. V. Vliet, T. A. Venkatesh, and S. Suresh, "Computational modeling of the forward and reverse problems in instrumented sharp indentation," *Acta Materialia*, vol. 49, 2001.

[84] N. Ogasawara, N. Chiba, and X. Chen, "Representative strain of indentation analysis," *Journal of Materials Research*, vol. 20, 2005.

[85] Y. T. Cheng and C. M. Cheng, "Scaling approach to conical indentation in elastic-plastic solids with work hardening," *Journal of Applied Physics*, vol. 84, 1998.

[86] N. Huber and C. Tsakmakis, "Determination of constitutive properties from spherical indentation data using neural networks. part i: The case of pure kinematic hardening in plasticity laws," *Journal of the Mechanics and Physics of Solids*, vol. 47, 1999.

[87] N. Huber and C. Tsakmakis, "Determination of constitutive properties from spherical indentation data using neural networks. part ii: Plasticity with nonlinear isotropic and kinematic hardening," *Journal of the Mechanics and Physics of Solids*, vol. 47, 1999.

[88] N. Huber and E. Tyulyukovskiy, "A new loading history for identification of viscoplastic properties by spherical indentation," *Journal of Materials Research*, vol. 19, 2004.

[89] E. Tyulyukovskiy and N. Huber, "Identification of viscoplastic material parameters from spherical indentation data: Part i. neural networks," *Journal of Materials Research*, vol. 21, 2006.

[90] D. Klotzer, C. Ullner, E. Tyulyukovskiy, and N. Huber, "Identification of viscoplastic material parameters from spherical indentation data: Part ii. experimental validation of the method," *Journal of Materials Research*, vol. 21, 2006.

[91] Y. T. Cheng and C. M. Cheng, "Can stress-strain relationships be obtained from indentation curves using conical and pyramidal indenters?," *Journal of Materials Research*, vol. 14, 1999.

[92] J. Alkorta, J. M. Martinez-Esnaola, and J. G. Sevillano, "Absence of one-to-one correspondence between elastoplastic properties and sharp-indentation load-penetration data," *Journal of Materials Research*, vol. 20, 2005.

[93] X. Chen, N. Ogasawara, M. Zhao, and N. Chiba, "On the uniqueness of measuring elastoplastic properties from indentation: The indistinguishable mystical materials," *Journal of the Mechanics and Physics of Solids*, vol. 55, 2007.

[94] M. Wang, J. Wu, X. Zhan, R. Guo, Y. Hui, and H. Fan, "On the determination of the anisotropic plasticity of metal materials by using instrumented indentation," *Materials and Design*, vol. 111, 2016.

[95] M. Wang, J. Wu, Y. Hui, Z. Zhang, X. Zhan, and R. Guo, "Identification of elastic-plastic properties of metal materials by using the residual imprint of spherical indentation," *Materials Science and Engineering A*, vol. 679, 2017.

[96] M. Mostafavi, D. M. Collins, B. Cai, R. Bradley, R. C. Atwood, C. Reinhard, X. Jiang, M. Galano, P. D. Lee, and T. J. Marrow, "Yield behavior beneath hardness indentations in ductile metals, measured by three-dimensional computed x-ray tomography and digital volume correlation," *Acta Materialia*, vol. 82, 2015.

[97] M. Mostafavi, R. Bradley, D. E. Armstrong, and T. J. Marrow, "Quantifying yield behaviour in metals by x-ray nanotomography," *Scientific Reports*, vol. 6, 2016.

[98] I. Babuska, Z. Sawlan, M. Scavino, B. Szabo, and R. Tempone, "Bayesian inference and model comparison for metallic fatigue data," *Computer Methods in Applied Mechanics and Engineering*, vol. 304, 2016.

[99] A. Rovinelli, M. D. Sangid, H. Proudhon, Y. Guilhem, R. A. Lebensohn, and W. Ludwig, "Predicting the 3d fatigue crack growth rate of small cracks using multimodal data via bayesian networks: In-situ experiments and crystal plasticity simulations," *Journal of the Mechanics and Physics of Solids*, vol. 115, 2018.

[100] J. Worthen, G. Stadler, N. Petra, M. Gurnis, and O. Ghattas, "Towards adjoint-based inversion for rheological parameters in nonlinear viscous mantle flow," *Physics of the Earth and Planetary Interiors*, vol. 234, 2014.

[101] S. Madireddy, B. Sista, and K. Vemaganti, "A bayesian approach to selecting hyperelastic constitutive models of soft tissue," *Computer Methods in Applied Mechanics and Engineering*, vol. 291, 2015.

[102] E. Asaadi and P. S. Heyns, "A computational framework for bayesian inference in plasticity models characterisation," *Computer Methods in Applied Mechanics and Engineering*, vol. 321, 2017.

[103] H. Rappel, L. A. Beex, and S. P. Bordas, "Bayesian inference to identify parameters in viscoelasticity," *Mechanics of Time-Dependent Materials*, vol. 22, 2018.

[104] E. E. Prudencio, P. T. Bauman, S. V. Williams, D. Faghihi, K. Ravi-Chandar, and J. T. Oden, "A dynamic data driven application system for real-time monitoring of stochastic damage," vol. 18, 2013.

[105] E. E. Prudencio, P. T. Bauman, D. Faghihi, K. Ravi-Chandar, and J. T. Oden, "A computational framework for dynamic data-driven material damage control, based on bayesian inference and model selection," *International Journal for Numerical Methods in Engineering*, vol. 102, 2015.

[106] P. Fernandez-Zelaia, V. R. Joseph, S. R. Kalidindi, and S. N. Melkote, "Estimating mechanical properties from spherical indentation using bayesian approaches," *Materials and Design*, vol. 147, 2018.

[107] A. Needleman, V. Tvergaard, and E. V. der Giessen, "Indentation of elastically soft and plastically compressible solids," *Acta Mechanica Sinica/Lixue Xuebao*, vol. 31, 2015.

[108] P. D. Hoff, *A first course in Bayesian statistical methods*, vol. 580. Springer, 2009.

[109] M. R. 2016a, *function normrnd*. Natick, Massachusetts: The MathWorks Inc., 2016.

[110] J. Luo, J. Lin, and T. A. Dean, "A study on the determination of mechanical properties of a power law material by its indentation force-depth curve," *Philosophical Magazine*, vol. 86, 2006.

[111] J. L. Bucaille, S. Stauss, E. Felder, and J. Michler, "Determination of plastic properties of metals by instrumented indentation using different sharp indenters," *Acta Materialia*, vol. 51, 2003.

[112] Y. P. Cao and J. Lu, "A new method to extract the plastic properties of metal materials from an instrumented spherical indentation loading curve," *Acta Materialia*, vol. 52, 2004.

[113] M. Beghini, L. Bertini, and V. Fontanari, "Evaluation of the stress-strain curve of metallic materials by spherical indentation," *International Journal of Solids and Structures*, vol. 43, 2006.

[114] J. Luo and J. Lin, "A study on the determination of plastic properties of metals by instrumented indentation using two sharp indenters," *International Journal of Solids and Structures*, vol. 44, 2007.

[115] J. J. Kang, A. A. Becker, W. Wen, and W. Sun, "Extracting elastic-plastic properties from experimental loading-unloading indentation curves using different optimization techniques," *International Journal of Mechanical Sciences*, vol. 144, 2018.

[116] L. Meng, P. Breitkopf, B. Raghavan, G. Mauvoisin, O. Bartier, and X. Hernot, "Identification of material properties using indentation test and shape manifold learning approach," *Computer Methods in Applied Mechanics and Engineering*, vol. 297, 2015.

[117] O. Iracheta, C. J. Bennett, and W. Sun, "A holistic inverse approach based on a multi-objective function optimisation model to recover elastic-plastic properties of materials from the depth-sensing indentation test," *Journal of the Mechanics and Physics of Solids*, vol. 128, 2019.

[118] *ABAQUS/CAE*. Johnston, RI: Simulia, Dassault Systemes, 2017.

[119] A. Needleman, "Postbifurcation behavior and imperfection sensitivity of elastic-plastic circular plates," *International Journal of Mechanical Sciences*, vol. 17, no. 1, pp. 1–13, 1975.

[120] G. R. Johnson and W. H. Cook, "Fracture characteristics of three metals subjected to various strains, strain rates, temperatures and pressures," *Engineering fracture mechanics*, vol. 21, no. 1, pp. 31–48, 1985.

[121] L. Lu, M. Dao, P. Kumar, U. Ramamurty, G. E. Karniadakis, and S. Suresh, "Extraction of mechanical properties of materials through deep learning from instrumented indentation," *Proceedings of the National Academy of Sciences of the United States of America*, vol. 117, 2020.

[122] E. Asaadi, P. S. Heyns, R. T. Haftka, and M. Tootkaboni, "On the value of test data for reducing uncertainty in material models: Computational framework and application to spherical indentation," *Computer Methods in Applied Mechanics and Engineering*, vol. 346, 2019.

[123] M. Wang and J. Wu, "Identification of plastic properties of metal materials using spherical indentation experiment and bayesian model updating approach," *International Journal of Mechanical Sciences*, vol. 151, 2019.

[124] L. Meng, P. Breitkopf, B. Raghavan, G. Mauvoisin, O. Bartier, and X. Hernot, "On the study of mystical materials identified by indentation on power law and voce hardening solids," *International Journal of Material Forming*, vol. 12, 2019.

[125] L. Meng, B. Raghavan, O. Bartier, X. Hernot, G. Mauvoisin, and P. Breitkopf, "An objective meta-modeling approach for indentation-based material characterization," *Mechanics of Materials*, vol. 107, 2017.

[126] L. Meng, P. Breitkopf, and G. L. Quilliec, "An insight into the identifiability of material properties by instrumented indentation test using manifold approach based on p-h curve and imprint shape," *International Journal of Solids and Structures*, vol. 106-107, 2017.

[127] Y. Toivola, A. Stein, and R. F. Cook, "Depth-sensing indentation response of ordered silica foam," *Journal of Materials Research*, vol. 19, 2004.

[128] U. Ramamurty and M. C. Kumaran, "Mechanical property extraction through conical indentation of a closed-cell aluminum foam," *Acta Materialia*, vol. 52, 2004.

[129] A. Kim and K. Tunvir, "Study of al-alloy foam compressive behavior based on instrumented sharp indentation technology," *Journal of Mechanical Science and Technology*, vol. 20, 2006.

[130] B. Li, Y. D. Gu, R. English, G. Rothwell, and X. J. Ren, "Characterisation of nonlinear material parameters of foams based on indentation tests," *Materials and Design*, vol. 30, 2009.

[131] W. Yan and C. L. Pun, "Spherical indentation of metallic foams," *Materials Science and Engineering A*, vol. 527, 2010.

[132] W. Y. Yan and C. L. Pun, "Spherical indentation method to measure mechanical properties of metallic foams," vol. 15, 2011.

[133] P. Clement, S. Meille, J. Chevalier, and C. Olagnon, "Mechanical characterization of highly porous inorganic solids materials by instrumented micro-indentation," *Acta Materialia*, vol. 61, 2013.

[134] A. Yonezu, K. Hirayama, H. Kishida, and X. Chen, "Characterization of the compressive deformation behavior with strain rate effect of low-density polymeric foams," *Polymer Testing*, vol. 50, 2016.

[135] A. Bouterf, J. Adrien, E. Maire, X. Brajer, F. Hild, and S. Roux, "Identification of the crushing behavior of brittle foam: From indentation to oedometric tests," *Journal of the Mechanics and Physics of Solids*, vol. 98, 2017.

[136] N. Kumar, S. N. Khaderi, and K. T. Rao, "Elasto-plastic indentation of auxetic and metal foams," *Journal of Applied Mechanics, Transactions ASME*, vol. 87, 2020.

[137] G. Sun, E. Wang, T. Zhao, G. Zheng, and Q. Li, "Inverse identification of cell-wall material properties of closed-cell aluminum foams based upon vickers nano-indentation tests," *International Journal of Mechanical Sciences*, vol. 176, 2020.

[138] V. S. Deshpande and N. A. Fleck, "Isotropic constitutive models for metallic foams," *Journal of the Mechanics and Physics of Solids*, vol. 48, 2000.

[139] A. M. Boyce, V. S. Deshpande, and N. A. Fleck, "On the indentation resistance of a pc layer on pvc foam substrate," *Advanced Engineering Materials*, vol. 19, 2017.

[140] Y. Zhang and A. Needleman, "Influence of assumed strain hardening relation on plastic stress-strain response identification from conical indentation," *Journal of Engineering Materials and Technology*, vol. 142, no. 3, 2020.

[141] S. B. Hutchens, A. Needleman, and J. R. Greer, "Analysis of uniaxial compression of vertically aligned carbon nanotubes," *Journal of the Mechanics and Physics of Solids*, vol. 59, 2011.

[142] E. Andrews, W. Sanders, and L. J. Gibson, "Compressive and tensile behaviour of aluminum foams," *Materials Science and Engineering A*, vol. 270, 1999.

[143] A. M. Harte, N. A. Fleck, and M. F. Ashby, "Fatigue failure of an open cell and a closed cell aluminum alloy foam," *Acta Materialia*, vol. 47, 1999.

[144] T. W. Capehart and Y. T. Cheng, "Determining constitutive models from conical indentation: Sensitivity analysis," *Journal of Materials Research*, vol. 18, 2003.

[145] G. M. Pharr and W. C. Oliver, "On the generality of the relationship among contact stiffness, contact area and elastic modulus during indentation," *Journal of Materials Research*, vol. 7, 1992.

[146] C. M. Cheng and Y. T. Cheng, "On the initial unloading slope in indentation of elastic-plastic solids by an indenter with an axisymmetric smooth profile," *Applied Physics Letters*, vol. 71, 1997.

[147] Y. T. Cheng and C. M. Cheng, "Scaling relationships in conical indentation of elastic-perfectly plastic solids," *International Journal of Solids and Structures*, vol. 36, 1998.

[148] R. Hill, "Similarity analysis of creep indentation tests," *Proceedings of the Royal Society of London. Series A: Mathematical and Physical Sciences*, vol. 436, 1992.

[149] B. Storakers and P. L. Larsson, "On brinell and boussinesq indentation of creeping solids," *Journal of the Mechanics and Physics of Solids*, vol. 42, 1994.

[150] Y. T. Cheng and C. M. Cheng, "Scaling relationships in indentation of power-law creep solids using self-similar indenters," *Philosophical Magazine Letters*, vol. 81, 2001.

[151] R. S. Ginder, W. D. Nix, and G. M. Pharr, "A simple model for indentation creep," *Journal of the Mechanics and Physics of Solids*, vol. 112, 2018.

[152] J. H. Lee, C. Zhou, C. J. Su, Y. F. Gao, and G. M. Pharr, "Similarity relationships in creep contacts and applications in nanoindentation tests," vol. 1224, 2010.

[153] H. Takagi and M. Fujiwara, "Set of conversion coefficients for extracting uniaxial creep data from pseudo-steady indentation creep test results," *Materials Science and Engineering A*, vol. 602, 2014.

[154] I. C. Choi, B. G. Yoo, Y. J. Kim, M. Y. Seok, Y. Wang, and J. I. Jang, "Estimating the stress exponent of nanocrystalline nickel: Sharp vs. spherical indentation," *Scripta Materialia*, vol. 65, 2011.

[155] P. S. Phani and W. C. Oliver, "A direct comparison of high temperature nanoindentation creep and uniaxial creep measurements for commercial purity aluminum," *Acta Materialia*, vol. 111, 2016.

[156] R. S. Ginder and G. M. Pharr, "Characterization of power-law creep in the solid-acid cshso4 via nanoindentation," *Journal of Materials Research*, vol. 34, no. 7, pp. 1130–1137, 2019.

[157] W. Wen, X. Jin, H. Liu, and W. Sun, "Determination of creep damage properties from small punch creep tests considering pre-straining effect using an inverse approach," *Mechanics of Materials*, vol. 139, 2019.

[158] M. Burley, J. E. Campbell, J. Dean, and T. W. Clyne, "A methodology for obtaining primary and secondary creep characteristics from indentation experiments, using a recess," *International Journal of Mechanical Sciences*, vol. 176, 2020.

[159] A. Bolshakov, W. C. Oliver, and G. M. Pharr, "Influences of stress on the measurement of mechanical properties using nanoindentation: Part ii. finite element simulations," *Journal of Materials Research*, vol. 11, 1996.

[160] S. Etienne, G. Guenin, and J. Perez, "Ultrasonic studies of the elastic coefficients of vitreous selenium about tg," *Journal of Physics D: Applied Physics*, vol. 12, 1979.

[161] R. S. Ginder and G. M. Pharr, "Creep behavior of the solid acid fuel cell material cshso4," *Scripta Materialia*, vol. 139, 2017.

[162] F. A. Mohamed, K. L. Murty, and J. W. Morris, "Harper-dorn creep in al, pb, and sn," *Metallurgical Transactions*, vol. 4, 1973.

[163] T. El-Ashram, "Structure and properties of rapidly solidified pure tin," *Radiation Effects and Defects in Solids*, vol. 161, 2006.

[164] B. Z. Lee and D. N. Lee, "Spontaneous growth mechanism of tin whiskers," *Acta Materialia*, vol. 46, 1998.

[165] I. N. Sneddon, "The relation between load and penetration in the axisymmetric boussinesq problem for a punch of arbitrary profile," *International Journal of Engineering Science*, vol. 3, 1965.

[166] J. Luo, M. Pritschow, A. Flewitt, S. Spearing, N. Fleck, and W. Milne, "Effects of process conditions on properties of electroplated ni thin films for microsystem applications," *Journal of the Electrochemical Society*, vol. 153, no. 10, p. D155, 2006.

[167] S. Fatehiboroujeni, N. Petra, and S. Goyal, "Linearized bayesian inference for youngâĂŹs modulus parameter field in an elastic model of slender structures," *Proceedings of the Royal Society A*, vol. 476, no. 2238, p. 20190476, 2020.

[168] M. Liu, I. McCue, and M. J. Demkowicz, "Quantifying surface deformation around micrometer-scale indents by digital image correlation," *Journal of Materials Research*, pp. 1–14, 2021.

[169] A. F. Bower, *Applied mechanics of solids*. CRC press, 2009.

[170] R. M. Brannon, *Rotation, Reflection, and Frame Changes; Orthogonal tensors in computational engineering mechanics*. Bristol, UK: IOP Publishing, 2018.

[171] T. Belytschko, W. K. Liu, B. Moran, and K. Elkhodary, *Nonlinear finite elements for continua and structures*. John wiley & sons, 2013.

[172] F. Dunne and N. Petrinic, *Introduction to computational plasticity*. Oxford University Press on Demand, 2005.

[173] E. A. de Souza Neto, D. Peric, and D. R. Owen, *Computational methods for plasticity: theory and applications*. John Wiley & Sons, 2011.

[174] J. Lubliner, *Plasticity theory*. Courier Corporation, 1990,2008.

[175] A. J. M. Spencer, *Continuum mechanics*. Courier Corporation, 2004.

[176] L. M. Kachanov, *Foundations of the Theory of Plasticity*, vol. 9. North-Holland Amsterdam, 1971.

[177] J. Chakrabarty, *Applied plasticity*, vol. 88. Springer, 2000.

[178] D. C. Drucker, "A definition of stable inelastic material," tech. rep., BROWN UNIV PROVIDENCE RI, 1957.

[179] A. E. Green and W. Zerna, *Theoretical elasticity*. Oxford University Press, Oxford, 1968.

[180] B. Budiansky, "Remarks on theories of solid and structural mechanics," *Problems of Hydrodynamics and Continuum mechanics*, vol. 77, pp. 77–83, 1969.

[181] A. Needleman, "On finite element formulations for large elastic–plastic deformations," in *Advances and Trends in Structures and Dynamics*, pp. 247–257, Elsevier, 1985.

[182] D. Peirce, C. F. Shih, and A. Needleman, "A tangent modulus method for rate dependent solids," *Computers & Structures*, vol. 18, no. 5, pp. 875–887, 1984.

APPENDIX A

BRIEF SUMMARY OF PLASTICITY THEORY

The classical plasticity theory for metal is briefly summarized. For a more detailed description of plasticity theory history, continuum mechanics and further discussions on special topics, see for example [169, 170, 171, 172, 173, 174, 175, 66, 176, 177, 178].

A.1 Rate-independent plasticity

Rate independent plasticity can be summarized in 4 components:

(1) Decomposition of strain increment or rate of deformation

$$d\epsilon_{ij} = d\epsilon^e_{ij} + d\epsilon^p_{ij} \tag{A-1}$$

We simply consider infinitesimal strain here, for finite strain the decomposition of rate of deformation can be used

$$d_{ij} = d^e_{ij} + d^p_{ij} \tag{A-2}$$

(2) Yield criterion

For example, the commonly used von Mises yield criterion can be expressed as

$$f(\sigma_{ij}, \bar{\epsilon}^p) = \sigma_e - \sigma_y \tag{A-3}$$

with von Mises effective stress σ_e defined by

$$\sigma_e = \sqrt{\frac{3}{2}\sigma'_{ij}\sigma'_{ij}} \qquad \sigma'_{ij} = \sigma_{ij} - \frac{1}{3}\sigma_{kk}\delta_{ij} \tag{A-4}$$

where $\boldsymbol{\sigma}$ is Cauchy stress, $\bar{\epsilon}^p$ is effective plastic strain, and σ_y is flow stress.

(3) Flow rule

Normality hypothesis requires the plastic strain increment perpendicular to the yield surface. (plastic strain rate tensor is perpendicular to a yield surface in the corresponding stress space.) It is one of the consequence of Drucker's postulate, it is about the stability of material during loading and unloading. We assume the relation between plastic strain increment and loading history (accumulated plastic strain and stress states) can be written as

$$d\epsilon_{ij}^{p} = d\bar{\epsilon}^{p} \frac{\partial \Psi}{\partial \sigma_{ij}} \tag{A-5}$$

If the plastic potential Ψ is taken to be yield function $f(\sigma_{ij}, \bar{\epsilon}^{p})$, it is called an associated flow rule since the flow rule is associated with a specific yield criterion. Otherwise, it is called a non-associated flow rule.

(4) Evolution equations

The evolution of variables with deformation needs to be described. For a simple case, only the evolution of flow stress with deformation is considered here by a strain hardening rule. For example, the flow stress is isotropically hardened by accumulated plastic strain magnitude ϵ_{p} in a power law form

$$\mathrm{F}_0: \quad \frac{\sigma_{\mathrm{e}}}{Y} = \left(1 + \frac{\epsilon_{\mathrm{p}}}{\epsilon_0}\right)^{N}, \quad \sigma_{\mathrm{e}} \geq Y \tag{A-6}$$

where Y is the initial yield stress, accumulated plastic strain magnitude is the integration of effective plastic strain increment along deformation history $\epsilon_{\mathrm{p}} = \int d\bar{\epsilon}^{p}$, N is strain hardening exponent and reference strain $\epsilon_0 = Y/E$. In rate-independent plasticity, consistency condition requires stress state cannot exceed yield surface, thus $\sigma_e = \sigma_y$ holds at plastic loading condition.

(5) Elastic unloading

The elastic unloading condition for an isotropically strain hardened material is

$$\sigma'_{ij} d\sigma_{ij} < 0 \tag{A-7}$$

It requires the angle between stress increment tensor and the current deviatoric stress tensor to be

larger than 90°, which brings the stress state back to the inner of yield surface in principle stress space.

Consider an example, an associated plastic flow rule is used for plastic strain increment $d\boldsymbol{\epsilon}^p$

$$d\epsilon_{ij}^p = d\bar{\epsilon}^p \frac{\partial f}{\partial \sigma_{ij}} \tag{A-8}$$

where the yield potential/yield surface is given by

$$f(\sigma_{ij}, \bar{\epsilon}^p) = \sigma_e - \sigma_y \tag{A-9}$$

with von Mises yield criterion

$$\sigma_e = \sqrt{\frac{3}{2}\sigma'_{ij}\sigma'_{ij}} \qquad \sigma'_{ij} = \sigma_{ij} - \frac{1}{3}\sigma_{kk}\delta_{ij} \tag{A-10}$$

where σ_e is von Mises effective stress and σ_y is flow stress. With these equations, the plastic flow rule can be simplified to

$$d\epsilon_{ij}^p = \frac{3}{2}\frac{\sigma'_{ij}}{\sigma_y} d\bar{\epsilon}^p \tag{A-11}$$

Square both sides of $\sigma_e = \sqrt{\frac{3}{2}\sigma'_{ij}\sigma'_{ij}}$ to get $\sigma_e^2 = \frac{3}{2}\sigma'_{ij}\sigma'_{ij}$, and do time derivative of the equation to have

$$\dot{\sigma}_e = \frac{3}{2}\frac{\sigma'_{ij}}{\sigma_e}\dot{\sigma}'_{ij} \tag{A-12}$$

Because $\dot{\sigma}_{ij} = \dot{\sigma}'_{ij}$, so that

$$\dot{\sigma}_e = \frac{3}{2}\frac{\sigma'_{ij}}{\sigma_e}\dot{\sigma}_{ij} \tag{A-13}$$

Multiply both sides by $\dot{\bar{\epsilon}}^p$ (or $d\bar{\epsilon}^p$) and move $\dot{\sigma}_e$ to the right side of equation to get

$$\dot{\bar{\epsilon}}^p = \frac{\dot{\bar{\epsilon}}^p}{\dot{\sigma}_e}\frac{3}{2}\frac{\sigma'_{ij}}{\sigma_e}\dot{\sigma}_{ij} \tag{A-14}$$

From the requirement of consistency condition $\dot{f} = 0$, the effective plastic strain increment $d\bar{\epsilon}^p$

can be expressed as

$$d\bar{\epsilon}^p = \frac{1}{E_p}\frac{3}{2}\frac{\sigma'_{ij}}{\sigma_y}d\sigma_{ij} \tag{A-15}$$

where E_p is the slope of flow stress to effective plastic strain

$$E_p = \frac{d\sigma_y}{d\bar{\epsilon}^p}$$

Given for a uniaxial stress-strain response $\sigma = E\epsilon^e = E_p\epsilon^p = E_t\epsilon$, with Eq.(A-1) we get

$$\frac{1}{E_p} = \frac{1}{E_t} - \frac{1}{E} \tag{A-16}$$

So that the plastic strain increment can be written as

$$d\epsilon^p_{ij} = \frac{3}{2}\frac{\sigma'_{ij}}{\sigma_y}(\frac{1}{E_t} - \frac{1}{E})\frac{3}{2}\frac{\sigma'_{kl}}{\sigma_y}d\sigma_{kl} = \frac{9}{4}(\frac{1}{E_t} - \frac{1}{E})\frac{\sigma'_{ij}\sigma'_{kl}}{\sigma_y^2}d\sigma_{kl} \tag{A-17}$$

A.2 Rate-dependent plasticity

One way to treat rate-dependent plasticity is simply by using an explicit strain rate hardening relation for the effective plastic strain rate. For example, the effective plastic strain rate $\dot{\bar{\epsilon}}_{\mathrm{p}}$ is directly given by an empirical hardening power rule

$$\dot{\bar{\epsilon}}_{\mathrm{p}} = \dot{\bar{\epsilon}}_0 \left(\frac{\sigma_{\mathrm{e}}}{g}\right)^{1/m} \tag{A-18}$$

where, $\dot{\epsilon}_0$ is a reference effective plastic strain rate, m is the rate sensitivity exponent, σ_{e} is the von Mises effective stress.

The hardening strength $g(\epsilon_{\mathrm{p}})$ in Eq. (A-18) can be given by a power law relation, for example

$$g\left(\epsilon_{\mathrm{p}}\right) = Y\left[1 + \frac{\bar{\epsilon}_{\mathrm{p}}}{\epsilon_0}\right]^N \tag{A-19}$$

where Y is a reference flow strength, $\bar{\epsilon}_{\mathrm{p}}$ is effective plastic strain and $\epsilon_0 = Y/E$ is the initial yield

strain.

Note that in both rate-independent and rate-dependent plasticity, we calculate plastic increment. However the concept of "time" in plasticity is a monotonically increasing parameter, which is used to measure the loading and deformation history. Time here is not the physical time in our daily life.

APPENDIX B

FORMULATION IN CONVECTED COORDINATES

For the completeness in aspect of displacement finite element analysis, the finite strain plasticity formulations based on convected coordinate are briefly summarized. Many equivalent formulations can be derived for the finite element analyses, only the formulations based on convected coordinates are adopted here. Works on convected coordinate formulations are given by Green and Zerna [179] and Budiansky [180]. The formulations here are summarized from Needleman [181] and Peirce et al. [182].

The convected coordinate net is introduced in the reference configuration, and changes as the body deforms. The convected coordinates for each material point is denoted by y^i $(i = 1, 2, 3)$, which can be regarded as the labels of material points. Thus all field variables can be expressed as functions of convected coordinates and time.

In general tensor analysis, subscripts represent covariant components, superscripts represent contravariant components. The conventional summation notation for dummy indices is adopted. The covariant base vectors in reference and current configurations are defined respectively as

$$\boldsymbol{g}_i = \frac{\partial \boldsymbol{X}}{\partial y^i} \qquad \bar{\boldsymbol{g}}_i = \frac{\partial \boldsymbol{x}}{\partial y^i} \tag{A-1}$$

The corresponding covariant metric tensors in reference and current configurations are

$$g_{ij} = \boldsymbol{g}_i \cdot \boldsymbol{g}_j \qquad \bar{g}_{ij} = \bar{\boldsymbol{g}}_i \cdot \bar{\boldsymbol{g}}_j \tag{A-2}$$

The contravariant base vectors in reference and current configurations can be obtained by

$$\boldsymbol{g}^i = g^{ij}\boldsymbol{g}_j \qquad \bar{\boldsymbol{g}}^i = \bar{g}^{ij}\bar{\boldsymbol{g}}_j \tag{A-3}$$

Where the contravariant metric tensors $g^{ij}, \bar{g}^{ij}$ are the inverse of their corresponding convariant metric tensors. The Lagrangian strain tensor is defined as

$$\boldsymbol{\eta} = \frac{1}{2}(\boldsymbol{F}^{\intercal}\boldsymbol{F} - \boldsymbol{I}) \tag{A-4}$$

Given the transformation between base vectors $\bar{\boldsymbol{g}}_i = \boldsymbol{F} \cdot \boldsymbol{g}_i$, a relation between covariant components of $\boldsymbol{d}$ in current configuration and $\dot{\boldsymbol{\eta}}$ in reference configuration can be obtained

$$\bar{\boldsymbol{g}}_i \cdot \boldsymbol{d} \cdot \bar{\boldsymbol{g}}_j = \boldsymbol{g}_i \cdot \dot{\boldsymbol{\eta}} \cdot \boldsymbol{g}_j \tag{A-5}$$

For elastic-viscoplastic solids, by adopting tangent modulus approach [182], the rate form of constitutive relation can be expressed as

$$\hat{\boldsymbol{\tau}} = \boldsymbol{C} : \boldsymbol{d} - \boldsymbol{R} \tag{A-6}$$

Where $\boldsymbol{C}$ is the tensor of incremental moduli for Jaumann stress rate. Small elastic strains are presumed, i.e. $\hat{\tau}^{ij} = C^{ijkl}d_{kl}$ and $\boldsymbol{C}$ is a constant. For the problem discussed here, the following specific expressions are derived [182]

$$\boldsymbol{C} = \boldsymbol{L}^e - (\frac{\xi}{1+\xi})\frac{1}{\omega}\boldsymbol{P}\boldsymbol{P}, \qquad \boldsymbol{R} = \frac{\dot{\varepsilon}_{pt}}{1+\xi}\boldsymbol{P} \tag{A-7}$$

$$\omega = \boldsymbol{p} : \boldsymbol{L} : \boldsymbol{p} + \left(\frac{\dot{\varepsilon}_{pt}}{\dot{\varepsilon}_0}\right)^m \frac{d\mathrm{g}}{d\varepsilon_p}, \qquad \xi = \frac{\kappa\Delta t\omega\dot{\varepsilon}_{pt}}{m\sigma_e}, \qquad \boldsymbol{P} = \boldsymbol{L}^e : \boldsymbol{p} \tag{A-8}$$

Where $\dot{\varepsilon}_{pt}$ is $\dot{\varepsilon}_p$ at time step t, Δt is time interval for integration. The weight parameter $\kappa \in [0, 1]$ with $\kappa = 0$ corresponds to the explicit Euler method. $\boldsymbol{p}$ is given by J2 flow theory

$$\boldsymbol{p} = \frac{3}{2}\frac{\boldsymbol{\sigma}'}{\sigma_e} \tag{A-9}$$

The relation between convected derivative and Jaumann rate of Kirchhoff stress is

$$\hat{\boldsymbol{\tau}} = \dot{\boldsymbol{\tau}}^c + \boldsymbol{d}\cdot\boldsymbol{\tau} + \boldsymbol{\tau}\cdot\boldsymbol{d} \tag{A-10}$$

Where the convected derivative of Kirchhoff stress is defined as

$$\dot{\boldsymbol{\tau}}^c = \dot{\tau}^{ij}\bar{\boldsymbol{g}}_i \otimes \bar{\boldsymbol{g}}_j \tag{A-11}$$

From Eqs. (A-6), (A-10) and (A-5), based on the current base vectors, the component form relation can be obtained as

$$\dot{\tau}^{ij} = L^{ijkl}\dot{\eta}_{kl} - R^{ij} \tag{A-12}$$

Where the tangent modulus for convected stress rate is written as

$$L^{ijkl} = C^{ijkl} - \frac{1}{2}\Big(\bar{g}^{ik}\tau^{jl} + \bar{g}^{jk}\tau^{il} + \bar{g}^{il}\tau^{jk} + \bar{g}^{jl}\tau^{ik}\Big) \tag{A-13}$$

The rate of nominal stress can be expressed in terms of Kirchhoff stress as

$$\dot{s}^{ij} = \dot{\tau}^{ik}F^j_{\cdot k} + \tau^{ik}\dot{u}^j_{,k} \tag{A-14}$$

After using Eqs. (A-12), (A-14) and the minor symmetry of elastic modulus tensor, Eq. (4.1) yields the finite element model given by

$$\Delta t\int_V \big(K^{ijkl}\dot{u}_{l,k} - R^{ik}F^j_{\cdot k}\big)\delta u_{j,i}\,dV = \Delta t\int_S \dot{T}^j\delta u_j\,dS - \left(\int_V s^{ij}\delta u_{j,i}\,dV - \int_S T^j\delta u_j\,dS\right) \tag{A-15}$$

With

$$K^{ijkl} = L^{piqk}F^l_{\cdot q}F^j_{\cdot p} + \tau^{ik}g^{jl} \tag{A-16}$$

APPENDIX C

VALUES OF ζ FOR CONSTANT LOAD AND HOLD INDENTATION CREEP

The tabulated values of $\zeta(n, \dot{\epsilon}_0 t_2)$ are given in Eqs. (A-1) to (A-3). For the values of n and $\dot{\epsilon}_0 t_2$ that are not tabulated, the value of $\zeta(n, \dot{\epsilon}_0 t_2)$ used in Eq. (5.13) is obtained by linear interpolation between tabulated values.

$$\zeta(1, \dot{\epsilon}_0 t_2) = \begin{cases} 4.7 \times 10^4, & \dot{\epsilon}_0 t_2 = 0.1 \\ 4.7 \times 10^3, & \dot{\epsilon}_0 t_2 = 1.0 \\ 4.7 \times 10^2, & \dot{\epsilon}_0 t_2 = 10.0 \\ 4.7 \times 10^1, & \dot{\epsilon}_0 t_2 = 100.0 \end{cases} \qquad \zeta(2, \dot{\epsilon}_0 t_2) = \begin{cases} 2.4 \times 10^5, & \dot{\epsilon}_0 t_2 = 0.1 \\ 4.7 \times 10^4, & \dot{\epsilon}_0 t_2 = 1.0 \\ 1.4 \times 10^4, & \dot{\epsilon}_0 t_2 = 10.0 \\ 4.7 \times 10^3, & \dot{\epsilon}_0 t_2 = 100.0 \end{cases} \tag{A-1}$$

$$\zeta(3, \dot{\epsilon}_0 t_2) = \begin{cases} 9.4 \times 10^4, & \dot{\epsilon}_0 t_2 = 0.1 \\ 4.7 \times 10^4, & \dot{\epsilon}_0 t_2 = 1.0 \\ 1.9 \times 10^4, & \dot{\epsilon}_0 t_2 = 10.0 \\ 9.4 \times 10^3, & \dot{\epsilon}_0 t_2 = 100.0 \end{cases} \qquad \zeta(4, \dot{\epsilon}_0 t_2) = \begin{cases} 1.4 \times 10^5, & \dot{\epsilon}_0 t_2 = 0.1 \\ 1.1 \times 10^5, & \dot{\epsilon}_0 t_2 = 1.0 \\ 9.4 \times 10^4, & \dot{\epsilon}_0 t_2 = 10.0 \\ 3.8 \times 10^4, & \dot{\epsilon}_0 t_2 = 100.0 \end{cases} \tag{A-2}$$

$$\zeta(5, \dot{\epsilon}_0 t_2) = \begin{cases} 1.4 \times 10^5, & \dot{\epsilon}_0 t_2 = 0.1 \\ 1.1 \times 10^5, & \dot{\epsilon}_0 t_2 = 1.0 \\ 9.4 \times 10^4, & \dot{\epsilon}_0 t_2 = 10.0 \\ 7.5 \times 10^4, & \dot{\epsilon}_0 t_2 = 100.0 \end{cases} \qquad \zeta(n > 5, \dot{\epsilon}_0 t_2) = \begin{cases} 1.4 \times 10^5, & \dot{\epsilon}_0 t_2 = 0.1 \\ 1.1 \times 10^5, & \dot{\epsilon}_0 t_2 = 1.0 \\ 9.4 \times 10^4, & \dot{\epsilon}_0 t_2 = 10.0 \\ 9.4 \times 10^4, & \dot{\epsilon}_0 t_2 = 100.0 \end{cases} \tag{A-3}$$

APPENDIX D

LIKELIHOOD ANALYSIS

One way to consider responses from multiple signal types is simply to organize responses from various test types into one matrix $(\boldsymbol{Y}_1; ...; \boldsymbol{Y}_{K_y})$, which is $(\sum_{q=1}^{K_y} K_{\mathrm{d}q}) \times 2$, $K_{\mathrm{d}q}$ is the number of data points in the response matrix $\boldsymbol{Y}_q$, $q = 1, ..., K_y$. Then we can treat the responses from multiple test types as a single signal type, Eq. (A-12).

Consider a simple case in which we have two signal types, i.e., $K_y = 2$, and suppose we have data vectors X and Y that are independent given θ (Here we consider the special case where θ is a scalar, but the results generalize to the case of multiple parameters). The data X and Y have log-likelihoods $\ell_1(\theta)$ and $\ell_2(\theta)$, respectively. This entails that the log-likelihood for the combined data (X, Y) is

$$\ell(\theta) = \ell_1(\theta) + \ell_2(\theta). \tag{A-1}$$

For the moment, think of ℓ as a general likelihood. Defining $\hat{\theta}$ to be the MLE, classical likelihood theory tells us (assuming standard regularity conditions) that

$$\mathrm{Var}(\hat{\theta}) \sim \frac{-1}{E[\ell''(\theta_0)]},$$

where θ_0 is the true parameter value and

$$\ell''(\theta) = \frac{\partial^2}{\partial \theta^2} \ell(\theta).$$

This result will be applied to the case where ℓ has the form (A-1) and to the individual likelihoods ℓ_1 and ℓ_2.

When (A-1) is the likelihood, we have

$$\ell'(\theta) = \ell_1'(\theta) + \ell_2'(\theta) \quad \text{and} \quad \ell''(\theta) = \ell_1''(\theta) + \ell_2''(\theta).$$

At this point we will assume that

$$\ell_1(\theta) = \sum_{i=1}^{m} \ell_{1i}(\theta) \quad \text{and} \quad \ell_2(\theta) = \sum_{j=1}^{n} \ell_{2j}(\theta),$$

where $\ell_{1i}(\theta) = \log f_1(X_i|\theta)$ and $\ell_{2j}(\theta) = \log f_2(Y_j|\theta)$. In other words, X and Y are i.i.d. samples. We will also assume that $m/(m+n) \to \rho$ $(0 < \rho < 1)$ as m, n tend to ∞. Now let ℓ''_{k1} denote the second partial derivative of ℓ_{k1} with respect to θ, $k = 1, 2$. Then

$$\begin{aligned} \mathrm{Var}(\hat{\theta}) &\sim \frac{-1}{(mE_1 + nE_2)} \\ &\sim \frac{1}{(m+n)} \cdot \frac{-1}{[\rho E_1 + (1-\rho)E_2]}, \end{aligned} \tag{A-2}$$

where

$$E_1 = E(\ell''_{11}(\theta_0)) \quad \text{and} \quad E_2 = E(\ell''_{21}(\theta_0)).$$

Another approach to estimating θ_0 would be to compute MLEs (separately) from the two samples and then use a convex combination of the two MLEs. Let $\hat{\theta}_1$ and $\hat{\theta}_2$ be the MLEs from the X and Y samples, respectively. Then we may use the estimator

$$\hat{\theta}_w = w\hat{\theta}_1 + (1-w)\hat{\theta}_2,$$

where w is fixed a priori. The variance of $\hat{\theta}_w$ is $w^2\mathrm{Var}(\hat{\theta}_1) + (1-w)^2\mathrm{Var}(\hat{\theta}_2)$. Using the likelihood theory above, we have

$$\mathrm{Var}(\hat{\theta}_1) \sim \frac{-1}{mE_1} \quad \text{and} \quad \mathrm{Var}(\hat{\theta}_2) \sim \frac{-1}{nE_2},$$

and so

$$\mathrm{Var}(\hat{\theta}_w) \sim \frac{-1}{m+n} \cdot \left[\frac{w^2}{\rho E_1} + \frac{(1-w)^2}{(1-\rho)E_2} \right]. \tag{A-3}$$

Of interest is comparing the variances (A-2) and (A-3). It is easily checked that the smallest right hand side of (A-3) is when $w = V_2/(V_1 + V_2)$, where

$$V_1 = \frac{-1}{\rho E_1} \quad \text{and} \quad V_2 = \frac{-1}{(1-\rho)E_2}.$$

With this choice of w,

$$\mathrm{Var}(\hat{\theta}_w) \sim \frac{1}{m+n}\frac{V_1 V_2}{(V_1+V_2)} = \frac{1}{(m+n)} \cdot \frac{-1}{[\rho E_1 + (1-\rho)E_2]}.$$

Remarks

- Suppose that $E_1 = E_2$, as would happen in the case where one divided an i.i.d. data set into two parts. Then the best choice for w is ρ, i.e., the best weights are proportional to the sample sizes.

- When the likelihoods are fundamentally different (i.e., $E_1 \neq E_2$), then $\mathrm{Var}(\hat{\theta}_w) > \mathrm{Var}(\hat{\theta})$ when w is not the optimal weight. Since the optimal weight depends on an unknown parameter, this is an important consideration. The weight could be estimated, but the error in estimation will undoubtedly make the finite sample variance of $\hat{\theta}_{\hat{w}}$ larger than that of $\hat{\theta}$.

- All things considered, it seems better to use the estimator based on the complete likelihood since it gives an estimator with variance no larger than the one from a convex combination.

This dissertation was typeset with LaTeX* by the author.

*LaTeXis a document preparation system developed by Leslie Lamport as a special version of Donald Knuth's TEX Program.